A long time ago in a lab far, far away...

Meanwhile, a team of only the bravest GeDI pilots is underway on a recon mission. Hidden in SPHERICAL NANOPARTICLES, they trojanically allow engulfment by the Stem Cell OUTER MEMBRANE RIM in order to reach the INNER PLASM...

Rescue Forces' coils of the Merged Rebellion Initiative (MRI) suddenly receive hopeful hyperintense signal from the INNER PLASM. All hope now rests on MRI to locate the signal in KAY-SPACE and read-out the viability of the POPULATION of the...

# STEM CELLS

# MRI-based stem cell imaging using Gd-nanocarriers

## MRI-beeldvorming van stamcellen met Gd-nanopartikels

Jamal Guenoun

Cover Design: A.W. Everaers/J. Guenoun
Layout: A.W. Everaers
Author: J. Guenoun
ISBN: 978-90-9030158-7
Cover: Alternative abstract of chapter 4, heavily inspired by *Star Wars*

# MRI-based stem cell imaging using Gd-nanocarriers

## MRI-beeldvorming van stamcellen met Gd-nanopartikels

Proefschrift

ter verkrijging van de graad van doctor aan de
Erasmus Universiteit Rotterdam
op gezag van de
rector magnificus

Prof.dr. H.A.P. Pols

en volgens besluit van het College voor Promoties.
De openbare verdediging zal plaatsvinden op

19 januari 2017 om 11.30 uur

Jamal Guenoun
geboren te 's-Gravenhage

Erasmus University Rotterdam

## Promotiecommissie:

| | |
|---|---|
| Promotor: | Prof.dr. G.P. Krestin |
| Copromotor: | Dr. M.R. Bernsen |
| Overige leden: | Prof.dr. C.W.G.M. Löwik<br>Prof.dr. A. Heerschap<br>Prof.dr. D.J.G.M. Duncker |

# Table of contents

# Chapter 1

# General Introduction Thesis Aim and Outline

*"The tails of lizards and of serpents, if they be cut off, will grow again"*

(Aristotle, History of Animals, book II, chap. 17, 508b 4-7)

# GENERAL INTRODUCTION

## The Stem Cell and its Potential

The regeneration of body parts is surely not a new concept to mankind. The recognition of the regenerative capabilities of an organism dates back to 330 BC, when Aristotle observed that a living lizard could grow back the lost tip of its tail. Since then, attempts at understanding the regenerative capabilities of human being have progressed in a slow pace. In the new millennium, biology and biotechnology are increasingly being recognized as a serious competitor of biochemistry, aiming to offer "biological solutions to biological problems." As a result, the interest in the area of stem cells has virtually exploded in the last decade. Edmund B. Wilson first mentioned the term "stem cell" in his book, The Cell in Development and Inheritance, in 1896. Stem cells are pluripotent cells with the unique ability to self-renew and differentiate into one or more specialized cell types, playing a crucial role in homeostasis and tissue repair. Following an injury, a stem cell self-renews, undergoing cell division to ultimately give rise to one daughter stem cell and one progenitor cell. Stem cells can be classified as (a) multipotent adult stem cells (ASCs) in the developed body (b) pluripotent embryonic stem cells (ESCs) harvested from a blastocyst and (c) induced pluripotent stem cells (iPSCs), which are somatic cells genetically reprogrammed to an embryonic stem cell state.

Stem cell therapy (or transplantation) is the use of stem and progenitor cells to replace defective cell populations, profiting from the plasticity and migratory capacity of stem cells.

After systemic or local transplantation, stem cells are able to migrate and differentiate at pathologic sites in the body to produce a therapeutic effect. Thus, cell-based therapies are valued as a promising innovative strategy to tackle diseases of various organs systems. Ultimately, personalized cell therapies for treating and curing human diseases are the ultimate goal of most stem cell-based research.

The first known human application dates back to 1959, when Edward Thomas aimed at a hematological reconstitution with isologous bone marrow in lethally irradiated patients with acute leukemia (101).

Since then, numerous animal studies have been carried out with moderate to major successes, focusing on diseases of various organ systems (7,60,89). For patients with bone marrow failure or leukemia autologous stem cell transplantation is an already established therapy strategy. Other more experimental applications include disorders of various origins: neurodegenerative (e.g. multiple sclerosis (51)), neurotrauma (cerebral (120) or spinal cord injury (22)), cardiovascular (myocardial infarction (12,66,66,85)) and musculoskeletal disorders, cancer (melanoma (110)), arthritis, diabetes (83,104), and peripheral vascular disease.

To illustrate, the US public clinical trials database, http://www.clinicaltrials.gov, shows 1377 completed and 1337 ongoing clinical trials using stem cells for a variety of diseases (accessed 22/04/2015, unknown status excluded).

## Challenges in Stem Cell Therapy

Based on the progress that has been obtained in small and large animal studies in the last decade, cellular transplantation was embraced as the Holy Grail in tissue regeneration, accelerating clinical translational applications. Despite the fact that the novelty of cell transplantation was ambitiously translated to the clinical arena, it failed to produce overwhelming clinical success stories. Clearly, humans are not just big mice. While some clinical studies

indeed showed a positive effect (59), they were increasingly contrasted by studies failing to prove such a beneficial clinical effect, an issue probably even underreported (25,35,70). These ambiguous results are not entirely surprising, realizing that stem cells face a daunting task during transplantation. The often hostile environment of ischemia, necrosis and/or inflammation that reigns within transplant accepting tissue, has a tremendous impact on stem cell function, potentially hampering the viability, differentiation and integration of the grafted cells into the host tissue (88). In addition, the spectrum of available types of stem cells is broad, each with its own biological phenotype and behavior. Currently, many cell types are being considered for cell-based therapy; here the challenge lies in determining which types are most suitable in trying to fulfill criteria regarding therapeutic efficacy, ease of access and practical use. Establishing the efficacy of different routes of administration of the cells is another point of research attention. Direct implantation, intravenous and even selective intraarterial (intracoronary *in casu* cardiac applications) administration lead each to a different biodistribution of cells. Stem cell function itself, however, is not the only or perhaps not even the most important parameter to monitor. Recent observations gained insights in transient paracrine actions of stem cells, aside from the regenerative ability. Trophic factors were reported to be released by stem cells, eliciting responses from resident cells (11,41). The efficacy of any cell therapy thus depends on the interaction of many different factors such as disease etiology, cell type, delivery route, cell retention/engraftment, activation of resident cells, and functional integration.

Efficacy, however, is not the only hurdle. With the rapid progress of research in this field, increased sociopolitical awareness raised concerns on the safety and ethics of stem cells. Moral objections were made to the creation of human embryos from which embryonic stem cells (ESCs) are derived. Opponents of stem cell research that uses human embryos, claimed that it must be accorded fundamental human rights from the moment of its conception (10). To them, removal of the ESCc at the blastocyst stage (around the third to fifth day of embryogenesis) resulting in embryonic death qualifies as homicide (10,79). These ethical worries are avoided by the use of adult stem cells (ASCs). ASCs are found throughout the body in differentiated organs. Several types are recognized, i.a. mesenchymal stem cells (MSCs), hematopoietic stem cells, neural stem cells, endothelial stem cells. Mesenchymal stem cells (MSCs), a type of ASC, are defined by their fibroblast-like morphology, adherence to plastic, and capacity for differentiation. MSCs are most often derived from bone marrow but can also be isolated from adipose tissue. In multiple in vitro studies their potential for cell therapy was shown. Since ASCs are adult cells that are often autologously acquired, the requirement to create an embryo is obviated. Unfortunately, compared with ESCs, the ability of ASCs to differentiate is less elaborate: being pluripotent (not multipotent) cells their differentiation is restricted to subsets of a certain lineage (in case of MSCs to osteogenic, chondrogenic, and adipogenic cells).

Takahashi and Yamanaka announced in 2006 that the ectopic expression of four genes (*Sox2*, *Oct4*, *Klf-4* and *c-Myc*) can reprogram differentiated adult skin cells to transform into pluripotent cells (97). These 'artificial' ESCs were coined 'induced pluripotent stem cells' (iPSCs, hiPSCs in humans). As the generation of these iPSCs would no longer require the use of embryos, many ethicists pronounced this discovery to have solved the ethical issues. Moreover, the autologous origin would bypass any issues with immunogenicity. Intriguingly, aside from the therapeutic potential, iPSCs were revealed to harbor diagnostic potential as well. iPSCs derived form a spinal muscular atrophy patient may mimic the neurodegenerative process characteristic of this genetically inherited disease *in vitro* (34), facilitating an 'in-dish' live study of disease. On the other side, critics claimed iPSCs to not behave enough like human embryonic stem cells and retain some "epigenetic memories" of their original somatic cells possibly interfering with differentiation. Even others were worried by the amount of required manipulation to cause unwanted mutations (52).

With regard to safety, it is crucial to be informed about any potential adverse effects or direct toxic effects of stem cells *in* vitro prior to any clinical translation. Many studies have shown the stem cells to remain their pluripotency and to be safe. The main concern is to control wayward stem cells, as risks of neoplastic transformation are in wait, inherent to the stem cell ability to unlimited proliferation. Indeed stem cells were shown to be able to induce teratomas or differentiate into malignant tumors of a single cell type (74,77).
Nonetheless, poorly understood is the interplay of the transplanted cells with the local, locoregional and even systemic environment, of which most actions remain hidden from researchers' observations ('black box'). Stem cell therapy thus heralds a complex process in which the stem cell fate is unclear. Eventually it was acknowledged that the translational step was perhaps too ambitious at the time and that a modest step back to benchside was warranted. To elucidate the stem cell fate, the 'gold standard' of histology is a widely accepted and valuable tool in preclinical research, but in the clinical setting it is of limited use. It only provides a snap-shot at a certain timepoint, inherently triggering the endstage of the experiment, rendering an *in vivo*, real-time, longitudinal and noninvasive follow-up impossible. Local diagnostic biopsy is theoretically possible but an invasive procedure and thus preferentially to be avoided in the delicate posttransplantation area. Facilitated by ongoing improvements and design of novel techniques, the field of imaging sciences at some point converged towards regenerative medicine, fueling joined efforts to add pieces to the stem cell puzzle: to track the cells *in vivo* making use of clinical imaging modalities.

## Cell Imaging: seeing Stem Cells at Work in vivo

Ergo, '*seeing the stem cells at work in vivo*' (94) is the goal to which increasing research efforts in this field have leveraged. Cell imaging has been defined as "the visualization of specific cells in an intact animal" thus concerning the imaging of entire cells whereas molecular imaging seeks to visualize molecules and sub-cellular components within individual cells (69). As an alternative to histology, (pre)clinical imaging techniques, such as magnetic resonance imaging (MRI), computed tomography (CT), positron emission tomography (PET), ultrasound (US), single photon emission computed tomography (SPECT) or optical imaging (OI) offer new dimensions for cell therapy monitoring. Not only do they provide anatomical information allowing detection of morphological changes, they also facilitate an analysis of functional properties, owing to novel techniques, such as assessment of the left ventricle function after stem cell transplantation for heart failure (84) (i.e. functional MRI) or of perfusion characteristics (using contrast media). Traditionally, the radiological assessment remains macrocellular by nature. At the other end of the imaging spectrum, clinical nuclear imaging techniques (PET, SPECT) target sub-cellular molecular processes by function, using any anatomical information solely as a frame to locate the process. However, none of these techniques is able to visualize the transplanted cells without prior 'labeling' or 'tagging' of the transplanted cells.
In between is the novel domain of 'cell imaging'. In cell imaging cells are labeled or tagged with a suitable contrast agent *in vitro* prior to cell transplantation, commonly achieved by exposing the cells to the labeling agent in culture (20,73). Through endocytosis the labeling agent is then incorporated in the intracellular compartments, allowing the labeled cells to be imaged in real-time noninvasively as cell clusters *in vivo*, or even as single cells (21). Alternatively, cells of interest can be labeled with suitable contrast agents *in vivo*.
While it was already in the early nineties that the feasibility of cell tracking *in vivo* was reported (20,73), it was not until 2005 that the first clinical trial applying cell tracking of labeled cells *in vivo* took place (110). In between, numerous additional studies confirmed the feasibility of cell labeling and cell tracking both *in vitro* and *in vivo* by different imaging modalities without significant toxicity while preserving the regenerative stem cell capacities (16,20,21,28,31,48).

As a prerequisite of a favorable cell therapy outcome, stem cell transplants must first of all take the hurdle of survival in the transplantation area, later followed by an exhibition of their regenerative properties: migration (homing), engraftment, differentiation and integration into tissue. Reported high cell death rates post-transplantation, resulting from result of multiple mechanical, cellular and host factors, raised concerns, as stem cell survival was assumed to be the first and most important prerequisite for successful transplantation. Several studies have demonstrated that only 10–30% of transplanted stem cells survive within a few days of transplantation, further decreasing to 5–15% over 10–12 week (32,57,72). Unsurprisingly, researchers immediately took this to heart directing their efforts at improving stem cell viability (87,117). Undoubtedly, to be able to actually 'see' cell transplant viability *in vivo* by current clinical imaging techniques (a topic covered in this thesis) would certain contribute to our understanding of the premature stem cell death. The combined application of the stem cell as a viable 'drug agent' and at the same time as a 'diagnostic contrast agent' implicates a convergence of two 'ics': the 'therapeutics' and the 'diagnostics', commonly known as '(nano)theranostics' in the field of nanomedicine and gene therapy. With regard to cell size, 'microtheranostics' is probably better suited.
Enthused by these novel developments, radiology departments around the globe, acknowledging the potential of (stem) cell imaging, started setting up specialized 'molecular or cell imaging centers' to contribute to this novel field of research. From a (clinical) radiologist's perspective, finally new doors had opened to assess disease and therapy more upstream at the cell level rather than the ordinary assessment of macrocellular morphology and anatomy.

## Imaging Modalities for Cell Imaging

The arsenal of imaging modalities is quite extended, ranging from tissue-based contrast imaging modalities like MRI, CT and US to photon-based imaging modalities such as PET, SPECT and optical imaging (OI, consisting of bioluminescence (BLI) and fluorescence imaging). Each imaging modality has a variety of tracers, labels or contrast agents and each imaging technique has its own advantages and disadvantages for cell tracking studies. A thorough selection of the most suitable imaging modality with accompanying tracer needs to be made. For stem cell tracking purposes the modality should be translational too, allowing use in humans. In spite of research that showed the feasibility of labeling MSCs with gold nanoparticles allowing detection by computed tomography (CT) (13) and the fact that CT is a noninvasive imaging modality, it has never played a major role in cell imaging due to radiation aspects, the lack of sensitivity and low contrast-to-noise, especially for soft tissue parts.
Among the noninvasive imaging modalities, ultrasound (US) remains a commonly utilized modality for high-resolution evaluation of especially superficial soft-tissue. Among its advantages are its non-invasiveness, low cost, portability, the ability of dynamic imaging, the real-time interactivity and lack of ionizing radiation. The expansion of this imaging modality for stem cell delivery and tracking is, unfortunately, limited by its depth-dependent spatial resolution, the inability of ultrasound waves to penetrate hard tissue (e.g. bone) and the difficulty of attaching a long-lived ultrasound-visible label.
Unlike tissue-contrast based imaging, the photon emission-based imaging modalities (i.e. PET, SPECT and OI) generate images by detecting the release of light or other forms of electromagnetic radiation. In bioluminescence imaging (BLI), light emitted from cells containing the luciferase enzyme is detected. Although it has proven beneficial in preclinical research, it is not suitable for use in humans as it (i) suffers from light scattering, limiting its use to small animals only and (ii) requires both genetic transformation and (iii) the invasive administration of luciferin substrate (81). The first limitation precludes the use of fluorescent imaging, an imaging modality that uses fluorophores as exogenous contrast agents, in humans as well.

In PET and SPECT signal capture is not based on light but on detection of high-energy γ-rays. PET and SPECT are not limited by signal penetration depths in tissue (94). In PET, decay of a radiotracer causes a positron to be emitted. Upon encounter of an electron a positron-electron "coincident" event results in an annihilation pair that emits two gamma ray photons in the opposite direction. SPECT involves detection of γ-rays too, but in a slightly different way. In SPECT imaging the gamma radiation is measured in two-dimensional projections that are reconstructed into a tomographic image, without a "coincident" event. This difference accounts for the higher sensitivity obtained from PET versus SPECT scans. However, SPECT and PET are not without limitations; (i) PET imaging in small animals requires (micro)pinhole apertures or micro-PET small-animal scanners to achieve high resolutions (200 μm and/or 1 mm3) required for small animal imaging. Moreover, (S)PE(C)T tracers (ii) undergo uptake in normal tissues (e.g., the heart with [18F-FDG] F18-fluoro-deoxyglucose) hampering the specificity, (iii) cause nonnegligible tissue photon attenuation, (iv) raise concerns regarding radiation damage to cells, (v) suffer from a generally short half-life and (vi) need to be present in adequately high cellular concentration to meet detection thresholds (24,94).
Studies aimed at clinical translatability, have therefore mainly focused on MRI. The main advantages of MRI over other techniques are (i) its excellent 3-dimensional anatomical imaging capabilities at high resolution (ii) together with functional imaging capabilities, (iii) the lack of ionizing radiation and (iv) the possibility of small animal imaging with clinical scanners requiring mere modification of surface coils. MRI is therefore regarded as the imaging technique of choice for clinically applicable cell tracking.

## Cell Labels for MRI

Compared with other imaging modalities, MRI provides an unprecedented anatomical resolution. However, its success in cell imaging suffers because of its intrinsic insensitivity (4). To overcome this relative weakness, efforts have focused on increasing the sensitivity of the contrast agent (CA) itself, or on an amplification of the intracellular accumulation using e.g. nanocarriers such as micelles (1,46,103), or liposomes (33,49,71).
Two types of MRI cell 'labels' are recognized: intrinsically active labels, producing signal without extrinsic intervention (direct labeling), and activatable ('switchable') cell labels such as reporter gene based contrast agents (indirect labeling) (5,29,65). Indirect labeling carries important advantages regarding the in vivo monitoring of cell fate and function but while widely used in animal models, this approach is currently far from clinical translation and beyond the scope of this thesis. Specific reviews on that topic are available elsewhere (17,107).
For cell transplants to be imaged by MRI, they must be distinguished from natural background noise signal. The ideal cell label or tracer is one which, after sufficient intracellular build-up, allows prolonged and stable retention enabling longitudinal imaging, is readily available at acceptable costs, is taken up by cells easily and efficiently, does not suffer from leakage prematurely, has a sufficiently low detection threshold differentiating it from the background and carries insignificant biological toxic and side effects, on genetic and phenotypic level.
Imaging agents for MRI-based cell tracking can be subdivided into the following categories: T2 contrast agents (superparamagnetic contrast agents, SPIOs), T1 contrast agents (paramagnetic contrast agents, typically containing gadolinium or manganese), CEST agents and non-proton contrast agents (typically containing fluorine). Each of these categories of contrast agents have specific properties with associated advantages and limitations (Table I). In many cases these agents have been used in the form of nanoparticles in order to increase their biocompatibility, delivery efficiency and/or signaling properties.

**Table 1** Various imaging modalities and their characteristics

| Imaging modality | Resolution[1] | Depth | Time for image acquisition | Quantitative | Target | Clinical use | Notes |
|---|---|---|---|---|---|---|---|
| MRI | 10-100 µm | no limit | minutes to hours | yes | Anatomical, physiological, molecular | yes | Non-invasive, non-radioactive, excellent spatial resolution but costly |
| CT | 50 µm | no limit | minutes | yes | Anatomical, physiological, | yes | Usually combined with PET or SPECT, high radiation exposure |
| PET/SPECT | 1-2 mm | no limit | minutes to hours | yes | Physiological, molecular | yes | Versatile imaging modality with many tracers and high sensitivity |
| Fluorescence reflectance imaging | 2-3 mm | < 1 cm | seconds to minutes | no | Physiological, molecular | yes | Suitable for imaging molecular events at surface tumor but have limited depth resolution |
| Bioluminescence imaging | several mm | cm | minutes | no | Molecular | no | Can detect gene expression |
| FMT | 1 mm | < 10 cm | minutes to hours | yes | Physiological, molecular | in development | Quantitative imaging of fluorochrome reporters |
| Intravital microscopy | 1 µm | < 400-800 µm | seconds to hours | no | Anatomical, physiological, molecular | in development | Single cell resolution but have limited depths |

## T2 Contrast Agents

Superparamagnetic iron oxide (SPIO) particles typically consist of a crystalline iron oxide (Fe3O4 or Fe2O3) core coated with a hydrophilic shell of dextran, citrate, polymers or lipids. The iron oxide crystals have a strong magnetic moment, causing a disturbance of the local magnetic field by which they affect the T2 relaxation of surrounding water protons resulting in local signal loss in MR images. SPIO particles have a stronger effect on MR relaxivity than paramagnetic agents (47).
Already in the early nineties studies using these SPIO agents for labeling of a variety of cells demonstrated safety of the use of SPIOs for intra-cellular labeling and the consequent tracking of the labeled cells by MRI (20,73). Rapid clinical implementation of commercially available FDA-approved (ferumoxides and ferucarbotran) SPIO particles followed (30,37). Main incentives for the interest in SPIO particles are their unparalleled detection sensitivities (see Table II) as MRI labels. However, the use of these agents in (pre)clinical studies revealed some practical and technical limitations: (i) SPIO-labeled stem cells still generate a signal void despite cell death, hampering the cell viability specificity (9,15), (ii) quantifying engraftment becomes unreliable because of the considerable residual signals generated by the persistence of iron-laden tissue macrophages after cell death (76,78,100), (iii) even in absence of residual signals the quantification of T2 and $T2^*$ relaxation times is difficult as it depends on intravoxel distribution (56), accelerated SPIO dilution occurs in highly proliferating cells as a result of iron metabolism in the physiological cellular pathways (113,114).
Unfortunately, these SPIOs have ceased to be manufactured for economic reasons (27) limiting the use of SPIOs for new and ongoing research. Despite this, efforts are made to generate new, optimized SPIO particles for cell labeling and imaging (19,58,64).

## $^{19}$F-based nanoparticles

Conventional MRI labeling techniques are based on the excitation of $^{1}$H nuclei. Athough $^{31}$P, $^{23}$Na and $^{13}$C can be excited by MR as well, their abundance in the human body restricts their use for cell imaging. Due to the natural absence of $^{19}$F nuclei in the body, 19F labeled cells are endorsed with a with high specificity (82). However, $^{19}$F imaging does require some dedicated hardware on a MRI system, which is usually not routinely available in most MRI centers.
For cell labeling, studies have mainly focused on the use on perfluorocarbons (PFC's) (92). A main advantage of PFC's is that each molecule contains a high number of $^{19}$F nuclei, increasing the signaling capacity per molecule. In order to promote biocompatibility and cell loading efficiency, formulations of PFC's used for cell labeling and imaging generally consist of coated nano-emulsions or polymer-based nanoparticles (45,91,93). A nano-emulsion based formulation of PFC's was also used in the very recently published first report on $^{19}$F-based cell imaging in humans (2). In this study, dendritic cells (DC's) were labeled with a PFC nano-emulsion formulation, with the purpose of visualizing the DC's after intradermal administration as part of a phase-I trial. While this study demonstrated the clinical feasibility of 19F-based cell tracking, the current main concern of $^{19}$F-based cell imaging, i.e. limited sensitivity, was also highlighted. The lowest amount of cell to be detected was between $4x10^5$ and $6.25x10^5$ cells/voxel. In comparison, in the first reported human application of iron-oxide-based cell imaging a significantly lower detection sensitivity of of $2x10^3$ cells/voxel was demonstrated (111). Nonetheless, the results were encouraging and will certainly further inspire already ongoing efforts to develop improved $^{19}$F-based cell imaging techniques. These involve efforts to increase cellular uptake by probe modifications or the use of transfection agents that promote cellular

uptake of particles (3,90,112), probe modifications that increase the signaling capacity per molecule (23,109) and hard- and software developments (6).



# T1 Contrast Agents

## Manganese

Similar to Gadolinium (see further), manganese is also a T1 contrast agent, shortening the relaxation time of surrounding water protons. Because of the concerns regarding the cellular toxicity of Gd ions, manganese has been studied as an alternative positive contrast agent for cell labeling. Manganese is a natural cellular component and functions, for instance, as a co-factor for enzymes and receptors. Manganese as a contrast agent has been used in the form of the FDA-approved manganese chloride. Initial studies on the use of manganese-based agents for cell labeling and imaging also used $MgCl_2$ (40). Moreover, because of the fact that manganese is transported by calcium channels, $MnCl_2$ has been proposed as a cell labeling agent by which a direct read out of the viability of cells would be possible (116). Because of the low relaxivity properties of $MgCl_2$, nanoparticle formulations of manganese have been explored as T1 agents for cell labeling. This involves manganese oxide particles with variations in coating with the goal to improve biocompatibility, stability and or relaxivity (61,115). Most recently silica coated MnO particles were shown to have excellent relaxivity properties, also at magnetic field strengths higher than 3.0T. This allowed for highly sensitive positive contrast detection of MnO-labeled cells, in the order of several thousand cells (Table 2). Unfortunately, however, in various reports significant effects of MnO particles on cell functionality have also been reported, such as reduced cell survival (95,116) and impaired multi-potent differentiation capacity (53,75). These findings may significantly reduce interest for clinical translation of such approaches.

## Gadolinium

Gadolinium ($Gd^{3+}$) chelates are the most commonly used contrast agents in clinical MRI and are generally characterized as T1 or positive contrast agents. The seven unpaired electrons of the $Gd^{3+}$ ion create a magnetic moment that shortens the T1 relaxation time of surrounding water protons typically resulting in signal enhancement on MR images.

Interaction of Gd-bound chelates with $H_2O$ protons decreases the water T1 and T2 relaxation times. The interactions occurring between Gd and $H_2O$ protons on the molecular level are twofold (122). 'Inner sphere relaxation' refers to the formation of a dipole-dipole interaction between a water molecule and the primary sphere of the paramagnetic $Gd^{3+}$ ion (with seven unpaired electrons). In this interaction, a chemical exchange occurs resulting in an enhanced relaxation of the water protons. Thus, the relaxation will be enhanced by an increased fraction of water molecules that can interact with Gd and by a shorter residence time of the water molecule with Gd (allowing Gd to interact with additional water molecules). 'Outer sphere relaxation' is a more complex concept. It is the result of the relative rotational and translational diffusion of water molecules and the paramagnetic ion. Basically stated, the relaxivity influence of the paramagnetic ion enhances when an increased number of water molecules can approach the paramagnetic ion and/or the further the paramagnetic ion can move through space and/or the closer the water protons can approach the paramagnetic ion.

The possibility of obtaining positive contrast from labeled cells instead of negative contrast as obtained with T2 contrast agents has been considered a major advantage, and stimulated the use of Gd-based nanoparticles for cell labeling. Remarkably, several studies reported a re-

duced longitudinal r1 relaxivity following cellular internalization of Gd *in vitro*, due to limited water exchange consequent to CA entrapment in cytoplasmic or subcellular compartments (14,18,38,54,55,62,86,98,99).
Despite the fact that various studies showed limited or no adverse effects of the Gd-based labeling agents on the functionality of labeled cells at relevant labeling concentrations (26,80,105,106), major concerns regarding the toxicity of the long term presence of ionic Gd exist (18,68,118) , which may limit introduction of such agents into the clinic. Gadolinium contrast agents have been associated with the occurrence of nefrogenic systemic fibrosis in patients with impaired kidney functions (44), and a negative effect on disease pathology of implanted neural stem cells labeled with the Gd-based contrast agent GRID (Gadolinium-Rhodamine Dextran) was reported in a rat stroke model (68).
As chelated Gd-based agents are too small molecules to be endocytosed by cells passively and because of sensitivity issues, strategies have been employed to encapsulate the Gd-chelates inside nanocarriers (e.g. liposomes, micelles) to attain significant amplification. Particulate Gd contrast agents were shown to be far more effective than regular Gd chelates in terms of the amount of Gd initially incorporated and the retention of Gd in the cell over time (43,80,106). Various particulate formulations of Gd-based cell tracking agents have been developed over the past few years including liposomal (8,39,50,55) and micellar (1,46,103) nanoparticles, polymer coated Gd-oxide particles (26,108), and carbon nanostructures (105) in order to increase cellular loading with Gd or to increase the signaling capacity by increasing the T1-relaxivity. Remarkably, several studies reported a reduced longitudinal r1 relaxivity following cellular internalization of Gd in vitro, due to limited water exchange consequent to CA entrapment in cytoplasmic or subcellular compartments (14,18,38,54,55,62,86,98,99). As this thesis centers on the use of liposomes as vehicles to carry Gd-chelates we will provide a short introduction on liposomes.

## Gadolinium-liposomes

Liposomes are nanoparticles consisting of a bilayer of (phospho)lipids, much like cellular bilayers. The bilayer consists of lipid constituents with hydrophobic head groups and hydrophilic tail groups. Various methods exist to fabricate liposomes. The most followed procedure is to dry an organic solution containing a mix of desired (phosho)lipids in a rotary evaporator under *in vacuo* conditions thus forming a thin lipid planar bilayer film. Hydration and sonication of this planar lipid film causes budding vesicles to enclose the hydration agent, resulting from phospholipids tail groups facing the inner area of the bilayer and the polar head groups facing the aqueous content. Multilamellar spheres are thus spontaneously formed, typically in a size range of 40-180 nm (121). The size can further be fine-tuned by passage through physical membrane pores of known size (extrusion). The versatility is demonstrated by the fact that both the constituents in the aqueous core and surface properties can be modulated. For example, the versatility is apparent from their use as an approved 'theranostic' anti-cancer drug (Doxil®), carrying contrast agent ('diagnostics') and drugs ('therapeutics') at the same time within a single liposome (36,63). Extensive studies proved the liposomes to be biocompatible and safe (102).
Gd-liposomes are formed by using a Gd contrast agent solution as the hydrating agent or by incorporation of Gd-lipids in the bilayer. Furthermore, the use of cationic synthetic lipids in the bilayer augments the uptake and endocytosis by anionic cell membranes. Gd-liposomes have been employed for a variety of applications in the form of either an intravenous contrast agent or a cell label. Their use as a 'stand-alone' intravenous contrast agents was demonstrated in multiple studies. For example, liposome encapsulated Gd-DTPA was demonstrated to detect early osteoarthritic changes in the knee (42) and shown to function as a longcirculating agent for MR angiography (MRA) (8). Alternatively, the incorporation of the Gd-lipid Gd-

**Table 2** Various contrast agents and their characteristics

| Probe | Basic imaging principle | Main advantage | Main disadvantage | Detection sensitivity (nr of cells)[#] | Used for cell tracking in human subjects. |
|---|---|---|---|---|---|
| Iron oxide nanoparticles | Shortening T2 relaxation of surrounding water protons. | High sensitivity | Lack of specific signal; difficult quantification | 1 cell (17, 18) | Yes (19-28) |
| Gd-based Nanoparticles | Shortening T1 relaxation of surrounding water molecules | Giving rise to signal enhancement | Issues regarding toxicity | 300-3000 cells[*1] (29-31) | No |
| Manganese-based nanoparticles | Shortening T1 relaxation of surrounding water molecules | Natural body mineral | Issues regarding toxicity | 1000-100.000 cells[*2] (32-34)<br>0.35 pg/cell<br>0.7 pg/cell | No |
| CEST agents | Transfer of selectively saturated, exchangeable spins to surrounding bulk water via chemical exchange. | Multi-spectral imaging | Requires specialized imaging techniques | 10.000 cells[*3] (35) | No |
| 19F-based nanoparticles | Magnetic spin of $^{19}F$ nuclei | Not naturally present in body, therefore providing unique signal. | Requires specialized imaging techniques | 2000-9000 cells[*4] (36, 37) | Yes (38) |

*1 at intra-cellular Gd concentrations of 0.05-70 pg/cell
*2 at intra-cellular Mn concentrations of 0.35-0.7 pg/cell
*3 at intra-cellular CEST agent concentrations of 3-4 mM/cell
*4 at intra-cellular $^{19}F$ concentrations of 0.35-0.7 pg/cell
[#] Detection sensitivity is highly dependent of various conditions, such as the cell type, intra-cellular loading, imaging parameters, and magnetic field strength

diethylenetriamine- pentaacetic acid (bis)stearylamide (Gd-DTPA-BSA) in liposomal bilayer together with phosphatidylserine (PS) resulted in apoptosis mimickers, facilitating the imaging of atherosclerotic plaques (67). Gd-DTPA-BSA was further used in liposomes containing the cyclic RGD-peptide to enable internalization by means of the $\alpha_v\beta_3$ integrin receptor in HUVEC cells *in vitro* (55). The work in this thesis focuses on the use of liposome encapsulated Gd.

To conclude, cell imaging is a promising strategy to answer vital questions regarding stem cell function. Cell imaging can contribute to elucidate specific aspect from the cell therapy 'black box', such as cell engraftment, cell viability, cell proliferation and differentiation, the immunogenicity and al tumorigenicity. These characteristics are paramount and form the root of success or failure of stem cell therapy.

# References


1. Accardo, A.; Tesauro, D.; Roscigno, P.; Gianolio, E.; Paduano, L.; D'Errico, G.; Pedone, C.; Morelli, G. Physicochemical properties of mixed micellar aggregates containing CCK peptides and Gd complexes designed as tumor specific contrast agents in MRI. J. Am. Chem. Soc. 126:3097–3107; 2004.
2. Ahrens, E. T.; Helfer, B. M.; O'Hanlon, C. F.; Schirda, C. Clinical cell therapy imaging using a perfluorocarbon tracer and fluorine-19 MRI. Magn. Reson. Med. Off. J. Soc. Magn. Reson. Med. Soc. Magn. Reson. Med. 72:1696–1701; 2014.
3. Ahrens, E. T.; Zhong, J. In vivo MRI cell tracking using perfluorocarbon probes and fluorine-19 detection. NMR Biomed. 26:860–871; 2013.
4. Aime, S.; Castelli, D. D.; Crich, S. G.; Gianolio, E.; Terreno, E. Pushing the Sensitivity Envelope of Lanthanide-Based Magnetic Resonance Imaging (MRI) Contrast Agents for Molecular Imaging Applications. Acc. Chem. Res. 42:822–831; 2009.
5. Alfke, H.; Stöppler, H.; Nocken, F.; Heverhagen, J. T.; Kleb, B.; Czubayko, F.; Klose, K. J. In vitro MR imaging of regulated gene expression. Radiology. 228:488–492; 2003.
6. Amiri, H.; Srinivas, M.; Veltien, A.; van Uden, M. J.; de Vries, I. J. M.; Heerschap, A. Cell tracking using (19)F magnetic resonance imaging: technical aspects and challenges towards clinical applications. Eur. Radiol. 25:726–735; 2015.
7. Antonic, A.; Sena, E. S.; Lees, J. S.; Wills, T. E.; Skeers, P.; Batchelor, P. E.; Macleod, M. R.; Howells, D. W. Stem cell transplantation in traumatic spinal cord injury: a systematic review and meta-analysis of animal studies. PLoS Biol. 11:e1001738; 2013.
8. Ayyagari, A. L.; Zhang, X.; Ghaghada, K. B.; Annapragada, A.; Hu, X.; Bellamkonda, R. V. Long-circulating liposomal contrast agents for magnetic resonance imaging. Magn Reson Med. 55:1023–9; 2006.
9. Baligand, C.; Vauchez, K.; Fiszman, M.; Vilquin, J.-T.; Carlier, P. G. Discrepancies between the fate of myoblast xenograft in mouse leg muscle and NMR label persistency after loading with Gd-DTPA or SPIOs. Gene Ther. 16:734–745; 2009.
10. Banja, J. D. Ethical Considerations in Stem Cell Research on Neurologic and Orthopedic Conditions. PM&R. 7:S66–S75; 2015.
11. Baraniak, P. R.; McDevitt, T. C. Stem cell paracrine actions and tissue regeneration. Regen. Med. 5:121–143; 2010.
12. Beitnes, J. O.; Hopp, E.; Lunde, K.; Solheim, S.; Arnesen, H.; Brinchmann, J. E.; Forfang, K.; Aakhus, S. Long-term results after intracoronary injection of autologous mononuclear bone marrow cells in acute myocardial infarction: the ASTAMI randomised, controlled study. Heart Br. Card. Soc. 95:1983–1989; 2009.
13. Betzer, O.; Shwartz, A.; Motiei, M.; Kazimirsky, G.; Gispan, I.; Damti, E.; Brodie, C.; Yadid, G.; Popovtzer, R. Nanoparticle-based CT imaging technique for longitudinal and quantitative stem cell tracking within the brain: application in neuropsychiatric disorders. ACS Nano. 8:9274–9285; 2014.
14. Billotey, C.; Wilhelm, C.; Devaud, M.; Bacri, J. C.; Bittoun, J.; Gazeau, F. Cell internalization of anionic maghemite nanoparticles: quantitative effect on magnetic resonance imaging. Magn. Reson. Med. Off. J. Soc. Magn. Reson. Med. Soc. Magn. Reson. Med. 49:646–654; 2003.
15. Bos, E. J. van den; Baks, T.; Moelker, A. D.; Kerver, W.; Geuns, R.-J. van; Giessen, W. J. van der; Duncker, D. J.; Wielopolski, P. A. Magnetic resonance imaging of haemorrhage within reperfused myocardial infarcts: possible interference with iron oxide-labelled cell tracking? Eur. Heart J. 27:1620–1626; 2006.
16. Van den Bos, E. J.; Wagner, A.; Mahrholdt, H.; Thompson, R. B.; Morimoto, Y.; Sutton, B. S.; Judd, R. M.; Taylor, D. A. Improved efficacy of stem cell labeling for magnetic resonance imaging studies by the use of cationic liposomes. Cell Transplant. 12:743–756; 2003.
17. Brader, P.; Serganova, I.; Blasberg, R. G. Noninvasive molecular imaging using reporter genes. J. Nucl. Med. Off. Publ. Soc. Nucl. Med. 54:167–172; 2013.
18. Brekke, C.; Morgan, S. C.; Lowe, A. S.; Meade, T. J.; Price, J.; Williams, S. C.; Modo, M. The in vitro effects of a bimodal contrast agent on cellular functions and relaxometry. NMR Biomed. 20:77–89; 2007.

19. Bridot, J.-L.; Stanicki, D.; Laurent, S.; Boutry, S.; Gossuin, Y.; Leclère, P.; Lazzaroni, R.; Vander Elst, L.; Muller, R. N. New carboxysilane-coated iron oxide nanoparticles for nonspecific cell labelling: NEW USPIO FOR CELL LABELLING. Contrast Media Mol. Imaging. 8:466–474; 2013.
20. Bulte, J. W.; Ma, L. D.; Magin, R. L.; Kamman, R. L.; Hulstaert, C. E.; Go, K. G.; The, T. H.; de Leij, L. Selective MR imaging of labeled human peripheral blood mononuclear cells by liposome mediated incorporation of dextran-magnetite particles. Magn. Reson. Med. Off. J. Soc. Magn. Reson. Med. Soc. Magn. Reson. Med. 29:32–37; 1993.
21. Bulte, J. W.; Zhang, S.; van Gelderen, P.; Herynek, V.; Jordan, E. K.; Duncan, I. D.; Frank, J. A. Neurotransplantation of magnetically labeled oligodendrocyte progenitors: magnetic resonance tracking of cell migration and myelination. Proc. Natl. Acad. Sci. U. S. A. 96:15256–15261; 1999.
22. Callera, F.; de Melo, C. M. T. P. Magnetic resonance tracking of magnetically labeled autologous bone marrow CD34+ cells transplanted into the spinal cord via lumbar puncture technique in patients with chronic spinal cord injury: CD34+ cells' migration into the injured site. Stem Cells Dev. 16:461–466; 2007.
23. Chalmers, K. H.; Kenwright, A. M.; Parker, D.; Blamire, A. M. 19F-lanthanide complexes with increased sensitivity for 19F-MRI: optimization of the MR acquisition. Magn. Reson. Med. Off. J. Soc. Magn. Reson. Med. Soc. Magn. Reson. Med. 66:931–936; 2011.
24. Chemaly, E. R.; Yoneyama, R.; Frangioni, J. V.; Hajjar, R. J. Tracking Stem Cells in the Cardiovascular System. Trends Cardiovasc. Med. 15:297–302; 2005.
25. Clifford, D. M.; Fisher, S. A.; Brunskill, S. J.; Doree, C.; Mathur, A.; Watt, S.; Martin-Rendon, E. Stem cell treatment for acute myocardial infarction. Cochrane Database Syst. Rev. 2:CD006536; 2012.
26. Di Corato, R.; Gazeau, F.; Le Visage, C.; Fayol, D.; Levitz, P.; Lux, F.; Letourneur, D.; Luciani, N.; Tillement, O.; Wilhelm, C. High-resolution cellular MRI: gadolinium and iron oxide nanoparticles for in-depth dual-cell imaging of engineered tissue constructs. ACS Nano. 7:7500–7512; 2013.
27. Corot, C.; Warlin, D. Superparamagnetic iron oxide nanoparticles for MRI: contrast media pharmaceutical company R&D perspective. Wiley Interdiscip. Rev. Nanomed. Nanobiotechnol. 5:411–422; 2013.
28. Crich, S. G.; Biancone, L.; Cantaluppi, V.; Duò, D.; Esposito, G.; Russo, S.; Camussi, G.; Aime, S. Improved route for the visualization of stem cells labeled with a Gd-/Eu-chelate as dual (MRI and fluorescence) agent. Magn. Reson. Med. Off. J. Soc. Magn. Reson. Med. Soc. Magn. Reson. Med. 51:938–944; 2004.
29. Cui, W.; Liu, L.; Kodibagkar, V. D.; Mason, R. P. S-Gal, a novel 1H MRI reporter for beta-galactosidase. Magn. Reson. Med. Off. J. Soc. Magn. Reson. Med. Soc. Magn. Reson. Med. 64:65–71; 2010.
30. Daldrup-Link, H. E.; Meier, R.; Rudelius, M.; Piontek, G.; Piert, M.; Metz, S.; Settles, M.; Uherek, C.; Wels, W.; Schlegel, J.; Rummeny, E. J. In vivo tracking of genetically engineered, anti-HER2/neu directed natural killer cells to HER2/neu positive mammary tumors with magnetic resonance imaging. Eur. Radiol. 15:4–13; 2005.
31. Daldrup-Link, H. E.; Rudelius, M.; Oostendorp, R. A. J.; Settles, M.; Piontek, G.; Metz, S.; Rosenbrock, H.; Keller, U.; Heinzmann, U.; Rummeny, E. J.; Schlegel, J.; Link, T. M. Targeting of hematopoietic progenitor cells with MR contrast agents. Radiology. 228:760–767; 2003.
32. Van Den Bos, E. J.; Taylor, D. A. Cardiac transplantation of skeletal myoblasts for heart failure. Minerva Cardioangiol. 51:227–243; 2003.
33. Devoisselle, J. M.; Vion-Dury, J.; Galons, J. P.; Confort-Gouny, S.; Coustaut, D.; Canioni, P.; Cozzone, P. J. Entrapment of gadolinium-DTPA in liposomes. Characterization of vesicles by P-31 NMR spectroscopy. Invest. Radiol. 23:719–724; 1988.
34. Ebert, A. D.; Yu, J.; Rose, F. F.; Mattis, V. B.; Lorson, C. L.; Thomson, J. A.; Svendsen, C. N. Induced pluripotent stem cells from a spinal muscular atrophy patient. Nature. 457:277–280; 2009.
35. Fadini, G. P.; Agostini, C.; Avogaro, A. Autologous stem cell therapy for peripheral arterial disease meta-analysis and systematic review of the literature. Atherosclerosis. 209:10–17; 2010.
36. Fang, J.-Y.; Wen, C.-J.; Zhang; Al-Suwayeh; Yen, T.-C. Theranostic liposomes loaded with quantum dots and apomorphine for brain targeting and bioimaging. Int. J. Nanomedicine. 1599; 2012.
37. Frank, J. A.; Miller, B. R.; Arbab, A. S.; Zywicke, H. A.; Jordan, E. K.; Lewis, B. K.; Bryant, L. H., Jr.; Bulte, J. W. Clinically applicable labeling of mammalian and stem cells by combining superparamagnetic iron oxides and transfection agents. Radiology. 228:480–7; 2003.

38. Geninatti Crich, S.; Cabella, C.; Barge, A.; Belfiore, S.; Ghirelli, C.; Lattuada, L.; Lanzardo, S.; Mortillaro, A.; Tei, L.; Visigalli, M.; Forni, G.; Aime, S. In vitro and in vivo magnetic resonance detection of tumor cells by targeting glutamine transporters with Gd-based probes. J Med Chem. 49:4926–36; 2006.
39. Ghaghada, K.; Hawley, C.; Kawaji, K.; Annapragada, A.; Mukundan, S., Jr. T1 relaxivity of core-encapsulated gadolinium liposomal contrast agents--effect of liposome size and internal gadolinium concentration. Acad Radiol. 15:1259–63; 2008.
40. Gilad, A. A.; Walczak, P.; McMahon, M. T.; Na, H. B.; Lee, J. H.; An, K.; Hyeon, T.; van Zijl, P. C. M.; Bulte, J. W. M. MR tracking of transplanted cells with "positive contrast" using manganese oxide nanoparticles. Magn. Reson. Med. 60:1–7; 2008.
41. Gnecchi, M.; Zhang, Z.; Ni, A.; Dzau, V. J. Paracrine Mechanisms in Adult Stem Cell Signaling and Therapy. Circ. Res. 103:1204–1219; 2008.
42. Gründer, W.; Biesold, M.; Wagner, M.; Werner, A. Improved nuclear magnetic resonance microscopic visualization of joint cartilage using liposome entrapped contrast agents. Invest. Radiol. 33:193–202; 1998.
43. Guenoun, J.; Koning, G. A.; Doeswijk, G.; Bosman, L.; Wielopolski, P. A.; Krestin, G. P.; Bernsen, M. R. Cationic Gd-DTPA liposomes for highly efficient labeling of mesenchymal stem cells and cell tracking with MRI. Cell Transpl. 2011.
44. Haneder, S.; Kucharczyk, W.; Schoenberg, S. O.; Michaely, H. J. Safety of magnetic resonance contrast media: a review with special focus on nephrogenic systemic fibrosis. Top. Magn. Reson. Imaging TMRI. 24:57–65; 2015.
45. Helfer, B. M.; Balducci, A.; Nelson, A. D.; Janjic, J. M.; Gil, R. R.; Kalinski, P.; de Vries, I. J. M.; Ahrens, E. T.; Mailliard, R. B. Functional assessment of human dendritic cells labeled for in vivo (19)F magnetic resonance imaging cell tracking. Cytotherapy. 12:238–250; 2010.
46. Hovland, R.; Gløgård, C.; Aasen, A. J.; Klaveness, J. Preparation and in vitro evaluation of a novel amphiphilic GdPCTA-[12] derivative; a micellar MRI contrast agent. Org. Biomol. Chem. 1:644–647; 2003.
47. Josephson, L.; Lewis, J.; Jacobs, P.; Hahn, P. F.; Stark, D. D. The effects of iron oxides on proton relaxivity. Magn. Reson. Imaging. 6:647–653; 1988.
48. Josephson, L.; Tung, C. H.; Moore, A.; Weissleder, R. High-efficiency intracellular magnetic labeling with novel superparamagnetic-Tat peptide conjugates. Bioconjug. Chem. 10:186–191; 1999.
49. Kabalka, G.; Buonocore, E.; Hubner, K.; Moss, T.; Norley, N.; Huang, L. Gadolinium-labeled liposomes: targeted MR contrast agents for the liver and spleen. Radiology. 163:255–258; 1987.
50. Kamaly, N.; Kalber, T.; Ahmad, A.; Oliver, M. H.; So, P. W.; Herlihy, A. H.; Bell, J. D.; Jorgensen, M. R.; Miller, A. D. Bimodal paramagnetic and fluorescent liposomes for cellular and tumor magnetic resonance imaging. Bioconjug Chem. 19:118–29; 2008.
51. Karussis, D.; Karageorgiou, C.; Vaknin-Dembinsky, A.; Gowda-Kurkalli, B.; Gomori, J. M.; Kassis, I.; Bulte, J. W. M.; Petrou, P.; Ben-Hur, T.; Abramsky, O.; Slavin, S. Safety and immunological effects of mesenchymal stem cell transplantation in patients with multiple sclerosis and amyotrophic lateral sclerosis. Arch. Neurol. 67:1187–1194; 2010.
52. Kim, K.; Doi, A.; Wen, B.; Ng, K.; Zhao, R.; Cahan, P.; Kim, J.; Aryee, M. J.; Ji, H.; Ehrlich, L. I. R.; Yabuuchi, A.; Takeuchi, A.; Cunniff, K. C.; Hongguang, H.; Mckinney-Freeman, S.; Naveiras, O.; Yoon, T. J.; Irizarry, R. A.; Jung, N.; Seita, J.; Hanna, J.; Murakami, P.; Jaenisch, R.; Weissleder, R.; Orkin, S. H.; Weissman, I. L.; Feinberg, A. P.; Daley, G. Q. Epigenetic memory in induced pluripotent stem cells. Nature. 467:285–290; 2010.
53. Kim, T.; Momin, E.; Choi, J.; Yuan, K.; Zaidi, H.; Kim, J.; Park, M.; Lee, N.; McMahon, M. T.; Quinones-Hinojosa, A.; Bulte, J. W. M.; Hyeon, T.; Gilad, A. A. Mesoporous Silica-Coated Hollow Manganese Oxide Nanoparticles as Positive T1 Contrast Agents for Labeling and MRI Tracking of Adipose-Derived Mesenchymal Stem Cells. J. Am. Chem. Soc. 133:2955–2961; 2011.
54. Kobayashi, H.; Kawamoto, S.; Saga, T.; Sato, N.; Ishimori, T.; Konishi, J.; Ono, K.; Togashi, K.; Brechbiel, M. W. Avidin-dendrimer-(1B4M-Gd)(254): a tumor-targeting therapeutic agent for gadolinium neutron capture therapy of intraperitoneal disseminated tumor which can be monitored by MRI. Bioconjug Chem. 12:587–93; 2001.

55. Kok, M. B.; Hak, S.; Mulder, W. J.; van der Schaft, D. W.; Strijkers, G. J.; Nicolay, K. Cellular compartmentalization of internalized paramagnetic liposomes strongly influences both T1 and T2 relaxivity. Magn Reson Med. 61:1022–32; 2009.
56. Kotek, G.; van Tiel, S. T.; Wielopolski, P. A.; Houston, G. C.; Krestin, G. P.; Bernsen, M. R. Cell quantification: evolution of compartmentalization and distribution of iron-oxide particles and labeled cells. Contrast Media Mol. Imaging. 7:195–203; 2012.
57. Van Laake, L. W.; Passier, R.; Monshouwer-Kloots, J.; Verkleij, A. J.; Lips, D. J.; Freund, C.; den Ouden, K.; Ward-van Oostwaard, D.; Korving, J.; Tertoolen, L. G.; van Echteld, C. J.; Doevendans, P. A.; Mummery, C. L. Human embryonic stem cell-derived cardiomyocytes survive and mature in the mouse heart and transiently improve function after myocardial infarction. Stem Cell Res. 1:9–24; 2007.
58. Leder, A.; Raschzok, N.; Schmidt, C.; Arabacioglu, D.; Butter, A.; Kolano, S.; de Sousa Lisboa, L. S.; Werner, W.; Polenz, D.; Reutzel-Selke, A.; Pratschke, J.; Sauer, I. M. Micron-sized iron oxide-containing particles for microRNA-targeted manipulation and MRI-based tracking of transplanted cells. Biomaterials. 51:129–137; 2015.
59. Lee, J. S.; Hong, J. M.; Moon, G. J.; Lee, P. H.; Ahn, Y. H.; Bang, O. Y. A long-term follow-up study of intravenous autologous mesenchymal stem cell transplantation in patients with ischemic stroke. Stem Cells. 28:1099–106; 2010.
60. Lees, J. S.; Sena, E. S.; Egan, K. J.; Antonic, A.; Koblar, S. A.; Howells, D. W.; Macleod, M. R. Stem cell-based therapy for experimental stroke: a systematic review and meta-analysis. Int. J. Stroke Off. J. Int. Stroke Soc. 7:582–588; 2012.
61. Létourneau, M.; Tremblay, M.; Faucher, L.; Rojas, D.; Chevallier, P.; Gossuin, Y.; Lagueux, J.; Fortin, M.-A. MnO-Labeled Cells: Positive Contrast Enhancement in MRI. J. Phys. Chem. B. 116:13228–13238; 2012.
62. Lewin, M.; Clement, O.; Belguise-Valladier, P.; Tran, L.; Cuenod, C. A.; Siauve, N.; Frija, G. Hepatocyte targeting with Gd-EOB-DTPA: potential application for gene therapy. Invest Radiol. 36:9–14; 2001.
63. Li, S.; Goins, B.; Zhang, L.; Bao, A. Novel multifunctional theranostic liposome drug delivery system: construction, characterization, and multimodality MR, near-infrared fluorescent, and nuclear imaging. Bioconjug. Chem. 23:1322–1332; 2012.
64. Liu, J.; Wang, L.; Cao, J.; Huang, Y.; Lin, Y.; Wu, X.; Wang, Z.; Zhang, F.; Xu, X.; Liu, G. Functional investigations on embryonic stem cells labeled with clinically translatable iron oxide nanoparticles. Nanoscale. 6:9025; 2014.
65. Louie, A. Y.; Hüber, M. M.; Ahrens, E. T.; Rothbächer, U.; Moats, R.; Jacobs, R. E.; Fraser, S. E.; Meade, T. J. In vivo visualization of gene expression using magnetic resonance imaging. Nat. Biotechnol. 18:321–325; 2000.
66. Lunde, K.; Solheim, S.; Aakhus, S.; Arnesen, H.; Abdelnoor, M.; Egeland, T.; Endresen, K.; Ilebekk, A.; Mangschau, A.; Fjeld, J. G.; Smith, H. J.; Taraldsrud, E.; Grøgaard, H. K.; Bjørnerheim, R.; Brekke, M.; Müller, C.; Hopp, E.; Ragnarsson, A.; Brinchmann, J. E.; Forfang, K. Intracoronary injection of mononuclear bone marrow cells in acute myocardial infarction. N. Engl. J. Med. 355:1199–1209; 2006.
67. Maiseyeu, A.; Mihai, G.; Kampfrath, T.; Simonetti, O. P.; Sen, C. K.; Roy, S.; Rajagopalan, S.; Parthasarathy, S. Gadolinium-containing phosphatidylserine liposomes for molecular imaging of atherosclerosis. J. Lipid Res. 50:2157–2163; 2009.
68. Modo, M.; Beech, J. S.; Meade, T. J.; Williams, S. C. R.; Price, J. A chronic 1 year assessment of MRI contrast agent-labelled neural stem cell transplants in stroke. NeuroImage. 47 Suppl 2:T133–142; 2009.
69. Modo, M.; Hoehn, M.; Bulte, J. W. Cellular MR imaging. Mol Imaging. 4:143–64; 2005.
70. Mothe, A. J.; Tator, C. H. Advances in stem cell therapy for spinal cord injury. J. Clin. Invest. 122:3824–3834; 2012.
71. Mulder, W. J. M.; Strijkers, G. J.; van Tilborg, G. A. F.; Griffioen, A. W.; Nicolay, K. Lipid-based nanoparticles for contrast-enhanced MRI and molecular imaging. NMR Biomed. 19:142–164; 2006.
72. Müller-Ehmsen, J.; Whittaker, P.; Kloner, R. A.; Dow, J. S.; Sakoda, T.; Long, T. I.; Laird, P. W.; Kedes, L. Survival and development of neonatal rat cardiomyocytes transplanted into adult myocardium. J. Mol. Cell. Cardiol. 34:107–116; 2002.

73. Norman, A. B.; Thomas, S. R.; Pratt, R. G.; Lu, S. Y.; Norgren, R. B. Magnetic resonance imaging of neural transplants in rat brain using a superparamagnetic contrast agent. Brain Res. 594:279–283; 1992.
74. Nussbaum, J.; Minami, E.; Laflamme, M. A.; Virag, J. A. I.; Ware, C. B.; Masino, A.; Muskheli, V.; Pabon, L.; Reinecke, H.; Murry, C. E. Transplantation of undifferentiated murine embryonic stem cells in the heart: teratoma formation and immune response. FASEB J. 21:1345–1357; 2007.
75. Pacchierotti, F.; Bellusci, M.; La Barbera, A.; Padella, F.; Mancuso, M.; Pasquo, A.; Grollino, M. G.; Leter, G.; Nardi, E.; Cremisini, C.; Giardullo, P. Biodistribution and acute toxicity of a nanofluid containing manganese iron oxide nanoparticles produced by a mechanochemical process. Int. J. Nanomedicine. 1919; 2014.
76. Pawelczyk, E.; Jordan, E. K.; Balakumaran, A.; Chaudhry, A.; Gormley, N.; Smith, M.; Lewis, B. K.; Childs, R.; Robey, P. G.; Frank, J. A. In vivo transfer of intracellular labels from locally implanted bone marrow stromal cells to resident tissue macrophages. PLoS One. 4:e6712; 2009.
77. Qiao, H.; Zhang, H.; Zheng, Y.; Ponde, D. E.; Shen, D.; Gao, F.; Bakken, A. B.; Schmitz, A.; Kung, H. F.; Ferrari, V. A.; Zhou, R. Embryonic Stem Cell Grafting in Normal and Infarcted Myocardium: Serial Assessment with MR Imaging and PET Dual Detection [1]. Radiology. 250:821–829; 2009.
78. Raynal, I.; Prigent, P.; Peyramaure, S.; Najid, A.; Rebuzzi, C.; Corot, C. Macrophage endocytosis of superparamagnetic iron oxide nanoparticles: mechanisms and comparison of ferumoxides and ferumoxtran-10. Invest Radiol. 39:56–63; 2004.
79. Robertson, J. A. Embryo Stem Cell Research: Ten Years of Controversy. J. Law. Med. Ethics. 38:191–203; 2010.
80. Rudelius, M.; Daldrup-Link, H. E.; Heinzmann, U.; Piontek, G.; Settles, M.; Link, T. M.; Schlegel, J. Highly efficient paramagnetic labelling of embryonic and neuronal stem cells. Eur. J. Nucl. Med. Mol. Imaging. 30:1038–1044; 2003.
81. Rudin, M.; Rausch, M.; Stoeckli, M. Molecular imaging in drug discovery and development: potential and limitations of nonnuclear methods. Mol. Imaging Biol. MIB Off. Publ. Acad. Mol. Imaging. 7:5–13; 2005.
82. Ruiz-Cabello, J.; Barnett, B. P.; Bottomley, P. A.; Bulte, J. W. M. Fluorine (19F) MRS and MRI in biomedicine. NMR Biomed. 24:114–129; 2011.
83. Saudek, F.; Jirák, D.; Girman, P.; Herynek, V.; Dezortová, M.; Kríz, J.; Peregrin, J.; Berková, Z.; Zacharovová, K.; Hájek, M. Magnetic resonance imaging of pancreatic islets transplanted into the liver in humans. Transplantation. 90:1602–1606; 2010.
84. Schächinger, V.; Assmus, B.; Britten, M. B.; Honold, J.; Lehmann, R.; Teupe, C.; Abolmaali, N. D.; Vogl, T. J.; Hofmann, W.-K.; Martin, H.; Dimmeler, S.; Zeiher, A. M. Transplantation of progenitor cells and regeneration enhancement in acute myocardial infarction: final one-year results of the TOPCARE-AMI Trial. J. Am. Coll. Cardiol. 44:1690–1699; 2004.
85. Schächinger, V.; Assmus, B.; Erbs, S.; Elsässer, A.; Haberbosch, W.; Hambrecht, R.; Yu, J.; Corti, R.; Mathey, D. G.; Hamm, C. W.; Tonn, T.; Dimmeler, S.; Zeiher, A. M.; REPAIR-AMI investigators. Intracoronary infusion of bone marrow-derived mononuclear cells abrogates adverse left ventricular remodelling post-acute myocardial infarction: insights from the reinfusion of enriched progenitor cells and infarct remodelling in acute myocardial infarction (REPAIR-AMI) trial. Eur. J. Heart Fail. 11:973–979; 2009.
86. Simon, G. H.; Bauer, J.; Saborovski, O.; Fu, Y.; Corot, C.; Wendland, M. F.; Daldrup-Link, H. E. T1 and T2 relaxivity of intracellular and extracellular USPIO at 1.5T and 3T clinical MR scanning. Eur. Radiol. 16:738–745; 2006.
87. Skuk, D.; Caron, N. J.; Goulet, M.; Roy, B.; Tremblay, J. P. Resetting the problem of cell death following muscle-derived cell transplantation: detection, dynamics and mechanisms. J. Neuropathol. Exp. Neurol. 62:951–967; 2003.
88. Song, H.; Song, B.-W.; Cha, M.-J.; Choi, I.-G.; Hwang, K.-C. Modification of mesenchymal stem cells for cardiac regeneration. Expert Opin. Biol. Ther. 10:309–319; 2010.
89. Van der Spoel, T. I. G.; Jansen of Lorkeers, S. J.; Agostoni, P.; van Belle, E.; Gyöngyösi, M.; Sluijter, J. P. G.; Cramer, M. J.; Doevendans, P. A.; Chamuleau, S. A. J. Human relevance of pre-clinical studies in stem cell therapy: systematic review and meta-analysis of large animal models of ischaemic heart disease. Cardiovasc. Res. 91:649–658; 2011.

90. Srinivas, M.; Boehm-Sturm, P.; Figdor, C. G.; de Vries, I. J.; Hoehn, M. Labeling cells for in vivo tracking using (19)F MRI. Biomaterials. 33:8830–8840; 2012.
91. Srinivas, M.; Cruz, L. J.; Bonetto, F.; Heerschap, A.; Figdor, C. G.; de Vries, I. J. M. Customizable, multi-functional fluorocarbon nanoparticles for quantitative in vivo imaging using 19F MRI and optical imaging. Biomaterials. 31:7070–7077; 2010.
92. Srinivas, M.; Heerschap, A.; Ahrens, E. T.; Figdor, C. G.; de Vries, I. J. M. 19F MRI for quantitative in vivo cell tracking. Trends Biotechnol. 28:363–370; 2010.
93. Srinivas, M.; Heerschap, A.; Ahrens, E. T.; Figdor, C. G.; de Vries, I. J. M. (19)F MRI for quantitative in vivo cell tracking. Trends Biotechnol. 28:363–370; 2010.
94. Srivastava, A. K.; Bulte, J. W. M. Seeing Stem Cells at Work In Vivo. Stem Cell Rev. 10:127–144; 2014.
95. Sterenczak, K. A.; Meier, M.; Glage, S.; Meyer, M.; Willenbrock, S.; Wefstaedt, P.; Dorsch, M.; Bullerdiek, J.; Escobar, H. M.; Hedrich, H.; Nolte, I. Longitudinal MRI contrast enhanced monitoring of early tumour development with manganese chloride (MnCl2) and superparamagnetic iron oxide nanoparticles (SPIOs) in a CT1258 based in vivo model of prostate cancer. BMC Cancer. 12:284; 2012.
96. Strijkers, G. J.; Hak, S.; Kok, M. B.; Springer, C. S., Jr.; Nicolay, K. Three-compartment T1 relaxation model for intracellular paramagnetic contrast agents. Magn Reson Med. 61:1049–58; 2009.
97. Takahashi, K.; Yamanaka, S. Induction of Pluripotent Stem Cells from Mouse Embryonic and Adult Fibroblast Cultures by Defined Factors. Cell. 126:663–676; 2006.
98. Tanimoto, A.; Oshio, K.; Suematsu, M.; Pouliquen, D.; Stark, D. D. Relaxation effects of clustered particles. J. Magn. Reson. Imaging JMRI. 14:72–77; 2001.
99. Terreno, E.; Geninatti Crich, S.; Belfiore, S.; Biancone, L.; Cabella, C.; Esposito, G.; Manazza, A. D.; Aime, S. Effect of the intracellular localization of a Gd-based imaging probe on the relaxation enhancement of water protons. Magn Reson Med. 55:491–7; 2006.
100. Terrovitis, J.; Stuber, M.; Youssef, A.; Preece, S.; Leppo, M.; Kizana, E.; Schar, M.; Gerstenblith, G.; Weiss, R. G.; Marban, E.; Abraham, M. R. Magnetic resonance imaging overestimates ferumoxide-labeled stem cell survival after transplantation in the heart. Circulation. 117:1555–62; 2008.
101. Thomas, E. D.; Lochte, H. L.; Cannon, J. H.; Sahler, O. D.; Ferrebee, J. W. Supralethal whole body irradiation and isologous marrow transplantation in man. J. Clin. Invest. 38:1709–1716; 1959.
102. Torchilin, V. P. Recent advances with liposomes as pharmaceutical carriers. Nat. Rev. Drug Discov. 4:145–160; 2005.
103. Torchilin, V. P. PEG-based micelles as carriers of contrast agents for different imaging modalities. Adv. Drug Deliv. Rev. 54:235–252; 2002.
104. Toso, C.; Vallee, J.-P.; Morel, P.; Ris, F.; Demuylder-Mischler, S.; Lepetit-Coiffe, M.; Marangon, N.; Saudek, F.; James Shapiro, A. M.; Bosco, D.; Berney, T. Clinical magnetic resonance imaging of pancreatic islet grafts after iron nanoparticle labeling. Am. J. Transplant. Off. J. Am. Soc. Transplant. Am. Soc. Transpl. Surg. 8:701–706; 2008.
105. Tran, L. A.; Hernández-Rivera, M.; Berlin, A. N.; Zheng, Y.; Sampaio, L.; Bové, C.; Cabreira-Hansen, M. da G.; Willerson, J. T.; Perin, E. C.; Wilson, L. J. The use of gadolinium-carbon nanostructures to magnetically enhance stem cell retention for cellular cardiomyoplasty. Biomaterials. 35:720–726; 2014.
106. Tseng, C.-L.; Shih, I.-L.; Stobinski, L.; Lin, F.-H. Gadolinium hexanedione nanoparticles for stem cell labeling and tracking via magnetic resonance imaging. Biomaterials. 31:5427–5435; 2010.
107. Vandsburger, M. H.; Radoul, M.; Cohen, B.; Neeman, M. MRI reporter genes: applications for imaging of cell survival, proliferation, migration and differentiation. NMR Biomed. 26:872–884; 2013.
108. Vivero-Escoto, J. L.; Rieter, W. J.; Lau, H.; Huxford-Phillips, R. C.; Lin, W. Biodegradable polysilsesquioxane nanoparticles as efficient contrast agents for magnetic resonance imaging. Small Weinh. Bergstr. Ger. 9:3523–3531; 2013.
109. De Vries, A.; Moonen, R.; Yildirim, M.; Langereis, S.; Lamerichs, R.; Pikkemaat, J. A.; Baroni, S.; Terreno, E.; Nicolay, K.; Strijkers, G. J.; Grüll, H. Relaxometric studies of gadolinium-functionalized perfluorocarbon nanoparticles for MR imaging. Contrast Media Mol. Imaging. 9:83–91; 2014.

110. De Vries, I. J. M.; Lesterhuis, W. J.; Barentsz, J. O.; Verdijk, P.; van Krieken, J. H.; Boerman, O. C.; Oyen, W. J. G.; Bonenkamp, J. J.; Boezeman, J. B.; Adema, G. J.; Bulte, J. W. M.; Scheenen, T. W. J.; Punt, C. J. A.; Heerschap, A.; Figdor, C. G. Magnetic resonance tracking of dendritic cells in melanoma patients for monitoring of cellular therapy. Nat. Biotechnol. 23:1407–1413; 2005.
111. De Vries, I. J. M.; Lesterhuis, W. J.; Barentsz, J. O.; Verdijk, P.; van Krieken, J. H.; Boerman, O. C.; Oyen, W. J. G.; Bonenkamp, J. J.; Boezeman, J. B.; Adema, G. J.; Bulte, J. W. M.; Scheenen, T. W. J.; Punt, C. J. A.; Heerschap, A.; Figdor, C. G. Magnetic resonance tracking of dendritic cells in melanoma patients for monitoring of cellular therapy. Nat. Biotechnol. 23:1407–1413; 2005.
112. Waiczies, S.; Lepore, S.; Sydow, K.; Drechsler, S.; Ku, M.-C.; Martin, C.; Lorenz, D.; Schütz, I.; Reimann, H. M.; Purfürst, B.; Dieringer, M. A.; Waiczies, H.; Dathe, M.; Pohlmann, A.; Niendorf, T. Anchoring dipalmitoyl phosphoethanolamine to nanoparticles boosts cellular uptake and fluorine-19 magnetic resonance signal. Sci. Rep. 5:8427; 2015.
113. Walczak, P.; Kedziorek, D. A.; Gilad, A. A.; Barnett, B. P.; Bulte, J. W. M. Applicability and limitations of MR tracking of neural stem cells with asymmetric cell division and rapid turnover: the case of the shiverer dysmyelinated mouse brain. Magn. Reson. Med. Off. J. Soc. Magn. Reson. Med. Soc. Magn. Reson. Med. 58:261–269; 2007.
114. Weissleder, R.; Stark, D. D.; Engelstad, B. L.; Bacon, B. R.; Compton, C. C.; White, D. L.; Jacobs, P.; Lewis, J. Superparamagnetic iron oxide: pharmacokinetics and toxicity. AJR Am. J. Roentgenol. 152:167–173; 1989.
115. Xiao, J.; Tian, X. M.; Yang, C.; Liu, P.; Luo, N. Q.; Liang, Y.; Li, H. B.; Chen, D. H.; Wang, C. X.; Li, L.; Yang, G. W. Ultrahigh relaxivity and safe probes of manganese oxide nanoparticles for in vivo imaging. Sci. Rep. 3 2013.
116. Yamada, M.; Gurney, P. T.; Chung, J.; Kundu, P.; Drukker, M.; Smith, A. K.; Weissman, I. L.; Nishimura, D.; Robbins, R. C.; Yang, P. C. Manganese-guided cellular MRI of human embryonic stem cell and human bone marrow stromal cell viability. Magn. Reson. Med. 62:1047–1054; 2009.
117. Zhang, M.; Methot, D.; Poppa, V.; Fujio, Y.; Walsh, K.; Murry, C. E. Cardiomyocyte grafting for cardiac repair: graft cell death and anti-death strategies. J. Mol. Cell. Cardiol. 33:907–921; 2001.
118. Zhang, S.; Jiang, Z.; Liu, X.; Zhou, L.; Peng, W. Possible gadolinium ions leaching and MR sensitivity over-estimation in mesoporous silica-coated upconversion nanocrystals. Nanoscale. 5:8146–8155; 2013.
119. Zhang, Z.; van den Bos, E. J.; Wielopolski, P. A.; de Jong-Popijus, M.; Bernsen, M. R.; Duncker, D. J.; Krestin, G. P. In vitro imaging of single living human umbilical vein endothelial cells with a clinical 3.0-T MRI scanner. Magma N. Y. N. 18:175–185; 2005.
120. Zhu, J.; Zhou, L.; XingWu, F. Tracking neural stem cells in patients with brain trauma. N. Engl. J. Med. 355:2376–2378; 2006.
121. Zumbuehl, O.; Weder, H. G. Liposomes of controllable size in the range of 40 to 180 nm by defined dialysis of lipid/detergent mixed micelles. Biochim. Biophys. Acta. 640:252–262; 1981.
122. Sattler, K. D. Handbook of nanophysics, Boca Raton: Taylor & Francis; 2011.

# THESIS AIM AND OUTLINE

In the past decades men has seen an upcoming use of stem cells to repair incurably diseased tissue. The exact and detailed role and fate of stem cells in host tissue after transplantation is yet to be unraveled though. Being able to 'see' the cells at work *in vivo* would definitely contribute to our understanding of their interaction with host tissue. This could be accomplished by clinical imaging techniques.
This thesis therefore addresses the feasibility of labeling mesenchymal stem cells (MSCs) with cell labels (mainly Gd-liposomes) by passive endocytosis, to facilitate 'tracking' of these labeled cells *in vivo* by two imaging techniques (magnetic resonance imaging (MRI) and bioluminescence imaging ((BLI)).
When we started our work in this research field in 2008, superparamagnetic iron oxide particles (SPIOs, a T2 contrast agent) were by far the most popular cell label for MRI-based cell tracking at that time. Nevertheless, SPIOs were not without drawbacks:

1. They cause signal loss, potentially to be confused with signal loss from (patho)physiological conditions such as hemorrhage, blood flow or air-pockets.
2. SPIOs are difficult if not impossible to perform T2 quantification on.
3. SPIOs appeared to generate non-cell associated contrast in case of transplanted cell death, resulting from macrophage engulfment, severely hampering their specificity.
4. T2 contrast agents are best visualized by T2-weighted sequences, which have an inherently lower signal-to-noise ratio than T1-weighted images.

Therefore this thesis is centered on the use of Gd-liposomes (a T1 contrast agent), which we hypothesized to be able to overcome these limitations since:

1. they cause hyperintensity on T1-weighted images, a feature quite rare for biological tissues, allowing good background discrimination.
2. T1 quantification techniques are much more straightforward
3. they are much more smaller and hypothesized to escape macrophage reuptake following cell death
4. they are imaged on T1-weighted images with a generally high SNR.

Gd-liposomes thus being a novelty in cell labeling which weren't characterized fully, we started in **chapter 2** by assessing the labeling efficiency of MSCs. We measured the cell incorporated Gd content as a result of both labeling time and lipid dose variations. Possible direct toxic effects of the Gd-liposomes causing cell death and possible interference with the differentiation and proliferation ability of MSCs were studied. With time-resolved confocal fluorescence laser scanning microscopy (CLSM), we studied the intracellullar clustering of Gd-liposomes and their fate over time, owing to the incorporation of fluorescent dyes in both the lipid membrane (rhodamine) and the intraliposomal space (calcein). The *in vitro* contrast behavior of Gd-liposomes was assessed by MR Imaging of a dilution range of labeled MSCs. An *in vivo* pilot experiment on 'cell viability visualization' was carried out, transplanting viable and nonviable MSCs into rodent soft tissue.
Histology was performed to detect cell and liposomal presence.

In **chapter 3** we further explored the effects of Gd compartmentalization on MRI signal *in vitro*, again by quantification of T1 and T2 relaxation times. To this extent we compared stock gadolinium (Gd-DO3A-Butrol) with both intact and ruptured liposomes and with both intact (viable) and lysed (nonviable) Gd-liposome labeled MSCs. We further studied the properties of Gd-liposomal formulations, such as liposomal size, suspension concentration and intraliposomal [Gd], in relation to MRI signal intensity. Measurements of the actual Gd content by

Inductively Coupled Plasma-Optical Emission Spectroscopy (ICP-OES) allowed us to put our findings in perspective with existing theories on intravoxel water distribution and diffusion, using a mathematical approach.

Because of intriguing findings in the pilot experiment and the need for clinical imaging methods to assess stem cell viability post-transplantation we extended the *in vivo* experiment in **chapter 4** in four dimensions: we (i) compared Gd-liposome labeled cells to SPIO-labeled cells, (ii) performed measurements of T1, T2 and T2* relaxation times of labeled cell clusters, (iii) performed a longitudinal follow-up for 15 days and lastly (iv) genetically enriched the cells with the bioluminescent reporter gene luciferase, resulting in dual labeled cells, Gd-liposome-labeled Fluc-MSCs and SPIO-labeled Fluc-MSCs. Our primary aim was to correlate changes in T1, T2, T2* relaxation times to actual cell transplant viability. Based on known literature, we expected for both contrast labels to see relaxation time differences between viable and non-viable MSCs, associated with (de)compartmentalization. Our secondary aim was to compare sensitivity (the detection limit) and specificity (truly cell-associated signal generation) of both contrast labels. This was all correlated with bioluminescence imaging (BLI), which is based on the principle of detection of light emitted by viable cells only, allowing a reliable validation of cell viability, sensitivity and specificity. Information on contrast label presence was obtained by histological staining and *ex vivo* methods, for SPIO and Gd-liposomes respectively.

Being the leading cause of death globally, cardiovascular disease (specifically myocardial infarction), drew our attention as a suitable disease model to study stem cell tracking. The ultimate goal of regenerating nonviable infarcted myocardial tissue by stem cell therapy was chased by many researchers at that moment. Beyond the unresolved safety and ethical issues, crucial questions: "What is the best route for cell delivery?" "What kind and how many cells?" and "When to inject?" remained. Thus, in **chapter 5** we aimed to give an overview of the latest proceedings and state-of-the-art of the various imaging techniques (MRI, PET, SPECT/CT, bioluminescence and fluorescence) for cardiac stem cell tracking. We presented the strengths and limitations of each approach, with a particular focus on clinical applicability.

In **chapter 6,** we used a quantitative MRI approach to investigate the changes in T2 relaxation time associated with proliferation, viability and death of SPIO-labeled Fluc-MSCs transplanted to the heart *in vivo*. The luciferase insert provided for validation of the actual cell viability. Reproducibility studies were performed in normal rats, imaged in different sessions, to assess the robustness of T2 quantification by a single cardiac phase cardiac triggered double inversion black blood 2D fast spin echo (BBFSE) sequence. Healthy rats underwent thoracotomy to receive intramyocardial transplantations of either viable or nonviable cells. Cell fate was monitored over a period of 15 days by BLI and MRI.

In **chapter 7** we further explored the quantification spectrum by aiming to assess the T1 relaxation time of healthy and myocardial (diseased) tissue in phantom studies and in rats *in vivo.* T1 quantification is clinically widely used for assessment of the extent of nonviable myocardium (on delayed enhancement images) and therefore suitable to monitor the effect of stem cell therapy delivered to the heart. For translational purposes it is imperative to have T1 quantification sequences that perform equally on fast beating (rats) and relatively slow-beating hearts (humans).

The Modified Look-Locker inversion recovery method (MOLLI), requiring an acquisition window of about 190 ms, is applicable for T1 quantification in humans (who have an RR interval of ± 1000 ms.), but not in rat hearts (with an RR interval is only 100-200 ms). The variable flip angle method for T1 quantification is a possible alternative but requires long scan

durations. In this chapter the published CINE inversion recovery acquisition on humans, modified to fit fast heart rates too (mCINE-IR), was applied on rats for the first time, enabling the possibility of translational studies with an identical sequence. Simulations were used to study signal evolution and heart rate dependency.

The results of this thesis are further discussed and summarized in **chapter 8**.

# PART A

# Contrast agent development and in vitro testing

Chapter 2

# Cationic Gd-DTPA Liposomes for Highly Efficient Labeling of Mesenchymal Stem Cells and Cell Tracking with MRI

Jamal Guenoun[1], Gerben A. Koning[2], Gabriela N. Doeswijk[1], Lizanne Bosman[1], Piotr A. Wielopolski[1], Gabriel P. Krestin[1], Monique R. Bernsen[1,3].

[1]Department of Radiology, Erasmus MC - University Medical Center Rotterdam, Rotterdam, the Netherlands
[2]Laboratory of Experimental Surgical Oncology, Section Surgical Oncology, Department of Surgery, Erasmus MC - University Medical Center Rotterdam, Rotterdam, The Netherlands
[3]Department of Nuclear Medicine, Erasmus MC - University Medical Center Rotterdam, Rotterdam, the Netherlands

Published in *Cell Transplant.* 2012;21(1):191-205

## Abstract

In the current study cell labeling was performed with water soluble Gadolinium-DTPA containing liposomes, to allow for cell tracking by MRI. Liposomes were used to assure a highly concentrated intracellular buildup of Gd, aiming to overcome the relatively low MRI sensitivity of Gd (as compared to T2 contrast agents). Liposomes were positively charged (cationic) to facilitate uptake by binding to anionic charges in the cell membrane of bone marrow-derived mesenchymal stem cells (MSCs). We assessed the cellular Gd load for varying labeling times (1h, 4h and 24h) and liposome concentrations (125, 250, 500, 1000 µM lipid), closely monitoring effects on cell viability, proliferation rate and differentiation ability. Labeling was both time- and dose-dependent. Labeling for 4h was most efficient regarding the combination of processing time and final cellular Gd uptake. Labeling for 4h with low-dose concentration (125 µM lipid, corresponding to 52±3 µM Gd) yielded an intracellular load of 30±2.5 pg Gd cell-1, without any effects on cell viability, proliferation and cell differentiation. Gd-liposomes, co-labeled with fluorescent dyes, exhibited a prolonged cellular retention, with an endosomal distribution pattern. In vitro assay over 20 days demonstrated a drop in the average Gd load *per cell,* as a result of mitosis. However, there was no significant change in the sum of the Gd load in all daughter cells at endpoint (20 d.), indicating an excellent cellular retention of Gd. MSCs labeled with Gd-liposomes were imaged with MRI at both 1.5T and 3.0T, resulting in excellent visualization both *in vitro* and *in vivo.* Prolonged *in vivo* imaging of 500,000 Gd-labeled cells was possible for at least two weeks (3.0T).
In conclusion, Gd-loaded cationic liposomes (125 µM lipid) are an excellent candidate to label cells, without detrimental effects on cell viability, proliferation and differentiation and can be visualized by MRI.

## Introduction

*In vivo* cell tracking is a growing field of research since it is considered to be a crucial technology for the development and implementation of cell therapy. Cell therapy in itself holds great promise for a variety of diseases and disorders such as cancer, cardiovascular disease, neurodegenerative diseases, and musculoskeletal disorders by providing unique opportunities for tissue regeneration and targeted therapy or drug delivery (7-10). In both pre-clinical and clinical studies, therapeutic benefit of cell therapy for all these aspects has been demonstrated (11-16). However, the success has been limited and variable and the understanding of the processes by which stem cell therapy results in therapeutic benefit are also poorly understood. Therefore, the ability to track the fate of transplanted cells *in vivo*, has been the focus of increasing numbers of research efforts.

Currently, MR imaging is considered the modality of choice for *in vivo* cell tracking in patients and large animals due to its high spatial resolution. In order to visualize cells by MRI, incorporation of MRI contrast agents (CAs) by the cells of interest is required. Two main classes of CAs are being used for this purpose, paramagnetic substances (T1 shortening CAs) like gadolinium (Gd)-chelates (17,18) and superparamagnetic particles (T2 shortening CAs) which are mainly iron-oxide based (19-22). Generally, the latter allow for more sensitive imaging, easier incorporation into the cell and harbor less intrinsic toxicity (23). This has led to a vast amount of studies using a variety of iron-oxide particles and labeling procedures (6,18,24-33). These studies showed that for virtually every cell type, sufficient iron-oxide can be incorporated in the cell allowing for sensitive detection, even at single cell level, without apparent toxic effects (6,18).

However, the use of T2 CAs in cell tracking carries several disadvantages regarding image interpretation. Firstly, T2 CAs cause a signal loss which may be confused with (patho) physiological conditions such as hemorrhage, blood flow or air-pockets (34-36) or with areas containing an endogenous high iron content, such as the liver, the spleen or tumors like melanomas. Secondly, due to susceptibility artifacts, the size of a cell cluster will be heavily overestimated on MRI. This will severely hamper interpretation of surrounding anatomical structures in a cell graft. Thirdly, iron-oxide particles are susceptible to reuptake by macrophages *in vivo* (37,38), which is especially relevant during direct cell implantation, because of the concurrent high cell death rates. Finally, T2 CAs are best visualized by T2 weighted sequences, which have an inherently lower signal-to-noise ratio than T1 weighted images.

More recently, Gd-chelates have been receiving increasing interest as an intra-cellular imaging probe (39-43). One of the main advantages of Gd-chelates over T2 CAs is their predominant positive contrast effect due to T1-shortening. Furthermore, as a result of its low molecular weight, the Gd-chelate can escape macrophage reuptake after cellular release due to e.g. cell death. This is a highly important advantage in the in vivo setting as it contributes to a high specificity of the MRI signal, aiding the assessment of overall cell viability after cell transplantion.

In this report the use of the clinically approved Gd-DTPA in cell labeling was studied. As Gd has an inherently relatively low MR sensitivity, cationic liposomes were used to concentrate the Gd, allowing a high intracellular build up (44). The rationale behind making them cationic, was to improve uptake by binding to anionic charges in the cell membrane. Liposomes have already widely been used for both diagnostic (23,27,41) and therapeutic purposes (45-47) or combinations thereof (48) and are a well-known vehicle in DNA-transfection studies (49-51). The most exciting feature is their versatility. Both the constituents in the aqueous core and surface properties can be modulated, allowing e.g. a combination of a diagnostic tracer with a therapeutic one ('theragnostics'). In order to facilitate a successful clinical translation of Gd-liposomes as a MRI-tracer in cell-tracking, efforts have to be made to assess the effects on cell behavior and viability and to overcome sensitivity issues by improving labeling efficiencies.

These issues have been hardly addressed so far. In this study these issues were addressed using bone-marrow derived mesenchymal stem cells.

# Material and Methods

## Liposome Preparation

Gd-DTPA was incorporated in cationic liposomes using the lipid-film hydration technique. A 100 µmol mixture of 1,2-dipalmitoyl-sn-glycero-3-phosphocholine (DPPC; Lipoid GmbH, Ludwigshafen, Germany), cholesterol (Sigma-Aldrich, St. Louis, MO, USA), 1,2-dioleoyl-3-trimethylammonium-propane (chloride salt) (DOTAP; Avanti Polar lipids, Alabaster, AL, USA) in the molar ratio 47:33:20 was dissolved in chloroform/methanol 2:1 (v/v) and evaporated *in vacuo* using a rotary evaporator (Büchi Rotavapor R-210, Büchi Labortechnik, Flawil, Switzerland). The lipid film was subsequently hydrated in either HEPES buffered saline (20 mM HEPES, 135mM NaCl, pH adjusted to 7.4) or Gd-DTPA (Magnevist; Bayer Schering Pharma AG, Berlin, Germany) to create control liposomes and paramagnetic liposomes, respectively.

Liposome solutions were extruded at 45ºC through a high-pressure Lipex thermoline extruder (Northern Lipids Inc, Vancouver, Canada) by sequential passing through Nuclepore polycarbonate membrane filters (Whatman, Newton, MA, USA) with pore diameters of 200 nm, 100 nm and 50 nm. Per filter type, 5 extrusion steps were applied. The resulting solution was ultracentrifuged twice (Beckman Coulter, Fullerton, CA, USA) at 300,000 G (4 °C). Supernatant was discarded. The resulting liposome pellet was typically resuspended in 2 ml HEPES.

## Characterization of Liposomes

The average diameter and size distribution of the liposomes in the final formulation were determined by dynamic light scattering (DLS) using a Zetasizer Nano (Malvern Instruments, Worcestershire, UK). The mean resultant size of different batches of Gd-DTPA liposomes as determined by DLS was 111-123 nm with a polydispersity index (PDI) of 0.04-0.09, whereas HEPES control liposomes were slightly larger with sizes 114-129 nm (PDI 0.06-0.12). The zeta potential was 43±7.0 mV. Relative Gd content was determined by Inductively Coupled Plasma-Optical Emission Spectroscopy (ICP-OES) and was 66±4 µg Gd/µmol total lipid. Liposomal phosphate content was assessed by spectrophotometric analysis according to Rouser (52).

## Cell Culture and Cell Labeling

Rat mesenchymal stem cells (MSCs; Millipore, Billerica, MA, USA) of passage 3 or 4 were used for all experiments at 70% subconfluency. MSCs were cultured in a humidified $CO_2$ incubator (Heraeus, Hanau, Germany) at 37°C and 5% $CO_2$ in Dulbecco's modified Eagle medium (Invitrogen; Carlsbad, CA, USA) supplemented with 2% FBS (Lonza; Basel, Switzerland), 2% penicillin/streptomycin (Invitrogen), 2% L-glutamine (Invitrogen), 1% MEM essential vitamin mixture (Lonza), 1% NEAA (Sigma-Aldrich) and 0.5% glutamax (Invitrogen). Unless stated otherwise, cells were grown in 75-$cm^2$ flat-bottom flasks (Corning, NY, USA). Cell labeling was performed on basis of lipid concentration. Lipid concentration in various experiments was 125, 250, 500 or 1000 µM, corresponding to 52±3, 104±6, 209±13 and 420±25 µM Gd respectively. Control cells were incubated with HEPES-containing liposomes.

Labeling was performed for 4h, unless otherwise stated. Cells were detached using accutase (Millipore) and underwent three washing steps in prewarmed phosphate-buffered saline (PBS). Following harvesting, cells were centrifuged at 300 G for 5 minutes to acquire a cell pellet.

## Uptake Efficiency and Gd Content Measurement

To assess the uptake efficiency as a function of labeling time (i.e. 1h, 4h, 24h) and lipid dosage (i.e. 0, 125, 250, 500 and 1000 µM total lipid) 4 x $10^5$ MSCs were seeded in 25-$cm^2$ flasks and labeled with Gd-liposomes at the indicated doses for the indicated times, resulting in 15 groups. The entire experiment was performed in triplicate.

Following incubation, cells were washed, harvested and centrifuged. Supernatant was then carefully aspirated and the obtained cell pellet was suspended in PBS allowing cells to be counted in a hemocytometer. After a second centrifugation step the cell pellet was suspended in 4 ml. Triton X-100 2% (St. Louis, MO). This solution was heated up at 55 °C in a thermoshaker and mixed for 30 min. at 6G to induce cellular and liposomal lysis. Three aliquots of 20µl Gd-liposomes were treated with Triton and vortexed as well. Both the total amount of internalized Gd and liposomal Gd were then measured using inductively coupled plasma-optical emission spectroscopy (ICP-OES; Optima 4300DV, Perkin Elmer, Norwalk, CT) operating at a wavelength of 342 nm. Cellular uptake efficiency was calculated as:

$$Eff_{uptake} = \frac{Gd_{pellet}}{Gd_{liposomal}} \qquad [1.]$$

where $Gd_{pellet}$ is defined as the total amount of Gd in the harvested cell pellet and $Gd_{liposomal}$ the amount of Gd in liposomes added to the culture medium. Counting the cells in the harvested pellet ($N_{cells}$), the mean cellular Gd concentration was derived from

$$Gd_{cellular} = \frac{Gd_{pellet}}{N_{cells}} \qquad [2.]$$

## In Vitro Toxicity Assay

Unless stated otherwise, all assays were performed with separate groups undergoing labeling with increasing dosages of Gd-DTPA liposomes (ie 0, 125, 250, 500 and 1000 µM lipid). All experiments were performed in triplicate.

Putative dose-dependent cytotoxicity of Gd-liposomes was studied with MTT-assays in a 96-well plate. Additional experiments were included to study a possible specific cytotoxic effect of the Gd-DTPA component, comparing effects on cells labeled with either Gd-liposomes or with control liposomes containing HEPES buffer only. The MTT-assay is based on the reduction of yellow MTT (3-(4,5-dimethylthiazol-2-yl)-2,5-diphenyl tetrazolium bromide) to purple formazan by living cells (53). In both experiments MSCs from the same batch were cultured (1.0 x $10^4$ MSCs per well) overnight in 100 µl culture medium in quintuplets, followed by 4h labeling at 70% subconfluency. At end of labeling, cells were washed three times with PBS with care in order not to destruct the monolayer. Twenty-four hours after start of labeling

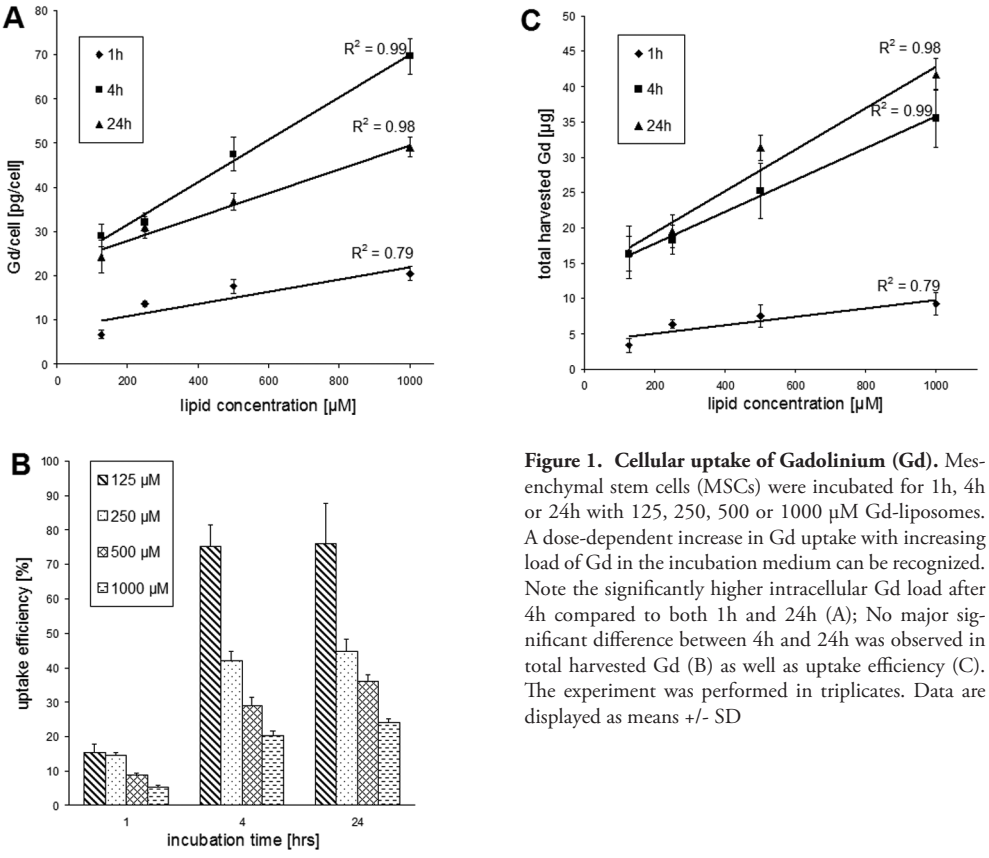


**Figure 1. Cellular uptake of Gadolinium (Gd).** Mesenchymal stem cells (MSCs) were incubated for 1h, 4h or 24h with 125, 250, 500 or 1000 µM Gd-liposomes. A dose-dependent increase in Gd uptake with increasing load of Gd in the incubation medium can be recognized. Note the significantly higher intracellular Gd load after 4h compared to both 1h and 24h (A); No major significant difference between 4h and 24h was observed in total harvested Gd (B) as well as uptake efficiency (C). The experiment was performed in triplicates. Data are displayed as means +/- SD

MTT substrate (5 µg/µl) was filtered through a 0.2µm filter membrane followed by addition of 50 µl to each well. Plates were then incubated for 3h at 37°C, followed by centrifugation. Medium was carefully aspirated and 100 µl DMSO was added to each well to lyse the cells and dissolve the insoluble formazan product. Absorbance was recorded after 30 min at 490 nm using a 96 well-plate reader (Victor2, Perkin Elmer, Norwalk, CT, USA). For internal validation of the MTT-assay, the correlation between cell amount and absorbance was assessed by inclusion of a serial dilution of unlabeled cells, ranging from 4.0 x $10^2$ to 2.5 x $10^4$ cells per well.

## Proliferation and Gd-retention assay

Long-term effects on proliferation were studied on cells which had been labeled for 4h with the previous mentioned dosages of Gd-DTPA liposomes. MSCs were counted in a hemocytometer on days 4, 7, 11, 15 and 20. Non-viable MSCs were included in the cell count as well, to avoid any bias from possible differences in cell death rates. At each time-point culturing was consistently continued with 7.5 x $10^5$ MSCs only, maintaining a practical workflow. Simultaneously, MSCs were collected and spun down at 300 m/$s^2$ for 5 min in triplicates. Total harvested Gd load of these samples was measured by ICP-OES in order to assess possible extracellular leakage of Gd.

## Differentiation assay

Effects of labeling with Gd-DTPA liposomes on the multi-lineage capacity of MSCs was determined. For this purpose 6 x $10^4$ MSCs were seeded per well in 24-well plates and allowed to form a confluent monolayer. Adipogenesis was stimulated for 20 days using both adipogenesis induction and maintenance medium (Millipore, Billerica, MA, USA) in three cycles, whereas osteogenesis was promoted for 13 days with osteogenesis induction medium (Millipore, Billerica, MA, USA). Finally, Oil Red O and Alizarin Red staining were performed in separate plates to detect adipocytes and osteocytes, respectively.

## Confocal Laser Scanning Microscopy

To study the integrity of liposomes following endocytosis, 0.1 mol% of rhodamine-PE (Avanti Polar lipids) was added during liposome preparation, serving as a fluorescent bilayer marker. The water-soluble, membrane-impermeable dye calcein (Sigma-Aldrich) was added to the hydration solution at a concentration of 12μM, at which concentration its fluorescence is maximal (54). MSCs were labeled for 4h, washed three times with PBS and imaged for 62h using a LSM 510 META confocal microscope (Zeiss, Oberkochen, Germany) in a closed humidified chamber at 37°C and 5% $CO_2$. Hoechst 33258 was used as a nuclear stain. Detailed examination was done using a 40x oil-immersion objective lens (NA 1.3). Scans were made in multitrack mode with a 405 nm diode laser for Hoechst 33258 excitation (420-480 nm BP filter), a 488 nm Argon laser for calcein (505-530 nm BP filter) and a 543 nm Helium-Neon laser for rhodamine (560-615 nm BP filter). MetaFluor software (Molecular Devices, Downingtown, PA, USA) was used for instrument control and image acquisition. Images were analyzed using Zeiss LSM Image Browser 4.2.0. Considering the broad bandwidths and asymmetrical spectral profiles of both calcein and rhodamine, bandpassfilters were set rationally to prevent cross-talk of fluorescence signal from both fluorophores. Nevertheless, additional control experiments were performed to confirm the absence of cross-talk, using single fluorophore labeled liposomes containing either calcein or rhodamine. All experiments were recorded with the same laser settings.

## MR imaging

Data acquisition was performed on a 1.5T (in vitro only) and on a 3.0T (in vitro and in vivo) clinical MRI scanner (Signa Excite; GE Medical Systems, Milwaukee IL, USA) using unmodified gradients and custom made surface coils with an inner diameter of 2 cm.

To study the MRI behavior of Gd-liposomes labeled MSCs in vitro, a stock solution of 1.84 x $10^5$ labeled MSCs in 0.3% liquid agar (BD, Sparks, MD, USA) was prepared. Care was taken to acquire a homogeneous suspension without formation of air bubbles. By serial dilution 8 concentrations in the range of 1.84 x $10^5$ - 1.45 x $10^3$ cells $\mu l^{-1}$ agar were prepared and filled out in a 384-wells plate. Surrounding wells were filled with water to prevent air-induced susceptibility artifacts. To produce T1-weighted images, the plates were imaged using a 2D spin-echo sequence with echo time (TE)= 10 ms and repetition time (TR)= 500 ms, a resolution of 40x40 $\mu m^2$ (FOV 2x2 cm, matrix 512x512), one acquisition and a slice thickness of 1.4 mm. The plates were scanned at room temperature (20 °C).

For in vivo imaging a suspension of 0.5 x $10^6$ MSCs in 20 μl PBS was injected subcutaneously or intramuscularly in the hind limb of Wistar rats (Harlan, Horst, the Netherlands). As a control, non-viable cells were injected as well. Cells were killed by repeated freeze-thawing (in liquid nitrogen). Viability was then checked by trypane blue assay.

For scanning, rats were anesthetized by i.p. injection of sufentanil and medethomidine both at 300 μg/kg body weight. Animals were scanned repeatedly over a two-week period at days 0,

5 and 14. A 3D SPGR sequence (with fat suppression) was applied, with TE=3.0 ms, TR=30 ms and $\alpha$=30°, at a resolution of 125x125 $\mu m^2$ and a slice thickness of 400 µm. This resulted in an acquisition time of 20 min. Animals were housed under standard conditions of light and accommodation, and were fed a standard laboratory diet ad libitum. All experiments with animals were performed with prior approval of the institutional animal care committee. After the 14 days follow up period animals were euthanized.

### Histology

For histological purposes, cells were labeled with liposomes containing rhodamine-PE (Avanti Polar lipids) and in some instances also with the nuclear dye Hoechst (Sigma-Aldrich). Hoechst was thus used to label cells with prior to intramuscular injection, not as a counterstain. Animals were sacrificed at day 1 or 5 after injection. Muscular tissue at the injection site was then carefully dissected out, cryopreserved in OCT Tissue-TEK (Sakura Europe, Alphen aan den Rijn, the Netherlands) and cryosectioned at 10 µm slices.

### Statistical analysis

All values are presented as mean±SD from triplicates and expressed in relation to unlabeled cells. Statistical significance between selected groups in both the viability and proliferation assay were determined with one-way ANOVA; for viability a Bonferroni post-hoc test was applied for selected pairs (Graphpad InStat 3.06; Graphpad Software Inc., San Diego, CA, USA). The degree of significance is given when appropriate (*$p < 0.05$; **$p < 0.01$; ***$p < 0.001$).

## Results

### Cellular Gd uptake

A concentration-dependent increase in intracellular Gd load was observed with increasing Gd liposome concentration in the incubation medium (Fig. 1A). This trend was less obvious at 1h exposure time. Intracellular Gd-load was highest (70±4 pg Gd $cell^{-1}$) by labeling with 1000µM lipid (420±25 µM Gd) for 4h.

According to Eq. (1), for each labeling period, maximal uptake efficiency was achieved using 125µM total lipid (Fig. 1B). Uptake efficiency was not significantly improved by prolonged incubation (> 4h). This is most likely caused by intracellular Gd dilution due to cell division, outweighing the *de novo* uptake of abundant Gd by daughter cells. Washout of Gd is considered less likely, as there was no striking difference in total harvested cell-associated Gd after 4h and 24h incubation time (Fig. 1C). As a result, considering time-efficiency, further experiments focusing on cell behavior were conducted using the 4h labeling protocol.

### In vitro toxicity and proliferation assays

MTT assays demonstrated a dose-dependent cytotoxic effect of labeling with both unloaded and Gd-loaded liposomes (Fig. 2A). As a validation of the technique, a double dilution series of unlabeled cells showed a nice linear relation with the measured absorbance (Fig. 2B). No significant effect on cell viability was observed at low dose liposome incubation (125 µM lipid)

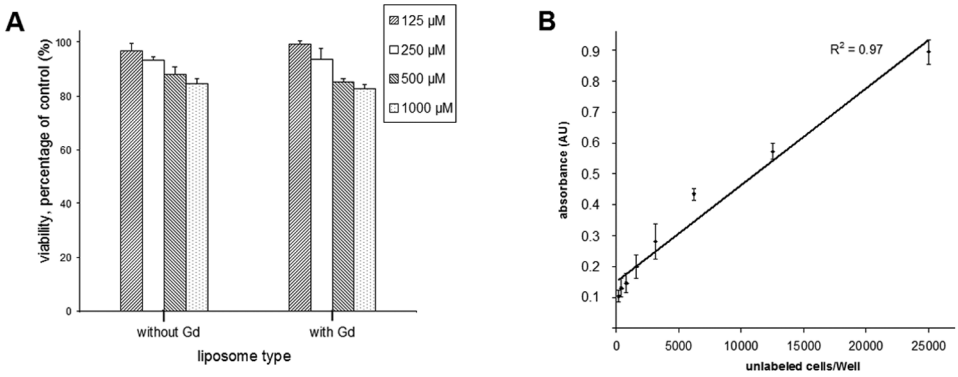


**Figure 2. Viability by MTT-assay as a function of Gd and lipid concentration.** Labeling time of 4h. Note the dose-dependent negative effect on cell survival at high lipid concentration (normalization to unlabeled control cells) (A). For each specific lipid dose, no significant difference ($p > 0.05$) in viability was found between the two liposome types. Linear relation between absorbance and unlabeled cell amount (B). Data are displayed as means +/- SD

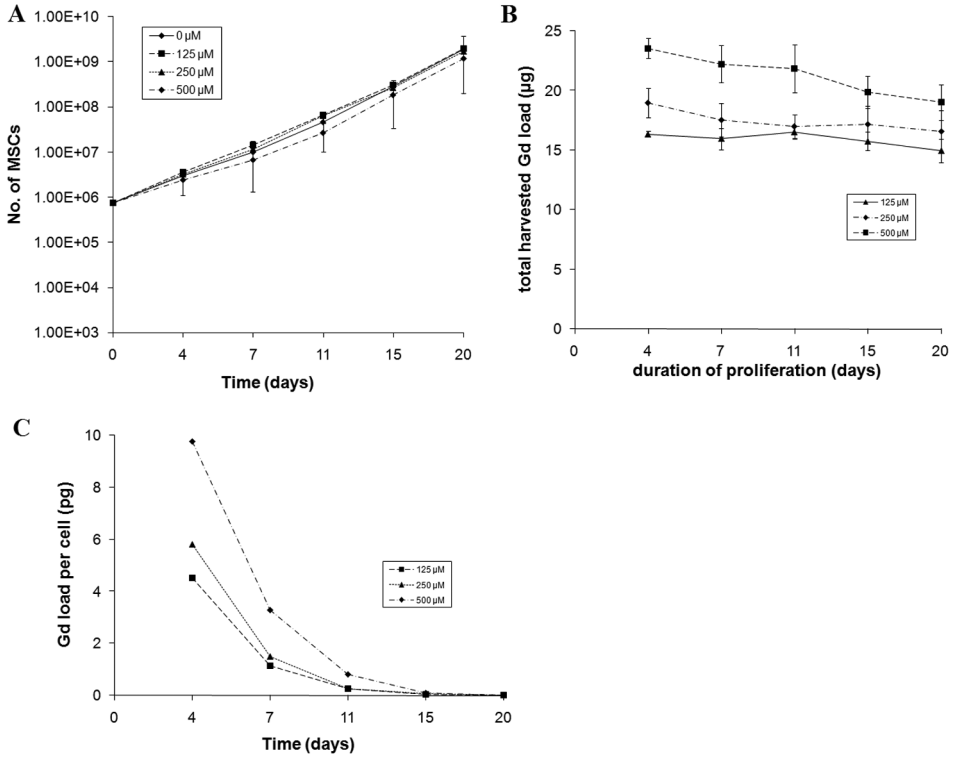


**Figure 3. Proliferation assay of MSCs.** The proliferation rate of labeled cells did not differ significantly ($p > 0.05$) from unlabeled control cells (A). Total harvested Gd load at each passage step is shown in (B). With ongoing proliferation, cellular Gd load decreased accordingly (C). Data in (A) and (B) are displayed as means +/- SD. Data in Fig 3C was calculated by dividing data points in B by corresponding data points in A (total harvested Gd load/ no. of cells)

for both liposome types ($p > 0.05$). However, higher concentrations (≥ 250 µM lipid) affected viability slightly negative ($p < 0.001$) in a dose-dependent manner. This trend was observed for both unloaded and Gd-loaded liposomes. No statistically significant difference was found in viability of cells labeled with identical concentrations of either of the two liposome types, throughout the entire examined concentration range ($p > 0.05$).

## Proliferation and Gd-retention assay

Assessment of proliferation was done by cell count over a period of 20 days (Fig 3). As derived from the viability assay, variations in cell death exist for different liposome concentrations. Therefore, both viable and non-viable MSCs were counted to exclude an influence on proliferation caused by differences in viability. Hence it may be assumed that the growth rates reflect merely cellular mitosis. None of the investigated doses exhibited a significant reduction in proliferation rate ($p > 0.05$), compared to control unlabeled cells.

At various time-points samples were taken for assessment of the total cellular Gd load. Due to mitosis, average Gd load *per cell* diminished rapidly (Fig. 3C). Data in Fig 3C was calculated by dividing data points in B by corresponding data points in A (total harvested Gd load/ no. of cells). No significant drop in the *total* Gd load occurred at 125 µM lipid (52±3 µM Gd) and 250 µM lipid (104±6 µM Gd) (fig. 3B). However, a small but significant ($p<0.05$) decrease was observed with 500 µM lipid (209±13 µM Gd) in the incubation medium. The decrease with this lipid dose may be explained by a lower harvested Gd amount, due to the relatively higher cell death (Fig. 2A). Even though care was taken to collect both viable and non-viable MSCs, it is possible that a reasonable amount of Gd from disintegrated non-viable cells was collected inadequately during centrifugation.

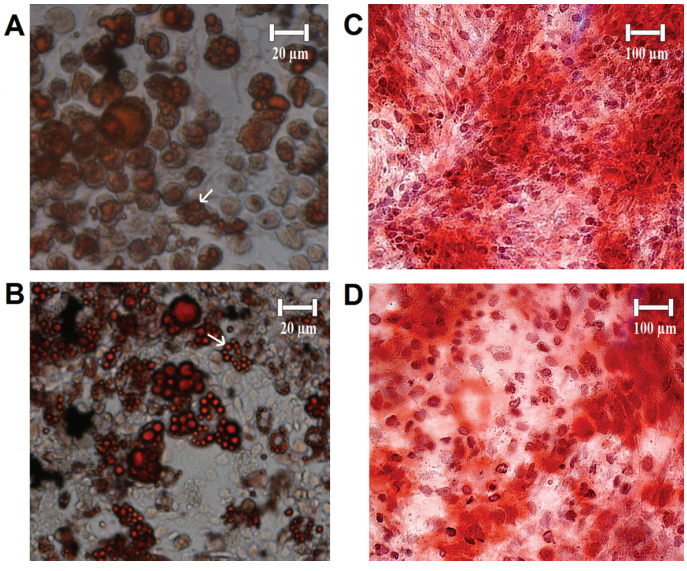


**Figure 4. Cell differentiation assay.** In vitro differentiation of MSCs is not inhibited by Gd-DTPA liposome labeling (shown are images of the highest incubation dose, 1000µM lipid). Differentiation into adipocytes (Oil Red O stain) was unimpaired for both control MSCs (A) and MSCs labeled with 1000 µM lipid (B). Differentiation into osteocytes was unimpaired as well for both control cells (C) and cells labeled with 1000 µM lipid (D). White arrows in A and B point to a lipid vacuole. MSCs labeled with doses < 1000 µM lipid exhibited similar differentiation phenotypes (data not shown).

## Adipogenesis, osteogenesi

An important issue in imaging of stem cell transplantation is the preservation of differentiation ability upon incorporation of a tracer. Adipogenic and osteogenic differentiation were induced with *in vitro* cell cultures. Oil red O staining revealed that MSC labeled with all tested Gd-liposome concentrations (125-1000 µM lipid) underwent adipogenic differentiation with efficiencies similar to unlabeled cells. Oil vacuoles could be detected in nearly all Gd-liposome labeled MSCs, being phenotypically indistinguishable from unlabeled MSCs. In addition, Alizarin Red staining showed a sustained osteogenic differentiation potential of Gd-labeled MSCs (Fig. 4).

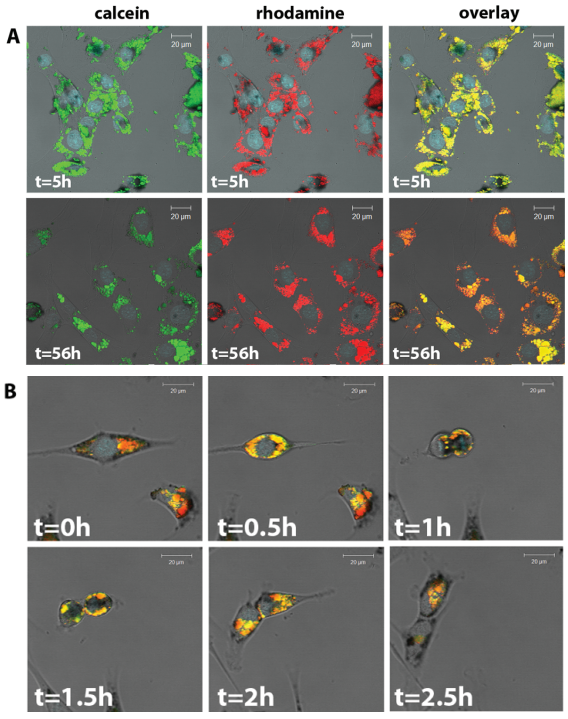


**Figure 5. Confocal fluorescence.** Time-resolved confocal laser scanning microscope (CLSM) images of MSCs labeled with Gd-liposomes (4 h), containing rhodamine in the bilayer and intraliposomal calcein. Images are bright field, with overlay from confocal fluorescence. Elapsed time after cell labeling is indicated. Colocalization of rhodamine (red) and calcein (green) fluorescence indicates towards intact liposomes, whereas the dotted appearance indicates an endosomal distribution. Note the absence of extracellular fluorescence leakage. Mitosis was unimpaired, with a roughly even distribution of liposomes over daughter cells (B). Indicated time represents elapsed time after start of mitosis. Scale bar is shown in the images.

## Confocal Laser Scanning Microscopy

After labeling with 125 µM lipid (52±3 µM Gd) for 4h, viable MSCs were imaged for 56h. Liposomes showed an intracellular accumulation, which was perinuclear in distribution. During the entire time range no obvious nuclear uptake was perceived. Based on the punctate appearance of both the liposomal membrane-associated rhodamine (red) and the core-encapsulated calcein (green), liposomes most likely resided in endosomes rather than having a diffuse cytosolic distribution (Fig. 5A). No extracellular leakage of fluorescence was recorded during the experiment. Although in a labeled state, MSCs were demonstrated to undergo mitotis with a roughly equal distribution of liposomes among daughter cells (Fig. 5B).
Absence of crosstalk was confirmed in experiments using control liposomes, containing either rhodamine-PE or calcein only (data not shown).

## MR imaging

*In vitro* concentrations of Gd-liposome labeled MSCs in the range of $1.45 \times 10^3$ - $1.84 \times 10^5$ cells $\mu l^{-1}$ agar were imaged to assess the signal intensity as a function of labeled cell concentration. On T1-weighted spin echo (SE)-images, the least cell concentration which could be discerned visually from surrounding water was assessed at $2.9 \times 10^3$ and $5.8 \times 10^3$ cells $\mu l^{-1}$ agar

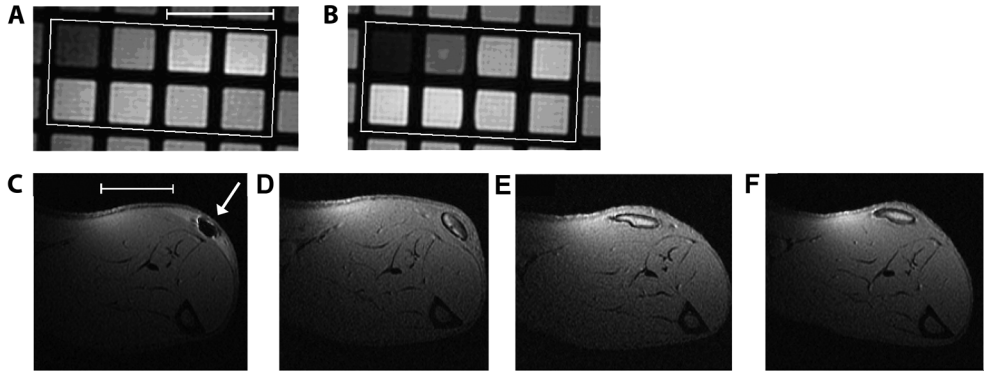


**Figure 6. MR-imaging.** T1-weighted images of MSCs labeled with 125µM Gd-liposomes for 4h. The same cells were scanned at both 1.5T (A) and 3.0T (B). Wells filled with cells are demarcated by the white box. Cell concentrations on the top row, from left to right: $1.84*10^5$, $9.28*10^4$, $4.64*10^4$ and $2.32*10^4$ MSCs $\mu l^{-1}$ agar. Lower row, from left to right: $1.16*10^4$, $5.80*10^3$, $2.90*10^3$ and $1.45*10^3$ MSCs $\mu l^{-1}$ agar. Longitudinal tracking of viable Gd-liposome labeled MSCs (white arrow) in the rat hind leg (3D T1W imaging) imaged at days (C) 1, (D) 5, (E) 7 and (F) 14 after transplantation. Both scale bars in A and C represent 10 mm. Scale bar in A applies to B as well. Scale bar in C applies to C-F.

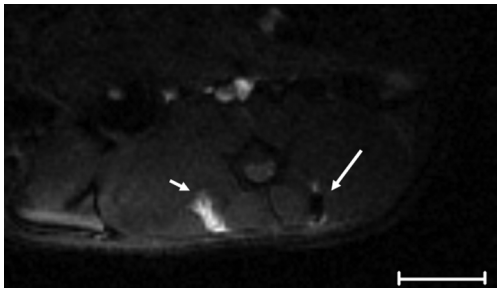

**Figure 7. MR-imaging.** GRE image (TR 8 ms., TE ms., $\alpha$=30° ) of both viable and non-viable Gd-labeled MSCs injected in the lower back muscle, imaged 1 hour after injection. Viable MSCs are visible as hypoenhancement with a hyperintense rim (large arrow), whereas non-viable MSCs exhibit a hyperenhancement (small arrow). Scale bar, 10 mm.

at 3.0T and 1.5T, respectively (Fig. 6A, B).
Strikingly, $1.84 \times 10^5$ cells $\mu l^{-1}$ agar gave rise to a signal loss at 1.5T. This was even more profound at 3.0T (Fig. 6B). This is probably due to a major T2-shortening in very concentrated samples (55,56).
Interestingly, the *in vivo* injected cell cluster in the hind limb exhibited a dualistic behavior. Injected cells were initially perceived as signal loss, slowly gaining in intensity over days (Fig. 6C).
Non-viable cells were injected in vivo as well, as a control. Viability was checked prior to injection, showing 98% of cells to be non-viable. Non-viable cells showed a remarkable hyperenhancement, immediately after injection. (Fig.7).

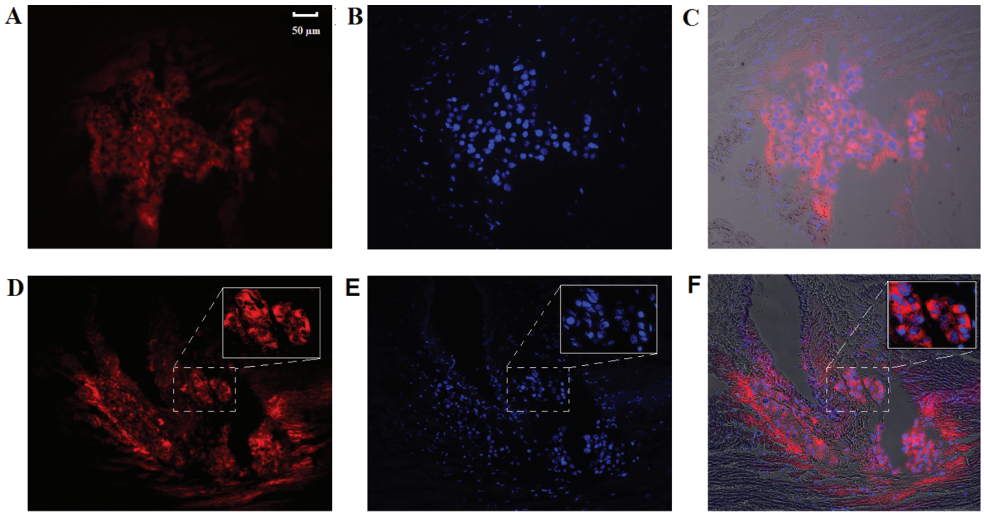


**Figure 8. Histological detection of cells labeled with rhodamine containing liposomes.** Intramuscular injected cells at day 1 (A-C) and day 5 (D-F) post-transplantation. Red fluorescence from the rhodamine-liposomes is clearly visible (A, D). The blue nuclear dye Hoechst, which was added to the cells in culture prior to injection, shows the injected cells at both day 1 (B) and day 5 (E). Overlay images (C, F). The insets in frame D, E and F show a 10x magnification of the area indicated by the dashed rectangle. Scale bar in A applies to A-F.

### Histology

On cryosections, cells could be retrieved at least at day 1 and day 5 after transplantation. Red fluorescence from the rhodamine-liposomes was visible in a perinuclear pattern at both day 1 (Fig. 8A) and was still perceived at day 5 (Fig. 8D).

## Discussion

The achievement of a high intracellular load of CA is an important condition to localize or track cells in cellular imaging. This holds true especially for MRI, since its sensitivity is generally lower with respect to other imaging modalities such as single-photon emission computed tomography (SPECT) or bioluminescence (57). Gd-DTPA is a widely used MR contrast agent which is approved by the U.S. Food and Drug Administration. Being hydrophilic, Gd-DTPA is not taken up spontaneously by cells. This limitation was challenged in this study, by incorporation of Gd-DTPA in cationic liposomes allowing an efficient uptake by cells through binding to anionic charges in the cell membrane.

A dose-dependent decrease in cell viability was observed with Gd-liposome doses increasing from 250 µM lipid, reaching a maximal decrease in viability of around 20% with 1000 µM lipid, the highest dose in this study. The decreased cell viability was also observed with empty, non Gd-containing liposomes, leading to the conclusion that the observed minor toxicity is caused by the cationic liposomes. With a different liposome formulation, in a recent study (41) no statistically significant reduction in labeled cell viability was reported for a lipid concentration up to 5mM, using Gd-DTPA-BSA liposomes. This difference is probably due to the lipid composition used in our formulations consisting of the cationic lipid DOTAP which role is to strongly enhance cellular interaction, but apparently also exerts some toxicity. Toxic-

ity of Gd-DTPA can be excluded, as Gd-liposomes did not cause any significant additional decrease in cell viability, compared to liposomes without Gd. Although DOTAP has been used extensively in DNA-transfection studies, reports on damage to cellular physiology exist (58), lacking however a clear assessment of dose toxicity (59). Interestingly, our experiments demonstrated the existence of a dose-dependent toxicity using > 125 µM lipid. The dose-dependent toxicity seems to be of minor relevance in cell labeling, considering the excellent Gd uptake at 125 µM lipid with an outstanding MR-visualization. In addition, a long term biological effect of the toxicity remains questionable, considering the absence of fluorescent Gd-liposomes in the cell nucleus, reducing the chance of interference with the cell DNA and thus long-term genetic damage. Furthermore, both proliferation and differentiation ability were not impaired by Gd-liposome labeling.

The apparent absence of Gd-chelate toxicity is in line with earlier studies (40), in which gadolinium 1,4,7-tris(carboxymethyl)-10-(2'-hydroxypropyl)-1,4,7,10-tetraazacyclododecane (Gd-HPDO3A) and Gd@C82fullerenol were used. To a certain extent, this tones down the initial safety concerns on the hypothesized dechelation of Gd-DTPA upon incorporation in endosomes, feared to result in potentially hazardous $Gd^{3+}$ ions (60). Additionally, the putative manifestation of nephrogenic systemic fibrosis (NSF) following transplantation of Gd-labeled cells is considered an important drawback in future clinical studies. NSF however, has been reported to occur merely in patients with an impaired kidney function (61). Consequently, this complication should be easily avoidable if these selected patient groups are excluded in future clinical studies.

The *in vitro* uptake of Gd-liposomes was both time- and dose dependent. Regarding dose-dependency, some parallels can be drawn between present results and previous reports by different authors. For example, labeling with cationic liposomes for 2 hours yielded an uptake of 12.5 pg Gd $cell^{-1}$ (uptake efficiency 31%) (23), comparable to our findings. Another analogy concerns the cellular Gd uptake, which was linearly proportional to the concentration of Gd-liposomes in the medium. A similar relation was described using Gd-HPDO3A (42) and Gadofluorine M (62).

Of note, labeling for 4h with 125 µM lipid (52±3 µM Gd) yielded an intracellular load of 29±2 pg $cell^{-1}$, without any detrimental effects on cell viability, cell proliferation and cell dif-

**Table 1** Reported intracellular gadolinium (Gd)-loads following labeling with Gd-compounds.

| Reference | Gd load (pg $cell^{-1}$) | Incubation time (h) | Labeling method | Compound | Cell viability (%) |
|---|---|---|---|---|---|
| (16) | 12.5 | 2 | cationic liposomes | Gd-DTPA (Magnevist) | 80.6±11.4 |
| (4) | 0.12 | 10 | protamine sulfate | Gd@C82 (fullerenol) | 100 |
| (53) | 13.1 | 16 | pinocytosis / electroporation | Gd-HPDO3A (Prohance) | * |
| This report, 2010 | 29±2 | 4 | cationic liposomes, 125 µM lipid | Gd-DTPA (Magnevist) | 99±1.37 |
| This report, 2010 | 70±4 | 4 | cationic liposomes, 1000 µM lipid | Gd-DTPA (Magnevist) | 83±1.5 |

*not reported

ferentiation. This amount is considerably higher (2-97x) than most intra-cellular Gd loads reported in other studies, as listed in Table 1. Even higher Gd loads (70±4 pg cell$^{-1}$) were achieved with 1000μM lipid (420±6 μM Gd), with some implications for cell viability however (-17±1.5%). An uptake of such a magnitude may be attributed to the abundant uptake of cationic liposomal lipids (DOTAP) through binding to anionic charges in the cell membrane. The advantages of electrochemical interaction in cell labeling have been reported before (63). Gd-liposome labeled MSCs maintained the multi-lineage ability, shown by the differentiation into both adipocytes and osteocytes.

Intracellular distribution is a fairly important issue to be aware of in MRI-cell tracking, affecting the relaxivity of both T1 (43) and T2 (64) contrast agents. Live cell confocal fluorescence revealed an initial endosomal distribution of the liposomes. A similar distribution pattern was reported for Gd-liposomes (41) and Gd-HPDO3A (43). By confocal fluorescence, no extracellular leakage or obvious extracellular membrane-attached liposomes were detected. This was further confirmed by ICP-OES measurements, revealing virtually no loss of Gd over at least 20 days with doses ≤ 250 μM lipid. This is of importance in cell tracking by MRI, considering the effect of compartmentalization on relaxivity. The use of Gd-liposomes will limit the occurrence of false-positive labeled cells, contributing to a more reliable quantification of transplanted cell fate. This is a clear advantage over iron-oxide particles, being notorious for clustering on the extracellular membrane (65), causing some ambiguities in relaxivity. Longitudinal confocal microscopy further confirmed the results from the MTT- and proliferation assay, demonstrating the preserved viability and mitosis of Gd-labeled cells over time.

As mentioned before, a major incentive for the use of intra-cellular Gd is the signal gain, as opposed to the signal loss rendered by iron-oxide particles. Interestingly, Gd-labeled cells were able to cause a signal *loss* both *in vitro* and *in vivo*. A signal loss *in vivo* was also reported in a study using a Gd-based, bi-functional agent called GRID (66). In that study, injection of GRID-labeled cells into the rat brain resulted in a hypo-intense tract surrounded by hyper-intense rim. This phenomenon was explained as a difference in cell density in the two areas. The strong T2-shortening effect of highly concentrated T1 CAs has been reported before (55,56). In our study this effect manifested *in vitro* at 1.84 x $10^5$ cells μl$^{-1}$ and *in vivo* at 2.5 x $10^4$ cells μl$^{-1}$, a tenfold difference. This difference implies that more factors are in play, for example differences in water diffusivity or the compartmentalization of Gd. The difference in signal behavior *in vitro* and *in vivo* is complex and *in vitro* results can not be extrapolated directly to the in vivo situation. For example, in vitro the cellular Gd concentration decreased according to proliferation (fig 3C), a known limitation of external labeling. The proliferation ability of cells in vivo however will hardly be the same. It is also possible that after injection the density of a labeled cell cluster increases, concurrently increasing the Gd load per voxel, causing differences in signal behaviour between in vitro or in vivo applications.

The increase over time in signal intensity *in vivo* has been reported before (67) and may be due to cell division leading to a net lower Gd concentration per cell or cell death with extracellular loss of Gd. The latter was confirmed by the injection of non-viable Gd-labeled cell controls (in which the membrane was ruptured), which caused a hyperenhancement (Fig 7). Compartmentalization of Gd affects T1 contrast by hindering the accessibility to surrounding water (53). Cell death with membrane rupture therefore improves the diffusion of water to Gd, leading to an increased R1 relaxation rate, causing a bright signal on MRI. In future studies, additional quantification techniques like e.g. bioluminescence could be used to further relate the MRI signal in detail to underlying biological events such as viability and proliferation.

Gd-liposomes can be considered a promising candidate to shift the emphasis in future cell labeling studies from T2 to T1 CAs. As the uptake of Gd-liposomes does not rely on receptor-mediated uptake, Gd-liposomes might prove a valuable labeling technique for multiple cell lines. They can overcome many of the disadvantages associated with T2 contrast agents. This might substantiate the use of Gd-liposomes in MRI-guided medicine.

## Conclusions

Labeling of mesenchymal stem cells with cationic Gd-liposomes for 4h resulted in high cellular Gd uptake. It represents an efficient labeling method, as prolonged incubation up to 24 h. did not further improve Gd uptake. Labeling with low concentrations of Gd-liposomes showed no effects on viability, proliferation rate and differentiation, while resulting in sufficient cellular Gd-uptake and MRI visualization both *in vitro* and *in vivo*. Gd-liposomes were located intracellular in endosomes, with excellent retention of Gd for at least 20 days. No obvious leakage of the Gd label from the cells was noted. Gd-labeled cells were clearly visualized on a 3.0 T clinical scanner. With the proposed labeling method, Gd-liposomes prove to be an excellent candidate for MRI cell tracking.

## Acknowledgements

The authors wish to thank dr. Alex Nigg for technical support in confocal fluorescence experiments, both Ula Woroniecka and Bert Wolterbeek (Technical University Delft, Delft, The Netherlands) for their assistance with the ICP-OES measurements and Ton Everaers for graphical support. This study was performed in part through support from ENCITE – funded by the European Community under the 7th Framework Programme. All authors confirm that there is no conflict of interest associated with this publication.

# References


1. Aarntzen EH, Srinivas M, Radu CG, Punt CJ, Boerman OC, Figdor CG, Oyen WJ, de Vries IJ. In vivo imaging of therapy-induced anti-cancer immune responses in humans. Cell Mol Life Sci 2013;70(13):2237-2257.
2. Srivastava AK, Bulte JW. Seeing stem cells at work in vivo. Stem Cell Rev 2014;10(1):127-144.
3. Castaneda RT, Khurana A, Khan R, Daldrup-Link HE. Labeling stem cells with ferumoxytol, an FDA-approved iron oxide nanoparticle. J Vis Exp 2011(57):e3482.
4. Srinivas M, Boehm-Sturm P, Aswendt M, Pracht ED, Figdor CG, de Vries IJ, Hoehn M. In vivo 19F MRI for cell tracking. J Vis Exp 2013(81):e50802.
5. Bernsen MR, Moelker AD, Wielopolski PA, van Tiel ST, Krestin GP. Labelling of mammalian cells for visualisation by MRI. Eur Radiol 2010;20(2):255-274.
6. Arbab AS, Liu W, Frank JA. Cellular magnetic resonance imaging: current status and future prospects. Expert Rev Med Devices 2006;3(4):427-439.
7. Cancedda R, Dozin B, Giannoni P, Quarto R. Tissue engineering and cell therapy of cartilage and bone. Matrix Biol 2003;22(1):81-91.
8. Corsten MF, Shah K. Therapeutic stem-cells for cancer treatment: hopes and hurdles in tactical warfare. Lancet Oncol 2008;9(4):376-384.
9. Einstein O, Ben-Hur T. The changing face of neural stem cell therapy in neurologic diseases. Arch Neurol 2008;65(4):452-456.
10. Smart N, Riley PR. The stem cell movement. Circ Res 2008;102(10):1155-1168.
11. Winter EM, Grauss RW, Hogers B, van Tuyn J, van der Geest R, Lie-Venema H, Steijn RV, Maas S, DeRuiter MC, deVries AA, Steendijk P, Doevendans PA, van der Laarse A, Poelmann RE, Schalij MJ, Atsma DE, Gittenberger-de Groot AC. Preservation of left ventricular function and attenuation of remodeling after transplantation of human epicardium-derived cells into the infarcted mouse heart. Circulation 2007;116(8):917-927.
12. Lipinski MJ, Biondi-Zoccai GG, Abbate A, Khianey R, Sheiban I, Bartunek J, Vanderheyden M, Kim HS, Kang HJ, Strauer BE, Vetrovec GW. Impact of intracoronary cell therapy on left ventricular function in the setting of acute myocardial infarction: a collaborative systematic review and meta-analysis of controlled clinical trials. Journal of the American College of Cardiology 2007;50(18):1761-1767.
13. Brazelton TR, Rossi FM, Keshet GI, Blau HM. From marrow to brain: expression of neuronal phenotypes in adult mice. Science (New York, NY 2000;290(5497):1775-1779.
14. Bang OY, Lee JS, Lee PH, Lee G. Autologous mesenchymal stem cell transplantation in stroke patients. Annals of neurology 2005;57(6):874-882.
15. Dozin B, Malpeli M, Cancedda R, Bruzzi P, Calcagno S, Molfetta L, Priano F, Kon E, Marcacci M. Comparative evaluation of autologous chondrocyte implantation and mosaicplasty: a multicentered randomized clinical trial. Clin J Sport Med 2005;15(4):220-226.
16. Quarto R, Mastrogiacomo M, Cancedda R, Kutepov SM, Mukhachev V, Lavroukov A, Kon E, Marcacci M. Repair of large bone defects with the use of autologous bone marrow stromal cells. The New England journal of medicine 2001;344(5):385-386.
17. Frank JA, Anderson SA, Kalsih H, Jordan EK, Lewis BK, Yocum GT, Arbab AS. Methods for magnetically labeling stem and other cells for detection by in vivo magnetic resonance imaging. Cytotherapy 2004;6(6):621-625.
18. Modo M, Hoehn M, Bulte JW. Cellular MR imaging. Mol Imaging 2005;4(3):143-164.
19. Bulte JW, Zhang S, van Gelderen P, Herynek V, Jordan EK, Duncan ID, Frank JA. Neurotransplantation of magnetically labeled oligodendrocyte progenitors: magnetic resonance tracking of cell migration and myelination. Proc Natl Acad Sci U S A 1999;96(26):15256-15261.
20. Josephson L, Tung CH, Moore A, Weissleder R. High-efficiency intracellular magnetic labeling with novel superparamagnetic-Tat peptide conjugates. Bioconjug Chem 1999;10(2):186-191.
21. Ris F, Lepetit-Coiffe M, Meda P, Crowe LA, Toso C, Armanet M, Niclauss N, Parnaud G, Giovannoni L, Bosco D, Morel P, Vallee JP, Berney T. Assessment of human islet labeling with clinical grade iron nanoparticles prior to transplantation for graft monitoring by MRI. Cell Transplant 2010.

22. Mai XL, Ma ZL, Sun JH, Ju SH, Ma M, Teng GJ. Assessments of proliferation capacity and viability of New Zealand rabbit peripheral blood endothelial progenitor cells labeled with superparamagnetic particles. Cell Transplant 2009;18(2):171-181.
23. Daldrup-Link HE, Rudelius M, Oostendorp RA, Settles M, Piontek G, Metz S, Rosenbrock H, Keller U, Heinzmann U, Rummeny EJ, Schlegel J, Link TM. Targeting of hematopoietic progenitor cells with MR contrast agents. Radiology 2003;228(3):760-767.
24. Bulte JW, Kraitchman DL. Monitoring cell therapy using iron oxide MR contrast agents. Curr Pharm Biotechnol 2004;5(6):567-584.
25. Sykova E, Jendelova P. Magnetic resonance tracking of transplanted stem cells in rat brain and spinal cord. Neuro-degenerative diseases 2006;3(1-2):62-67.
26. Groman EV, Bouchard JC, Reinhardt CP, Vaccaro DE. Ultrasmall mixed ferrite colloids as multidimensional magnetic resonance imaging, cell labeling, and cell sorting agents. Bioconjug Chem 2007;18(6):1763-1771.
27. Meincke M, Schlorf T, Kossel E, Jansen O, Glueer CC, Mentlein R. Iron oxide-loaded liposomes for MR imaging. Front Biosci 2008;13:4002-4008.
28. Suzuki Y, Zhang S, Kundu P, Yeung AC, Robbins RC, Yang PC. In vitro comparison of the biological effects of three transfection methods for magnetically labeling mouse embryonic stem cells with ferumoxides. Magn Reson Med 2007;57(6):1173-1179.
29. Walczak P, Ruiz-Cabello J, Kedziorek DA, Gilad AA, Lin S, Barnett B, Qin L, Levitsky H, Bulte JW. Magnetoelectroporation: improved labeling of neural stem cells and leukocytes for cellular magnetic resonance imaging using a single FDA-approved agent. Nanomedicine 2006;2(2):89-94.
30. Williams JB, Ye Q, Hitchens TK, Kaufman CL, Ho C. MRI detection of macrophages labeled using micrometer-sized iron oxide particles. J Magn Reson Imaging 2007;25(6):1210-1218.
31. So PW, Kalber T, Hunt D, Farquharson M, Al-Ebraheem A, Parkes HG, Simon R, Bell JD. Efficient and rapid labeling of transplanted cell populations with superparamagnetic iron oxide nanoparticles using cell surface chemical biotinylation for in vivo monitoring by MRI. Cell Transplant 2010;19(4):419-429.
32. Schafer R, Ayturan M, Bantleon R, Kehlbach R, Siegel G, Pintaske J, Conrad S, Wolburg H, Northoff H, Wiskirchen J, Weissert R. The use of clinically approved small particles of iron oxide (SPIO) for labeling of mesenchymal stem cells aggravates clinical symptoms in experimental autoimmune encephalomyelitis and influences their in vivo distribution. Cell Transplant 2008;17(8):923-941.
33. van Tiel ST, Wielopolski PA, Houston GC, Krestin GP, Bernsen MR. Variations in labeling protocol influence incorporation, distribution and retention of iron oxide nanoparticles into human umbilical vein endothelial cells. Contrast Media Mol Imaging 2010;5(5):247-257.
34. Reichenbach JR, Venkatesan R, Yablonskiy DA, Thompson MR, Lai S, Haacke EM. Theory and application of static field inhomogeneity effects in gradient-echo imaging. J Magn Reson Imaging 1997;7(2):266-279.
35. van den Bos EJ, Baks T, Moelker AD, Kerver W, van Geuns RJ, van der Giessen WJ, Duncker DJ, Wielopolski PA. Magnetic resonance imaging of haemorrhage within reperfused myocardial infarcts: possible interference with iron oxide-labeled cell tracking? European heart journal 2006;27(13):1620-1626.
36. Jara H, Yu BC, Caruthers SD, Melhem ER, Yucel EK. Voxel sensitivity function description of flow-induced signal loss in MR imaging: implications for black-blood MR angiography with turbo spin-echo sequences. Magn Reson Med 1999;41(3):575-590.
37. Pawelczyk E, Jordan EK, Balakumaran A, Chaudhry A, Gormley N, Smith M, Lewis BK, Childs R, Robey PG, Frank JA. In vivo transfer of intracellular labels from locally implanted bone marrow stromal cells to resident tissue macrophages. PLoS ONE 2009;4(8):e6712.
38. Raynal I, Prigent P, Peyramaure S, Najid A, Rebuzzi C, Corot C. Macrophage endocytosis of superparamagnetic iron oxide nanoparticles: mechanisms and comparison of ferumoxides and ferumoxtran-10. Invest Radiol 2004;39(1):56-63.
39. Aime S, Cabella C, Colombatto S, Geninatti Crich S, Gianolio E, Maggioni F. Insights into the use of paramagnetic Gd(III) complexes in MR-molecular imaging investigations. J Magn Reson Imaging 2002;16(4):394-406.
40. Anderson SA, Lee KK, Frank JA. Gadolinium-fullerenol as a paramagnetic contrast agent for cellular imaging. Invest Radiol 2006;41(3):332-338.

41. Kok MB, Hak S, Mulder WJ, van der Schaft DW, Strijkers GJ, Nicolay K. Cellular compartmentalization of internalized paramagnetic liposomes strongly influences both T1 and T2 relaxivity. Magn Reson Med 2009;61(5):1022-1032.
42. Crich SG, Biancone L, Cantaluppi V, Duo D, Esposito G, Russo S, Camussi G, Aime S. Improved route for the visualization of stem cells labeled with a Gd-/Eu-chelate as dual (MRI and fluorescence) agent. Magn Reson Med 2004;51(5):938-944.
43. Terreno E, Geninatti Crich S, Belfiore S, Biancone L, Cabella C, Esposito G, Manazza AD, Aime S. Effect of the intracellular localization of a Gd-based imaging probe on the relaxation enhancement of water protons. Magn Reson Med 2006;55(3):491-497.
44. van den Bos EJ, Wagner A, Mahrholdt H, Thompson RB, Morimoto Y, Sutton BS, Judd RM, Taylor DA. Improved efficacy of stem cell labeling for magnetic resonance imaging studies by the use of cationic liposomes. Cell Transplant 2003;12(7):743-756.
45. Seynhaeve AL, Hoving S, Schipper D, Vermeulen CE, de Wiel-Ambagtsheer G, van Tiel ST, Eggermont AM, Ten Hagen TL. Tumor necrosis factor alpha mediates homogeneous distribution of liposomes in murine melanoma that contributes to a better tumor response. Cancer Res 2007;67(19):9455-9462.
46. Laginha KM, Verwoert S, Charrois GJ, Allen TM. Determination of doxorubicin levels in whole tumor and tumor nuclei in murine breast cancer tumors. Clin Cancer Res 2005;11(19 Pt 1):6944-6949.
47. Alemdar AY, Sadi D, McAlister VC, Mendez I. Liposomal formulations of tacrolimus and rapamycin increase graft survival and fiber outgrowth of dopaminergic grafts. Cell Transplant 2004;13(3):263-271.
48. Koning GA, Krijger GC. Targeted multifunctional lipid-based nanocarriers for image-guided drug delivery. Anticancer Agents Med Chem 2007;7(4):425-440.
49. Li S, Rizzo MA, Bhattacharya S, Huang L. Characterization of cationic lipid-protamine-DNA (LPD) complexes for intravenous gene delivery. Gene therapy 1998;5(7):930-937.
50. Kofler P, Wiesenhofer B, Rehrl C, Baier G, Stockhammer G, Humpel C. Liposome-mediated gene transfer into established CNS cell lines, primary glial cells, and in vivo. Cell Transplant 1998;7(2):175-185.
51. Imaoka T, Date I, Miyoshi Y, Ono T, Furuta T, Asari S, Ohmoto T, Yasuda T, Tsuda M. Preliminary results of gene transfer to central nervous system by continuous injection of DNA-liposome complex. Cell Transplant 1995;4 Suppl 1:S23-26.
52. Rouser G, Fkeischer S, Yamamoto A. Two dimensional then layer chromatographic separation of polar lipids and determination of phospholipids by phosphorus analysis of spots. Lipids 1970;5(5):494-496.
53. Mosmann T. Rapid colorimetric assay for cellular growth and survival: application to proliferation and cytotoxicity assays. Journal of immunological methods 1983;65(1-2):55-63.
54. Allen TM, Cleland LG. Serum-induced leakage of liposome contents. Biochim Biophys Acta 1980;597(2):418-426.
55. Aoki I, Takahashi Y, Chuang KH, Silva AC, Igarashi T, Tanaka C, Childs RW, Koretsky AP. Cell labeling for magnetic resonance imaging with the T1 agent manganese chloride. NMR Biomed 2006;19(1):50-59.
56. Brekke C, Morgan SC, Lowe AS, Meade TJ, Price J, Williams SC, Modo M. The in vitro effects of a bimodal contrast agent on cellular functions and relaxometry. NMR Biomed 2007;20(2):77-89.
57. Villa C, Erratico S, Razini P, Fiori F, Rustichelli F, Torrente Y, Belicchi M. Stem cell tracking by nanotechnologies. Int J Mol Sci 2010;11(3):1070-1081.
58. Filion MC, Phillips NC. Toxicity and immunomodulatory activity of liposomal vectors formulated with cationic lipids toward immune effector cells. Biochim Biophys Acta 1997;1329(2):345-356.
59. Soenen SJ, Brisson AR, De Cuyper M. Addressing the problem of cationic lipid-mediated toxicity: the magnetoliposome model. Biomaterials 2009;30(22):3691-3701.
60. Bulte JW. In vivo MRI cell tracking: clinical studies. AJR Am J Roentgenol 2009;193(2):314-325.
61. Leiner T, Kucharczyk W. NSF prevention in clinical practice: summary of recommendations and guidelines in the United States, Canada, and Europe. J Magn Reson Imaging 2009;30(6):1357-1363.
62. Henning TD, Saborowski O, Golovko D, Boddington S, Bauer JS, Fu Y, Meier R, Pietsch H, Sennino B, McDonald DM, Daldrup-Link HE. Cell labeling with the positive MR contrast agent Gadofluorine M. Eur Radiol 2007;17(5):1226-1234.

63. Thorek DL, Tsourkas A. Size, charge and concentration dependent uptake of iron oxide particles by non-phagocytic cells. Biomaterials 2008;29(26):3583-3590.
64. Henning TD, Wendland MF, Golovko D, Sutton EJ, Sennino B, Malek F, Bauer JS, McDonald DM, Daldrup-Link H. Relaxation effects of ferucarbotran-labeled mesenchymal stem cells at 1.5T and 3T: discrimination of viable from lysed cells. Magn Reson Med 2009;62(2):325-332.
65. van Buul GM, Farrell E, Kops N, van Tiel ST, Bos PK, Weinans H, Krestin GP, van Osch GJ, Bernsen MR. Ferumoxides-protamine sulfate is more effective than ferucarbotran for cell labeling: implications for clinically applicable cell tracking using MRI. Contrast Media Mol Imaging 2009;4(5):230-236.
66. Modo M, Cash D, Mellodew K, Williams SC, Fraser SE, Meade TJ, Price J, Hodges H. Tracking transplanted stem cell migration using bifunctional, contrast agent-enhanced, magnetic resonance imaging. Neuroimage 2002;17(2):803-811.
67. Rudelius M, Daldrup-Link HE, Heinzmann U, Piontek G, Settles M, Link TM, Schlegel J. Highly efficient paramagnetic labelling of embryonic and neuronal stem cells. Eur J Nucl Med Mol Imaging 2003;30(7):1038-1044.

Chapter 3

# Compartmentalization of Gd-liposomes: the quenching effect explained

Jamal Guenoun[1], Gabriela N. Doeswijk[1], Gabriel P. Krestin[1], Monique R. Bernsen[1,2].

[1]Department of Radiology, Erasmus MC - University Medical Center Rotterdam, Rotterdam, the Netherlands
[2]Department of Nuclear Medicine, Erasmus MC - University Medical Center Rotterdam, Rotterdam, the Netherlands

*Published in Contrast Media Mol Imaging. 2016 Mar;11(2):106-14*

# Abstract

**Purpose:** Cationic liposomes carrying high concentrations of Gd can be used as an efficient cell labeling agent. In a compartmentalized state, Gd can cause signal loss (relaxivity quenching). The effect of liposomal [Gd], liposomal size and compartmentalization state on relaxivity quenching was assessed.

**Methods and Materials:** Dependency of SI on intraliposomal [Gd] was assessed comparing three different [Gd] (0.3, 0.6 and 1.0M Gd) in both small (80nm) and large (120 nm) cationic liposomes. In addition, five compartmentalization states were compared: free Gd, intact Gd-liposomes, ruptured Gd-liposomes, Gd-liposomes in intact cells and Gd-liposomes in ruptured cells (simulating cell death). Gd also causes $R_2$ effects, which is often overlooked. Therefore both $R_1$ and $R_2$ relaxation rate of a dilution range were measured by $T_1$- and $T_2$-mapping on a 7T dedicated animal MR scanner.

**Results:** Less is more. As the unidirectional water efflux rate (outbound across the liposome membrane, $\kappa_{le}$) is proportional to the surface/volume ratio, smaller liposomes yielded a consistently higher $R_1$ than larger liposomes. For equal voxel [Gd] less concentrated liposomes (0.3M Gd) yielded higher $R_1$/ $R_2$ ratio because of the higher liposomal water fraction ($v_l$). Gd exhibits a dualistic behavior: from hypointensity to hyperintensity to hypointensity, with decreasing [Gd]. Regarding compartmentalization less membrane barriers means a higher $R_1$/ $R_2$ ratio.

**Conclusion:** Gd-liposomes exhibit a versatile contrast behaviour, dependent on the compartmentalization state, liposomal size, intraliposomal [Gd] and liposome number. Both $R_1$ and $R_2$ effects contribute to this. The versatility allows one to tailor the optimal liposomal formulation to desired goals in cell labeling and tracking.

# Introduction

Cellular imaging is the key for non-invasive assessment of cell transplantation therapies. In this rapidly evolving field many aspects of the *in vivo* kinetics of transplanted cells still need to be understood. Magnetic resonance imaging (MRI) provides excellent opportunities in this particular field thanks to its versatile properties. Combining the right ligand with a MR sensitive contrast agent, magnetic resonance imaging is capable of exposing a wide range of previously visually occult in-vivo molecular or cellular processes to the naked eye.
The two types of MRI contrast agents (CAs) currently most widely used are $T_1$ agents (Gadolinium (Gd) and to a lesser extent manganese (Mn)) or $T_2$ agents (iron oxide particles). Much (pre)clinical experience has been gained in the past decades with Gd-based contrast agents, such as Gd-DTPA (Magnevist, Schering, Germany) and Gd-DO3A-Butrol (Gadovist, Schering). Their use as a cell labeling agent has however been limited, presumably because of the lower sensitivity obtained when compared to iron oxide particles. Nonetheless, cationic liposomes loaded with high concentrations of Gd can be used as an efficient cell labeling agent for sensitive cellular MRI imaging (1). Gd-based contrast agents have been used successfully in several other studies as well (2-7). As Gd mainly shortens $T_1$ relaxation times (and to a lesser extent $T_2$ relaxation times), its classical application consists of the generation of signal gain (hyper intense or positive contrast) on $T_1$-weighted images. Strikingly, in a compartmentalized (intracellular) state, Gd can cause signal loss (hypointense or negative contrast), known as 'relaxivity quenching' (3,7,8). Although initially thought of as a drawback (9), a recent study by us showed that contrast changes as a result of (de)quenching can be advantageous, allowing for a visual and quantitative distinction between viable and non-viable Gd-liposome labeled cells by MRI (10). Relaxivity quenching thus might harbor more potential for cellular labeling than currently known. This at the time novel finding of dynamic contrast behaviour *in vivo*, encouraged us to study Gd signal quenching in more detail. Relaxivity of Gd is mainly affected by four parameters: the number of water molecules in the inner coordination sphere of the complex, the proton exchange rate in this inner sphere (depending on the water concentration of the relevant compartments and the compartmentalization), the rotational correlation times (related to the size of the molecule) and the electron spin relaxation rates.
As encapsulation of Gd (inside liposomes and/or inside cells) affects the water exchange rate and availability, a better understanding of relaxivity (de)quenching could contribute to an enhanced image interpretation with regard to cell division, cell density and Gd-liposome load. No doubt, this would further open up possibilities in image-guided monitoring of cell transplantation. Although most studies concerning Gd report merely $T_1$ longitudinal times, in the same study we observed that Gd compartmentalization (in liposomes) increased $r_2$ relaxivity (compared to 'free' Gd). Both $T_1$ and $T_2$ relaxation times of Gd-lipsomes and Gd-liposome labeled cells were assessed, as signal intensity is dependent on both. Realizing that high payloads of CAs are involved in cell labeling, we focus on the high intraliposomal [Gd] concentrations (0.3 M - 1.0 M Gd), which, to our knowledge, haven't been studied before.

# Material and Methods

## Liposome preparation

As described before (1), liposomes were prepared to serve as a vehicle to transfer Gd to cells. In brief, Gd-DO3A-Butrol (Gadovist; Bayer Schering Pharma, Berlin, Germany) was incorporated in cationic liposomes using the lipid-film hydration technique followed by filtration through polycarbonate filters (Whatman, Newton, MA, USA).

## Cell labeling and preparation

Fluc-MSCs of passage 4 were used for all experiments. Dulbecco's modified Eagle medium (Invitrogen; Carlsbad, CA, USA) enriched with additives was used as culture medium. In short, Fluc-MSCs were labeled with 125 µM Gd-liposomes for 4h, harvested by trypsinization, washed 3 times in PBS and centrifuged at 300 G for 5 minutes to discard of unincorporated contrast agent (1). After centrifugation and cell counting, Fluc-MSCs cells were resuspended to their final concentration in Ficoll 1.07 g/mL (*in vitro* experiments) or PBS (*in vivo* experiments).

## Experiment 1: Liposomal size and Gd load

To assess possible effects of liposomal size and liposomal Gd concentration on $T_1$ and $T_2$ relaxation time, varying liposomal formulations were prepared. Liposomes were encapsulated with Gd-DO3A-butrol (Gadovist 1.0 M) in three different intraliposomal Gd concentrations: 1.0 M Gd (undiluted), 0.6 M Gd and 0.3 M Gd (diluted in HEPES). From each batch, both large and small liposomes were created. Large liposomes were produced by 5 times filtration through 200 nm polycarbonate membrane filters followed by 5 times filtration through 100 nm filters. Smaller liposomes were created by 5 additional passes through 50 nm filters, followed by ultracentrifugation to separate non-encapsulated from encapsulated Gd. Six different liposomal formulations were acquired finally: 1.0 M Gd with size 127 nm (1.0 $M_L$) and PDI 0.076, 1.0 M Gd with size 83 nm and PDI 0.054 (1.0 $M_S$), 0.6 Gd with size 119 nm and PDI 0.045 (0.6 $M_L$), 60% Gd with size 93 nm and PDI 0.069 (0.6 $M_S$), 30% Gd with size 124 nm and PDI 0.071 (0.3 $M_L$), 30% Gd with size 91 nm and PDI 0.066 (0.3 $M_S$). The subscript abbreviations $_L$ and $_S$ refer to the size of the liposomal vesicles with $_L$ indicating large and $_S$ indicating small. The average diameter and size distribution of the liposomes in the final formulation was determined by dynamic light scattering (DLS) using a Zetasizer Nano (Malvern Instruments, Worcestershire, UK). Liposomal phosphate content was assessed by spectrophotometric analysis according to Rouser (11). As quenching occurs at high concentrations of Gd, we aimed to produce very concentrated Gd-liposomes. To this end the resulting liposome pellet of each batch was resuspended in 400 µl HEPES. A serial dilution of each suspension was then prepared and filled out in a 384 Well plate, followed by MRI scanning.

## Experiment 2: Gd compartmentalization

To assess the effects of Gd compartmentalization on $T_1$ and $T_2$ relaxation time, 5 Gd compartmentalization states were compared: viable Gd-liposome labeled MSCs, lysed (non-viable) Gd-liposome labeled MSCs, intact Gd-liposomes, lysed Gd-liposomes and free Gd-DO3A-Butrol. Both lysed cells and lysed liposomes were obtained by repeated freeze thawing in liquid nitrogen. Cell death was assessed by Trypane Blue assay, whereas liposomal breakdown was assessed by DLS.

In all *in vitro* experiments stock batches were prepared in Ficoll, preventing cell sedimentation during imaging (12), and a serial dilution was then filled out in a 384 well plate. $T_1$ and $T_2$ relaxation times of the top as well as the bottom slice were measured, to make sure sedimentation did not occur. Surrounding wells were filled with water to prevent susceptibility artefacts from air and very concentrated samples.

### MRI data acquisition and analysis

MRI data were acquired at room temperature on a 7T dedicated animal scanner (Discovery MR901; GE Medical Systems, Milwaukee IL, USA and Agilent Technologies, Santa Clara, CA, USA) with unmodified gradients and custom made surface coils (inner diameter of 5 cm). Spin echo (SE) sequences with multiple TR (100-2800 ms; TE10 ms) and multiple TE (10-100 ms; TR 600 ms) were used to obtain $T_1$ longitudinal relaxation times and $T_2$ transverse relaxation times, respectively. Sequences were acquired with a field of view (FOV) = 5.0 x 5.0 $cm^2$, matrix = 160 x 160, slice thickness = 1.4 mm and NEX = 2. Using Matlab (version R2007b) $T_1$ and $T_2$ times were calculated. Relaxation times were calculated as follows:

$$\Delta R1_x = \frac{1}{T1_x} - \frac{1}{T1_{ref}} \qquad [1.]$$

In which $T_{1x}$ and $T_{1ref}$ represent the $T_1$ of the Gd-containing sample of interest and the $T_1$ of the surrounding wells containing the suspension solution (HEPES or Ficoll), respectively. The same formula was applied to derive the $\Delta R_2$ using $T_2$, respectively. $T_{1ref}$ and $T_{2ref}$ *in vitro* were assessed to be 3100±120 ms and 167±18 ms., respectively. A voxel-by-voxel linear least squares fit of the natural logarithm of the signal amplitude versus at least 6 echo times (TE) was performed to construct $R_2$ maps. For $R_1$ maps at least 6 repetition times (TR) were used.

### Gd content measurement

The Gd concentration in either liposomes or cells was measured by Inductively Coupled Plasma-Optical Emission Spectroscopy (ICP-OES; Optima 4300DV, Perkin Elmer, Norwalk, CT) operating at a wavelength of 342 nm. Aliquots containing either liposomes or cells were suspended in 4 ml. Triton X-100 2% (St. Louis, MO), heated up at 55 °C and mixed for 30 min. at 6 g to induce cellular and liposomal lysis. For internal validation, stock Gd-DO3A-Butrol was included in the measurements as well. This allowed an inter-group comparison of $T_1$ and $T_2$ relaxation times, as a function of Gd concentration.

### Statistical analysis

All values are presented as mean±SD from triplicates and expressed in relation to unlabeled cells.

## Results and discussion

### Experiment 1: The effect of liposomal size and Gd load on signal quenching

$T_1$ and $T_2$ relaxation times of a dilution range of the Gd-liposome suspensions (1.0 $M_L$ Gd, 1.0 $M_S$ Gd, 0.6 $M_L$ Gd, 0.6 $M_S$ Gd, 0.3 $M_L$ Gd, 0.3 $M_S$ Gd) were acquired. Assessment of the actual Gd concentration by ICP-OES (Table 1), allowed an inter-group comparison of the $\Delta R_1$ and $\Delta R_2$, as a function of Gd concentration. For some of the most concentrated samples the $T_1$ longitudinal relaxation could not be measured, because it was impossible to fit a curve through these data points; these data points were therefore omitted.

Our data showed that all undiluted samples caused prominent signal hypointensities, except for 0.3 $M_S$ Gd-lipos. 0.3 $M_S$ liposomes have the highest $R_1$ relaxivity (i.e. the slope of a linear curve fit through the $\Delta R_1$ data points). Furthermore, the $R_1$ effects are more pronounced for liposomes with a lower intraliposomal Gd concentration or of a smaller size and for more concentrated liposome suspensions (containing a larger liposome number). Next, the $r_1$ relaxivity of all Gd-liposome suspensions is lower as compared to uncompartmentalized Gd-DO3A-Butrol. To understand these data we need to take a look at the factors that control $r_1$ relaxivity, both on the molecular (Gd-chelate) and liposomal level. As known, interaction of Gd-bound chelates with water protons decreases the water $T_1$ and $T_2$ relaxation times. The interactions occurring between Gd and $H_2O$ protons on the molecular level are twofold (13). 'Inner sphere relaxation' refers to the formation of a dipole-dipole interaction between a water molecule and the primary sphere of the paramagnetic $Gd^{3+}$ ion (with seven unpaired electrons). In this interaction, a chemical exchange occurs resulting in an enhanced relaxation of the water protons. Thus, the relaxation will be enhanced by an increased fraction of water molecules that can interact with Gd and by a shorter residence time of the water molecule with Gd (allowing Gd to interact with additional water molecules). 'Outer sphere relaxation' is a more complex concept. It is the result of the relative rotational and translational diffusion of water molecules and the paramagnetic ion. Basically stated, the relaxivity influence of the paramagnetic ion enhances when an increased number of water molecules can approach the paramagnetic ion and/or the further the paramagnetic ion can move through space and/or the closer the water protons can approach the paramagnetic ion. The liposomal suspension represents a two-compartment system, the intraliposomal and the extraliposomal compartment separated by the liposomal membrane. Gd is contained in the intraliposomal compartment. Diffusion of water across the liposomal membrane thus extends the influence of Gd into the non-contrast containing compartment. The apparent (measured) voxel signal intensity is dependent on the relaxation rate and the cross-compartmental water exchange rates. As long as the $H_2O$ exchange rate is fast enough on the time scale of $T_1$, protons excited in one compartment can relax in another compartment (14). The longitudinal relaxation is then in fast-exchange. The exchange rates can be derived mathematically. For a single liposome with radius *r*, with a volume expressed as $V = 4/3\pi r^3$ and surface area as $A = 4\pi r^2$, the unidirectional water efflux rate constant (the reciprocal average liposomal water lifetime) across its membrane can be expressed as (15):

$$\kappa_{le} = \frac{1}{\tau_l} = P_{dl}\frac{A_l}{V_l} = \frac{3P_d}{r_l} \qquad [2.]$$

$P_{dl}$, representing the diffusional permeability of the liposomal membrane, was derived by interpolation from the NMRD profiles of similar cholesterol containing liposomes ($10^{-3}cm^{-1}$) (16). The occurring exchange is dependent on both the influx ($\kappa_{el}$) and efflux water exchange rates ($\kappa_{le}$) and the water volume fraction of the liposomal ($v_l$) and extraliposomal ($v_e$) compartment. The unidirectional water influx rate across the liposomal membrane can thus be expressed as:

$$\kappa_{el} = \kappa_{le}\frac{\nu_l}{\nu_e} \qquad [3.]$$

In fast-exchange, the apparent voxel relaxation rate will be a weighted average of the relaxation rate of each compartment - independent of the exchange rate -, assuming a monoexponential signal recovery (17). This occurs as long as the sum of the exchange rates ($\kappa_{el} + \kappa_{le}$) is much higher than the difference between the compartmental relaxation rates (the relaxographic 'shutter speed') (17,18):

$$\kappa_{el} + \kappa_{le} >> | R1_l - R1_e | \qquad [4.]$$

However, if the exchange rate turns to a much smaller value than the difference between the compartmental relaxation rates:

$$\kappa_{el} + \kappa_{le} << | R1_l - R1_e | \qquad [5.]$$

the system turns from fast-exchange to a slow-exchange state (17). In case of slow exchange, distinct compartmental relaxation times exists, which are dependent on exchange. Liposome encapsulated Gd represents such a slow-exchange state because of the barrier the liposomal membrane imposes on diffusion, causing the exchange rate of $H_2O$ to be slower than the $T_1$ proton relaxation time. This hinders an even distribution of the $T_1$ relaxation time across the entire voxel.

## $R_1$ effects

A dilution range of the Gd-liposomes was imaged (Fig. 1). Higher Gd concentrations did not automatically produce higher signal intensities. Instead, all undiluted samples caused prominent signal hypointensities, even on $T_1$W images, except for 0.3 $M_S$ Gd-liposomes. With increasing dilution the signal intensity rises steeply to a certain maximum, followed by a slow decrease in SI. Visually, signal intensity is highest for a fivefold diluted 0.3 $M_s$ liposome solution (3.9 mM Gd in suspension), as confirmed by the calculated signal intensity (Fig. 6).
The $\Delta R_1$ relaxation rate was plotted against the liposomal Gd concentration ($[Gd_l]$) for each of the six formulations (Fig. 2). The $R_1$ effects of the intraliposomal Gd concentration, the liposomal size and number will be discussed in detail next.

## $R_1$ effects: intraliposomal Gd concentration

At comparable liposomal sizes, 0.3 M Gd-liposomes possess a higher $r_1$ relaxivity than 0.6 M Gd formulations, whereas the latter possess higher $r_1$ than 1.0 M Gd formulations. This inverted relation might seem paradoxical at first glance. However, it can be clarified by the $H_2O$ availability in proximity to Gd. Previously mentioned, liposome encapsulated Gd represents a slow-exchange state. Fig. 2 indeed confirms that the $r_1$ relaxivity of all Gd-liposome suspensions is lower as compared to uncompartmentalized Gd-DO3A-Butrol. In a slow-exchange state the volume distribution of $H_2O$ over the two compartments matters, more specifically the ratio of the liposomal ($v_l$) and extraliposomal ($v_e$) volume water fractions, $v_l/v_e$ (Eq. [2]). The

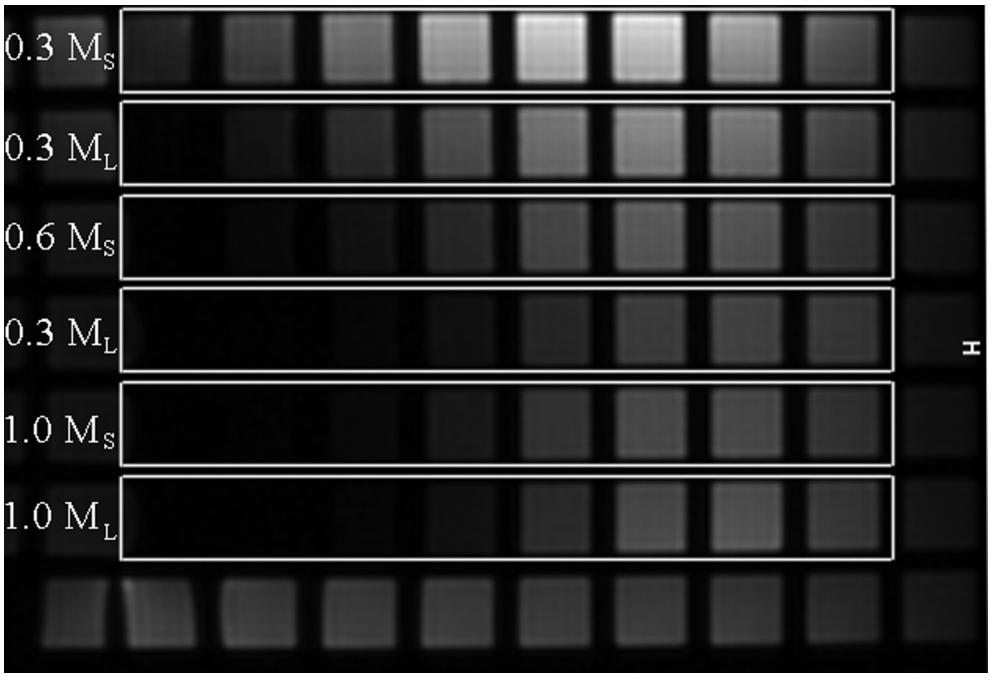


**Fig 1** Size and concentration-dependent contrast effects of Gd-liposomes
Experiment 1. $T_1$-weighted image (TE 10 ms, TR 400 ms) of a 384 Wells plate containing a 1:1 serial dilution of various Gd-liposomes preparations. Gd-liposomes with different intraliposomal [Gd] decreasing in concentration from left to right were scanned. From top to bottom: 0.3 $M_S$ Gd, 0.3 $M_L$ Gd, 0.6 $M_S$ Gd, 0.6 $M_L$ Gd, 1.0 $M_S$ Gd and 1.0 $M_L$ Gd liposomes. The subscript $_S$ and $_L$ refer to small and large Gd-liposomes, respectively (refer to text for sizes). Note the severe signal intensity loss from highly concentrated samples.

higher $r_1$ relaxivity of 0.3 M Gd-liposomes is attributable to a larger liposomal water volume fraction ($v_l$), for which, in turn, two reasons may be mentioned. Firstly, compared to suspensions with higher [$Gd_l$], a suspension of Gd-liposomes with a lower $[Gd_l]$ contains less Gd molecules per single liposome and thus more liposomes at equal $[Gd_v]$. More liposomes means an increase in $v_l$ and a decrease in $v_e$, increasing $v_l/v_e$. For example, 3.33 times more liposomes are inside a suspension of 0.3 M than in a suspension of 1.0 M Gd-liposomes. Secondly, 0.3 M Gd-liposomes are created from 1.0 M Gd-DO3A-Butrol (containing 69 volume % $H_2O$) diluted with HEPES buffer which contains a higher volume percentage of $H_2O$ (82 volume % $H_2O$), additionally increasing $v_l$ by a factor 1.13 (69%*0.3+82%*0.7). This totals a net $v_l$ increase of a factor 3.77 (=3.33*1.31). Thus 0.3 M Gd-liposomes clearly profit from an increased number of intraliposomal water molecules in the vicinity of Gd-molecules. The $v_l/v_e$ ratio was calculated by measuring the [Gd] in suspension by ICP (from which we derived $[Gd_v]$), using the following equations. Liposomal Gd mass ($M_{Gd\,l}$) can be derived by the product of $[Gd_l]$ (in g/l) and the single liposomal volume ($v_l$):

$$M_{Gd\,l} = [Gd_l]\ V_l \qquad [6.]$$

For 1.0 M Gd-DO3A-Butrol the [Gd] is 157.25 g/l (as Gd has a molar mass of 157.25 g/mol). The number of liposomes ($N_l$) in suspension follows by dividing the total Gd mass in the suspension (after liposomal lysis) ($M_{Gd\,tot}$) by the single liposomal Gd mass ($M_{Gd\,l}$):

$$N_l = \frac{M_{Gd\,tot}}{M_{Gd\,l}} \qquad [7.]$$

Given that the volume % $H_2O$ in undiluted Gd-DO3A-butrol equals 69% and the volume % $H_2O$ in HEPES buffer equals 82%, the sum of intraliposomal $H_2O$ volume of all liposomes together ($V_{l\,tot}^{H2O}$) can be calculated:

$$V_{l\,tot}^{H2O} = N_l V_l \{0.69 v_{Gd} + 0.82(1 - v_{Gd})\} \qquad [8.]$$

in which $v_{Gd}$ represents the intraliposomal Gd-DO3A-butrol volume fraction (e.g. 0.6 for 0.6M Gd-lipsomes). The liposomal $H_2O$ volume fraction ($v_l$) can then be derived as follows:

$$v_l = \frac{V_{l\,tot}^{H2O}}{V_{l\,tot}^{H2O} + V_{bulk}^{H2O}} = \frac{V_{l\,tot}^{H2O}}{V_{l\,tot}^{H2O} + (V_s - V_{l\,tot})} \qquad [9.]$$

where $V_{bulk}^{H2O}$ is the total extraliposomal (bulk) volume, $V_s$ is the liposome suspension volume and $V_{l\,tot}$ the total liposomal volume ($=N_l V_l$). This being an equation of which all parameters are known, $v_l$ was derived. As the total water volume fraction ($v_e + v_l$) equals 1, $v_l$ was inputted in the following equation to calculate the water volume fraction ratio of the two compartments:

$$\frac{V_l}{V_e} = \frac{V_l}{1 - V_l} \qquad [10.]$$

Plotting the water volume fraction ratio $v_l/v_e$ as a function of $[Gd_v]$ shows the $v_l/v_e$ indeed to be largest for the 0.3M Gd-liposomes, followed by 0.6M and 1.0 M Gd-liposomes, consecutively (Fig. 3). The increased $v_l/v_e$ ratio increases the water influx exchange rate ($\kappa_{el}$). With an unchanged efflux rate ($\kappa_{le}$), the sum of exchange rates thus increases, resulting in enhanced $T_1$ relaxation effects (Eq. [3]).
In addition, 0.3 M Gd-liposomes exhibit a relaxographic 'shutter-speed' $|R_{1l} - R_{1e}|$ of 1.1 $mM^{-1}$ $s^{-1}$, which is 3.8 times lower for than 1.0 M Gd-liposomes. Thus the combined effect of the decreased relaxographic 'shutter-speed' $|R_{1l} - R_{1e}|$ and increased $v_l/v_e$ ratio drive the 0.3 M Gd-liposomes more towards a fast exchange state. The approximation of the rate constants is visible from Fig 4, where the rate constants are plotted as a function of $[Gd_v]$. The overall effect is an increased higher 'net' voxel $r_1$ relaxivity for 0.3M than either 0.6M or 1.0 M Gd-liposomes.

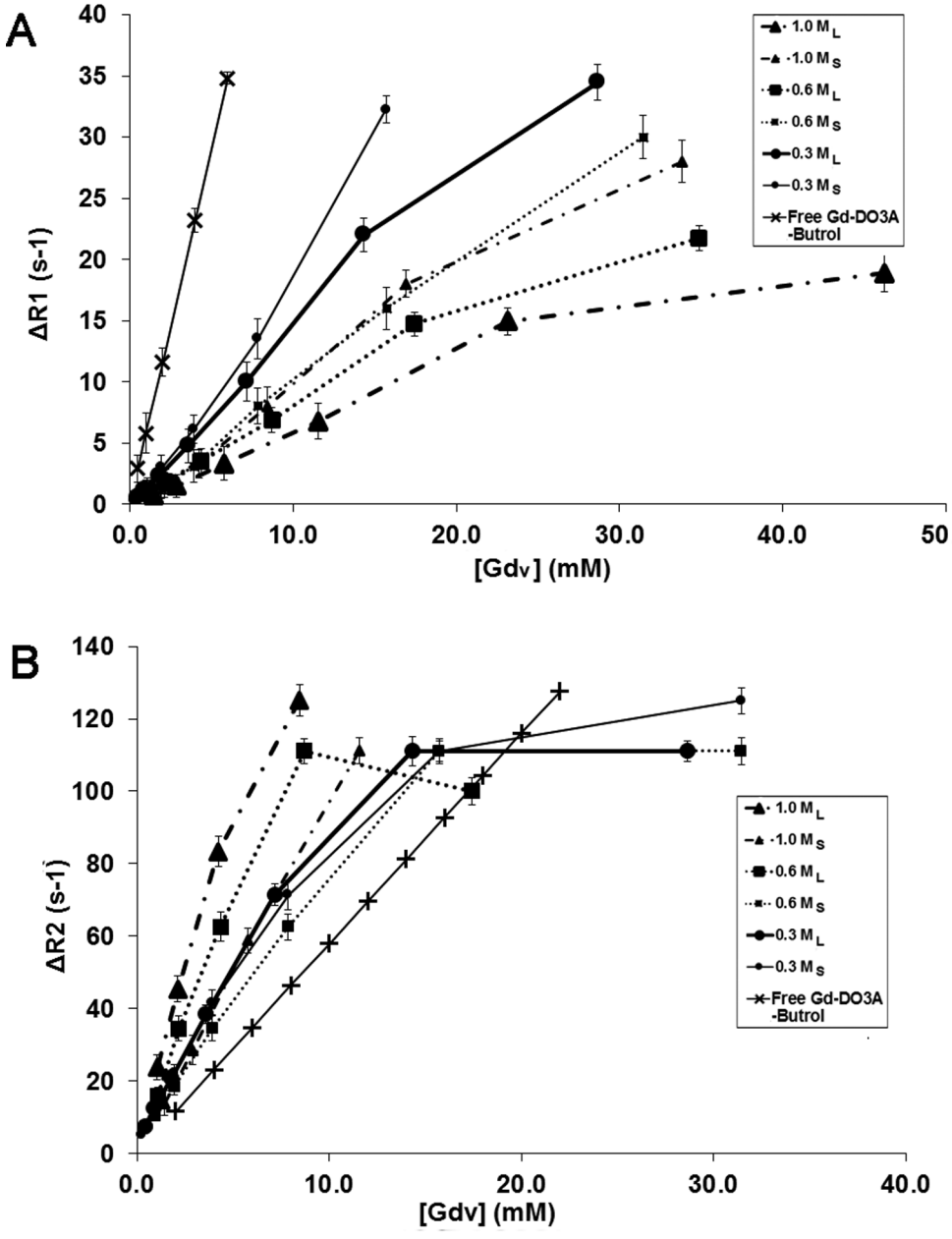


**Fig 2** Experiment 1. Line-chart depicting $\Delta R_1$ (A) and $\Delta R_2$ (B) relaxation rates as a function of voxel Gd concentration ($[Gd_v]$) for a range of Gd-liposomes with three different intraliposomal [Gd] ($[Gd_l]$), 1.0 M, 0.6 M and 0.3 M Gd. Data are presented as mean ± SD (n=3 different samples, SD refers to intersample SD).

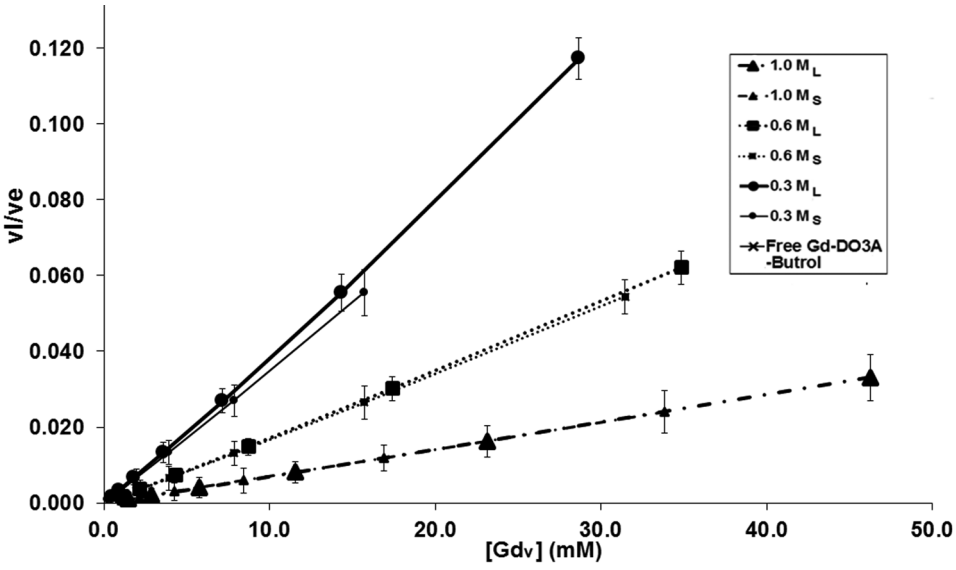


**Fig 3** Experiment 1. The ratio of the intraliposomal water volume fraction ($v_l$) and the extraliposomal bulk water fraction ($v_e$) was plotted against voxel Gd concentration ($[Gd_v]$). The $v_l$/ve ratio is largest for the 0.3M Gd-liposomes, followed by 0.6M and 1.0 M Gd-liposomes, consecutively.

## $R_1$ effects: voxel Gd concentration [$Gd_v$] or liposome number

The $T_1$ mapping data (Fig. 2) shows the $\Delta R_1$ relaxation rates for all $[Gd_l]$ to increase with an increasing liposome number (i.e. a higher voxel Gd concentration, $[Gd_v]$), irrespective of the tested range of $[Gd_l]$). Again, as mentioned above, an increasing number of liposomes increases the ratio $v_l / v_e$, thereby increasing the influx rate ($\kappa_{el}$) (Eq. [3]). As the liposomal Gd load $[Gd_l]$ remains constant with in a serial dilution, $|Rl_l - Rl_e|$ remains constant too; this propagates the system towards fast-exchange, being in agreement with findings by other authors (18). Furthermore, the $R_1$ curves bend off with increasing voxel [Gd] (Fig. 2), indicating some kind of saturation. The cause for this could lie in the molar ratio $H_2O$/Gd, which dramatically decreases with increasing liposome number (Fig. 5). In the voxel [Gd] range 0-40 mM a 65 fold decrease in the molar ratio $H_2O$/Gd occurs, severely lowering the chance of interaction. The maximal intraliposomal $H_2O$ water volume fraction for all undiluted Gd-liposome formulations (0.3M-1.0M) is in the range of 0.1-0.25, so the majority of $H_2O$ molecules are in the extraliposomal free space.

## $R_1$ effects: liposomal size

Smaller liposomes consistently exhibited a higher $r_1$ relaxivity than their larger counterparts (Fig. 2). The explanation for this is straightforward. As a result of the larger surface to volume ratio, smaller liposomes have a higher efflux rate ($\kappa_{le}$) (Eq. [2]). This augments the sums of exchange rates, contributing to faster exchange.

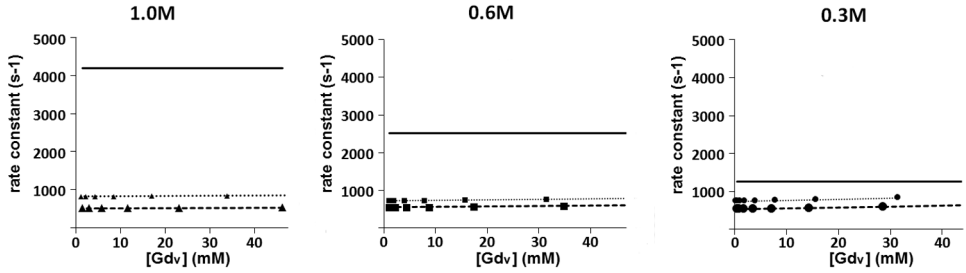


**Fig 4** Experiment 1. Rate constants ($s^{-1}$) of Gd-liposomes with an intraliposomal [$Gd_l$] of 1.0 M (left), 0.6 M (middle) and 0.3 M (right) as a function of the voxel [Gd], [$Gd_v$]. Undashed lines ( —— ) represent the relaxographic 'shutter-speed' $|R_{1l} - R_{1e}|$, which is equal for small and large liposomes with the same *[$Gd_l$]*. The sum of exchange rates ($\kappa_{le} + \kappa_{el}$) of small liposomes is drawn with dotted lines (····), whereas the sum of exchange rates ($\kappa_{le} + \kappa_{el}$) for large liposomes is drawn with dashed lines (----). Note the approximation of the rate constants with decreasing intraliposomal [$Gd_l$]. The approximation of the rate constant $|R_{1l} - R_{1e}|$ and the sum of exchange rates ($\kappa_{le} + \kappa_{el}$) is maximal for 0.3 M Gd-liposomes.

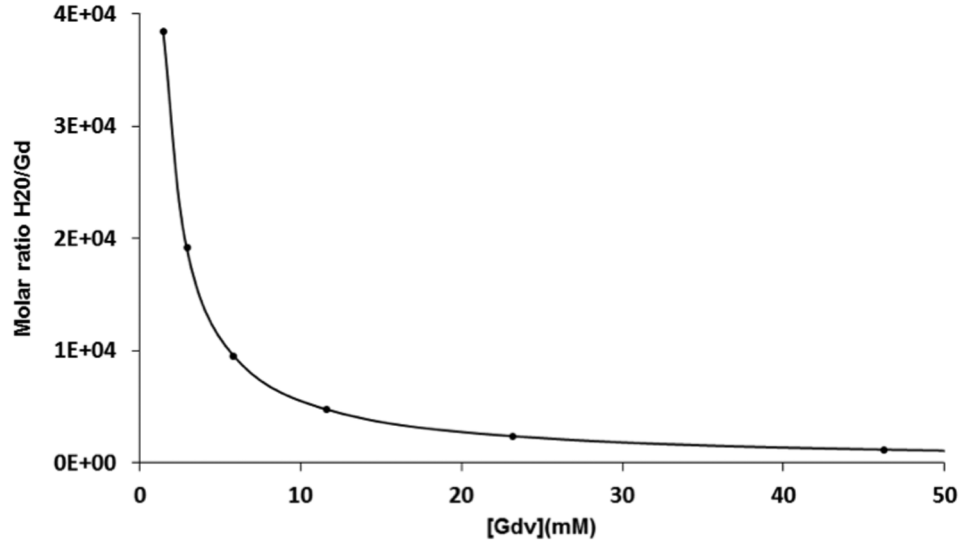


**Fig 5** Experiment 1. The molar ratio $H_20$/Gd of an arbitrary Gd-liposome suspension is plotted as a function of the voxel Gd concentration (*[$Gd_v$]*). The molar ratio $H_2O$/Gd decreases exponentially with an increasing *[$Gd_v$]*, which may account for the lower interaction chance of $H_2O$ with Gd atoms, and be part of the '$R_1$ saturation' occurring with increasing *[$Gd_v$]* (see Fig. 2).

## $R_2$ effects

In many studies on compartmentalized Gd contrast agents to date, the effect on $R_2$ relaxation rate was not considered. However, Gd-based contrast agents have a biphasic effect on SI dependent on the concentration and can introduce a $T_2$ effect (severe signal loss) at high concentrations, even on $T_1$-weighted pulse sequences.

In our study $R_2$ relaxation rates increased according to the liposomal Gd load *[$Gd_l$]*, i.e. the higher the intraliposomal Gd load the higher the $r_2$ relaxivity (i.e. the slope of a linear curve fit through the $\Delta R_2$ data points) (Fig. 2). For all Gd-liposomes, $r_2$ relaxivity was higher than for

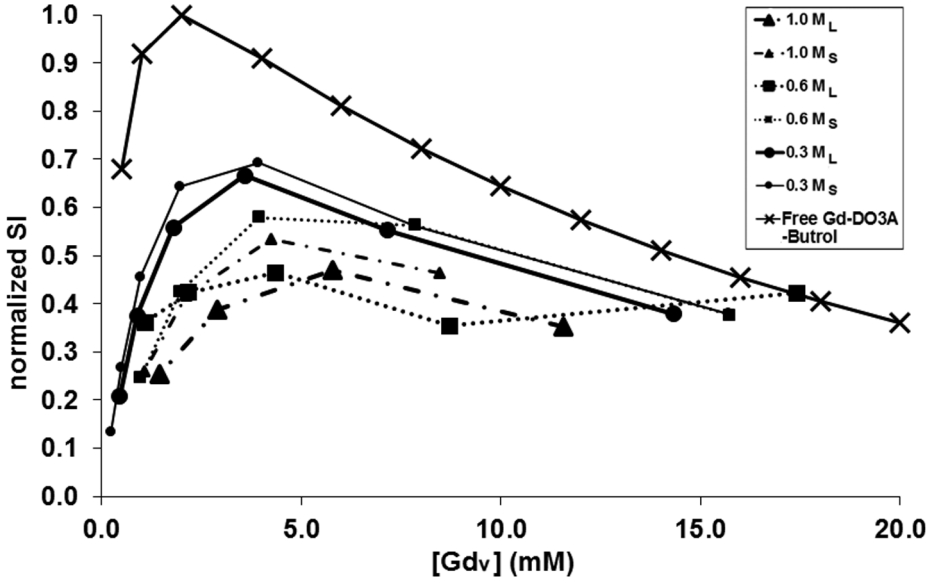


**Fig 6** Experiment 1. Simulated dose response of Gd-liposomes with varying intraliposomal Gd-concentration. Typical SE sequence (TR 500, TE 10 ms) as a function of the voxel Gd concentration, *[Gd$_v$]*. Initially $T_1$ relaxation dominates but as the CA concentration becomes sufficiently high $T_1$-saturation as well as counter-acting $T_2$ relaxation becomes dominant resulting in signal loss at higher concentrations. There is significant signal intensity quenching for all Gd-liposomes along the entire testes concentration range, compared to free Gd-DO3A-Butrol. The highest SI of all liposomes is achieved by 0.3 M small Gd-liposomes (91 nm), closely followed by larger liposomes (124 nm) with the same *[Gd$_l$]*.

free Gd. This is explained by the liposomal clustering of the Gd-atoms causing a heterogeneous distribution across the voxel, increasing the local magnetic susceptibility differences, which in turn lead to intravoxel dephasing, an effect which is further magnified by an increasing [Gdv ]. In general the $r_2$ relaxivity increased with increasing *[Gd$_l$ ]* (Fig. 2). For similar *[Gd$_l$ ]*, the $r_2$ relaxivity was higher for larger liposomes. The basis mechanism underlying this might be the increased clustering of proton spins in larger liposomes, thereby enhancing spin-spin relaxation (which induces loss of phase coherence). Furthermore, it may be caused by the larger number of smaller liposomes per voxel at similar [Gdv ], resulting in a less heterogenous distribution of spin moments across the voxel. These findings are important, as the signal intensity or perceived final contrast is dictated by both $R_1$ and $R_2$ effects. In addition, being aware of the intravoxel dephasing effect allows to choose the optimal MRI sequence, according to the desired outcome. Spin-echo (SE) sequences can reverse this effect by a 180 degree inversion pulse, a gradient-echo sequence can't.

## Combined $R_1$ and $R_2$ effects: signal intensity

Differences in concentration of compartmentalized Gd can generate contrast effects across the entire range from hypo- to hyperintensity (Fig. 1). Considering this versatility of Gd-liposomes, it is essential to be informed about the dose response of the signal intensity (SI). Having shown that compartmentalization affects $T_1$ as well as $T_2$ relaxation times, both parameters need to be taken into account. Signal intensity for a spin-echo sequence is described by (19):

$$SI = M_z(1 - e^{-TR/T1})e^{-TE/T2} \quad [11.]$$

A simulated dose response curve of the tested Gd-liposomes in a typical SE sequence (TR 500, TE 10 ms) was generated for all Gd-liposomes (Fig. 6). Initially $T_1$-relaxation dominates but as the CA concentration becomes sufficiently high $T_1$-saturation as well as counter-acting $T_2$-relaxation becomes dominant resulting in signal loss at higher concentrations. There is significant signal intensity quenching for all Gd-liposomes, compared to free Gd-DO3A-butrol. Compared to free Gd-DO3A-butrol the biexponential curves for Gd-liposomes are shifted to the right, attaining their maximal SI at higher voxel [Gd]. Of all liposomes, 0.3 M small Gd-liposomes (91 nm) achieve the highest SI, closely followed by larger liposomes (124 nm) with the same $[Gd_l]$. As previously explained, the $R_1$ effects underlying this are the combined effect of the decreased relaxographic 'shutter-speed' $|R1_l - R1_e|$, the increased sum of exchange rates ($\kappa_{le}+\kappa_{el}$) (due to the increased ratio $v_l/v_e$ resulting from an increased liposome number) and lower $R_2$ effects because of lower field inhomogeneities.
Understanding these effects allows one to titrate the optimal intraliposomal ($[Gd_l]$) and voxel Gd concentration ($[Gd_v]$) according to the needs and desired application for a specific MRI sequence.

**Experiment 2: The effect of compartmentalization state on signal quenching**
To assess the effect of the extent of compartmentalization, 5 different compartmentalization states of Gd were compared *in vitro*: viable Gd-liposome labeled MSCs, lysed (non-viable) Gd-liposome labeled MSCs, intact Gd-liposomes, lysed Gd-liposomes and free Gd-DO3A-butrol. Taking in consideration the high voxel [Gd] ($[Gd_v]$) for stock liposomes, a large number of cells was required (>10E7), to allow for inter-group comparisons to be made. The range of $[Gdv]$ is therefore smaller than for experiment 1 (Fig. 7).

## $R_1$ effects
Gd compartmentalization in either a liposomal or a cellular-liposomal form reduces $r_1$ longitudinal relaxivity as compared to free Gd-DO3A-butrol (Fig 7). In parallel, the $r_1$ relaxivity in the lysed groups (lysed cells or lysed liposomes) was larger than the $r_1$ of the intact groups (intact cells or intact liposomes). The main reason for this lies in the fact that after lysis of the cell and/or liposome membrane an important barrier between bulk $H_2O$ molecules and Gd is abrogated, allowing free interaction. The $r_1$ relaxivity for the lysed groups though still remains slightly lower than for free Gd-DO3A-butrol. A presumable cause could be found in the fact that the solution contains an additional amount of liposomal and cellular debris, resulting in a net lower $H_2O$ fraction, compared to free Gd-DO3A-butrol. In addition, the debris could pose a remaining barrier for $H_2O$ molecules in their diffusional pathways.

## $R_2$ effects
Compartmentalization of Gd, in both liposomes and cells, increases the $r_2$ relaxivity (Fig. 7), compared to free Gd-DO3A-butrol. This is in accordance with the findings in experiment 1. Again, this can be explained by the heterogeneous distribution of Gd across the voxel in compartmentalized form, increasing the local magnetic susceptibility differences leading to

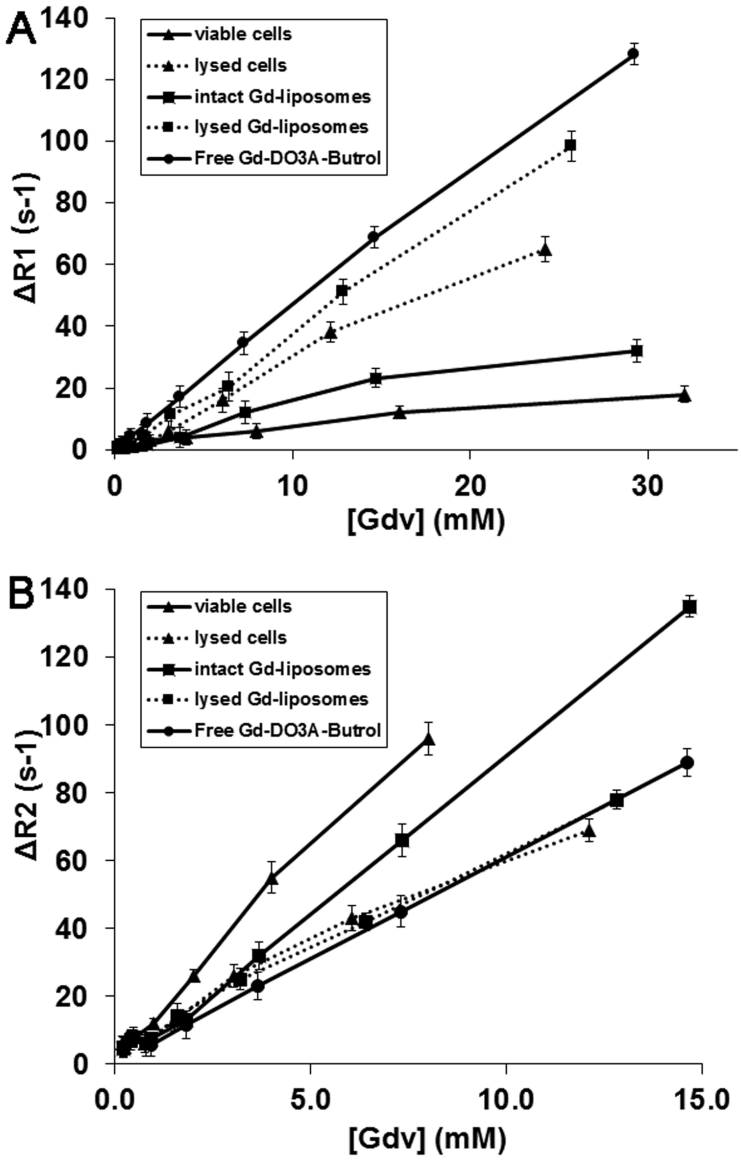


**Fig 7** Experiment 2. Line-chart depicting the effect of compartmentalization on $\Delta R_1$ (A) and $\Delta R_2$ (B) relaxation rate as a function of voxel Gd concentration ($[Gd_v]$) of several different Gd-suspensions (1.0 M): viable Gd-liposome labeled MSCs, non-viable Gd-liposome labeled MSCs, intact Gd-liposomes, ruptured Gd-liposomes and free Gd-DO3A-Butrol. Data are presented as mean ± SD (n=3 different samples, SD refers to intersample SD).

intravoxel dephasing. The $r_2$ relaxivity for Gd-liposomes in viable (intact) cells was larger than for intact liposomes. Presumably, the clustering of Gd-liposomes inside cells leads to a more heterogeneous suspension than a suspension containing mere Gd-liposomes, in which the liposomes can diffuse.

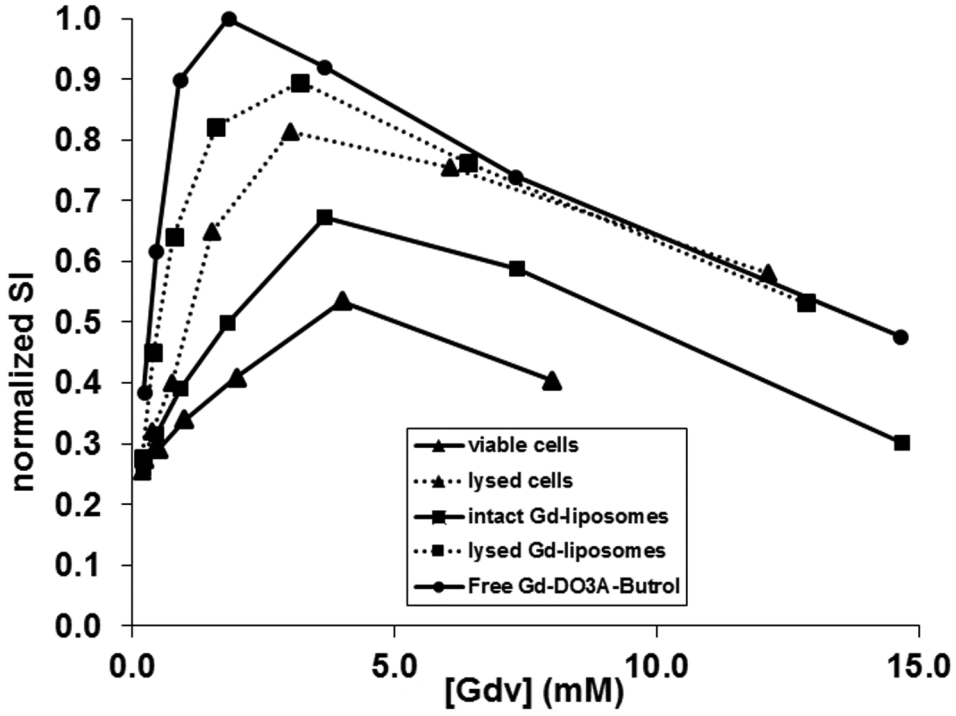


**Fig 8** Experiment 2. Simulated dose response of Gd-liposomes in various compartmentalization states. Typical SE sequence (TR 500, TE 10 ms) as a function of the voxel Gd concentration, [$Gd_v$]. Similar to Fig. 2, $T_2$-relaxation results in signal loss at higher concentrations. There is significant signal intensity quenching for all compartmentalization states, compared to free Gd-DO3A-Butrol.

### Combined $R_1$ and $R_2$ effects: signal intensity

Similar to experiment 1, a simulated dose-dependent signal intensity curve of the 5 compartmentalization groups of Gd-liposomes was generated for a typical SE sequence (TR 500, TE 10 ms) (Fig. 8). Naturally, free Gd-DO3A-butrol performs best with regard to the maximum SI, closely followed by lysed Gd-liposomes. Lysed Gd-liposomes outperform lysed Gd-liposomes labeled cells in SI, obviously because of a slightly larger $R_1$ effect. A lysed state performs better in reaching a high SI (for both liposomes and cells) than an intact state, because of the combination of an increased $R_1$ and a decreased $R_2$ effect.

## Conclusions

Internalization of Gd liposomes has proven to be an efficient way to load cells with Gadolinium (1,10,20). However, Gd can exhibit a dynamic contrast behaviour, eliciting a contrast effect anywhere in the range from hypo- to hyperintensity. This can be used advantageously as a qualitative measure of cell viability (47). As Gd can induce quenching effects as a result of either compartmentalization, liposome size, intraliposomal Gd concentration or $R_2$ effects, we studied the relation between these parameters and signal intensity. Since the main effort in MRI-based cell tracking with Gd is to augment the sensitivity (21) e.g. by achieving a high

payload of Gd per cell or a high $r_1$ relaxivity of the used Gd contrast agent, we directed special interest to the high Gd concentration range (0.3-1.0 M Gd). We show here that an increasing intraliposomal Gd concentration (>0.3 M Gd) has a deteriorating effect on signal intensity, due to both a reduced $r_1$ and increased $r_2$ relaxivity. Internalization of the Gd-particles into liposomes creates an intraliposomal compartment with large $r_1$ but small volume fraction and an extraliposomal compartment with large volume fraction but small $r_1$. The final voxel signal intensity will thus be a combined result of the in- and efflux $H_2O$ rates, the $H_2O$ volume fractions ratio of the compartments and $R_2$ effects. Compartmentalization of Gd-liposomes in cells further compromises the maximum achievable signal intensity.

Four main conclusions can be drawn.

Suspensions of Gd-liposomes with a lower intraliposomal [Gd] benefit from a higher $v_l / v_e$ ratio (liposomal /extraliposomal $H_2O$ volume fraction), a lower relaxographic 'shutter-speed' $|R_{1l} - R_{1e}|$ and a lower $R_2$ effect resulting in less signal quenching. Less is more. However, even for the less concentrated 0.3 M Gd-liposomes, the water exchange rate across the liposomal membrane is still not high enough to distribute this high relaxivity over the entire voxel, resulting in signal quenching compared to free Gd.

Smaller liposomes gain higher $r_1$ relaxivity and higher SI due to the larger surface-to-volume ratio, resulting in a larger efflux $H_2O$ rate ($\kappa_{le}$). Consequently water exchange across the liposomal membrane is more efficient leading to a reduced quenching effect.

Concentrated liposome suspensions, i.e. containing high number of liposomes, are characterised by large $R_2$ effects and reduced $R_1$ effects, resulting in more signal quenching.

Compared to free Gd, compartmentalized Gd (in liposomes or cells) suffers from a decreased $R_1$ and increased $R_2$ effect, inducing signal loss and thus significantly contributing to the quenching effect. Especially in cell labeling studies where efforts are undertaken to augment Gd sensitivity, this effect needs to be taken into account. On the other hand, the versatility of contrast generation by encapsulated Gd can serve as a tool for read-out of functional cell status, since viable and lysed cells generate different contrast (10).

Understanding the underlying principles which lead to the observed results (i.e. the interplay between intra- and extraliposomal water fractions, the difference between the intra- and extraliposomal relaxation rates and the increased $R_2$ effect as a result of compartmentalization) allows one to tailor the optimal liposomal Gadolinium concentration according to the desired goal.

# References


1. Guenoun J, Koning GA, Doeswijk G, Bosman L, Wielopolski PA, Krestin GP, Bernsen MR. Cationic Gd-DTPA liposomes for highly efficient labeling of mesenchymal stem cells and cell tracking with MRI. Cell Transplant 2012;21(1):191-205.
2. Biancone L, Crich SG, Cantaluppi V, Romanazzi GM, Russo S, Scalabrino E, Esposito G, Figliolini F, Beltramo S, Perin PC, Segoloni GP, Aime S, Camussi G. Magnetic resonance imaging of gadolinium-labeled pancreatic islets for experimental transplantation. NMR Biomed 2007;20(1):40-48.
3. Geninatti Crich S, Cabella C, Barge A, Belfiore S, Ghirelli C, Lattuada L, Lanzardo S, Mortillaro A, Tei L, Visigalli M, Forni G, Aime S. In vitro and in vivo magnetic resonance detection of tumor cells by targeting glutamine transporters with Gd-based probes. J Med Chem 2006;49(16):4926-4936.
4. Ghaghada K, Hawley C, Kawaji K, Annapragada A, Mukundan S, Jr. T1 relaxivity of core-encapsulated gadolinium liposomal contrast agents--effect of liposome size and internal gadolinium concentration. Acad Radiol 2008;15(10):1259-1263.
5. Lewin M, Clement O, Belguise-Valladier P, Tran L, Cuenod CA, Siauve N, Frija G. Hepatocyte targeting with Gd-EOB-DTPA: potential application for gene therapy. Invest Radiol 2001;36(1):9-14.
6. Strijkers GJ, Mulder WJ, van Heeswijk RB, Frederik PM, Bomans P, Magusin PC, Nicolay K. Relaxivity of liposomal paramagnetic MRI contrast agents. MAGMA 2005;18(4):186-192.
7. Terreno E, Geninatti Crich S, Belfiore S, Biancone L, Cabella C, Esposito G, Manazza AD, Aime S. Effect of the intracellular localization of a Gd-based imaging probe on the relaxation enhancement of water protons. Magn Reson Med 2006;55(3):491-497.
8. Billotey C, Wilhelm C, Devaud M, Bacri JC, Bittoun J, Gazeau F. Cell internalization of anionic maghemite nanoparticles: quantitative effect on magnetic resonance imaging. Magn Reson Med 2003;49(4):646-654.
9. Brekke C, Morgan SC, Lowe AS, Meade TJ, Price J, Williams SC, Modo M. The in vitro effects of a bimodal contrast agent on cellular functions and relaxometry. NMR Biomed 2007;20(2):77-89.
10. Guenoun J, Ruggiero A, Doeswijk G, Janssens RC, Koning GA, Kotek G, Krestin GP, Bernsen MR. In vivo quantitative assessment of cell viability of gadolinium or iron-labeled cells using MRI and bioluminescence imaging. Contrast Media Mol Imaging 2013;8(2):165-174.
11. Rouser G, Fkeischer S, Yamamoto A. Two dimensional then layer chromatographic separation of polar lipids and determination of phospholipids by phosphorus analysis of spots. Lipids 1970;5(5):494-496.
12. Sutton EJ, Henning TD, Boddington S, Demos S, Krug C, Meier R, Kornak J, Zhao S, Baehner R, Sharifi S, Daldrup-Link H. In vivo magnetic resonance imaging and optical imaging comparison of viable and nonviable mesenchymal stem cells with a bifunctional label. Mol Imaging 2010;9(5):278-290.
13. Sattler KD. Handbook of nanophysics. Nanomedicine and nanorobotics. Boca Raton: Taylor & Francis; 2009.
14. Bauer WR, Schulten K. Theory of contrast agents in magnetic resonance imaging: coupling of spin relaxation and transport. Magn Reson Med 1992;26(1):16-39.
15. Chen ST, Springer CS, Jr. Ionophore-catalyzed cation transport between phospholipid inverted micelles manifest in DNMR. Biophys Chem 1981;14(4):375-388.
16. Koenig SH, Ahkong QF, Brown RD, 3rd, Lafleur M, Spiller M, Unger E, Tilcock C. Permeability of liposomal membranes to water: results from the magnetic field dependence of T1 of solvent protons in suspensions of vesicles with entrapped paramagnetic ions. Magn Reson Med 1992;23(2):275-286.
17. Donahue KM, Weisskoff RM, Burstein D. Water diffusion and exchange as they influence contrast enhancement. J Magn Reson Imaging 1997;7(1):102-110.
18. Strijkers GJ, Hak S, Kok MB, Springer CS, Jr., Nicolay K. Three-compartment T1 relaxation model for intracellular paramagnetic contrast agents. Magn Reson Med 2009;61(5):1049-1058.
19. Yamada S, Matsuzawa T, Yamada K, Yoshioka S, Ono S, Hishinuma T. A modified signal intensity equation of Carr-Purcell-Meiboom-Gill pulse sequence for MR imaging. The Tohoku journal of experimental medicine 1989;158(3):203-209.
20. Kok MB, Hak S, Mulder WJ, van der Schaft DW, Strijkers GJ, Nicolay K. Cellular compartmentalization of internalized paramagnetic liposomes strongly influences both T1 and T2 relaxivity. Magn Reson Med 2009;61(5):1022-1032.

21. Aime S, Castelli DD, Crich SG, Gianolio E, Terreno E. Pushing the sensitivity envelope of lanthanide-based magnetic resonance imaging (MRI) contrast agents for molecular imaging applications. Accounts of chemical research 2009;42(7):822-831.

# PART B

# In vivo applications and quantification

Chapter 4

# In Vivo Quantitative Assessment of Cell Viability of Gadolinium or Iron-Labeled Cells using MRI and Bioluminescence Imaging

Jamal Guenoun[1*], Alessandro Ruggiero[1*], Gabriela N. Doeswijk[1], Roel C. Janssens[2], Gerben A. Koning[3], Gyula Kotek[1], Gabriel P. Krestin[1], Monique R. Bernsen[1,4].
*Both authors contributed equally to this work.

[1]Department of Radiology, Erasmus MC - University Medical Center Rotterdam, Rotterdam, the Netherlands
[2]Department of Genetics, Erasmus MC - University Medical Center Rotterdam, Rotterdam, the Netherlands
[3]Laboratory of Experimental Surgical Oncology, Section Surgical Oncology, Department of Surgery, Erasmus MC - University Medical Center Rotterdam, Rotterdam, The Netherlands
[4]Department of Nuclear Medicine, Erasmus MC - University Medical Center Rotterdam, Rotterdam, the Netherlands

Published in *Contrast Media Mol Imaging*. 2013 Mar-Apr;8(2):165-74

## Abstract

In cell therapy, noninvasive monitoring of *in vivo* cell fate is challenging. In this study we investigated possible differences in R1, R2 or R2* relaxation rate as a measure of overall cell viability of mesenchymal stem cells labeled with Gd-liposomes (Gd-MSCs) or iron oxide nanoparticles (SPIO-MSCs). Cells were also transduced with a luciferase vector, facilitating a correlation between MRI findings and cell viability using bioluminescence imaging (BLI).

Viable Gd-MSCs were clearly distinguishable from nonviable Gd-MSCs under both *in vitro* and *in vivo* conditions, clearly differing quantitatively (ΔR1 and ΔR2) as well as by visual appearance (hypo- or hyperintense contrast). Immediately post-injection, viable Gd-MSCs caused a substantially larger ΔR2 and lower ΔR1 effect compared to nonviable MSCs. With time, the ΔR1 and ΔR2 relaxation rate showed a good negative correlation with increasing cell number following proliferation.

Upon injection, no substantial quantitative or visual differences between viable and non-viable SPIO-MSCs were detected. Moreover, non-viable SPIO-MSCs caused a persisting signal void *in vivo*, compromising the specificity of this contrast agent. *In vivo* persistence of SPIO particles was confirmed by histological staining.

A large difference was found between SPIO- and Gd-labeled cells in the accuracy of MR relaxometry in assessing the cell viability status. Gd-liposomes provide a more accurate and specific assessment of cell viability than SPIO particles. Viable Gd-cells can be differentiated from nonviable Gd-cells even by visual interpretation. These findings clearly indicate Gd to be the favourable contrast agent in qualitative and quantitative evaluation of labeled cell fate in future cell therapy experiments.

## Introduction

In recent years, cell transplantation has evolved into a promising treatment option for a variety of diseases and disorders such as cancer, cardiovascular disease, neurodegenerative diseases, and musculoskeletal disorders. This field has clearly benefited from the technological advancements in imaging sciences as the majority of clinical trials have involved the use of one or more imaging modalities to evaluate therapeutic efficacy of stem cell transplants (1-4). Molecular imaging techniques enable a complete assessment of the implanted stem cells (viability, proliferation, migration, differentiation) and contribute to important insights into the mechanism of action of stem cells (5-6). However, not all preclinical visualization tools can be easily translated to clinical applications. One of the critical issues to address in cell transplantation is the noninvasive assessment of cell engraftment and survival in the long term. In pre-clinical research, investigation of cell viability usually requires the use of laborious *ex vivo* histological techniques. As histology provides only a snap-shot at a certain time point, an intra-individual longitudinal assessment of stem cell fate needs a different approach. The ability to noninvasively deduce basic functional information from cell transplants, would provide a powerful tool for evaluating therapy effect and initiate progress towards translational research.

MRI is a favourable imaging modality owing to its high spatial resolution, lack of use of ionizing radiation, excellent soft tissue visualization and functional information. Visualization of transplanted cells with MRI can be relatively easily accomplished by labeling the cells with MRI contrast agents (7). Until now, iron-oxide-based T2 contrast agents (CAs) (8-11) were considered the CA of choice, mainly given their high sensitivity. However, their use carries some serious limitations. Iron particles released from apoptotic cells will undergo re-uptake by locally attracted macrophages (12-18), causing a false-positive MRI signal. This is a relevant issue in imaging of cell transplants. For example, in cell grafting for repair of myocardial infarction, over 90% cell death occurs in the first 24 hours post-transplantation (19-21). Furthermore, once iron particles have been cleared by macrophages, the magnetic label can be transferred to other cells of the monocyte/macrophage system and presumably also to many other cell types (22). This further complicates the iron clearance pathway, deteriorating the specificity of the MRI signal even more and clearly illustrating the difficulties in unambiguous identification of transplanted SPIO labeled cells.

The use of the T1 CA Gd-DTPA might overcome these limitations. As macrophage endocytosis is mainly size-dependent (13), it is hypothesized that the low molecular weight (500Da) Gd-DTPA molecule can escape macrophage re-uptake. Following labeled cell death, the swift diffusion of Gd will therefore increase the specificity of MRI signal read-out. Previously, it was shown that labeling with Gd-liposomes produces excellent MR visibility of mesenchymal stem cells (23). Remarkably, several studies reported a reduced longitudinal relaxivity following cellular internalization of Gd *in vitro* (24-27). This 'quenching' is mainly caused by the decreased accessibility of $H_2O$ to compartmentalized Gd (28-29). To our knowledge, the 'quenching' of Gd hasn't been studied *in vivo* up to now. We hypothesize that cell death, and the subsequent release and decompartmentalization of Gd will result in an increased T1 shortening *in vivo*.

The aim of this study was to assess whether the contrast characteristics of Gd- or SPIO-labeled cells can be used to extract information on overall cell transplant viability in vivo. For validation of MRI findings cells transduced with the luciferase gene were used for additional bioluminescence imaging (BLI) as well. As the activity of the luciferase enzyme is dependent on $Mg^{2+}$, ATP and $O_2$, it will be active in viable cells only, thus providing an excellent validation tool for cell viability assessment (30).

# Material and Methods

## Preparation and characterization of liposomes

Gd-DTPA was incorporated in cationic liposomes using the lipid-film hydration technique, as described before (23). Briefly, a 100 µmol mixture of 1,2-dipalmitoyl-sn-glycero-3-phosphocholine (DPPC) (Lipoid GmbH, Ludwigshafen, Germany), cholesterol (Sigma-Aldrich, St. Louis, MO, USA), 1,2-dioleoyl-3-trimethylammonium-propane (chloride salt) (DOTAP) (Avanti Polar lipids, Alabaster, AL, USA) and rhodamine-PE (Avanti Polar lipids) in the molar ratio 47:33:20:0.1 was dissolved in chloroform-methanol, evaporated and hydrated in Gd-DTPA (Magnevist) (Bayer Schering Pharma AG, Berlin, Germany). Following extrusion through 200 and 100 nm filters and ultracentrifugation to separate nonencapsulated from encapsulated Gd, the liposome pellet was resuspended in 2 ml HEPES.

Liposomal size was determined by dynamic light scattering (DLS) using a Zetasizer Nano (Malvern Instruments, Worcestershire, UK). The mean resultant size of Gd-DTPA liposomes was 101 nm with a polydispersity index (PDI) of 0.07. The zeta potential was 43±7.0 mV.

Liposomal phosphate content was assessed by spectrophotometric analysis according to Rouser (50). Relative Gd content was determined by inductively coupled plasma-optical emission spectroscopy (ICP-OES; Optima 4300DV, Perkin Elmer, Norwalk, CT, USA) operating at a wavelength of 342 nm) and was 66 ± 4 µg Gd/µmol total lipid.

## Virus construction and production

A self-inactivating lentivirus was prepared by transient transfection of HEK293T cells in 6 x 19 cm dishes. Briefly, pND-Cag-Luc (60 µg per dish) was cotransfected into HEK293T cells with a mixture of pMDLg/pRRE (30 µg per dish), pMD2.G (15 mg per dish) and pRSV-Rev (15 µg per dish) packaging plasmids using polyethylemine.

Lentiviral supernatant was collected at 48 h and 72 h, filtered (0.45 mm) and concentrated by ultracentrifugation with a Beckman 45Ti rotor at 20K (4 ºC, 2 h). The pellet was then resuspended in 1ml phosphate-buffered saline (PBS). Mesenchymal stem cells (Millipore, Billerica, MA, USA) were grown to 50% confluency in a 24 well plate in DMEM/F10, 10% Fetal Calf Serum (FCS), penicillin/streptomycin (P/S) and infected with 50 µl lenti-viral stock, resulting in luciferase-expressing MSCs.

## Cell Labeling and Preparation

Fluc-MSCs of passage 2 or 3 were used for all experiments at 70% subconfluency. MSCs were cultured in Dulbecco's modified Eagle medium (Invitrogen; Carlsbad, CA, USA) supplemented with 2% FBS (Lonza; Basel, Switzerland), 2% penicillin-streptomycin (Invitrogen), 2% $_{L}$-glutamine (Invitrogen), 1% Modified Eagle Medium (MEM) essential vitamin mixture (Lonza), 1% Nonessential amino acids (NEAA) (Sigma-Aldrich; St. Louis, MO, USA) and 0.5% glutamax (Invitrogen).

Following two washing steps with PBS (Invitrogen, Breda, The Netherlands), the culture medium was replaced by Optimem (Invitrogen). Cells were then labeled for 24 h with SPIO (Endorem™; Guerbet S.A., Paris, France) containing 100 µg Fe $ml^{-1}$ culture medium (51) or with 125 µM Gd-liposomes for 4h (23). Labeling with 125 µM Gd-liposomes for 4h yields an intracellular Gd content of 30 ± 2.5 pg/cell, as reported before (23). Following labeling, cells were harvested by trypsinization, washed 3 times in PBS and centrifuged at 300 *g* for 5 min to discard of unincorporated contrast agent.

After centrifugation, cells were equally divided over two separate tubes and further processed to use as either viable cells or dead cells. Nonviable cells were obtained by repeated freeze thawing of one final suspension in liquid nitrogen. Cell death was assessed by Trypane Blue assay. For *in vitro* experiments, cell pellets were each suspended in Ficoll solution with a density of 1.07 g $mL^{-1}$, to prevent cell sedimentation during imaging (52). For *in vivo* experiments, the cell pellet was suspended in PBS.

## MRI and BLI Phantom studies

From the same stock of cells serial dilutions containing live or dead cells were suspended in 50 µl Ficoll and transferred to a 96-well plate (BLI phantom). Surrounding wells were filled with water to prevent susceptibility artifacts owing to air and/or very concentrated samples.
MRI data were acquired by using a 3 T clinical scanner (Signa Excite; GE Medical Systems, Milwaukee, WI, USA) with unmodified gradients and custom made surface coils (inner diameter of 5 cm). Spin echo (SE) sequences with multiple TR (100 - 2800 ms; echo time (*TE*) 10 ms) and multiple *TE* (10-100 ms; *TR* 600 ms) were used to obtain T1 longitudinal relaxation times and T2 transverse relaxation times, respectively. T2* transverse relaxation times were obtained with a 3D gradient echo sequence (GRE) (matrix = 234 x 234, slice thickness = 0.7 mm and number of excitations (NEX) = 2, using lower *TE*s (3-36 ms). Sequences were acquired with a field of view (FOV) = 5.0 x 5.0 $cm^2$, matrix = 160 x 160, slice thickness = 1.4 mm and NEX = 2. To calculate T1, T2 and T2* times, we used two independent methods: An in-house developed algorithm script for Matlab (version R2007b) and an Image J plugin (MRI analysis calculator by Karl Schmidt). The MRI analysis calculator has been used previously by other authors (53,54). Relaxation times were calculated as follows:

$$\Delta R1_x = \frac{1}{T1_x} - \frac{1}{T1_{ref}} \qquad [1]$$

In which $T1_{cells}$, represents the T1 of the cell cluster (both *in vitro* and *in vivo*) and $T1_{ref}$ the T1 of the surrounding wells containing Ficoll (*in vitro)* or of normal muscle (*in vivo)*. The same equation was applied to derive the ΔR2 and ΔR2* using T2 and T2*, respectively. T1ref and T2ref in vitro were assessed to be 3100 ± 120 ms and 167 ± 18 ms respectively. T1ref and T2ref in vivo were assessed to be 1500 ± 91 ms and 36 ± 7.0 ms respectively. A voxel-by-voxel linear least squares fit of the natural logarithm of the signal amplitude versus at least 6 echo times (TE) was performed to construct R2 and R2* maps. For R1 maps at least 6 repetition times (TR) were used.
For BLI phantoms, luciferase activity of Fluc-MSCs was measured by using the Xenogen IVIS Spectrum (Caliper LS, Hopkington, MA, USA) 10 min after the addition of D-luciferine at a final concentration of 50 µg $µl^{-1}$ (integration time 10, 20, 30, 40, 50, and 60 s; f/stop 1; binning medium; field of view B). Optical intensity is reported as photons/second/area/steradian (p/s/$cm^2$/sr). Data were analyzed with the software Living Image version 3.2 (Caliper LS).

## Cell Transplantation and In Vivo imaging

All animal experiments were conducted in compliance with dutch law and with the approval of the Institutional Animal Welfare Committee. Animals were provided with food and water *ad libitum*. All animal procedures were performed under anesthesia by inhalation of 2% iso-

flurane (Baxter Healthcare, Deerfield, IL, USA)-oxygen mixture. Wistar rats (4-6 weeks) were obtained from Harlan (Horst, the Netherlands) and were allowed to acclimatize at the Erasmus MC vivarium for 1 week prior to cell injection.
Viable or dead Fluc-MSCs (5 x $10^6$) labeled with Gd-liposome or SPIO were administered in the lower back by intramuscular injection (50 µl). The location of injection was properly marked on the skin.

## In vivo studies

For T1, T2 and T2* mapping purposes the same sequences were used as *in vitro*. Formula (1) was applied, except that T1, T2 and T2* values from healthy spinal muscle were used as reference instead of Ficoll. BLI was performed from 5 min after intraperitoneal (i.p.) injection of $_D$-luciferine (Promega) for 1h. Animals were scanned repeatedly over a two-week period at days 0, 2, 5, 10 and 15.

## Immunohistochemistry

At end of follow up, muscular tissue at the injection site was carefully resected. Injection sites were identified by the markings on the skin. BLI imaging and macroscopic visual examination were further used to confirm the site of injection. Briefly, tissue was transferred to 4% paraformaldehyde, transferred to 30% sucrose for 1 day, followed by immersion in OCT (Tissue-TEK). Tissue was cryo-sectioned to obtain 10 mm-thick samples. Sections were stained for iron using Perl's iron stain (Klinipath BVBA, Duiven, the Netherlands) and counterstained with hematoxylin (Sigma-Aldrich).

## Gd and SPIO In Vitro and Ex Vivo Measurements

The total amount of cellular internalized SPIO or Gd content was measured by ICP-OES in three 20 µl aliquots of a SPIO- and Gd-labeled MSC stock solution, respectively. Aliquots were suspended in 4 ml. Triton X-100 2% (St. Louis, MO, USA), heated up at 55 °C and mixed for 30 min at 6 g to induce cellular and liposomal lysis. Cellular content of the CA was calculated as:

$$CA_{cellular} = \frac{CA_{pellet}}{N_{cells}} \qquad [2]$$

To measure the amount of retained Gd in the injected muscle, ICP was performed on the ipsi- and contralateral muscle as well. For this purpose, muscle was dissected in small pieces, and crushed in a microdismembrator. Crushed tissue was resuspended in 1% Triton/PBS, lyophilized and finally digested using HNO3 and $H_2O_2$ at 110 °C.

## Data analysis

All values are presented as mean±SD from at least triplicate samples and expressed in relation to unlabeled cells. For correlation assessment Spearman r coefficient was determined (Graph-

pad InStat 3.06; Graphpad Software Inc., San Diego, CA, USA). The degree of significance is given when appropriate (*p < 0.05; **p < 0.01; ***p < 0.001).

# Results

## In vitro contrast behavior

A Trypan Blue exclusion test showed the actual death rate of cells, rendered non-viable by repeated freeze thawing, to be 99% (Fig. 1). Non-viable cells remained largely intact. In addition, to confirm the specificity of BLI for viable cells, photon emission by dead cells was shown to be absent (Fig. 2a,b). Linear regression analysis showed the amount of emitted photons and the number of viable cells to be linearly proportional (Fig. 2b). These findings supported the use of BLI as a validation tool for our MR results.

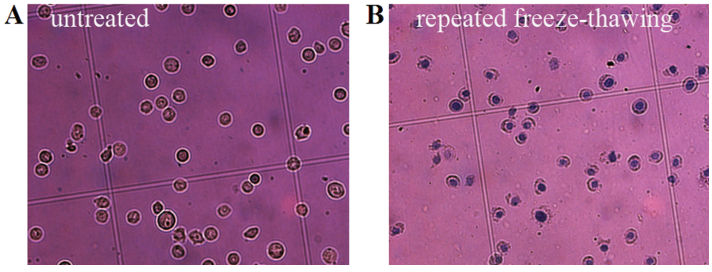


**Fig. 1** Light microscopy image showing Trypan Blue exclusion test on Gd-liposome labeled MSCs prior to transplantation. Viable Gd-MSCs (a) exclude the Trypane Blue dye, whereas nonviable MSCs (b) stain blue due to membrane disintegrity.

Heavily concentrated samples of viable Gd-MSCs (mesenchymal stem cells) generated a signal void (hypointensity) on MR images, an effect which is known as 'quenching' (Fig. 3a). In contrast, similar concentrations of nonviable Gd-MSCs generated a bright signal (hyperintensity) allowing them to be visually distinguished from viable Gd-MSCs.
The ΔR1 (Fig. 4a) and ΔR2 (Fig. 4b) relaxation rate were found to be linearly proportional to the Gd-labeled cell amount across the entire range of cell numbers studied, thus allowing the

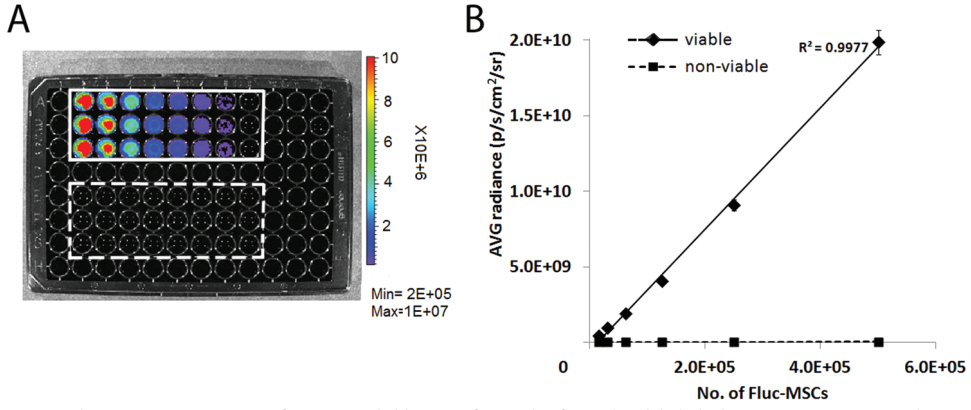


**Fig. 2** Bioluminescence imaging of a 1:1 serial dilution of a stock of $5*10^5$ unlabeled Fluc-MSCs. BLI image showing signal from viable MSCs (rectangular box) and the absence of signal from non-viable MSCs (dashed rectangular box) (a). Total amount of captured photons was linearly proportional to MSC concentration (b).

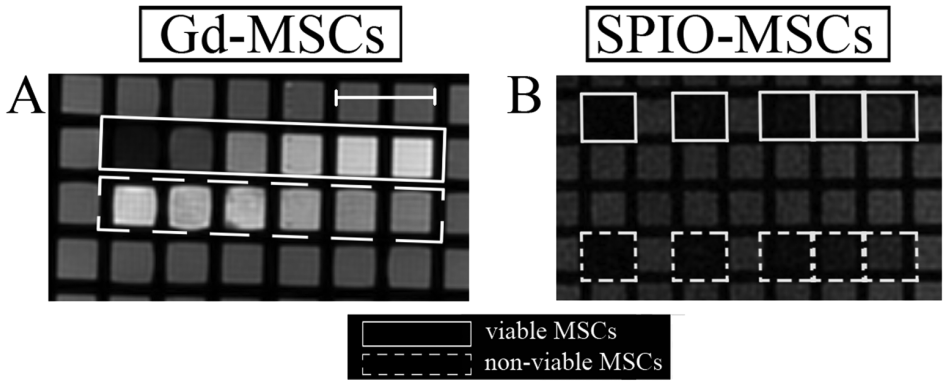


**Fig. 3** MR-imaging of in vitro serial dilution series of viable (undashed boxes) vs non-viable (dashed boxes) labeled MSCs at 3.0T. T1-weighted image of Gd-liposomes labeled MSCs, varying in concentration from left to right $1.65*10^5$, $8.3*10^4$, $4.1*10^4$, $2.1*10^4$, $1.0*10^4$ and $5.1*10^3$ MSCs $\mu l^{-1}$ Ficoll (a) and T2-weighted image of SPIO-labeled MSCS varying in concentration from left to right $1.65*10^5$, $8.3*10^4$, $4.1*10^4$, $2.1*10^4$ and $1.0*10^4$ MSCs $\mu l^{-1}$ Ficoll (b). Scale bar represents 10 mm and applies to both (a) and (b).

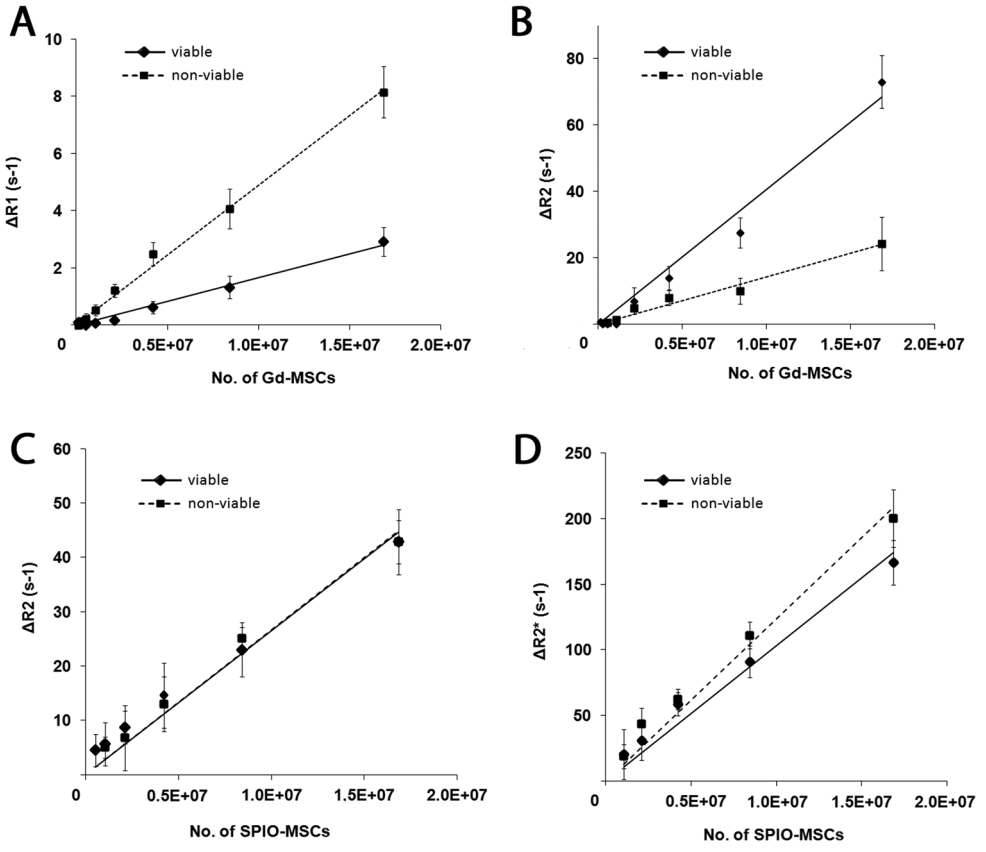


**Fig. 4** ΔR1 (a), ΔR2 (b,c) and R2* (d) as a function of Gd or SPIO labeled cell density. The longitudinal r1 (a) and transverse cellular r2 relaxivity (b,c) were obtained by a linear fit of the data. Data are presented as mean ± SD (n=3 different samples, SD refers to intersample SD).

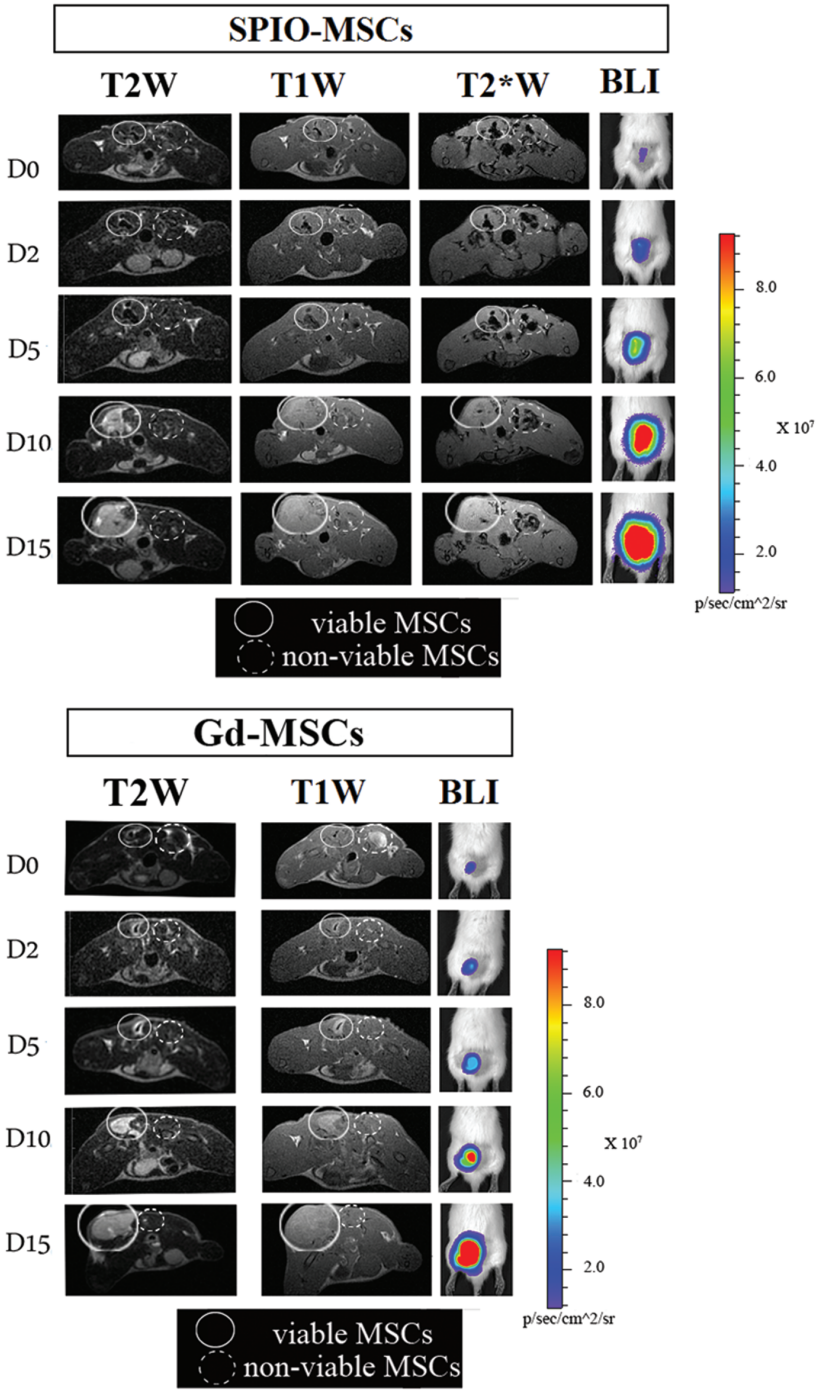


**Fig. 5** Dual modality longitudinal imaging of MSCs transplanted in the lower back muscle. Imaging of SPIO-MSCs (a) and Gd-MSCs (b) on T2-weighted FSE (TE 120 ms, TR 3000, NEX 4) T1-weighted SE (TE 10 ms, TR 1200 ms) and T2*-weighted GRE (TE 8 ms, TR 50 ms, α 16º) images. BLI shows considerable viable cell proliferation, visible on MRI as a gradual decrease (Gd-MSCs) and increase (SPIO-MSCs) in signal intensity.

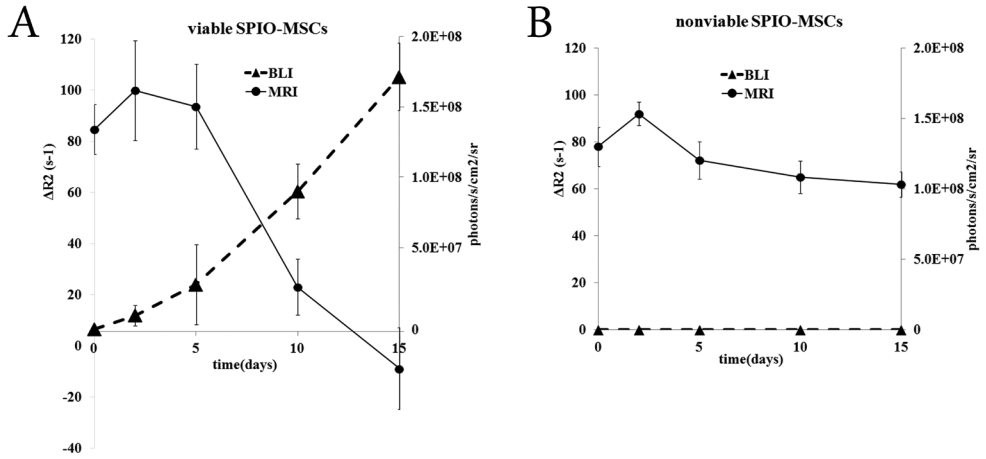


**Fig. 6** In vivo measurement of the ΔR2 and ΔR2* relaxation rate of SPIO-MSCs. The ΔR2 effect from viable SPIO-MSCs gradually decreased over time, accompanied by an increasing BLI signal. Non-viable cells displayed a marginal decrease in ΔR2 over time. Data are presented as mean ± SD (n=6 rats, SD refers to inter animal SD).

measurement of the relaxivity per cell. The r1 and r2 cellular relaxivities ($r1^{\varnothing}$ respectively $r2^{\varnothing}$) were determined from the slopes of the regression lines of the R1 and R2 relaxation rates against cell number. For viable Gd cells this yielded an $r1^{\varnothing}$ of 2 x $10^{-7}$ $s^{-1}$ $cell^{-1}$ and $r2^{\varnothing}$ of 4 x $10^{-6}$ $s^{-1}$ $cell^{-1}$. For non-viable Gd-cells $r1^{\varnothing}$ and $r2^{\varnothing}$ were 5 x $10^{-7}$ $s^{-1}$ $cell^{-1}$ and 1 x $10^{-6}$ $s^{-1}$ $cell^{-1}$, respectively.
As both viable and nonviable SPIO-MSCs (Fig. 3b) generated a signal void, a viability assessment based on mere visual distinction was not possible. Moreover, T2 and T2* measurements showed no substantial difference in the ΔR2 (Fig. 4c) or ΔR2* (Fig. 4d) relaxation rate between viable and nonviable SPIO-MSCs. For both viable and non-viable SPIO-MSCs $r2^{\varnothing}$ was assessed to be 2 x $10^{-4}$ $s^{-1}$ $cell^{-1}$. The $r2^{*\varnothing}$ relaxivity for viable SPIO-MSCs was 9 x $10^{-6}$ $s^{-1}$ $cell^{-1}$ and for nonviable cells it was 0.1 x $10^{-6}$ $s^{-1}$ $cell^{-1}$.

## Longitudinal in vivo contrast behavior

As expected, nonviable MSCs from both groups did not generate bioluminescent signal *in vivo* (Fig. 5a, b). All injected cell grafts were clearly visualized on MRI following injection (Fig. 5a, b). Optimized T1, T2 and T2*-weighted sequences were used to cover the entire range of cell visibility during the follow-up time and cell division. SPIO-MSCs caused a signal void (hypointensity), regardless of the cell viability (Fig. 5a). In the acute post-transplantation stage, no substantial differences in visual appearance or R2 and R2* values were detected between viable and nonviable SPIO-MSCs (Fig. 7a,b). Over time, the number of detected photons increased at the site of viable cells injection (Fig. 5). In parallel, a substantial drop in ΔR2 relaxation rate from viable SPIO-MSCs (23 ± 11 $s^{-1}$) occurred from day 5 onwards (Fig. 7a), whereas ΔR2 from nonviable cells was virtually unchanged (65 ± 7 $s^{-1}$ at day 14 vs 78 ± 8 $s^{-1}$ at day 0; Fig. 7b). Signal void from viable SPIO-MSCs was barely visible on T2-weighted scans at day 15, except for a small hypointense core on both T2 and T2*-weighted scans (Fig. 5a). This increase in signal intensity was accompanied by an increased bioluminescence signal.
Viable Gd-MSCs showed a different dynamic signal behavior. Immediately post-transplantation, they were consistently detected as a hypointense area on T1-weighted scans ('quenched signal intensity'), whereas a similar density of nonviable Gd-MSCs resulted in increased signal intensity (hyperintensity) at the injection site (Fig. 5b). In contrast to SPIO-MSCs, hyperintense

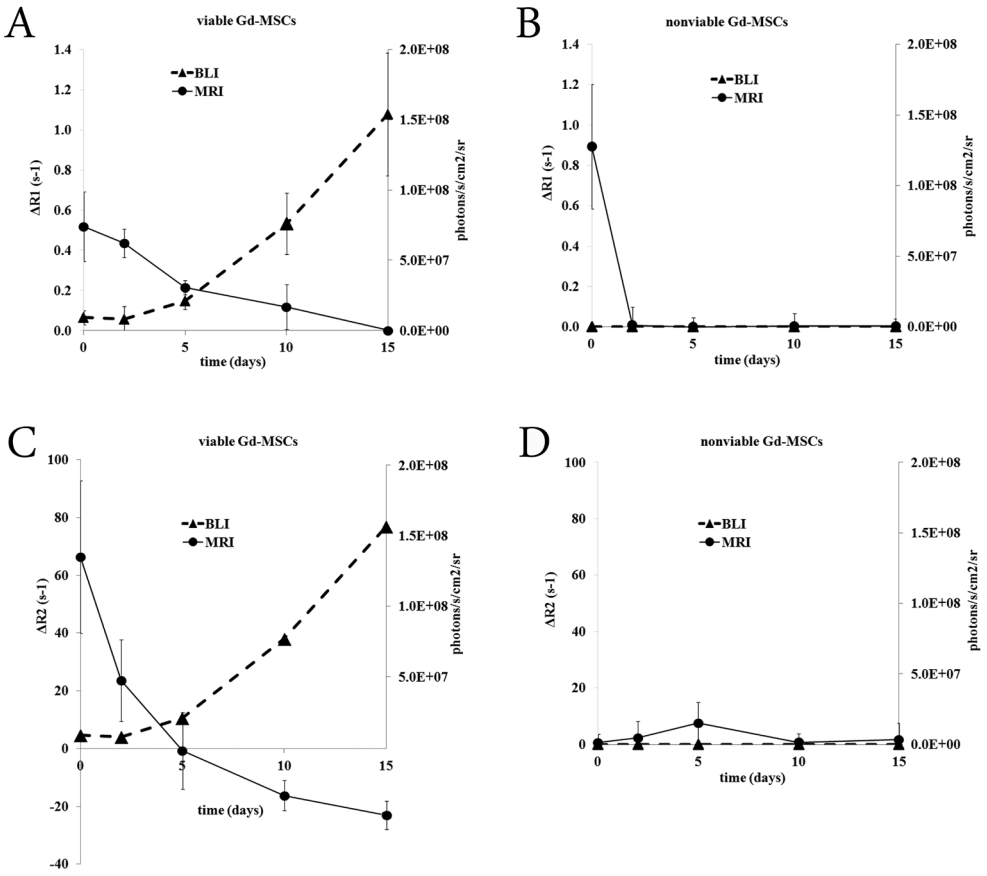


**Fig. 7** In vivo measurement of R1 and R2 relaxation rate of Gd-MSCs. Upon injection, viable Gd-MSCs cause a substantially larger ΔR2 but smaller ΔR1 effect than non-viable Gd-MSCs. ΔR1 and ΔR2 relaxation rate correlated well with the increasing cell number (Spearman r correlation coefficient 0.89 and 0.90 respectively, $p<0.05$). Data are presented as mean ± SD (n=6 rats, SD refers to inter animal SD).

signal from nonviable Gd-MSCs had already resolved already after 2 h post-transplantation (data not shown). In addition, substantial differences in R1 and R2 relaxation rates between viable and nonviable Gd-MSCs (Fig. 6) were measured as well. At day 0, the ΔR1 effect (0.5 ± 0.2 $s^{-1}$; Fig. 7a) of viable Gd-MSCs was nearly half of the ΔR1 from non-viable MSCs (0.9 ± 0.3 $s^{-1}$; Fig. 6b), while causing a substantially larger ΔR2 effect (66±26 $s^{-1}$;Fig. 6c) compared with nonviable MSCs (0.6 ± 2.9 $s^{-1}$; Fig. 6d). Both the ΔR1 and ΔR2 relaxation rate correlated very well with the increasing cell number following proliferation (Spearman r correlation coefficient 0.89 and 0.90, respectively; $p < 0.05$). $T1_{ref}$ and $T2_{ref}$ (the T1 respectively T2 of normal muscle tissue) were assessed to be 1500 ± 91 ms and 36 ± 7.0 ms respectively.

## Retention of Contrast Agent Gd

The retrieved amount of Gd from viable cells was 84 ± 10% of the injected amount. Of the initially injected Gd amount 9 ± 2% was retrieved at sites of transplanted nonviable cells (Table 1). Red fluorescent signal from Gd-liposomes was not detectable at sites where non-viable Gd-MSCs

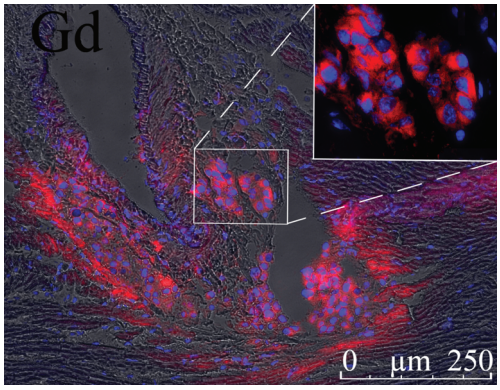


Fig. 8 Histological detection of cells labeled with rhodamine containing Gd-liposomes, in skeletal muscle tissue (day 15 post-transplantation). Red fluorescence from the rhodamine-liposomes is clearly visible as is the blue nuclear dye Hoechst, add-ed to the cells in culture prior to injection. Inset shows a 10x magnification of the area indicated by the rectangle.

had been injected. Viable transplanted Gd-MSCs were clearly identified at the site of transplantation at day 15 by the blue Hoechst dye and the perinuclear red dye from liposomes (Fig. 8). At sites of injection with nonviable SPIO-MSCs, iron was shown to be still present (Fig. 9), in close proximity to post-injection hemorrhages.

**Fig. 9** Histological detection of skeletal muscle tissue (day 15 post-transplantation), priorly transplanted with non-viable SPIO-MSCs. Perl's iron stain shows iron (black arrows) to be still present, in close proximity of erythrocytes (white arrows).

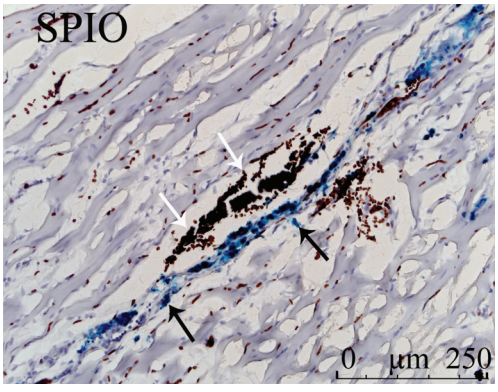


## Discussion

Molecular imaging has rapidly become a necessary tool for the validation and optimization of stem cell engrafting strategies in preclinical and clinical studies. One of the most critical and unresolved issues is the noninvasive assessment of the survival and proliferation of cells after implantation. Several available approaches using reporter genes allow the in vivo monitoring of cell survival, monitored by either MRI (31,32), bioluminescence (30) or nuclear techniques such as PET/SPECT (33,34). The reporter gene technique however, being quite invasive, cannot be easily translated to the clinical arena. Therefore we sought to investigate a minimally invasive labeling technique that reflects the actual viability of labeled cells, and validated it by BLI.

A future translation of MRI-based cell tracking to clinical medicine will require an excellent sensitivity and specificity of the contrast probe or an acceptable trade-off between these two requirements, depending on the application. High sensitivity might be essential to investigate

the long-term fate of implanted stem cells, since probe dilution upon cell proliferation reduces the detection capabilities. Alternatively, a high specificity is demanded by applications such as cellular transplantation, to detect cell graft rejection at an early stage.

In the current study we have shown Gd to be more specific than SPIO nanoparticles. Irrelevant signal from non-viable Gd-MSCs resolved already 2 h post-transplantation (data not shown) while at the original injection site of nonviable SPIO-MSCs hypointense MRI signal persisted for at least 15 days. In a recent study by Baligand *et al.*, it was reported that even 95 days post-transplantation, false-positive SPIO signal was still detectable in immunorejected grafts (35). Terrovitis et al. concluded that MRI of iron oxide-labeled stem cells is not a reliable technique for quantifying engraftment in the heart because of the considerable residual signals generated by the persistence of iron-laden tissue macrophages after cell death (17). Reuptake by macrophages of previously released SPIO seems to play a major role in this phenomenon (12-16). Specificity is a very important issue, especially in direct injections, involving high cell mortality rates; it would lead to massive release SPIO followed by macrophage uptake, thereby severely increasing the amount of false positives (decreased specificity). In contrast, as a result of its biological short half-life and low molecular weight (36,37), the vast majority of extracellular complexed Gd will diffuse out rapidly to end up intravascularly, followed by renal excretion (38). Theoretically it is thus less likely that complexed Gd released by injected dead cells undergoes reuptake by surrounding phagocytic cells. This is in line with our observations that only a fraction of the initially injected Gd quantity, contained in nonviable MSCs, was retrieved at the site of injection at day 15 (Table 1).

The intrinsic lower sensitivity of Gd, in comparison with SPIO, has been one of the main reasons for its limited use for cell tracking purposes (39). However, we observed that viable Gd-MSCs still generated sufficient hyperintense contrast up to at least 10 days post-transplantation. At day 10 viable SPIO-MSCs no longer caused a pronounced signal loss. A small hypointense core remained though, which contributed to a still significant $\Delta R2$ value of the whole cell cluster area. Loss of hypointensity (increase in signal intensity) is known to be caused by dilution owing to cell proliferation, which was confirmed by our bioluminescence and MRI data, showing a substantial cell number increase. An additional disadvantage of SPIO was reported in a study by Walczak et al. (40), stating that accelerated SPIO dilution occurs in highly proliferating cells as a result of iron metabolism in the physiological cellular pathways (41). This effect has very likely played a role in the current study as well. The fact that Gd is not metabolized intracellularly can therefore be a major incentive to use Gd instead of SPIO, especially for highly proliferating cells. Baligand et al. reported the detection of Gd-myoblasts up to 2 weeks (35). In that study, however, the amount of Gd retained intramuscularly was not reported and no correlation was made with cell death or cell proliferation. Hence it was not clear whether Gd signal decay was due to either the effective elimination of released Gd from dying cells (high specificity) or proliferation-induced Gd-dilution (low sensitivity) or a combination of both. The cell proliferation, as perceived by the increased mass effect of viable cells on MRI, the consecutive contrast dilutions and concurrent bioluminescence data, indicates towards a tumoral-like behavior of the cells used in this study. It is unclear as to why this happened, but the introduction of the luciferase construct may have contributed to this effect. For our study purposes, this proliferation was surely not a detrimental effect, as it allowed us to study the effect of fast proliferation on MRI contrast appearance. However, for a future translation to clinical stem cell therapy, it is undebatable that this tumor-like behavior is a major drawback. Luciferase-transfected cells will certainly not be used in the clinical practice, probably eliminating already one of the risk factors for tumor transformation. Nonetheless, before proceding to the clinical stage, the malignant potential of any cell to be used for cell transplantation has to be ruled out.

Several reports exist on the quantitative differentiation of cell-bound SPIO from free SPIO (as may occur after cell death), making use of either the R2 and/or R2* transverse relaxation rate. According to Kuhlpeter et al. compartmentalized, cell-bound SPIO causes a larger R2*

than free SPIO (42). The opposite effect was described in a recent study by Henning *et al.* (43), reporting a statistically significant difference in T2 transverse relaxation time between viable and nonviable lysed cells, but not in T2*. In the latter study, however, differences were reported only in vitro and could not be reproduced in vivo in arthritic joints. These differences in quantification results can be attributed to the somewhat complex nature of SPIO quantification. Quantification of SPIO-labeled cells is not straightforward. R2 relaxation rate is not only dominated by the iron content but also by the distribution of iron within a voxel (44-46). Quantification of the R2* relaxation rate on the other hand can be hindered by macroscopic susceptibility artifacts arising from air-tissue interfaces (47). Supposing that free SPIO can indeed be differentiated quantitatively from intracellular incorporated SPIO, this feature will be useless to distinguish between viable and nonviable cells as soon as bystander macrophages enter the transplantation site to engulf the free SPIO particles, released by non-viable cells. In the current study, our T2 measurements showed no substantial difference in the ΔR2 relaxation rate between viable and nonviable SPIO-MSCs. This was not unexpected as changes in T2 are governed for a large part by decompartmentalization of SPIO particles. Although cells had been freeze-thawed multiple times, they remained relatively intact. As SPIO particles are significantly larger than low molecular weight Gd, it seems unlikely that early in the cell death process SPIO particles will diffuse out. In later stages of cell death with concurrent cell fragmentation, SPIO particle decompartmentalization will start to affect R2 and/or R2*.

In this study we showed that Gd-MSCs exhibit a distinct relaxivity as a direct result of the cell viability both *in vitro* and *in vivo*, nonviable Gd-MSCs having a virtually absent R1 and R2 relaxation rate. Recalling that Gd-MSCs ΔR1 and ΔR2 relaxation rate correlated very well with the increasing cell number following proliferation (r 0.89 and 0.90, respectively; $p < 0.05$), Gd labeling of MSCs can thus very well be used as a tool to track cell fate in vivo.

Of interest, viable Gd-MSCs showed a concentration dependent signal intensity behavior (Fig 3a); It is a known phenomenon that at higher Gd concentrations (irrespective of compartmentalization) Gd produces a substantial T2 effect (T2 time shortening) (48). This shortened T2 time subsequently produces a decreased signal intensity ('signal quenching'), as can be derived from the Bloch equation $SI = M_z(1-e^{-TR/T1})e^{-TE/T2}$ (48). Again, this signal quenching was observed with viable Gd-MSCs directly post-transplantation. This allowed for a clear visual distinction of viable from nonviable cells, making this a valuable qualitative tool for fast read-out of cell fate. This quenching occurred in vitro as well, but at a higher cell density. This is believed to be due in part to differences in water availability, diffusivity and concentration effects in vivo. Even when cells are being transplanted at a similar concentration as in vitro, the density of grafted cells *in vivo* will increase because of tissue pressure, resistance and liquid resorption, resulting in an increased Gd load per voxel. Proliferation will inevitably result in cellular Gd dilution and thus a decreased Gd load per voxel, referred to as 'dequenching'. In the current study this was observed as a hypointense quenched cell graft core, with peripheral hyperintensity. As for the striking contrast difference between viable and nonviable Gd-MSCs a plausible explanation is the following. Gd exerts its T1-shortening effect (i.e. R1 increase) by interacting with surrounding water molecules. It can thus be understood that it will be challenging for water to reach Gd that resides in endosomes inside viable cells with an intact membrane. Furthermore, efflux of Gd from viable cells will be highly unlikely. This 'quenching' effect as a result of cellular Gd compartmentalization was reported previously by Terreno et al. (27). Similarly, in another study by Biancone *et al.* (49) an initial increase in signal intensity of endosomally contained Gd-HPDO3A was reported. This was explained to occur as a result of intracellular redistribution after endosomal degradation. We mimicked the compartmentalization effects in vitro (Fig. 4), comparing viable intact cells with nonviable leaky cells. Interestingly, our measurements confirmed that both ΔR1 (decrease; Fig. 4a) *and* ΔR2 (increase; Fig. 4b) are affected by compartmentalization, causing the typical Gd signal 'quenching' in viable cells. 'Quenching' by viable Gd-cells can thus be explained by a decrease

in the ΔR1/ΔR2 ratio. Nonviable cells however, allowing both an efflux of Gd and/or influx of water molecules more easily, will exhibit an increased ΔR1/ΔR2 ratio. Quantification methods based on T1 or T2 may provide a valuable but laborious and time-consuming tool, both on the data acquisition side as well as on the data processing side. Clearly, this is not a relevant disadvantage for research applications. However, for a successful translation to clinical practice, where time-efficiency is of utmost importance, a qualitative, fast and visually interpretable tool is key. In this paper, we made use of Gd to allow for a nonambiguous distinction between cell death and viability. A combined interpretation of the quantitative (ΔR2/ΔR1) and qualitative findings (contrast changes) may present an important noninvasive tool to track the actual cell fate of transplanted cells in real time, using mere MRI. In fact, visual evaluation of contrast changes from Gd-cells, allows us to assess overall cell viability of a transplanted cell graft. Summarizing, to make statements on the *overall* cell viability and fate of a transplanted cell cluster, this means that a visible hypointense signal reflects viable cells; 'dequenching' (hypointense to hyperintense contrast) indicates cell proliferation; the persistent visibility of hyperintense signal indicates the ongoing presence of viable cells; quick appearance of hyperintense signal followed by consecutive quick disappearance indicates cell death; slow decrease in hyperintense signal indicates ongoing cell proliferation. These may be considered as rough rules of thumb. Most important, as long as contrast is seen on T1W images, there is still a substantial overall cell viability of the cell cluster. For a more detailed cell fate evaluation a correlation to R1 and R2 values remains essential. Nevertheless, as a result of the high specificity, these rules of thumbs may prove beneficial in a clinical setting, for example, when immediate monitoring of cell graft rejection is needed. To our knowledge, our study is the first to report the Gd quenching effect as an easy to interpret qualitative tool for cell viability assessment.

## Acknowledgements

This study was performed in part through support from ENCITE – funded by the European Community under the 7th Framework Programme. All authors confirm that there is no conflict of interest associated with this publication.

# References


1. Bolli R, Chugh AR, D'Amario D, Loughran JH, Stoddard MF, Ikram S, Beache GM, Wagner SG, Leri A, Hosoda T, Sanada F, Elmore JB, Goichberg P, Cappetta D, Solankhi NK, Fahsah I, Rokosh DG, Slaughter MS, Kajstura J, Anversa P. Cardiac stem cells in patients with ischaemic cardiomyopathy (SCIPIO): initial results of a randomised phase 1 trial. Lancet 2011;378(9806):1847-1857.
2. Hopp E, Lunde K, Solheim S, Aakhus S, Arnesen H, Forfang K, Edvardsen T, Smith HJ. Regional myocardial function after intracoronary bone marrow cell injection in reperfused anterior wall infarction - a cardiovascular magnetic resonance tagging study. J Cardiovasc Magn Reson 2011;13:22.
3. Connick P, Kolappan M, Patani R, Scott MA, Crawley C, He XL, Richardson K, Barber K, Webber DJ, Wheeler-Kingshott CA, Tozer DJ, Samson RS, Thomas DL, Du MQ, Luan SL, Michell AW, Altmann DR, Thompson AJ, Miller DH, Compston A, Chandran S. The mesenchymal stem cells in multiple sclerosis (MSCIMS) trial protocol and baseline cohort characteristics: an open-label pre-test: post-test study with blinded outcome assessments. Trials 2011;12:62.
4. Leistner DM, Fischer-Rasokat U, Honold J, Seeger FH, Schachinger V, Lehmann R, Martin H, Burck I, Urbich C, Dimmeler S, Zeiher AM, Assmus B. Transplantation of progenitor cells and regeneration enhancement in acute myocardial infarction (TOPCARE-AMI): final 5-year results suggest long-term safety and efficacy. Clin Res Cardiol 2011;100(10):925-934.
5. Lee Z, Dennis JE, Gerson SL. Imaging stem cell implant for cellular-based therapies. Exp Biol Med (Maywood) 2008;233(8):930-940.
6. Magnitsky S, Walton RM, Wolfe JH, Poptani H. Magnetic resonance imaging as a tool for monitoring stem cell migration. Neurodegener Dis 2007;4(4):314-321.
7. Bernsen MR, Moelker AD, Wielopolski PA, van Tiel ST, Krestin GP. Labelling of mammalian cells for visualisation by MRI. Eur Radiol 2010;20(2):255-274.
8. Bulte JW, Kraitchman DL. Monitoring cell therapy using iron oxide MR contrast agents. Curr Pharm Biotechnol 2004;5(6):567-584.
9. Frank JA, Miller BR, Arbab AS, Zywicke HA, Jordan EK, Lewis BK, Bryant LH, Jr., Bulte JW. Clinically applicable labeling of mammalian and stem cells by combining superparamagnetic iron oxides and transfection agents. Radiology 2003;228(2):480-487.
10. Hoehn M, Kustermann E, Blunk J, Wiedermann D, Trapp T, Wecker S, Focking M, Arnold H, Hescheler J, Fleischmann BK, Schwindt W, Buhrle C. Monitoring of implanted stem cell migration in vivo: a highly resolved in vivo magnetic resonance imaging investigation of experimental stroke in rat. Proc Natl Acad Sci U S A 2002;99(25):16267-16272.
11. Matuszewski L, Persigehl T, Wall A, Schwindt W, Tombach B, Fobker M, Poremba C, Ebert W, Heindel W, Bremer C. Cell tagging with clinically approved iron oxides: feasibility and effect of lipofection, particle size, and surface coating on labeling efficiency. Radiology 2005;235(1):155-161.
12. Amsalem Y, Mardor Y, Feinberg MS, Landa N, Miller L, Daniels D, Ocherashvilli A, Holbova R, Yosef O, Barbash IM, Leor J. Iron-oxide labeling and outcome of transplanted mesenchymal stem cells in the infarcted myocardium. Circulation 2007;116(11 Suppl):I38-45.
13. Berman SC, Galpoththawela C, Gilad AA, Bulte JW, Walczak P. Long-term MR cell tracking of neural stem cells grafted in immunocompetent versus immunodeficient mice reveals distinct differences in contrast between live and dead cells. Magn Reson Med 2011;65(2):564-574.
14. Cahill KS, Gaidosh G, Huard J, Silver X, Byrne BJ, Walter GA. Noninvasive monitoring and tracking of muscle stem cell transplants. Transplantation 2004;78(11):1626-1633.
15. Pawelczyk E, Jordan EK, Balakumaran A, Chaudhry A, Gormley N, Smith M, Lewis BK, Childs R, Robey PG, Frank JA. In vivo transfer of intracellular labels from locally implanted bone marrow stromal cells to resident tissue macrophages. PloS one 2009;4(8):e6712.
16. Raynal I, Prigent P, Peyramaure S, Najid A, Rebuzzi C, Corot C. Macrophage endocytosis of superparamagnetic iron oxide nanoparticles: mechanisms and comparison of ferumoxides and ferumoxtran-10. Invest Radiol 2004;39(1):56-63.

17. Terrovitis J, Stuber M, Youssef A, Preece S, Leppo M, Kizana E, Schar M, Gerstenblith G, Weiss RG, Marban E, Abraham MR. Magnetic resonance imaging overestimates ferumoxide-labeled stem cell survival after transplantation in the heart. Circulation 2008;117(12):1555-1562.
18. van Buul GM, Kotek G, Wielopolski PA, Farrell E, Bos PK, Weinans H, Grohnert AU, Jahr H, Verhaar JA, Krestin GP, van Osch GJ, Bernsen MR. Clinically translatable cell tracking and quantification by MRI in cartilage repair using superparamagnetic iron oxides. PLoS One 2011;6(2):e17001.
19. Azarnoush K, Maurel A, Sebbah L, Carrion C, Bissery A, Mandet C, Pouly J, Bruneval P, Hagege AA, Menasche P. Enhancement of the functional benefits of skeletal myoblast transplantation by means of coadministration of hypoxia-inducible factor 1alpha. J Thorac Cardiovasc Surg 2005;130(1):173-179.
20. Jackson KA, Majka SM, Wang H, Pocius J, Hartley CJ, Majesky MW, Entman ML, Michael LH, Hirschi KK, Goodell MA. Regeneration of ischemic cardiac muscle and vascular endothelium by adult stem cells. J Clin Invest 2001;107(11):1395-1402.
21. Zhang M, Methot D, Poppa V, Fujio Y, Walsh K, Murry CE. Cardiomyocyte grafting for cardiac repair: graft cell death and anti-death strategies. J Mol Cell Cardiol 2001;33(5):907-921.
22. Luciani N, Wilhelm C, Gazeau F. The role of cell-released microvesicles in the intercellular transfer of magnetic nanoparticles in the monocyte/macrophage system. Biomaterials 2010;31(27):7061-7069.
23. Guenoun J, Koning GA, Doeswijk G, Bosman L, Wielopolski PA, Krestin GP, Bernsen MR. Cationic Gd-DTPA liposomes for highly efficient labeling of mesenchymal stem cells and cell tracking with MRI. Cell Transplant 2011.
24. Brekke C, Morgan SC, Lowe AS, Meade TJ, Price J, Williams SC, Modo M. The in vitro effects of a bimodal contrast agent on cellular functions and relaxometry. NMR Biomed 2007;20(2):77-89.
25. Kobayashi H, Kawamoto S, Saga T, Sato N, Ishimori T, Konishi J, Ono K, Togashi K, Brechbiel MW. Avidin-dendrimer-(1B4M-Gd)(254): a tumor-targeting therapeutic agent for gadolinium neutron capture therapy of intraperitoneal disseminated tumor which can be monitored by MRI. Bioconjug Chem 2001;12(4):587-593.
26. Lewin M, Clement O, Belguise-Valladier P, Tran L, Cuenod CA, Siauve N, Frija G. Hepatocyte targeting with Gd-EOB-DTPA: potential application for gene therapy. Invest Radiol 2001;36(1):9-14.
27. Terreno E, Geninatti Crich S, Belfiore S, Biancone L, Cabella C, Esposito G, Manazza AD, Aime S. Effect of the intracellular localization of a Gd-based imaging probe on the relaxation enhancement of water protons. Magn Reson Med 2006;55(3):491-497.
28. Strijkers GJ, Mulder WJ, van Heeswijk RB, Frederik PM, Bomans P, Magusin PC, Nicolay K. Relaxivity of liposomal paramagnetic MRI contrast agents. MAGMA 2005;18(4):186-192.
29. Terreno E, Sanino A, Carrera C, Castelli DD, Giovenzana GB, Lombardi A, Mazzon R, Milone L, Visigalli M, Aime S. Determination of water permeability of paramagnetic liposomes of interest in MRI field. J Inorg Biochem 2008;102(5-6):1112-1119.
30. Muller-Taubenberger A. Application of fluorescent protein tags as reporters in live-cell imaging studies. Methods Mol Biol 2006;346:229-246.
31. Gilad AA, Winnard PT, Jr., van Zijl PC, Bulte JW. Developing MR reporter genes: promises and pitfalls. NMR Biomed 2007;20(3):275-290.
32. Louie AY, Huber MM, Ahrens ET, Rothbacher U, Moats R, Jacobs RE, Fraser SE, Meade TJ. In vivo visualization of gene expression using magnetic resonance imaging. Nat Biotechnol 2000;18(3):321-325.
33. Gambhir SS, Barrio JR, Phelps ME, Iyer M, Namavari M, Satyamurthy N, Wu L, Green LA, Bauer E, MacLaren DC, Nguyen K, Berk AJ, Cherry SR, Herschman HR. Imaging adenoviral-directed reporter gene expression in living animals with positron emission tomography. Proc Natl Acad Sci U S A 1999;96(5):2333-2338.
34. Tjuvajev JG, Stockhammer G, Desai R, Uehara H, Watanabe K, Gansbacher B, Blasberg RG. Imaging the expression of transfected genes in vivo. Cancer Res 1995;55(24):6126-6132.
35. Baligand C, Vauchez K, Fiszman M, Vilquin JT, Carlier PG. Discrepancies between the fate of myoblast xenograft in mouse leg muscle and NMR label persistency after loading with Gd-DTPA or SPIOs. Gene Ther 2009;16(6):734-745.
36. Lin SP, Brown JJ. MR contrast agents: physical and pharmacologic basics. J Magn Reson Imaging 2007;25(5):884-899.

37. Oksendal AN, Hals PA. Biodistribution and toxicity of MR imaging contrast media. J Magn Reson Imaging 1993;3(1):157-165.
38. Aime S, Caravan P. Biodistribution of gadolinium-based contrast agents, including gadolinium deposition. J Magn Reson Imaging 2009;30(6):1259-1267.
39. Chemaly ER, Yoneyama R, Frangioni JV, Hajjar RJ. Tracking stem cells in the cardiovascular system. Trends Cardiovasc Med 2005;15(8):297-302.
40. Walczak P, Kedziorek DA, Gilad AA, Barnett BP, Bulte JW. Applicability and limitations of MR tracking of neural stem cells with asymmetric cell division and rapid turnover: the case of the shiverer dysmyelinated mouse brain. Magn Reson Med 2007;58(2):261-269.
41. Weissleder R, Stark DD, Engelstad BL, Bacon BR, Compton CC, White DL, Jacobs P, Lewis J. Superparamagnetic iron oxide: pharmacokinetics and toxicity. AJR Am J Roentgenol 1989;152(1):167-173.
42. Kuhlpeter R, Dahnke H, Matuszewski L, Persigehl T, von Wallbrunn A, Allkemper T, Heindel WL, Schaeffter T, Bremer C. R2 and R2* mapping for sensing cell-bound superparamagnetic nanoparticles: in vitro and murine in vivo testing. Radiology 2007;245(2):449-457.
43. Henning TD, Wendland MF, Golovko D, Sutton EJ, Sennino B, Malek F, Bauer JS, McDonald DM, Daldrup-Link H. Relaxation effects of ferucarbotran-labeled mesenchymal stem cells at 1.5T and 3T: discrimination of viable from lysed cells. Magn Reson Med 2009;62(2):325-332.
44. Bowen CV, Zhang X, Saab G, Gareau PJ, Rutt BK. Application of the static dephasing regime theory to superparamagnetic iron-oxide loaded cells. Magn Reson Med 2002;48(1):52-61.
45. Rad AM, Arbab AS, Iskander AS, Jiang Q, Soltanian-Zadeh H. Quantification of superparamagnetic iron oxide (SPIO)-labeled cells using MRI. J Magn Reson Imaging 2007;26(2):366-374.
46. Kotek G, van Tiel ST, Wielopolski PA, Houston GC, Krestin GP, Bernsen MR. Cell quantification: evolution of compartmentalization and distribution of iron-oxide particles and labeled cells. Contrast Media Mol Imaging 2012;7(2):195-203.
47. Arbab AS, Janic B, Haller J, Pawelczyk E, Liu W, Frank JA. In Vivo Cellular Imaging for Translational Medical Research. Curr Med Imaging Rev 2009;5(1):19-38.
48. Graves MJ. Pulse sequences for contrast-enhanced magnetic resonance imaging. Radiography 2007;13:e20-e30.
49. Biancone L, Crich SG, Cantaluppi V, Romanazzi GM, Russo S, Scalabrino E, Esposito G, Figliolini F, Beltramo S, Perin PC, Segoloni GP, Aime S, Camussi G. Magnetic resonance imaging of gadolinium-labeled pancreatic islets for experimental transplantation. NMR Biomed 2007;20(1):40-48.
50. Rouser G, Fkeischer S, Yamamoto A. Two dimensional then layer chromatographic separation of polar lipids and determination of phospholipids by phosphorus analysis of spots. Lipids 1970;5(5):494-496.
51. Van Tiel ST, Wielopolski PA, Houston GC, Krestin GP, Bernsen MR. Variations in labeling protocol influence incorporation, distribution and retention of iron oxide nanoparticles into human umbilical vein endothelial cells. Contrast Media Mol Imaging 2010.
52. Sutton EJ, Henning TD, Boddington S, Demos S, Krug C, Meier R, Kornak J, Zhao S, Baehner R, Sharifi S, Daldrup-Link H. In vivo magnetic resonance imaging and optical imaging comparison of viable and nonviable mesenchymal stem cells with a bifunctional label. Mol Imaging 2010;9(5):278-290.
53. Jacobs S, Ruusuvuori E, Sipila ST, Haapanen A, Damkier HH, Kurth I, Hentschke M, Schweizer M, Rudhard Y, Laatikainen LM, Tyynela J, Praetorius J, Voipio J, Hubner CA. Mice with targeted Slc4a10 gene disruption have small brain ventricles and show reduced neuronal excitability. Proc Natl Acad Sci U S A 2008;105(1):311-316.
54. Cotrim AP, Hyodo F, Matsumoto K, Sowers AL, Cook JA, Baum BJ, Krishna MC, Mitchell JB. Differential radiation protection of salivary glands versus tumor by Tempol with accompanying tissue assessment of Tempol by magnetic resonance imaging. Clin Cancer Res 2007;13(16):4928-4933.

Chapter 5

# Cell tracking in cardiac repair: what to image and how to image

Alessandro Ruggiero[1], Daniel L. J. Thorek[2], Jamal Guenoun[1], Gabriel P. Krestin[1], Monique R. Bernsen[1,3]

[1]Department of Radiology, Erasmus MC - University Medical Center Rotterdam, Rotterdam, the Netherlands
[2]Department of Radiology, Memorial Sloan-Kettering Cancer Center, New York, NY, USA
[3]Department of Nuclear Medicine, Erasmus MC - University Medical Center Rotterdam, Rotterdam, the Netherlands

Published in *Eur Radiol.* 2012 Jan;22(1):189-204

## Abstract

Stem cell therapies hold the great promise and interest for cardiac regeneration among scientists, clinicians and patients. However, advancement and distillation of a standard treatment regimen are not yet finalised. Into this breach step recent developments in the imaging biosciences. Thus far, these technical and protocol refinements have played a critical role not only in the evaluation of the recovery of cardiac function but also in providing important insights into the mechanism of action of stem cells. Molecular imaging, in its many forms, has rapidly become a necessary tool for the validation and optimisation of stem cell engrafting strategies in preclinical studies. These include a suite of radionuclide, magnetic resonance and optical imaging strategies to evaluate non-invasively the fate of transplanted cells. In this review, we highlight the state-of-the-art of the various imaging techniques for cardiac stem cell tracking presenting the strengths and limitations of each approach, with a particular focus on clinical applicability.

## Introduction

In the last decade a great amount of research and clinical interest has been directed at stem cells (SC) for their potential to regenerate otherwise permanently damaged tissues. Work with these pluripotent cells has begun to be broadly explored, giving new hope for regenerative approaches in the therapy of myocardial infarction (MI).
Early success in preclinical studies demonstrated that stem cell-based therapy holds the potential to limit the functional degradation of cardiac function after MI (1). This instigated clinical translation at a rapid pace (Table 1). Since the first study in 2002 which showed safety and effectiveness on intracoronary transplantation of autologous SC (2), several randomised, controlled clinical trials have been performed. Due to the absence of standardised protocols (cell number, timing and route of injection, baseline patient characteristics and techniques of evaluating cardiac function), results have been mixed. However, recent metaanalyses have shown that improvement in ejection fraction (EF), ventricular dimension and infarct area, despite being modest, are statistically significant (3-5).
This field clearly benefited from the advancements in imaging sciences as almost all clinical trials involved the use of one or more imaging techniques to evaluate the therapeutic efficacy of stem cell transplantion. Clinically established techniques allow for the evaluation of myocardial contractility, viability and perfusion, but do not provide the direct visualisation of transplanted stem cells, therefore their effective presence and viability can be only presumed. Ideally, transplanted cells in the infarcted myocardium are expected to survive engraftment, be self-renewing and differentiate into cardiac cells (cardiomyocytes, endothelial cells or smooth muscle cells) forming electromechanical junctions with adjacent viable tissues. However, the longterm improvement appears to be most closely related to paracrine effects rather than transdifferentiation of the cell transplant and heart muscle regeneration (6).
Great strides in imaging techniques and technologies have been made that enable the cellular and molecular imaging of transplanted stem cells, their short and long term fate and in some instances their viability and differentiation status.

## Stem cells for cardiac repair

Currently adult stem cells, embryonic stem cells (ESC) and induced pluripotent stem cells (iPS) can be used to regenerate heart tissue. Adult stem cells comprise skeletal myoblasts (SM), mesenchymal stem cells (MSC), bone marrow-derived stem cells (BMC), endothelial (EPC) and cardiac progenitor (CPC) cells. SM were the first option to be used in stem cell transplant as they are available from an autologous source (therefore lacking ethical or immunogenicity issues), and have been demonstrated to provide functional benefit after myocardial infarction in animals (7). However, in a recent clinical trial no sustained benefit in the global EF was observed and increased number of early postoperative arrhythmic events was reported (8).
BMC transplantation has been shown to improve heart function in animal models (1,9). However, others have identified that most of the cells injected adopted a mature haematopoietic transformation and only a small number of cardiomyocytes expressed the genetic markers of the transplanted cells (10,11). Mesenchymal stem cells (MSC) constitute the stromal compartment of bone marrow and, importantly, are not hematopoietic. These are able to differentiate into a variety of cell types (12) and improvement in whole heart function has been described in a swine model of myocardial infarction (13). Visceral and subcutaneous adipose tissue have been shown to contain vascular/adipocyte progenitor cells and adult multipotent mesenchymal cells (adipose tissue-derived stromal cells ( 14)). ASC have been reported to improve left ventricular function in animal models of myocardial infarction (15). The circulating endothe-

**Table 1** Selected randomised clinical trials (>50 patients) of stem cell transplantation following myocardial infarction

| Study | Pts | Cell type | Assessment method | Outcome |
|---|---|---|---|---|
| REPAIR-AMI (101-102) | 204 | Intracoronary BMC vs placebo | LV angiography | At 4 months LVEF increased in BMC vs placebo (mean±SD) increase, (5.5±7.3% vs. 3.0±6.5%; P=0.01). At 12 months: death, recurrence of myocardial infarction, rehospitalization for heart failure significantly reduced. |
| ASTAMI (103, 104) | 100 | Intracoronary BMC vs control | 99mTc-SPECT; echo; MRI | No effect on global left ventricular function at 6 months and 3 years. |
| BOOST (105, 106) | 60 | Intracoronary BMC vs control | MRI; [11C] acetate PET | At 4 months no effect on LVEF and LV volumes. Reduction of infarct volume (measured by serial contrast-enhanced MRI) was greater in BMC patients than in controls |
| TOPCARE-AMI (16) | 59 | Intracoronary BMC vs CPC | LV angiography; MRI | At 4 months LV angiography showed significant increase of LVEF (50±10% to 58±10%), and significant decrease of end-systolic volumes (54±19 ml to 44±20 ml) without differences between the two cell groups. At 12 months MRI showed reduced infarct size and absence of reactive hypertrophy. |
| Meluzin et al. (108) | 60 | Intracoronary BMC (high and low doser) vs control | Echo; 99mTc-SPECT;18F-FDG PET | LVEF improved in the group receiving the highest dose (108 cells) by 6%, 7%, and 7% at months 3, 6, and 12, respectively. |
| MAGIC (8) | 97 | SMB vs placebo injected in and around the scar | Echo | No improvement in regional or global LV function at 6 months. |
| Chen et al. (109) | 69 | Intracoronary BMSC (bone marrow mesenchymal stem cells) vs placebo | 18F-FDG; Echo | At 3 months LVEF significantly increased in the BMSC group (67±11%) compared to controls (53±8%) and the same group before implantation (49±9%). No change in LVEF at 6 months versus 3 months. |
| Dill T et al. (110) | 204 | Intracoronary BMC vs placebo | MRI | In the BMC group, EF increased significantly by 3.2±1.3 absolute percentage points at 4 months, and this increase was sustained at 12 months (+3.4±1.3 absolute percentage points vs baseline). In the placebo group, EF was unchanged (+0.6±1.2 absolute percentage points, at 12 months. |

BMC, bone marrow stem cells; CPC, circulating progenitor cells; SMB, skeletal myoblast. Pts, number of patients. LVEF, left ventricular ejection fraction

lial progenitor cells (EPC) represent a more accessible source of autologous SC and have been used in clinical trials (16]. The existence of a subpopulation of resident cardiac SC (RCSC) has been reported that is self-renewing, clonogenic and multipotent, capable of differentiating in myocytes, smooth muscle and endothelial cells (17). Promising results have been reported in preclinical studies (18), and results of phase I clinical trials, started in 2009, are awaited with interest.

To date, ESC-derived cardiomyocytes (19) and ESC-derived endothelial cells (20) have been successfully used to treat heart disease in animal models. However several problems are related to their use, including immunological incompatibility with the host (21), the tendency to form teratomas (22) and ethical controversies. Several studies have been performed to manipulate the expression of transcription factors with the goal of transforming somatic cells (derived from an autologous source, such as keratinocytes and fat stromal cells) into induced pluripotent stem cells (iPS) (23). These cells possess the same advantages as ESC, without the associated immunological and ethical complications. Cardiomyocytes have been successfully obtained from iPS in vitro (24) and their transplantation in animal models of infarction resulted in improved myocardial function (25).

To summarise, ESC and iPS have the greater potential for cardiomyogenesis, while the formation of new cardiomyocytes by transdifferentiation of SM and BMC has so far not been supported with convincing evidence. It should be noted that several studies have reported moderate improvements in whole cardiac function after transplantation of SM and BMC (7,26). It has been demonstrated that SCs are responsible for paracrine effects, consisting of the release of various cytokines or growth factors (eg. VEGF, bFGF) that increase collateral perfusion and neoangiogenesis and influence the contractile characteristics of chronically failing myocardium (26).

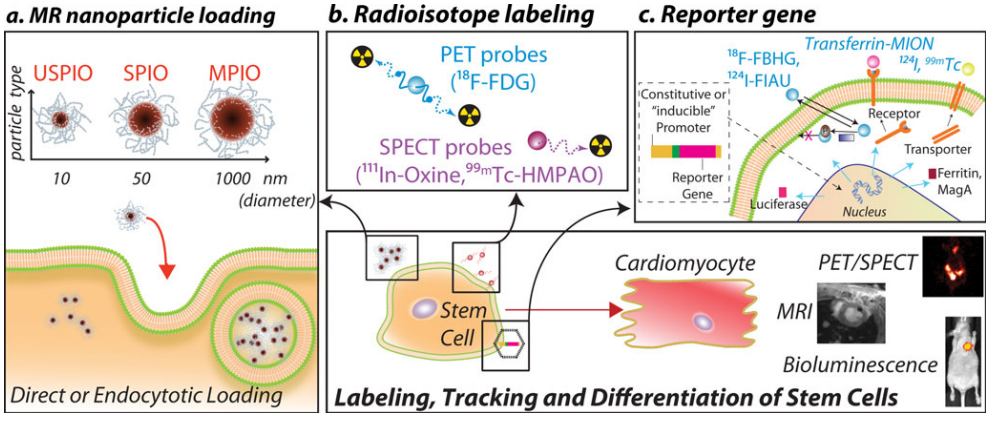


**Fig. 1** Schematic representation of the current technologies available for stem cell (SC) tracking. Before implantation SC can be passively loaded with: a superparamagnetic nanoparticles that allow for the MR detection of labeled cells as areas of signal loss; b radiolabeled PET or SPECT probes. c Reporter gene approaches consist of the introduction through viral or non-viral-vectors of a reporter gene driven by a constitutive or inducible promoter. The reporter gene undergoes transcription to mRNA, which is translated into a protein that can be: 1) an enzyme (as HSV1-tk or luciferase), 2) a receptor (as transferrin receptor or hSSTR [human somatostatin receptor]) 3) a transporter (hNIS [human sodium iodide symporter]) 4) intracellular iron storage protein (ferritin). When a complementary reporter probe is administered, it concentrates or activates only at the site where the reporter gene is expressed. The level of probe accumulation is proportional to the level of reporter gene expression and can be monitored to evaluate the number of cells or the induction of a specific reporter gene.

**Table 2** Selected cell tracking studies of SC

| Study | Species | Cell type | Detection method | Delivery | Results |
|---|---|---|---|---|---|
| MRI | | | | | |
| Kraitchman et al. (111) | swine | MSC | SPIO | Intramyocardial -percutaneous | Detection of tranplanted cells (25.8%) up to 3 weeks. |
| Amado et al. (112) | swine | MSC | SPIO | Intramyocardial -percutaneous | Gradual loss of intensity of the SPIO label but retection of tranplanted cells (42.4%±15) at 8 weeks. |
| Stuckey et al. (113) | rat | BMC | GFP-SPIO | Intramyocardial -direct | No improvement in LEVF. Detection of tranplanted cells up to 16 weeks confirmed by MR and immunofluorescence. |
| Amsalem et al. (43) | rat | MSC | SPIO | Intramyocardial -direct | At 4 weeks after injection, most of the transplanted labeled MSCs did not survive and their iron content was engulfed by resident macrophages. Injection of labeled or unlabeled cells attenuate ventricular dilatation and dysfunction after MI. |
| Ebert et al. (114) | mice | mESC | SPIO | Intramyocardial -direct | Detection up to 4 weeks by MRI. LVEF identical between the tranplanted group and control. |
| Terrovitis et al. (45) | rat | hCDCrCDC | SPIO | Intramyocardial -direct | Signal void persisted after 3 weeks in both syngeneic and xenogeneic cell implantation. Immunohistochemistry identifies the iron containing cells as macrophages. |
| Radionuclide | | | | | |
| Chin et al. (62) | swine | MSC | 111In-oxine | Intravenous | Significant lung activity that obscured the assessment of myocardial cell tracking. |
| Brenner et al.(63) | rat | HPC-CD34+ | 111In-oxine | Intracavitary (left ventriculum) | Impairment of cell proliferation and differentiation induced by 111In-oxine. At 96 h only 1% of radioactivity was detected in the heart. |
| Blackwood (65) | dog | BMC | 111In-tropolone | Intramyocardial -direct | Viability at day 6 after intramyocardial injection was calculated to be 75%. |

| | | | | | |
|---|---|---|---|---|---|
| Terrovitis et al. (82) | rat | rCDC | 18F-FDG | Intramyocardial -direct | Different retention values were observed at 1 h after injection of cells with normal condition (17.8%±7.3), arrested heart (75.8%±18.3), adenosine injection (35.4%±5.3) and adenosine plus fibrin glue (39.3%±11.6). |
| Mitchell et al. (66) | dog | EPC | 111In-tropolone | Intramyocardial –percutaneous | 15 days after intramyocardial injection SPECT/CT imaging demonstrated comparable degrees of retention: 57%±15 for the subepicardial injections and 54%±26 for the subendocardial injections. |
| Multimodal | | | | | |
| Terrovitis et al. | rat | rCDC | 99mTc, 124I; hNIS | Intramyocardial -direct | Detection up to 6 days after injection and their presence validated by ex vivo imaging and qPCR. |
| Qiao et al. (98) | rat | mESC | SPIO; HSV1-tk+ 18F-FHBG | Intramyocardial -direct | Increasing 18F -FHBG uptake up to 4 weeks. Most of the SPIO were contained in infiltrating macrophages at week 4. Teratoma formation. Increased LVEF. Only <0.5% of the implanted cell were cardiomyocytes. |
| Chapon et al. (115) | rat | rBMC | SPIO; 18F-FDG | Intramyocardial -direct | MRI detection of SPIO labeled cells grafted in the heart up to 6 weeks, confirmed by hystology. At 1 week increased 18 F-FDG uptake in BMC implanted heart vs control. No improvement of heart function. |
| Higuchi et al. (99) | rat | hEPC | SPIO; NIS +124I | Intramyocardial -direct | Rapid decrease of 124I uptake after day 3. Signal not detectable at day 7. MRI signal void remained unchanged throughout the follow-up period. Histology confirmed the presence of transplanted cells on day 1 but not on day 7, when iron was contained only in resident macrophages. |
| Li et al. (116) | rat | RCSC | Fluc + D-Luciferin; 18F-FDG PET; echocardiography; MRI | Intramyocardial -direct | Implanted cells detected up to 7 weeks by bioluminescence. No improvement in cardiac function assessed by 18F-FDG PET, MRI, echocardiogram and invasive hemodynamic pressure volume-analysis. |

BMC (bone marrow derived Stem Cells); MSC mesenchymal stem cells; mESC (mouse embryonic stem cells); hCDC (human cardiac derived stem cells), rCDC (rat cardiac derived stem cells); HPC (hematopoietic progenitor cells); hEPC, human Endothelial Progenitor Cells; RCSC (resident cardiac stem cells); NIS (sodium iodide symporter); Fluc (firefly luciferase); hNIS (human sodium-iodide symporter; MI, Myocardial infarction

**Table 3** What to image and how two image

| Imaging modality | Spatial resolution (mm) | Sensitivity (mol/L) | Cell Manipulation | What to image | How to image | Advantages | Disadvantages |
|---|---|---|---|---|---|---|---|
| Fluorescence Imaging | FRI: 2–3 mm; FMT: 1 mm | $10^{-9}$–$10^{-12}$ | Cells labeled with near-infrared probes (fluorochromes, Quantum dots, etc.) | Residence, homing, quantification (FMT) | Direct imaging; at NIR wavelenghts can image deep tissue | Multiplexed imaging | Not suitable for clinical translation; relatively low spatial resolution |
| Bioluminescence Imaging | 3–5 | $10^{-15}$–$10^{-17}$ | Cells transduced to express luciferase | Residence, homing, viability, differentiation, quantification | After systemic injection of D-Luciferine or Coelenterazine | Easy, high sensitivity, highthroughput, low cost; assessment of cell viability | Not suitable for clinical translation; surface imaging; relatively low spatial resolution; requires completely dark environment |
| PET | 1-2 (μPET); 6–10 (clinical PET) | $10^{-11}$–$10^{-12}$ | Cells loaded with $^{18}$F-FDG; $^{64}$Cu labeled compounds | Residence, homing, quantification | Direct imaging | High sensitivity, translational | Radiation; only short term cell tracking |
| | | | Cells transduced to express PET reporter genes (HSV1tk, HSV1-sr39tk ) | Residence, homing, differentiation, quantification | After systemic injection of correspondent radiolabeled probe ($^{18}$F-FHBG, $^{18}$F -FEAU, etc.) | High sensitivity, long term cell tracking; assessment viability | Radiation; only short term cell tracking |
| SPECT | 0.5-2 (μSPECT); 7–15 (clinical SPECT) | $10^{-10}$–$10^{-11}$ | Cells labeled with $^{99m}$Tc-, $^{111}$In-labeled compounds | Residence, homing, quantification | Direct imaging | High sensitivity, translational; assessment viability | Radiation; only short term cell tracking |

| | | | | | | | |
|---|---|---|---|---|---|---|---|
| | | | Cells transduced to express reporter genes (hNIS ) | Residence, homing, viability, differentiation, quantification, | After systemic injection of correspondent radiolabeled probe ($^{99m}$Tc, etc.) | High sensitivity, long term cell tracking | Radiation; need to transduce cells; potential immunogenicity |
| MRI | 0.01–0.1 (small animal); 0.5–1.5 (clinical) | $10^{-3}$–$10^{-5}$ | Cells labeled with Iron Oxides; Gd or Mn chelates; perfluorocarbon (19F) | Residence, homing, migration, quantification | Direct imaging | High spatial resolution; high soft tissue contrast; functional imaging | Relatively low sensitivity; long scanning times; probe dilution upon cell proliferation; persistence of SPIO after cell death (macrophage) |
| | | | Cells transduced to express MRI reporter genes β-galactosidase, transferrin receptor, ferritin, MagA and lysine-rich proteins | Residence, homing, quantification, migration, differentiation | Direct imaging or after injection of iron oxides (transferrin receptor, ferritin) | High spatial resolution; high soft tissue contrast; functional imaging; no probe dilution; | Low sensitivity; need to transduce cells; potential immunogenicity |

NIR, Near-Infra red imaging; FRI, Fluorescence reflectance imaging; FMT, Fluorescence molecular tomography

## Imaging of stem cell

The ability to image and monitor the biodistribution, viability and possibly the differentiation status of implanted SCs is of massive clinical and research benefit. All of the preclinical and clinical imaging techniques have been leveraged towards this goal; each providing unique advantages and limitations. Figure 1 illustrates the major paradigms for the labeling of SC for detection by the various imaging approaches. Table 2 reports the most important preclinical studies in the field. Table 3 summarises the most relevant features of each imaging technique.

## MRI

Magnetic resonance imaging (MRI) is a widely established technique for the evaluation of cardiac anatomy and function, often through the addition of paramagnetic contrast material (27). Taking advantage of its excellent spatial (10–100 μm [small animal MRI]); 500–1500 μm [clinical]) and temporal resolution SC labeled with superparamagnetic and paramagnetic agents can be visualised (28,29). Multispectral non-1H MR imaging (specifically 19F) has also been exploited to enable tracking of transplanted cells.

## Superparamagnetic iron oxide nanoparticles

Superparamagnetic iron oxide (SPIO) nanoparticles provide labeled cells with a large magnetic moment and are detectable by MR imaging devices or benchtop relaxometers. SPIO functions by acting as magnetic inhomogeneities, locally disturbing the magnetic field. This leads to enhanced dephasing of protons, resulting in decreased signal intensity on T2-weighted and T2*-weighted images (Figs. 2 and 3). These nanoparticles often consist of a core of iron oxide (magnetite and/or maghemite) with a polymeric or polysaccharide coating. They are widely viewed to be biocompatible, have a limited effect on cell function and can be synthesized to be biodegradable. According to their size (diameter), these are classified as ultrasmall paramagnetic iron oxide (USPIO, <10 nm), monocrystalline iron oxide particles (MION, or crosslinked CLIO; 10–30 nm), standard superparamagnetic iron oxide (SPIO; 60–150 nm) and micronsized iron oxide particles (MPIO, 0.7–1.6 μm). Of note, ferucarbotran (Resovist®; Bayer Schering Pharma, Berlin, Germany) and ferumoxides (Feridex I.V.®, Advanced Magnetic Industries, Cambridge, Maryland, USA; Endorem®, Guerbet, Gorinchem, the Netherlands) have been approved by the FDA for contrast enhanced-MRI imaging of liver tumors (30) and metastatic involvement of lymph nodes (31).
Cell uptake is mediated through the size and electrostatic charge conditions of the SPIO (32), schematically illustrated in Fig. 1a. Further, loading can be augmented through the addition of cell penetrating peptides, electroporation or transfection agents (33).
Studies reported that SPIOs do not affect cell viability, proliferation, differentiation or migration (34-38). However, recent work has raised several concerns, such as decreased MSC migration and colony-formation ability (39), and interference with cell function (40,41). A major issue beyond potential cellular effects is the question of contrast specificity to the presence of cells. Namely, the hypointense signal is maintained at a site regardless of cell viability and SPIO are present not necessarily within implanted SC at longer time points (42), but rather in phagocytosing monocytes following SC death (43). Recently, Winter et al. reported the absence of any discrimination between healthy successfully engrafted SC and dead SC phagocytosed by macrophages within the heart. In particular, no differences in signal voids up

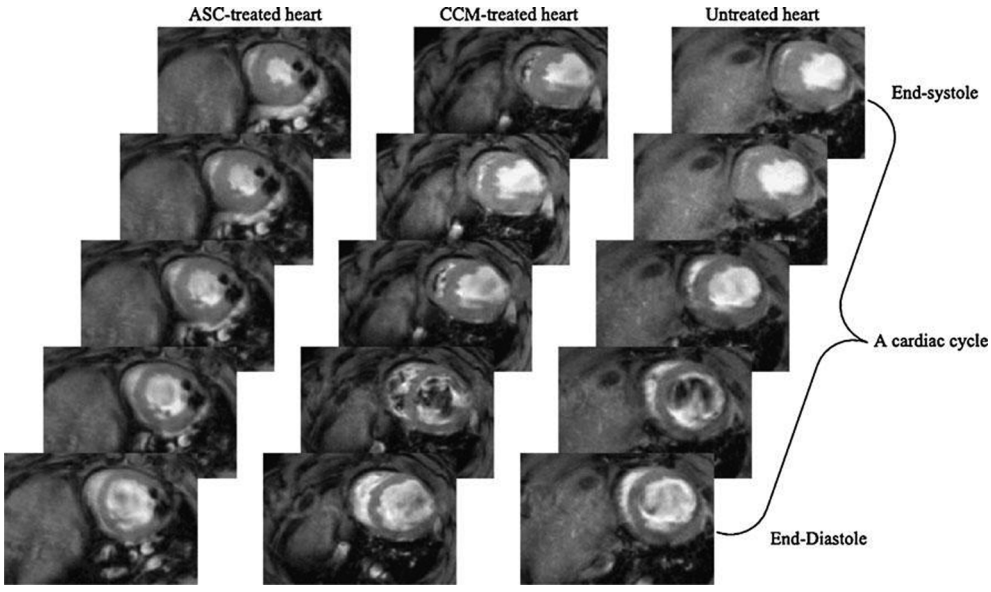


**Fig. 2** Anatomical and functional MR evaluation after transplantion of adipose-derived stem cell (ASC) and relative controls: cell culture medium (CCM), and untreated hearts. The CCM-treated and untreated hearts showed evident thinning in the anterior wall of the left ventricle. From Wang, L. et al. Am J Physiol Heart Circ Physiol 297: H1020-H1031 2009 (15) (with permission)

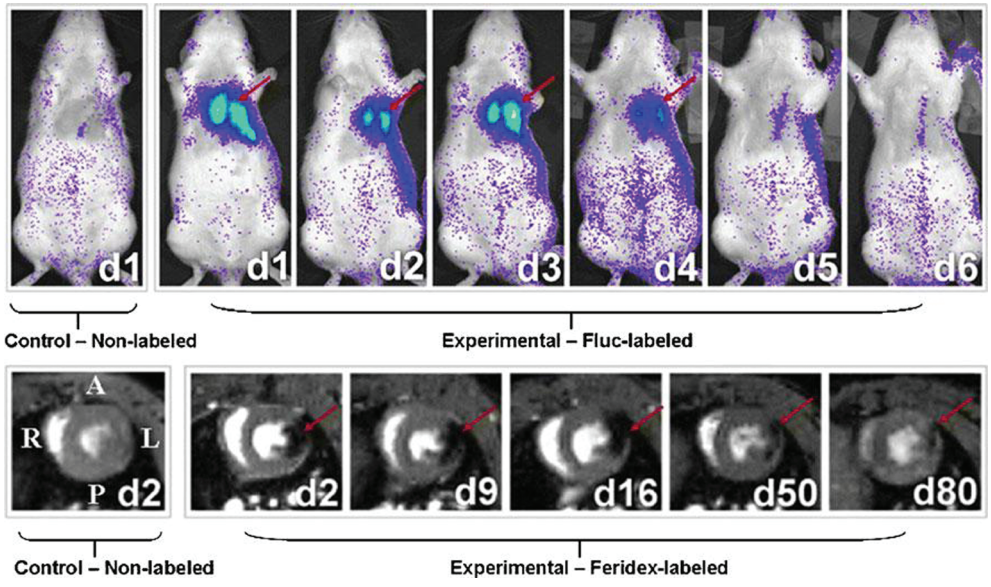


**Fig. 3** Longitudinal BLI and MRI of H9c2 cells after transplantation. BLI shows a robust distinct heart signal on day 1 (red arrow), compared to no discernable signal in a representative control rat having received non-labeled cells (top panel, left). The signal increases slightly on day 3 but decreases rapidly to near background levels by day 6. MRI imaging of a representative rat injected with the same amount of cells labeled with Feridex shows a large hypointense signal (red arrow) in the anterolateral wall of the myocardium. The size of the signal decreases slightly over time, and the signal persists for at least 80 days post cell injection. No signal is observed in control rat that received non-labeled cells (bottom panel, left) Chen, I. Y et al. Mol Imaging Biol. 2009 May-Jun;11:178–87. (42) (with permission)

to more than 40 days were observed with dead and viable cells recipient with respect to size, number and localisation (44). Similarly, it has been demonstrated that MRI overestimates the SPIO labeled SC survival after transplantation in the heart (45). Furthermore, SPIO-induced hypointensity can sometimes be difficult to interpret because it may be obscured by the presence of endogenous blood derivates, such as hemosiderin (46). The clinical translation of SPIO for cell tracking is further reduced now that ferumoxides (Feridex® or Endorem®) are no longer available in the USA and Europe. However, the use of iron oxides approaches should not be discouraged as they provide very high sensitivities. New compounds with improved tissue clearance properties (therefore higher specificities) are awaited from material sciences research.

## Paramagnetic ions

Cell labeling with "positive contrast" such as gadolinium (Gd) chelates and manganese (Mn) chloride compounds allow the visualisation of SC as hyperintense signal on T1-weighted images. Internalization of Gd can be accomplished by exposure of cells to Gd chelates or through the use of liposomal formulations (33). MRI sensitivity in the detection of Gd-labeled cells is lower compared to SPIO-labeled cells and is dependent upon contrast behaviour and relaxivity in the cellular compartment (endosomes) in which they are localised (47,48). This is a result of the reduced water accessibility to chelated ions following intracellular concentration, resulting in decreased relaxivity. To overcome these issues several approaches have been considered to drive the endosomal escape of paramagnetic compounds (49). Furthermore, safety issues might be related to the rapid dechelation of compounds at the low pH of lysosomes and endosomes raising concerns related to free Gd3+ ions (50).
Sub-millimolar concentrations of Mn chloride (MnCl2) have been sufficient to enable SC labeling and detection for both in vitro and in vivo MR, with no detectable toxicity. Also in the same study the potential of MnCl2 labeling in the assessment of SC viability by T1 and T2 mapping was investigated in in vitro studies (51). Mn-oxide nanoparticles have recently been used to label and track implanted glioma cells. Of considerable interest, the feasibility of successfully tracking two cell populations simultaneously has been suggested, where one is labeled with Mn-Oxide and the other with SPIOs (52). These and other paramagnetic ion techniques offer the hope that positive contrast approaches will enable sensitive MR tracking of SC in vivo. Novel nanotechnology approaches are becoming available for stem cell tracking such as gadolinium-containing carbon nanocapsules (Gadonanotubes), whose T1 relaxivity is greater than that of any known material to date (outperforming clinically available Gd-based contrast agents by 40-fold) (53). They will definitely play a role in the future of imaging sciences as soon as their toxicity profiles, currently under investigation, have been clarified.

## 19F MR

Similar to the imaging of relaxation of 1H from water, 19F can be used as the basis of the signal for MR spectroscopy and image formation. While this technique is not implemented widely in the clinic, there are unique advantages to fluorine-MR that make it an attractive option for SC tracking in myocardial applications. 19F is not present naturally in soft tissues therefore its signal is exclusively derived from the exogenous contrast agent applied, be it a perfluorocarbon particle or fluorinated nucleosides (54). 19F MRI can be used with existing 1H imaging hardware since 19F and 1H gyromagnetic ratios differ by only 6%.
Importantly, 19F signal can be overlaid on 1H-MR anatomical images for a highly selective, high-resolution map of cell transplantation. This technique allows for quantitative determination of the cell population (55). A perfluorocarbon particle loaded cell scheme has been

used to show the unequivocal and unique signature for SC, enabling spatial cell localization via19F-MRI and quantitation via 19F-spectroscopy (56). Perfluorocarbons have been extensively studied and used as blood substitutes, therefore their toxicity profiles are known. 19F cell tracking has attracted interest, but is still at an early stage of development. It should be noted that this method does suffer from the drawback of lower sensitivity requiring longer imaging times. Efforts are underway to address these deficits including imaging hardware, imaging sequences, and label improvement and 19F MR imaging is expected to play a role in cell tracking in the future (54).

## Radionuclide imaging

Imaging of SC has also taken advantage of the high sensitivity ($10^{-10}$–$10^{-12}$ mol/L vs $10^{-3}$–$10^{-5}$ mol/L of MRI) and quantitative (acute cell retention as a percentage of the net injected dose per weight, [%ID/g]) characteristics of radionuclide imaging (57). However, PET and particularly SPECT have inferior spatial resolution (1–2 mm) compared with MRI. Moreover, radionuclide-labeled cells can only be visualised as long as the radioactivity is still detectable (e.g. $^{18}$F: 110 min; $^{111}$In: 2.8 days; $^{99m}$Tc: 6 h). This sets an appreciable limitation on the radioisotopes direct labeling value for medium- and long-term SC transplant monitoring. SPECT has been largely used to investigate the short-term fate of transplanted cells labeled with radioactive compounds such as $^{111}$In-oxine (58-63), $^{99m}$Tc-hexamethylprophylene amine oxine (HMPAO) (64) or $^{111}$In-tropolone (65,66). A persistent limitation for deployment of SPECT is that in order to generate useful (quantitative) images within a reasonable time frame, the administration of relatively large doses of radioactivity are required. This poses the concern of inherent radiation damage (reduced viability and proliferation). In the case of $^{111}$In, Auger electrons are also emitted leading to adverse biological effects in very short distances (from the nm to μm range). Brenner et al., demonstrated that despite the homing of progenitor cells into the infarction area, cell labeling with $^{111}$In-oxine impairs significantly the viability, proliferation and differentiation at 48 h after implantation (63). Similar results were observed after exposure of murine haematopoietic progenitor cells at even much lower levels of radioactivity (67). The use of other compounds, such as $^{111}$In-tropolone, inhibited cell proliferation 3 days after labeling (68). To abrogate these effects, it has been suggested that only a fraction of the SC population be labeled (69). Regardless of the method used, very few studies have reported the absence of any cell function impairment (58,62). These studies underline the need for further in vitro studies considering different SC, exposed to different activities and importantly following the same labeling protocol.

Positron emission tomography (PET) has been regarded as having higher sensitivity (2 to 3 orders of magnitude) and better spatial and temporal resolution than SPECT (70). 18F-Fluorodeoxyglucose (18F-FDG) has been used for cell labeling and short term imaging in preclinical (71) and clinical settings

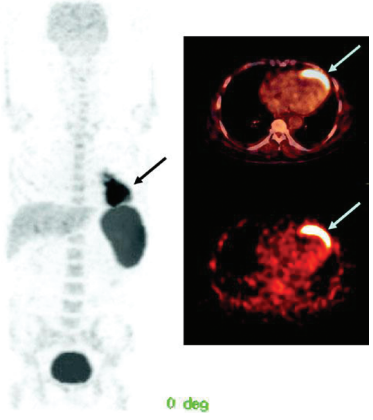


**Fig. 4** PET/CT images of a patient with history of anterior wall infarction. After percutaneous intervention 18 F-FDG labeled cells were implanted via intracoronary catheter and images obtained at 2 hrs after the procedure. Total amount of SC at the injection site was measured (2.1% of injected dose). From Kang et al. J Nucl Med 2006; 47:1295–1301. (73) (with permission)

(Fig. 4) (72,73). After intracoronary injection all stem cells showed poor engraftment regardless of cell type and number of implanted cells (61,72,73). In all cases intravenous injection of SC did not show detectable homing of cells to the myocardium (72,73).
Augmenting the higher sensitivity, the wider availability of hybrid PET-CT systems allows for a combination of anatomical non-invasive coronary angiography and cell tracking. This multimodal imaging capability and clinical availability are tempered somewhat by the the short half-life of 18F. Isotopes with longer half-life, such as 64Cu (12.7 h) have been suggested (74). However, with radionuclide based techniques pursued so far, only the immediate fate of transplanted stem cells can be interrogated.

## Reporter genes

Reporter gene approaches have significant potential to reveal insights into the mechanisms and fate of SC therapies. The reporter gene paradigm requires often the appropriate combination of reporter transgene and a reporter probe, such that the reporter gene product has to interact with an imaging probe (optical, nuclear, magnetic) and when this event occurs the signal may be detected and quantified with the corresponding imaging technique (Fig. 1c).
Several advantages of reporter gene approaches have been described (75). Namely, this system identifies with exquisite specificity only viable cells (which actively contain the gene product) and allows long term tracking of transduced SC (circumventing issues of probe dilution with cellular proliferation). Reporter genes can be designed as "constitutive" whose signal is "always turned on" (suitable for the evaluation of transplantation, migration and proliferation of stably transduced SC) or "inducible" reporter gene which is activated and regulated by specific endogenous transcription factors and promoters (75,76) providing a non-invasive readout of information regarding SC differentiation.
The most widely used reporter gene for radiotracer based imaging is HSV1-tk (Herpes simplex virus type 1 thymidine kinase) and its mutant, the HSV1-sr39tk. Unlike mammalian TK1, this enzyme efficiently phosphorylates purine and pyrimidine analogues which results in trapping and accumulation of these ligands. It has been successfully used in association with 18F or 124I -2′-deoxy-2′-fluoro-5-iodo-1-[β]-D-arabinofuranosyluracil (18F-FIAU and 124I-FIAU), 18F 2′-fluoro-5-ethyl-1-[β]-D-arabinofuranosyluracil (18F-FEAU), and 9-(4-[18F]fluoro-3-hydroxymethylbutyl) guanine (18F-FHBG) (75,77). Wu et al., pioneered the reporter gene approach in the heart by imaging in vivo transplanted cells (expressing luciferase or HSV1-sr39tk) up to 2 weeks by 18F-FHBG PET imaging or BLI (78). Furthermore, Cao et al., reported survival and proliferation (through increasing signal up to 4 weeks) of murine ES stably transduced with a triple fusion reporter gene, enabling simultaneous PET, bioluminescence and fluorescence imaging (79). Despite the advantage of signal amplification (through probe phosphorylation and accumulation within cells) of HSV-tk based approaches, its immunogenicity might limit use in humans (80). To overcome this limitation, the human mitochondrial thymidine kinase type 2 (hTK2) have been proposed (81). An alternative is the sodium iodide symporter (51) as a PET and SPECT reporter gene used in conjunction with $^{124}$I or $^{99m}$Tc (pertechnetate), respectively (75,82). Here, despite the lack of probe/signal amplification observed in receptor- and transporter-based techniques (as $^{124}$I or $^{99m}$Tc are free to diffuse out of the cells), hNIS is not immunogenic (since it is expressed in the thyroid, stomach salivary gland, choroid plexus but not in the heart) and does not require complex radiosynthesis of the probes. Nevertheless, in reporter gene approach for the imaging of SC-based cardiac therapy several important issues remain. First, the non-physiological expression of reporter gene proteins may perturb the critical SC cellular and therapeutic functions. To be fully reliable, this system has to guarantee the long term expression of the reporter gene in

the proliferating population. Adenoviral transfection is hampered by episomal gene expression (the reporter gene is not integrated in the chromatin, and because they are not replicating, they become diluted with cell proliferation) and by immunogenicity (leakiness of immunogenic adenoviral proteins that can lead to an immune response) (83). On the other hand, lentiviral vectors accomplish the integration of the reporter gene in the host cell chromatin allowing stable expression in dividing cells (84) and circumventing immunogenicity (85). Even when lentiviral vectors are used however, transgene expression can be silenced by DNA methylation especially when strong promoters, such as CMV, are used to drive the expression of the reporter gene (86). The integration of the reporter gene within the genome has raised concerns about the risk of mutagenesis and potential oncogenicity (87).
The imaging of differentiation in vivo was recently investigated by Kammili et al., by employing a novel dual-reporter mouse embryonic SC line. Here, enhanced yellow fluorescent protein (EYFP) was used as a "constitutive reporter", and the firefly luciferase reporter as an "inducible reporter". This latter gene was under the control of the cardiac sodium-calcium exchanger 1 (Ncx1) promoter which showed increased activity upon differentiation of SC into beating cardiomyocytes (76).
Several candidates have been proposed as MRI reporter genes such as β-galactosidase, transferrin receptor, ferritin, MagA and lysine-rich proteins (88,89). Recently, SM engineered to express ferritin have been transplanted in infarcted heart and detected (as decreased signal up to 25%) up to 3 weeks (90). Several studies have been reported with the application of MR reporters, however, none of these strategies have led to a significant number of follow-up studies. This is due to the low sensitivity of MRI for imaging of gene activity in vivo.

## Optical imaging

### BLI

In contrast to the immediate clinical impact of magnetic and nuclear tomographic imaging, optical imaging techniques such as bioluminescence, planar and fluorescence-mediated tomography have been largely restricted to use in preclinical models. Bioluminescence imaging is commonly used for cell tracking in SC transplantation studies (78,79,91) (Figs. 3 and 5). SC are transduced with a luciferase gene and implanted in the recipient animal. Following injection, the probe (D-Luciferin) is oxidized only in the cells expressing luciferase in presence of ATP, O2 and Mg2+ resulting in light photons being emitted (which can be detected by ultrasensitive charge-coupled device [CCD] cameras). BLI has many advantages: it is highly sensitive, quantitative, simple and inexpensive. However, the barrier to clinical translation lies in the inherent limitations imposed by poor tissue penetration (1–2 cm) (allowing only surface imaging), high rates of scattering of visible wavelength photons on the human scale and low resolution (3–5 mm) (which hamper the exact evaluation of the exact location of the cells) (57).

### Fluorescence

Direct labeling of SC with fluorescent probes for visualisation in vitro and in vivo has been fueled by the availability of near infrared (NIR) probes, as their spectral properties are matched to lower tissue attenuation in the so-called NIR-window. This provides greater signal penetration of tissue through reduced light absorption and tissue scattering. Therefore they have clinical potential, however limited to near-surface or intraoperative imaging stem cell tracking. Near infrared imaging provides high sensitivity as well as tomographic capabilities and there is no evidence at present that dyes released after cell death are taken up by macrophages. Intra-

coronary delivery of MSC labeled with the NIR dye IR-786 has been successfully tracked in a swine model of myocardial infarction and sensitivity of 10.000 cells has been reported (92). Quantum dots (QD) are a class of inorganic, fluorescent nanoparticles that have been successfully used to label SC. Biocompatibility of QD at low concentrations has been demonstrated

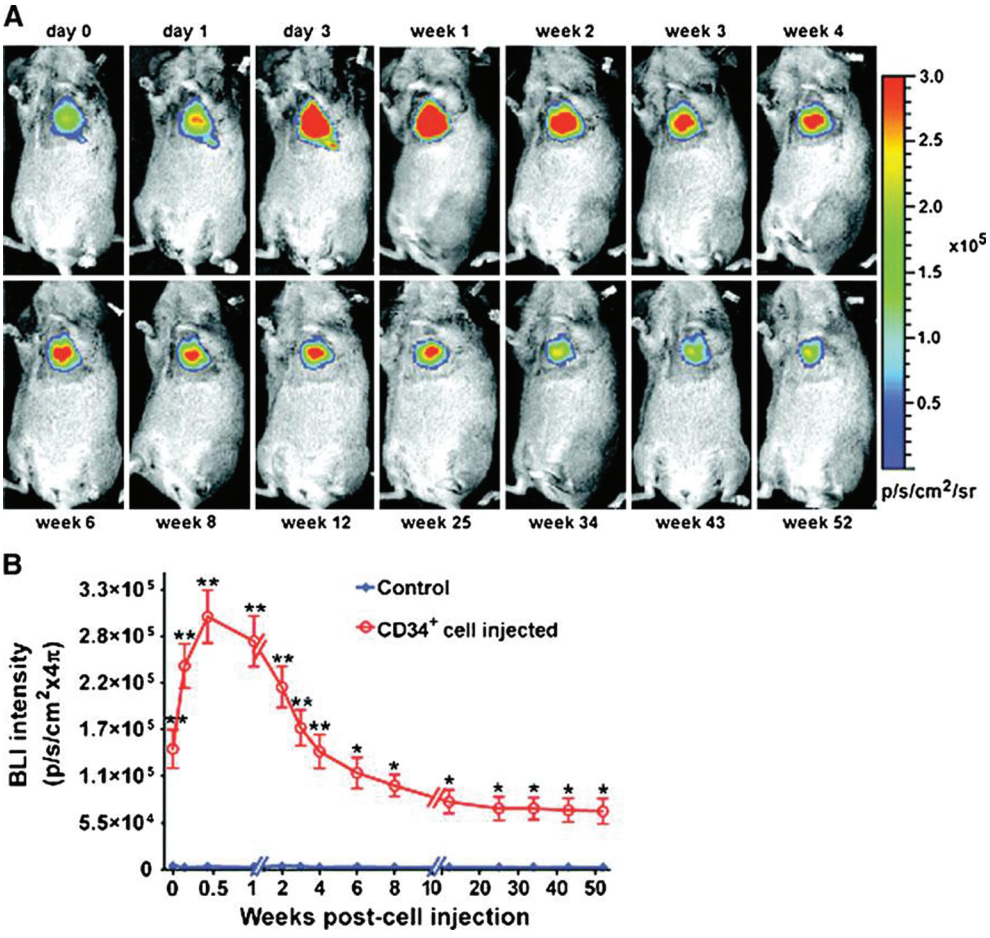


**Fig. 5** Bioluminescence imaging of CD34+ cells expressing the TGL gene (HSV1-tk, e-GFP, f-luc) and implanted in the heart of a SCID mouse. Systemically administered luciferin is activated (oxidized by luciferase) in the injected cells. Here we see follow- up of implanted cells up to 52 weeks post-implantation. Measurement of emitted light in CD34+ implants is higher than in controls (PBS injection). From Wang, J. et al. Circ Res 2010;106:1904–1911. (91) (with permission)

in vitro in MSC cultures (93) and the absence of adverse effects on cell viability, proliferation or differentiation reported (94). One of the most attractive qualities of these nanoparticles is their capacity for multiplexed imaging. The tracking of different cell populations is concurrently achieved by labeling cells with different QDs. Multiplex optical imaging of QD-labeled embryonic stem cells have been reported up to 14 days from injection in mice (94). Moreover, it has been shown that single QD-MSC can be detected in histological sections for at least 8 weeks after delivery (95). The long-term effects on SC functionality are still unknown, however

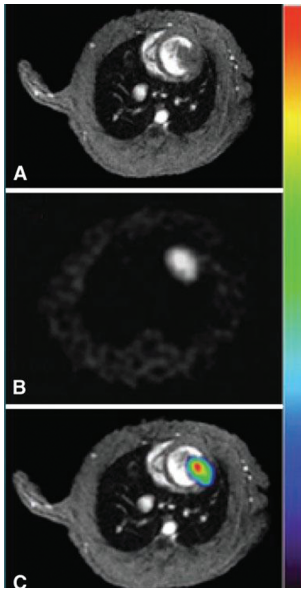


**Fig. 6** Co-registration of MRI **A** and $^{18}$ F-FHBG PET **B** of murine ESC transduced with HSV1-sr39tk and passively labeled with SPIO. Images depict the presence and tracking of SC 14 days after transplantation. This hybrid imaging **C** approach leverages the advantages of each technique; the fine anatomical resolution of MR and the specificity of nuclear imaging. From Qiao et al. Radiology 250:3, 821–829. (98) (with permission)

concerns are related to their metallic core include its exposure or dissolution which may result in toxicity, particularly from heavy metals such as Pb, Cd and Se (96,97).

## Multimodal imaging

The possibility of complementing the sensitivity of radio-nuclide or optical techniques with the high-resolution anatomical information from MRI is a key player in the clinical and research future of SC tracking. To date, the most interesting approach has been to develop transgenic cells that carry an optical/nuclear imaging reporter together with passive labeling with MRI contrast agents before administration. Qiao et al. assessed the survival and proliferation of SPIO-labeled murine ESC transduced with HSV1-sr39tk longitudinally (4 weeks) following injection into the healthy or infarcted myocardium. ESCs grafted and underwent proliferation, as shown by increasing uptake of 18F-FHBG in PET (Fig. 6) and decreasing the size of MR hypointense areas due to SPIO dilution. Interestingly at week 4 the majority of SPIO labels (released upon cell death) were phagocytized and contained in infiltrating macrophages rather than the ESC. Despite teratoma formation, a slight increase in left ventricular ejection fraction in ESC-treated animals was observed, mainly as a result of paracrine effects, as cardiac differentiation of implanted ESC was less than 0.5% (98). In a similar study human EPC derived from CD34+

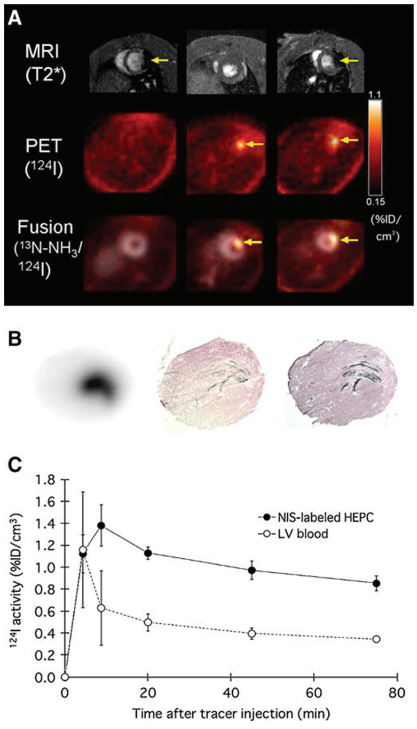


**Fig. 7 A** MRI (upper row), 124I-PET (middle row), and fusion images 13 N-NH3 (gray scale)/ 124I (colour scale) (bottom row) of rat heart 1 day after injection of EPC labeled with iron (left), NIS only (middle), or both iron and NIS (right). Signal void of iron-labeled HEPCs is observed by MRI whereas HEPCs expressing NIS showed focal $^{124}$I accumulation by PET. **B** Consecutive myocardial sections showing the presence of transplanted cells: autoradiography for $^{124}$I uptake mediated by NIS reporter (left), X-galactosidase staining for LacZ gene expression of graft cells (middle), and Prussian blue staining for iron particle detection (right). **C** Mean±SD time–activity curves after $^{124}$I administration of transplanted cell and left ventricular blood measured by PET. From Higuchi T et al. J Nucl Med, 50:1088– 1094. (99) (with permission)

mononuclear cells of umbilical cord blood were transduced with NIS reporter gene and labeled with SPIOs. Rapid loss of viable grafted cells was observed, as 124I PET accumulation decreased below detection limit at 3 days after transplant. However, MRI signal void resulting from SPIO persisted, corresponding to retention of SPIOs within macrophages after graft cells' death (Fig. 7) (99). Triple fusion reporter gene have been widely applied for multimodality fluorescence, bioluminescence and nuclear imaging approaches (100). Recently, in a quadmodal optical, PET, CT and MRI coregistration approach CD34+ cells were transduced with a triple fusion reporter gene (e-GFP, f-Luc and HSV1-tk). Bioluminescence imaging revealed that cells persisted in the heart up to 12 months and MRI studies reported improvement in the left ventricular ejection fraction was preserved up to 6 months (Fig. 5) (91).

## Conclusion

Many of the approaches to image stem cells are promising but further work is required before a wide clinical translation becomes reality. Beyond the unresolved safety and ethical issues, crucial questions: "What is the best route for cell delivery?" "What kind and how many cells?" and "When to inject?" remain.
It has become clear that there is no single 'best method' in cell tracking. Rather there is an array of high sensitivity, high spatial resolution and functional techniques that work best in combination. The persistent trends in molecular imaging are: to focus on the development of novel MR-compatible probes able to monitor and track with sufficient sensitivity and specificity the fate of transplanted cells, new PET/SPECT reporter genes with lessened immunogenicity and oncogenicity issues, and the application of related radioprobes with better pharmacokinetic profiles.

## Acknowledgements

This article has been supported in part by the ENCITE (funded by the European Community under the 7th Framework program) and by the NIH R25T CA096945.

# References


1. Orlic D, Kajstura J, Chimenti S et al (2001) Bone marrow cells regenerate infarcted myocardium. Nature 410:701–705.
2. Strauer BE, Brehm M, Zeus T et al (2002) Repair of infarcted myocardium by autologous intracoronary mononuclear bone marrow cell transplantation in humans. Circulation 106:1913–1918
3. Abdel-Latif A, Bolli R, Tleyjeh IM et al (2007) Adult bone marrow-derived cells for cardiac repair: a systematic review and meta-analysis. Arch Intern Med 167:989–997.
4. Lipinski MJ, Biondi-Zoccai GG, Abbate A et al (2007) Impact of intracoronary cell therapy on left ventricular function in the setting of acute myocardial infarction: a collaborative systematic review and meta-analysis of controlled clinical trials. J Am Coll Cardiol 50:1761–1767.
5. Martin-Rendon E, Brunskill SJ, Hyde CJ, Stanworth SJ, Mathur A, Watt SM (2008) Autologous bone marrow stem cells to treat acute myocardial infarction: a systematic review. Eur Heart J 29:1807–1818.
6. Korf-Klingebiel M, Kempf T, Sauer T et al (2008) Bone marrow cells are a rich source of growth factors and cytokines: implications for cell therapy trials after myocardial infarction. Eur Heart J 29:2851–2858.
7. Taylor DA, Atkins BZ, Hungspreugs P et al (1998) Regenerating functional myocardium: improved performance after skeletal myoblast transplantation. Nat Med 4:929–933
8. Menasche P, Alfieri O, Janssens S et al (2008) The Myoblast Autologous Grafting in Ischemic Cardiomyopathy (MAGIC) trial: first randomized placebo-controlled study of myoblast transplantation. Circulation 117:1189–1200.
9. Yoon YS, Wecker A, Heyd L et al (2005) Clonally expanded novel multipotent stem cells from human bone marrow regenerate myocardium after myocardial infarction. J Clin Invest 115:326–338.
10. Balsam LB, Wagers AJ, Christensen JL, Kofidis T, Weissman IL, Robbins RC (2004) Haematopoietic stem cells adopt mature haematopoietic fates in ischaemic myocardium. Nature 428:668–673.
11. Murry CE, Soonpaa MH, Reinecke H et al (2004) Haematopoietic stem cells do not transdifferentiate into cardiac myocytes in myocardial infarcts. Nature 428:664–668.
12. Ferrari G, Cusella-De Angelis G, Coletta M et al (1998) Muscle regeneration by bone marrow-derived myogenic progenitors. Science 279:1528–1530
13. Quevedo HC, Hatzistergos KE, Oskouei BN et al (2009) Allogeneic mesenchymal stem cells restore cardiac function in chronic ischemic cardiomyopathy via trilineage differentiating capacity. Proc Natl Acad Sci USA 106:14022–14027.
14. Polascik TJ, Manyak MJ, Haseman MK et al (1999) Comparison of clinical staging algorithms and 111indium-capromab pendetide immunoscintigraphy in the prediction of lymph node involvement in high risk prostate carcinoma patients. Cancer 85:1586–1592.
15. Wang L, Deng J, Tian Wet al (2009) Adipose-derived stem cells are an effective cell candidate for treatment of heart failure: an MR imaging study of rat hearts. Am J Physiol Heart Circ Physiol 297:H1020–H1031.
16. Schachinger V, Assmus B, Britten MB et al (2004) Transplantation of progenitor cells and regeneration enhancement in acute myocardial infarction: final one-year results of the TOPCAREAMI Trial. J Am Coll Cardiol 44:1690–1699.
17. Beltrami AP, Barlucchi L, Torella D et al (2003) Adult cardiac stem cells are multipotent and support myocardial regeneration. Cell 114:763–776
18. Dawn B, Stein AB, Urbanek K et al (2005) Cardiac stem cells delivered intravascularly traverse the vessel barrier, regenerate infarcted myocardium, and improve cardiac function. Proc Natl Acad Sci USA 102:3766–3771.
19. Laflamme MA, Chen KY, Naumova AV et al (2007) Cardiomyocytes derived from human embryonic stem cells in pro-survival factors enhance function of infarcted rat hearts. Nat Biotechnol 25:1015–1024.
20. Li Z, Wu JC, Sheikh AY et al (2007) Differentiation, survival, and function of embryonic stem cell derived endothelial cells for ischemic heart disease. Circulation 116(Suppl):I46–I54.
21. Swijnenburg RJ, Schrepfer S, Cao F et al (2008) In vivo imaging of embryonic stem cells reveals patterns of survival and immune rejection following transplantation. Stem Cells Dev 17:1023–1029.
22. Nussbaum J, Minami E, Laflamme MA et al (2007) Transplantation of undifferentiated murine embryonic stem cells in the heart: teratoma formation and immune response. FASEB J 21:1345–1357.

23. Yu J, Vodyanik MA, Smuga-Otto K et al (2007) Induced pluripotent stem cell lines derived from human somatic cells. Science 318:1917–1920.
24. Zwi L, Caspi O, Arbel G et al (2009) Cardiomyocyte differentiation of human induced pluripotent stem cells. Circulation 120:1513–1523.
25. Nelson TJ, Martinez-Fernandez A, Yamada S, Perez-Terzic C, Ikeda Y, Terzic A (2009) Repair of acute myocardial infarction by human stemness factors induced pluripotent stem cells. Circulation 120:408–416.
26. Kocher AA, Schuster MD, Szabolcs MJ et al (2001) Neovascularization of ischemic myocardium by human bone-marrow-derived angioblasts prevents cardiomyocyte apoptosis, reduces remodeling and improves cardiac function. Nat Med 7:430–436.
27. Karamitsos TD, Francis JM, Myerson S, Selvanayagam JB, Neubauer S (2009) The role of cardiovascular magnetic resonance imaging in heart failure. J Am Coll Cardiol 54:1407–1424.
28. Chen IY, Wu JC Cardiovascular molecular imaging: focus on clinical translation. Circulation 123:425–443.
29. Kiessling F (2008) Noninvasive cell tracking. Handb Exp Pharma-col (185 Pt 2):305–321.
30. Semelka RC, Helmberger TK (2001) Contrast agents for MR imaging of the liver. Radiology 218:27–38.
31. Harisinghani MG, Barentsz J, Hahn PF et al (2003) Noninvasive detection of clinically occult lymph-node metastases in prostate cancer. N Engl J Med 348:2491–2499.
32. Thorek DLJ, Tsourkas A (2008) Size, charge and concentration dependent uptake of iron oxide particles by non-phagocytic cells. Biomaterials 29:3583–3590.
33. Bernsen MR, Moelker AD, Wielopolski PA, van Tiel ST, Krestin GP Labelling of mammalian cells for visualisation by MRI. Eur Radiol 20:255–274.
34. Arbab AS, Pandit SD, Anderson SA et al (2006) Magnetic resonance imaging and confocal microscopy studies of magnetically labeled endothelial progenitor cells trafficking to sites of tumor angiogenesis. Stem Cells 24:671–678.
35. Hsiao JK, Chu HH, Wang YH et al (2008) Macrophage physiological function after superparamagnetic iron oxide labeling. NMR Biomed 21:820–829.
36. Delcroix GJ, JacquartM, Lemaire L et al (2009)Mesenchymal and neural stem cells labeled with HEDP-coated SPIO nanoparticles: in vitro characterization and migration potential in rat brain. Brain Res 1255:18–31.
37. Farrell E, Wielopolski P, Pavljasevic P et al (2009) Cell labelling with superparamagnetic iron oxide has no effect on chondrocyte ehaviour. Osteoarthr Cartil 17:961–967.
38. Magnitsky S, Walton RM, Wolfe JH, Poptani H (2008) Magnetic resonance imaging detects differences in migration between primary and immortalized neural stem cells. Acad Radiol 15:1269–1281.
39. Schafer R, Kehlbach R, Muller M et al (2009) Labeling of human mesenchymal stromal cells with superparamagnetic iron oxide leads to a decrease in migration capacity and colony formation ability. Cytotherapy 11:68–78
40. Yang J-X, Tang W-L, Wang X-X (2010) Superparamagnetic iron oxide nanoparticles may affect endothelial progenitor cell migration ability and adhesion capacity. Cytotherapy 12:251–259
41. Kostura L, Kraitchman DL, Mackay AM, Pittenger MF, Bulte JWM (2004) Feridex labeling of mesenchymal stem cells inhibits chondrogenesis but not adipogenesis or osteogenesis. NMR Biomed 17:513–517
42. Chen I, Greve J, Gheysens O et al (2009) Comparison of optical bioluminescence reporter gene and superparamagnetic iron oxide MR contrast agent as cell markers for noninvasive imaging of cardiac cell transplantation. Mol Imaging Biol 11:178–187
43. Amsalem Y, Mardor Y, Feinberg MS, et al (2007) Iron-Oxide Labeling and Outcome of Transplanted Mesenchymal Stem Cells in the Infarcted Myocardium. Circulation 116(suppl):I-38-45.
44. Winter EM, Hogers B, van der Graaf LM, Gittenberger-de Groot AC, Poelmann RE, van der Weerd L Cell tracking using iron oxide fails to distinguish dead from living transplanted cells in the infarcted heart. Magn Reson Med 63:817–821.
45. Terrovitis J, Stuber M, Youssef A et al (2008) Magnetic resonance imaging overestimates ferumoxide-labeled stem cell survival after transplantation in the heart. Circulation 117:1555-1562.
46. van den Bos EJ, Baks T, Moelker AD et al (2006) Magnetic resonance imaging of haemorrhage within reperfused myocardial infarcts: possible interference with iron oxide-labelled cell tracking? Eur Heart J 27:1620–1626

47. Brekke C, Morgan SC, Lowe AS et al (2007) The in vitro effects of a bimodal contrast agent on cellular functions and relaxometry. NMR Biomed 20:77–89.
48. Aime S, Castelli DD, Crich SG, Gianolio E, Terreno E (2009) Pushing the sensitivity envelope of lanthanide-based magnetic resonance imaging (MRI) contrast agents for molecular imaging applications. Acc Chem Res 42:822–831.
49. Gianolio E, Arena F, Strijkers GJ, Nicolay K, Hogset A, Aime S Photochemical activation of endosomal escape of MRI-Gd-agents in tumor cells. Magn Reson Med.
50. Bulte JW (2009) In vivo MRI cell tracking: clinical studies. AJR Am J Roentgenol 193:314–325.
51. Yamada M, Gurney PT, Chung J et al (2009) Manganeseguided cellular MRI of human embryonic stem cell and human bone marrow stromal cell viability. Magn Reson Med 62:1047–1054.
52. Gilad AA, Walczak P, McMahon MT et al (2008) MR tracking of transplanted cells with "positive contrast" using manganese oxide nanoparticles. Magn Reson Med 60:1–7.
53. Tran LA, Krishnamurthy R, Muthupillai R, et al. Gadonanotubes as magnetic nanolabels for stem cell detection. Biomaterials 31:9482–9491.
54. Srinivas M, Heerschap A, Ahrens ET, Figdor CG, de Vries IJ (2010) (19)F MRI for quantitative in vivo cell tracking. Trends Biotechnol 28:363–370.
55. Srinivas M, Morel PA, Ernst LA, Laidlaw DH, Ahrens ET (2007) Fluorine-19 MRI for visualization and quantification of cell migration in a diabetes model. Magn Reson Med 58:725–734
56. Partlow KC, Chen J, Brant JA et al (2007) 19F magnetic resonance imaging for stem/progenitor cell tracking with multiple unique perfluorocarbon nanobeacons. FASEB J 21:1647–1654.
57. Massoud TF, Gambhir SS (2003) Molecular imaging in living subjects: seeing fundamental biological processes in a new light. Genes Dev 17:545–580.
58. Aicher A, Brenner W, Zuhayra M et al (2003) Assessment of the tissue distribution of transplanted human endothelial progenitor cells by radioactive labeling. Circulation 107:2134–2139.
59. Barbash IM, Chouraqui P, Baron J et al (2003) Systemic delivery of bone marrow-derived mesenchymal stem cells to the infarcted myocardium: feasibility, cell migration, and body distribution. Circulation 108:863–868.
60. Hou D, Youssef EA, Brinton TJ et al (2005) Radiolabeled cell distribution after intramyocardial, intracoronary, and interstitial retrograde coronary venous delivery: implications for current clinical trials. Circulation 112(9 Suppl):I150–I156.
61. Schachinger V, Aicher A, Dobert N et al (2008) Pilot trial on determinants of progenitor cell recruitment to the infarcted human myocardium. Circulation 118:1425–1432.
62. Chin BB, Nakamoto Y, Bulte JW, Pittenger MF, Wahl R, Kraitchman DL (2003) 111In oxine labelled mesenchymal stem cell SPECT after intravenous administration in myocardial infarction. Nucl Med Commun 24:1149–1154.
63. Brenner W, Aicher A, Eckey T et al (2004) 111In-labeled CD34+hematopoietic progenitor cells in a rat myocardial infarction model. J Nucl Med 45:512–518.
64. Penicka M, Lang O, Widimsky P et al (2007) One-day kinetics of myocardial engraftment after intracoronary injection of bone marrow mononuclear cells in patients with acute and chronic myocardial infarction. Heart 93:837–841.
65. Blackwood KJ, Lewden B, Wells RG et al (2009) In vivo SPECT quantification of transplanted cell survival after engraftment using (111)In-tropolone in infarcted canine myocardium. J Nucl Med 50:927–935.
66. Mitchell AJ, Sabondjian E, Sykes J, et al. Comparison of initial cell retention and clearance kinetics after subendocardial or subepicardial injections of endothelial progenitor cells in a canine myocardial infarction model. J Nucl Med 51:413–417.
67. Nowak B, Weber C, Schober A et al (2007) Indium-111 oxine labelling affects the cellular integrity of haematopoietic progenitor cells. Eur J Nucl Med Mol Imaging 34:715–721.
68. Yoon JK, Park BN, Shim WY, Shin JY, Lee G, Ahn YH In vivo tracking of 111In-labeled bone marrow mesenchymal stem cells in acute brain trauma model. Nucl Med Biol 37:381–388.
69. Gholamrezanezhad A, Mirpour S, Ardekani JM et al (2009) Cytotoxicity of 111In-oxine on mesenchymal stem cells: a timedependent adverse effect. Nucl Med Commun 30:210–216.

70. Rahmim A, Zaidi H (2008) PET versus SPECT: strengths, limitations and challenges. Nucl Med Commun 29:193–207.
71. Doyle B, Kemp BJ, Chareonthaitawee P et al (2007) Dynamic tracking during intracoronary injection of 18F-FDG-labeled progenitor cell therapy for acute myocardial infarction. J Nucl Med 48:1708–1714.
72. Hofmann M, Wollert KC, Meyer GP et al (2005) Monitoring of bone marrow cell homing into the infarcted human myocardium. Circulation 111:2198–2202.
73. Kang WJ, Kang HJ, Kim HS, Chung JK, Lee MC, Lee DS (2006) Tissue distribution of 18F-FDG-labeled peripheral hematopoietic stem cells after intracoronary administration in patients with myocardial infarction. J Nucl Med 47:1295–1301
74. Adonai N, Nguyen KN, Walsh J et al (2002) Ex vivo cell labeling with 64Cu-pyruvaldehyde-bis(N4-methylthiosemicarbazone) for imaging cell trafficking in mice with positron-emission tomography. Proc Natl Acad Sci USA 99:3030–3035.
75. Serganova I, Mayer-Kukuck P, Huang R, Blasberg R (2008) Molecular imaging: reporter gene imaging. Handb Exp Pharmacol (185 Pt 2):167–223.
76. Kammili RK, Taylor DG, Xia J, et al. Generation of novel reporter stem cells and their application for non-invasive molecular imaging of cardiac-differentiated stem cells in vivo. Stem Cells Dev.
77. Ruggiero A, Brader P, Serganova I, et al. Different strategies for reducing intestinal background radioactivity associated with imaging HSV1-tk expression using established radionucleoside probes. Mol Imaging 9:47–58.
78. Wu JC, Chen IY, Sundaresan G et al (2003) Molecular imaging of cardiac cell transplantation in living animals using optical bioluminescence and positron emission tomography. Circulation 108:1302–1305.
79. Cao F, Lin S, Xie X et al (2006) In vivo visualization of embryonic stem cell survival, proliferation, and migration after cardiac delivery. Circulation 113:1005–1014.
80. Berger C, Flowers ME, Warren EH, Riddell SR (2006) Analysis of transgene-specific immune responses that limit the in vivo persistence of adoptively transferred HSV-TK-modified donor T cells after allogeneic hematopoietic cell transplantation. Blood 107:2294–2302.
81. Ponomarev V, Doubrovin M, Shavrin A et al (2007) A humanderived reporter gene for noninvasive imaging in humans: mitochondrial thymidine kinase type 2. J Nucl Med 48:819–826.
82. Terrovitis J, Kwok KF, Lautamaki R et al (2008) Ectopic expression of the sodium-iodide symporter enables imaging of transplanted cardiac stem cells in vivo by single-photon emission computed tomography or positron emission tomography. J Am Coll Cardiol 52:1652–1660.
83. Gray SJ, Samulski RJ (2008) Optimizing gene delivery vectors for the treatment of heart disease. Expert Opin Biol Ther 8:911–922.
84. Ma Y, Ramezani A, Lewis R, Hawley RG, Thomson JA (2003) High-level sustained transgene expression in human embryonic stem cells using lentiviral vectors. Stem Cells 21:111–117.
85. Toelen J, Deroose CM, Gijsbers R et al (2007) Fetal gene transfer with lentiviral vectors: long-term in vivo follow-up evaluation in a rat model. Am J Obstet Gynecol 196(352):e351–e356.
86. Krishnan M, Park JM, Cao F et al (2006) Effects of epigenetic modulation on reporter gene expression: implications for stem cell imaging. FASEB J 20:106–108.
87. Mikkers H, Berns A (2003) Retroviral insertional mutagenesis: tagging cancer pathways. Adv Cancer Res 88:53–99
88. Zurkiya O, Chan AW, Hu X (2008) MagA is sufficient for producing magnetic nanoparticles in mammalian cells, making it an MRI reporter. Magn Reson Med 59:1225–1231.
89. Gilad AA, McMahon MT, Walczak P et al (2007) Artificial reporter gene providing MRI contrast based on proton exchange. Nat Biotechnol 25:217–219.
90. Naumova AV, Reinecke H, Yarnykh V, Deem J, Yuan C, Charles EM Ferritin overexpression for noninvasive magnetic resonance imaging-based tracking of stem cells transplanted into the heart. Mol Imaging 9:201–210.
91. Wang J, Zhang S, Rabinovich B, et al. Human CD34+ cells in experimental myocardial infarction: long-term survival, sustained functional improvement, and mechanism of action. Circ Res 106:1904–1911.
92. Ly HQ, Hoshino K, Pomerantseva I et al (2009) In vivo myocardial distribution of multipotent progenitor cells following intracoronary delivery in a swine model of myocardial infarction. Eur Heart J 30:2861–2868.

93. Muller-Borer BJ, Collins MC, Gunst PR, Cascio WE, Kypson AP (2007) Quantum dot labeling of mesenchymal stem cells. J Nanobiotechnology 5:9.
94. Lin S, Xie X, Patel MR et al (2007) Quantum dot imaging for embryonic stem cells. BMC Biotechnol 7:67.
95. Rosen AB, Kelly DJ, Schuldt AJ et al (2007) Finding fluorescent needles in the cardiac haystack: tracking human mesenchymal stem cells labeled with quantum dots for quantitative in vivo three-dimensional fluorescence analysis. Stem Cells 25:2128–2138.
96. Hardman R (2006) A toxicologic review of quantum dots: toxicity depends on physicochemical and environmental factors. Environ Health Perspect 114:165–172
97. Lovric J, Bazzi HS, Cuie Y, Fortin GR, Winnik FM, Maysinger D (2005) Differences in subcellular distribution and toxicity of green and red emitting CdTe quantum dots. J Mol Med 83:377–385.
98. Qiao H, Zhang H, Zheng Y et al (2009) Embryonic stem cell grafting in normal and infarcted myocardium: serial assessment with MR imaging and PET dual detection. Radiology 250:821–829.
99. Higuchi T, Anton M, Dumler K et al (2009) Combined reporter gene PET and iron oxide MRI for monitoring survival and localization of transplanted cells in the rat heart. J Nucl Med 50:1088–1094.
100. Ray P, De A, Min JJ, Tsien RY, Gambhir SS (2004) Imaging trifusion multimodality reporter gene expression in living subjects. Cancer Res 64:1323–1330
101. Schachinger V, Erbs S, Elsasser A et al (2006) Intracoronary bone marrow-derived progenitor cells in acute myocardial infarction. N Engl J Med 355:1210–1221.
102. Schachinger V, Erbs S, Elsasser A et al (2006) Improved clinical outcome after intracoronary administration of bone-marrow-derived progenitor cells in acutemyocardial infarction: final 1-year results of the REPAIR-AMI trial. Eur Heart J 27:2775–2783.
103. Beitnes JO, Hopp E, Lunde K et al (2009) Long-term results after intracoronary injection of autologous mononuclear bone marrow cells in acute myocardial infarction: the ASTAMI randomised, controlled study. Heart 95:1983–1989.
104. Lunde K, Solheim S, Aakhus S et al (2006) Intracoronary injection of mononuclear bone marrow cells in acute myocardial infarction. N Engl J Med 355:1199–1209.
105. Wollert KC, Meyer GP, Lotz J et al (2004) Intracoronary autologous bone-marrow cell transfer after myocardial infarction: the BOOST randomised controlled clinical trial. Lancet 364:141–148.
106. Meyer GP, Wollert KC, Lotz J et al (2009) Intracoronary bone marrow cell transfer after myocardial infarction: 5-year followup from the randomized-controlled BOOST trial. Eur Heart J 30:2978–2984.
107. Janssens S, Dubois C, Bogaert J et al (2006) Autologous bone marrow-derived stem-cell transfer in patients with ST-segment elevation myocardial infarction: double-blind, randomised controlled trial. Lancet 367:113–121.
108. Meluzin J, Janousek S, Mayer J et al (2008) Three-, 6-, and 12-month results of autologous transplantation of mononuclear bone marrow cells in patients with acute myocardial infarction. Int J Cardiol 128:185–192.
109. Chen SL, Fang WW, Ye F et al (2004) Effect on left ventricular function of intracoronary transplantation of autologous bonemarrow mesenchymal stem cell in patients with acute myocardial infarction. Am J Cardiol 94:92–95.
110. Dill T, Schachinger V, Rolf A et al (2009) Intracoronary administration of bone marrow-derived progenitor cells improves left ventricular function in patients at risk for adverse remodeling after acute ST-segment elevation myocardial infarction: results of the Reinfusion of Enriched Progenitor cells And Infarct Remodeling in Acute Myocardial Infarction study (REPAIRAMI) cardiac magnetic resonance imaging substudy. Am Heart J 157:541–547.
111. Kraitchman DL, Heldman AW, Atalar E et al (2003) In vivo magnetic resonance imaging of mesenchymal stem cells in myocardial infarction. Circulation 107:2290–2293.
112. Amado LC, Saliaris AP, Schuleri KH et al (2005) Cardiac repair with intramyocardial injection of allogeneic mesenchymal stem cells after myocardial infarction. Proc Natl Acad Sci USA 102:11474–11479.
113. Stuckey DJ, Carr CA, Martin-Rendon E et al (2006) Iron particles for noninvasive monitoring of bone marrow stromal cell engraftment into, and isolation of viable engrafted donor cells from, the heart. Stem Cells 24:1968–1975.
114. Ebert SN, Taylor DG, Nguyen HL et al (2007) Noninvasive tracking of cardiac embryonic stem cells in vivo using magnetic resonance imaging techniques. Stem Cells 25:2936–2944.

115. Chapon C, Jackson JS, Aboagye EO, Herlihy AH, Jones WA, Bhakoo KK (2009) An in vivo multimodal imaging study using MRI and PET of stem cell transplantation after myocardial infarction in rats. Mol Imaging Biol 11:31–38.
116. Li Z, Lee A, Huang M et al (2009) Imaging survival and function of transplanted cardiac resident stem cells. J Am Coll Cardiol 53:1229–1240

Chapter 6

# *In vivo* MRI mapping of iron oxide labeled stem cells transplanted in the heart

Ruggiero A[1 *], Guenoun J[1 *], Schmidt H[2], Doeswijk GN[1], Klein S[2], Houston GC[3], Krestin GP[1], Kotek G[1], Bernsen MR[1,4]
*Both authors contributed equally to this work.

[1]Department of Radiology, Erasmus MC - University Medical Center Rotterdam, Rotterdam, The Netherlands
[2]Biomedical Imaging Group, Erasmus MC - University Medical Center Rotterdam, Rotterdam, The Netherlands
[3]GE Healthcare
[4]Department of Nuclear Medicine, Erasmus MC - University Medical Center Rotterdam, Rotterdam, The Netherlands

Published in *Contrast Media Mol Imaging*. 2013 Nov-Dec;8(6):487-94

# Abstract

**Background:** In various stem cell therapy approaches poor cell survival has been recognized as an important factor limiting therapeutic efficacy. Therefore noninvasive monitoring of cell fate is warranted for developing clinically effective stem cell therapy. In this study we investigated the feasibility of the use of voxel-based $R_2$ mapping as a tool to monitor the in vivo stem cell fate in myocardium when the cells are labeled with iron oxide particles (SPIO).
**Materials and methods:** Single cardiac phase with cardiac triggered double inversion black blood 2D fast Spin echo (BBFSE) images were acquired on the short axis of hearts. Reproducibility studies were performed in normal rats (n=4) imaged in different sessions. A double cell labeling approach was used in which mesenchymal stem cells were transduced with the luciferase gene and subsequently labeled with ferumoxide particles (SPIO). Living labeled cells were injected in the myocardium of healthy Wistar rats (n=9). For control purposes animals were also injected with dead, labeled cells (n=5) or saline (n=3). Cell fate was monitored over a period of 8 weeks by bioluminescence imaging following injection of D-Luciferine and quantitative magnetic resonance imaging, using a black blood FSE sequence with multiple echo times (between 4.4 and 26.4 ms).
**Results:** Bioluminescence imaging revealed a significant increase of cell number during the first week (peak day 7) with a steep decrease of cell numbers to undetectable levels during the second week. MR imaging showed a sharp increase of $R_2$ values shortly after injection at the injection site (peak day 5), followed by a very gradual decrease of $R_2$ over a period of 15 days. No difference in appearance on $T_2$-weighted images or in $R_2$-values was observed between living and dead cells over the entire time period studied.
**Conclusion:** No significant correlation between the bioluminescence optical data and $R_2$ values were observed. Quantitative MR imaging by means of $R_2$-mapping is not suitable for the *in vivo* assessment of stem cell fate in rat myocardium as validated by bioluminescence imaging. These results do not follow previous *in vitro* reports where it was proposed that based on the difference in $r_2$ relaxivity between intra-cellular and extra-cellular SPIO, living cells may be distinguished from death cells based on their $R_2$ profile. Cell proliferation, cell migration, cell death, extracellular SPIO dispersion or aggregation exhibit different relaxivities. In vivo these processes happen simultaneously, making quantification very complex, if not impossible.

## Introduction

Regenerative approaches in the treatment of myocardial infarction have been widely investigated in the past few years fuelling new hopes for patients and scientists. Preclinical evidence that stem-cell-based-therapy has the potential to limit the degradation of cardiac function after myocardial infarction, led to the rapid development of several clinical trials (1). Recent meta-analyses reported a modest, but statistically significant improvement in the ejection fraction, ventricular dimension and infarct area (2, 3). One or more imaging techniques were greatly exploited in these clinical trials, however only indirect indications of the efficacy of stem cell transplantation was provided by the evaluation of myocardial contractility, viability and perfusion. While these results depict a promising picture of the stem cell-based therapy, questions have been raised regarding actual grafting, transformation and proliferation of stem cells in the host tissue (therefore recovery of the physiological functions of the organ) or whether or not the transplanted cells simply exert paracrine effects (which can induce the recovery of the host tissue) (4).

Molecular imaging (MI) techniques allow the direct visualization of stem cells, their short and long term fate and eventually their viability (5). Two cell labelling approaches are generally used for these purposes: reporter genes or chemical-based contrast agents (5). The former requires the introduction of a reporter gene into the cells of interest, through viral or non-viral-vectors. The reporter gene encodes for a protein (enzymes, receptor, transporter) able to interact with a correspondent reporter probe which is activated or concentrated only in the cells expressing the reporter gene. Probe accumulation is proportional to the expression level of the reporter gene therefore the number of living cells or the induction of a specific reporter gene can be quantified. Passive loading of cells with radioactive agents ($^{18}$F-FDG, $^{111}$In-Oxine, etc.) for positron emission tomography (PET)/single photon emission (SPECT) or contrast agents (iron oxides, Gadolinium, Manganese, 19F) for Magnetic resonance imaging (MRI) is another approach commonly used for cell tracking (5, 6).

Labelling with superparamagnetic iron oxide (SPIO) nanoparticles has been extensively studied as they act as magnetic inhomogeneities, locally disturbing the magnetic field, inducing a significant decrease of T2- and T2*-relaxation rates (hypointense signal). Studies reported that SPIOs do not affect cell viability, proliferation, differentiation or migration (7-10). However, a major drawback is related to the persistence of the hypointense signal at the site of transplant regardless of labelled cell viability. In fact, at longer time points SPIO-induced signal loss is not necessarily associated with implanted cells but rather with phagocytosing monocytes (11, 12). Intriguingly, SPIO induced relaxivities have been shown to be dependent on their location; i.e. the relaxivities are different when SPIOs are compartmentalized within the intracellular space or dispersed in the extracellular space (13, 14). Indeed, decreased T2 values have been reported in lysed versus viable SPIO-labelled cells, this effect is related to limited SPIO-proton interaction in the intracellular compartment compared to unlimited proton interactions of SPIO released from disrupted cells (15, 16).

The majority of cell tracking studies in the heart have focused on the potential of SPIO labelling and MRI longitudinal follow-up of implanted cells, relying on a semi-quantitative approach based on signal intensity (signal-to-noise measurements). A quantitative approach, has already been used for the evaluation of SPIO labelled cells *in vivo* (17), but it has never been exploited to assess SPIO labelled cells implanted in the heart. In this work, we aimed: 1) to perform quantitative R2 mapping of the heart at 7T; 2) to assess reproducibility and robustness of the technique; 3) to assess longitudinally in vivo the R2 changes related to cell proliferation and cell death as evaluated by bioluminescence of double-labelled mesenchymal stem cells (MSCs).

# Materials and Methods

## Rat mesenchymal stem cells expressing firefly luciferase

The plasmid pND-Cag-Fluc was co-transfected into 293T cells with a mixture of Endofree Maxi-kit (Quiagen, Hilden Germany), VSVG (45mg/dish), pMD and pRev using polyethylenimine (Sigma Aldrich, St Louis, MO, USA). Lentivirus supernatant was collected at 48 h and 72 h, filtered (0.45mm) and concentrated by sediment centrifugation. The pellet was then resuspended in 1 ml phospate buffered saline (PBS). Rat mesenchymal stem cells (rMSC; Millipore, Billerica, MA, USA) were grown to 50% confluency in a 24 well plate in Dulbecco's modified Eagle medium (DMEM) /F10 (Invitrogen; Carlsbad, CA, USA), 10% fetal calf serum (FCS) and infected with 50 µl lenti-viral stock. Viral titer was assessed on concentrated supernatant by HIV-p24 ELISA (Dupont, Wilmington, DE, USA). Transduced rMSC (rMSC-Fluc) were expanded and plated at low densities. The expression of Fluc was evaluated by using a luminometer and clones with the highest expression of Fluc were selected and expanded.

## Cell labelling with SPIO

rMSC-Fluc were cultured in DMEM supplemented with 2% FBS (Lonza; Basel, Switzerland), 1% MEM essential vitamin mixture (Lonza), 1% NEAA (Sigma-Aldrich; St. Louis, MO) 2% v/v penicillin/streptomycin, 2% v/v L-glutamine, and 0.5% v/v glutamax (Invitrogen). Cells were grown at 80% confluency and incubated with a mixture of ferumoxide-protamine sulfate. Cells were labelled as previously described (18, 19). Briefly, ferumoxides (Endorem, Guerbet S.A., Paris, France; hydrodynamic diameter of 120-180 nm) were diluted in serum free DMEM to a final concentration of 100ug/ml; protamine sulfate was added to a final concentration of 5 ug/ml. After 5 minutes of intermitted shaking the solution was added to the cells. 24 hours later cells were washed three times with 10U/ml heparinized PBS, harvested by trypsinization, put through a 40 mm cell-strainer and counted. Non-viable cells were obtained by repeated freeze/thawing and brief sonication of the injection solution.
Inductively coupled plasma Optical Emission Spectroscopy (ICP-OES; Optima 4300DV, Perkin Elmer, Norwalk, CT) was used to quantify the intracellular uptake of iron.

## Viability assessment of labelled cells

To assess any potential effect of cell labelling on cell viability or proliferation we labelled cells (wild type and expressing luciferase) with SPIO (triplicate samples), harvested cells at different days, and counted the number of cells on an automatic cell counter. Doubling time was estimated assuming a exponential growth model: $A_t = A_o 2^{t/td}$ (At, cell number at time t; A0, cell number at time 0; t time; $t_d$, doubling time) (20).

## Cell transplantation and in vivo imaging

All animal experiments were conducted in compliance with the independent Institutional Animal Welfare Committee. For assessing the reproducibility of R2 mapping by MR Imaging techniques, rats (Wistar; Harlan; Horst, the Netherlands) (n=4) underwent anesthesia and MRI for a total of 4 sessions each (different days).
For experiments regarding tracking of implanted cells by MRI, rats (Wistar; Harlan; Horst, the Netherlands) received intra-myocardial injections. Briefly, animals were induced with 2%

isoflurane (Baxter Healthcare, Deerfield, IL)/oxygen mixture, and kept under anesthesia by the intraperitoneal administration of a combination of Fentanyl (300 ug/kg) and Medetomidine (300 ug/kg). Animals were ventilated by orotracheal intubation, followed by left thoracotomy. After intra-myocardial injection, the chest was closed, pneumothorax reduced and buprenorfine (0.1 mg/kg) administered subcutaneously. Group 1 (n=9) received 1.5 x$10^6$ viable rMSC SPIO-labelled cells; group 2 (n=5) received 1.5 x$10^6$ non-viable SPIO-labelled cells; group 3 (n=3) received PBS injection (sham experiment).

## Imaging studies

### Bioluminescence

Optical bioluminescence was performed by using the charged coupled camera device Xenogen IVIS Spectrum (Caliper Life Sciences, Hopkington, MA, USA), 5 minutes after intraperitoneal administration of 150 mg/Kg of D-Luciferine (Promega). Each rat was imaged up to 30 minutes (integration time, 30, 60, 120 s and 180s; f/stop,1; binning, medium; field of view, B) to follow the pharmacokinetic profile of luciferin activation. Optical intensity was quantified in units of photons/second/$cm^2$/steradian. Regions of interest were used to calculate the optical peak value at the level of the implanted cells in the heat. Data were analyzed with the software Living Image 2.6 (Caliper LS, Perkin Elmer).

### Magnetic resonance imaging

MRI data were acquired by using a 7T scanner (Agilent-GE Discovery MR901 scanner, Milwaukee IL, USA) with 300 mT/m max gradient. A 150mm diameter quadrature coil was used for transmit and 4ch Rx surface coil array for receive purposes (Rapid Biomedical. Würzburg, Germany).

All animals underwent longitudinal MRI. Every exam started with routine cine sequences (2-chamber view and 4-chamber view) to allow the proper positioning on the heart axial plane and the selection of the most representative section. The overall time required for slice positioning and scanning was 20 min.

Single cardiac phase with cardiac triggered double inversion black blood 2D fast Spin echo (BBFSE) images were acquired on the short axis of hearts. The effective echo times of the separate scans were TE= 4.4, 8.8, 13.2, 17.6, 22, 26.4 ms, the repetition time was ~ TR= 600 ms. The resolution of images was: FOV= 50x50 mm, matrix= 256x256, slice thickness 1.8 mm. The scan time for all TE images was ~ 5 minutes. The triggering was provided by peripheral pulse oxygenation level monitoring on the hind leg of the rats (SA Instruments, Stony Brook, NY, USA). The echo train length was 8, the echo spacing was 4.2 ms, optimized to achieve the required span of available TE values, and yet making sure that the echo train does not extend beyond the cardiac resting phase.

### Image processing

For reproducibility experiments, the inner and outer boundary of the myocardium were manually drawn on the short axis image with the shortest TE, which has the highest signal-to-noise ratio (SNR). To correct for motion artifacts the image set was registered to the images with the shortest TE using a two-step approach. Five anatomical landmarks of the myocardium were manually selected to enable a point based rigid registration, which was used as an initialization for an intensity based mutual information based rigid registration. The myocardium region was divided into standard sectors (21) and the 6 mid-ventricular regions were considered. The mean T2 and the standard deviation were calculated for each region and each day.

For the quantification of SPIO-labelled rMSC, a region-of-interest (ROI) was manualy drawn on the short axis image at the level of the signal void (site of injection).

A T2 map was then generated using a Maximum Likelihood (ML) estimator approach which takes the Rician noise distribution of the magnitude MR images into account. This ML formulation also yields the Cramer-Rao Lower Bounds (CRLB) on the precision of the fits. The square root of the CRLB (srCRLB) is a lower bound on the standard deviation of the T2 and can therefore be used as an error estimate in ms.

## Histology

For histological evaluation, hearts were harvested at 2 days and 15 days after injection, washed in ice-cold PBS, and fixed for 24 h in 4% paraformaldehyde, embedded in Tissue-TEK OCT compound (Sakura, Finetek U.S.A Inc.), frozen at –80 °C, and cryosectioned to obtain 10-mm-thick samples. Slides were stained for iron by using the Accustain kit (Iron stain; Sigma-Aldrich) and imaged by light microscopy.

## Statistics

Statistical data were evaluated using Graphpad Prism 5.0 (Graphpad Software). Statistical comparisons between two experimental groups were performed using t- tests (unpaired comparisons); comparison of multiple groups was performed with two-way ANOVA using Bonferroni's multiple comparison post hoc analysis. All statistical comparisons were two-sided, and the level of statistical significance was set at $P < 0.05$. Unless differently specified, all values were reported as Mean ± SEM.

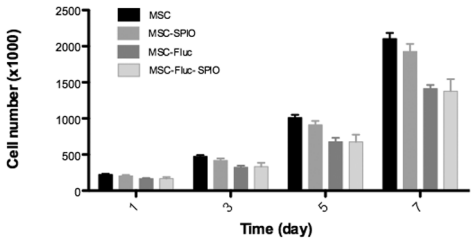


**Fig. 1** *Effect of cell labeling on growth profile*. MSC and MSC-Fluc were labeled with SPIO, cultured up to 7 days and cells were counted at different time points. A lower cell count was observed in the MSC-Fluc (doubling time: 2.02 days) compared to the MSC (doubling time: 1.85 days) at all time-points ($P<0.05$). A lower cell count was observed with MSC-SPIO labeled cells compared to control cells (MSC) only on day 7 ($P<0.05$). SPIO labeling of rMSC-Fluc cell did not have any statistically significant effect on cell proliferation compared to unlabeled control.

# Results

## Viability assessment

Analysis of iron content by ICP measurements revealed 7.58 ± 0.09 iron pg/cell (rMSC) and 7.67 ± 0.14 iron pg/cell (rMSC-Fluc) after the labelling procedure. The difference was not statistically significant. In order to assess whether the cell manipulation (Fluc transduction) or cell labelling could affect cell viability, cell proliferation studies were performed (Figure 1). The presence of the Fluc gene in these cells reduced proliferation rate compared to the wild type as lower cell counts were observed in the MSC-Fluc compared to the MSC at all time points ($P<0.05$). Lower cell counts were observed with MSC-SPIO labelled cells compared to control cells, only on day 7 ($P<0.05$). SPIO labelling of rMSC-Fluc cells did not have any statistically significant effect on cell proliferation compared to unlabelled control. Doubling times (expressed in days) were calculated to be: 1.85 (MSC unlabelled), 1.86 (MSC labelled with

SPIO), 2.02 (MSC-Fluc unlabelled), 2.05 (MSC-Fluc labelled with SPIO). Doubling time of MSC-Fluc was statistically different from MSC at all time points (P<0.05).

## Reproducibility study

Using a BBFSE-based mapping approach, the robustness of the R2 value measurements was assessed . Figure 2 shows a representative axial slice of a healthy rat heart (no injection). The exponential of the signal decay was optimal and calculated errors were relatively small. The signal was quite homogenous with T2 values (22.47±1.92 ms) in the preferred area for cell injection (anterior and anterolateral segment). However, some regions such as the septal and the inferolateral region were more prone to movement artifacts (e.g. breathing) and were associated with a less reliable curve fitting.

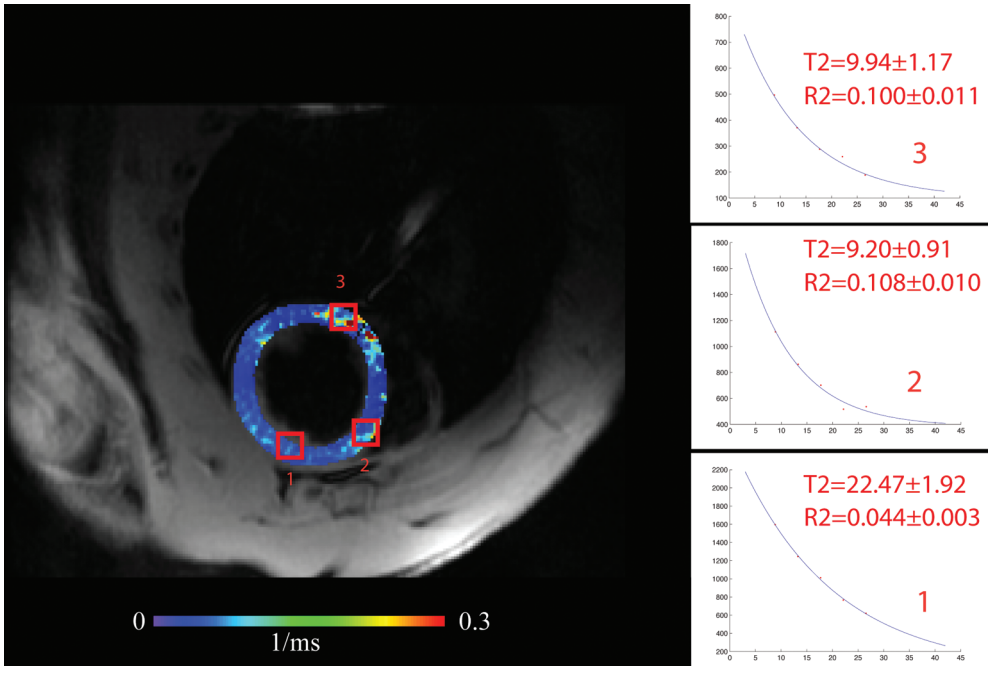


**Fig. 2** *R2 value variability in healthy rat heart.* Representative image depicting an axial slice of a healthy rat heart with super-imposed R2 values measured by using a BBFSE based mapping approach. The exponential curve of the signal decay is optimal and calculated errors (mean ±SD) are reported. The signal is quite homogenous in the area corresponding to the preferred cell injection site in this paper (anterior and anterolateral segment). However some regions such as the septal region and the inferolateral region are affected by movement artifacts (breathing, blood flow) and are associated with not reliable curve fitting.

Reproducibility studies were performed in 4 animals scanned 4 times each to assess the robustness of the technique (Fig 3). Regarding repeated measures of T2/R2 in subsequent imaging sessions the following variability was observed: anterior, region 1 (21.72 ms ±1.49); anteroseptal, region 2 (22.68 ms ± 1.7), region 3 (26.17 ms ± 2.13), region 4 (22.62 ms ± 1.68), region 5 (25.99 ms ± 2.49), region 6 (21.54 ms ± 1.86) (Fig 3). 1-way ANOVA was used to test spatial variability of R2 and T2 values of the six different heart segments of 4 animals. We did not observe a statistically significant difference among the segments (P=0.67).

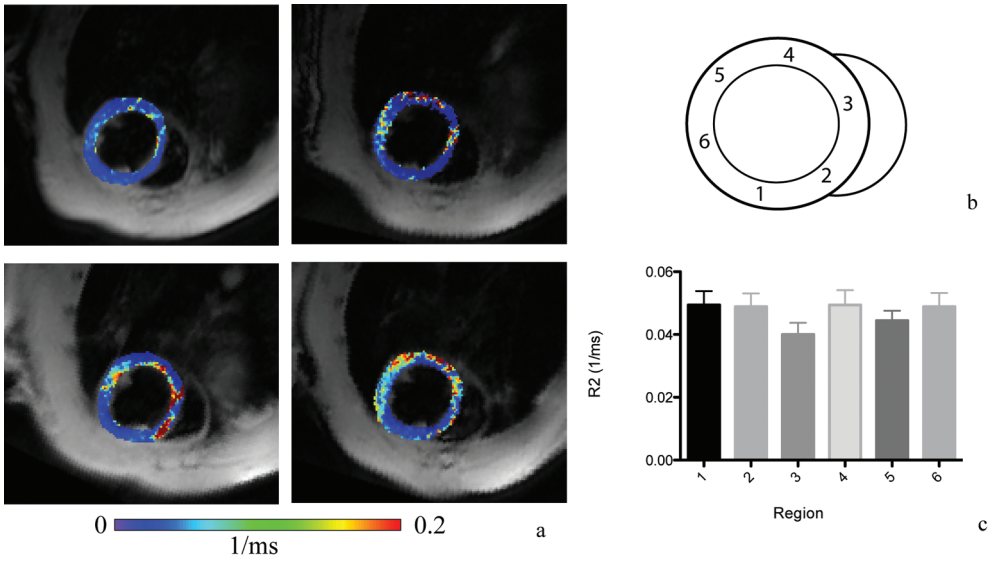


**Fig. 3** *Reproducibility study.* This figure shows a representative BBFSE image with super-imposed R2 mapping values, of an animal imaged in 4 separate sessions **(a)**. Schematic drawing of the region distribution. Region 1: anterior; Region 2: antero-septal; Region 3: inferoseptal; Region 4: inferior; region 5: inferolateral; region 6: anterolateral **(b)**. The graph illustrates the variability of R2 values (mean ± SEM) observed in the different heart regions of 4 animals in 4 different imaging sessions. **(c)**

## Imaging cell fate

The viability and proliferation of implanted cells was assessed longitudinally *in vivo* by both bioluminescence imaging and MR imaging. We observed an increase in optical signal over days 3-7 (compared to day 3 a 3.21-fold and 15.37-fold increase at day 5 and 7 respectively) upon injection of viable cells, most probably related to cell proliferation in the implantation site. On day 10 the signal had declined substantially (0.7-fold reduction compared to highest peak at day 7) and reached background levels on day 15.

In MR images, large areas of hypointensity, generated by iron labelled cells, were clearly visible in the MRI scans of the injected hearts. Importantly, no difference was observed in terms of size, number and distribution of these signal voids between live and non-viable cells. Longitudinal MRI scans were performed to assess the changes in T2 relaxivity over time, related to SPIO dilution or potential decompartimentalization upon cell proliferation or cell death rspectively. Quantification of the signal revealed a 2-fold significant increase ($P<0.05$) in R2 between day 3 and 5 after injection (Fig 4). This was probably related to the early reabsorption of the injection volume with re-distribution of the cells in the implantation site. From day 5 onwards, R2 values decreased. In sham injected animals, no changes in the R2 values over time were observed at the site of the presumed injection.

No statistical correlation with the proliferation or viability profile monitored by bioluminescence was observed ($P=0.1$).

We investigated whether the relaxivity changes associated with the decompartmentalization of iron oxides might be quantified by MRI. We injected a solution of SPIO labelled MSC-Fluc no longer viable (as an effect of repeated freeze/thawing cycles and brief sonication), therefore containing the same amount of SPIO of viable cells but dispersed in the extracellular compartment. No difference was observed in terms of size, number and distribution of the generated signal voids between live and non-viable cells on weighted images. Higher R2 values were

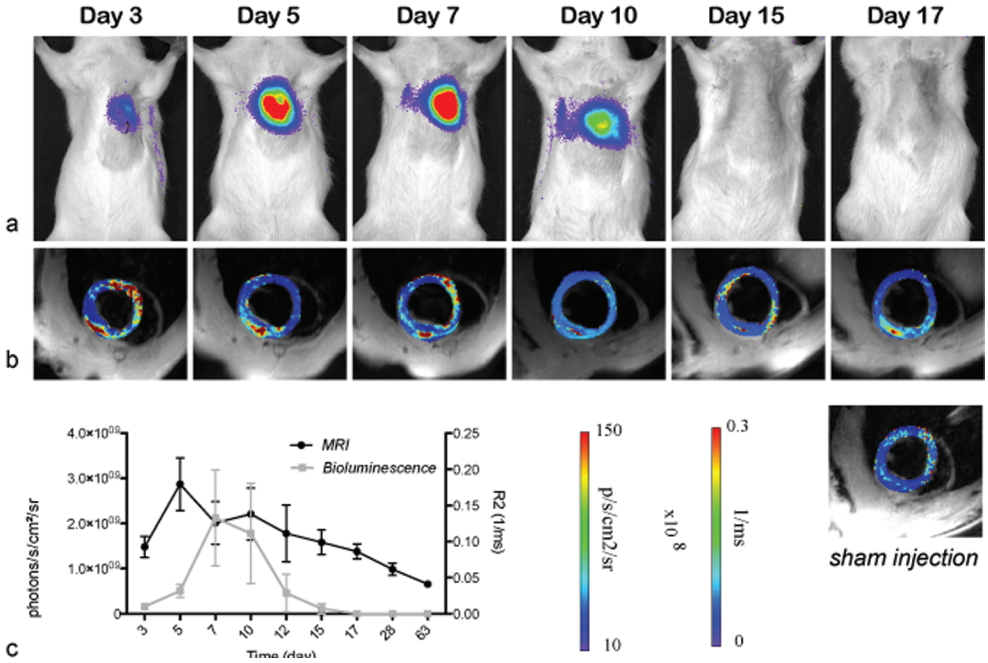


**Fig. 4** *Longitudinal imaging of cell fate by Bioluminescence and MRI*. A. Representative images showing the evolution over time of bioluminescent signal (according to the colorscale provided) emitted by intra-myocardially injected rMSC-Luc-SPIO cells, B. Representative images showing evolution of R2 values (according to the colorscale provided) superimposed on a BBFSE image of a short axis slice of a rat heart at the level of injection with rMSC-Luc-SPIO cells. Bottom right image represents data observed in sham-operated animals. C. Graph showing evolution of bioluminescent signal values and R2 values of rat hearts following intra-myocardial injection of rMSC-Luc-SPIO cells (mean ±SEM).

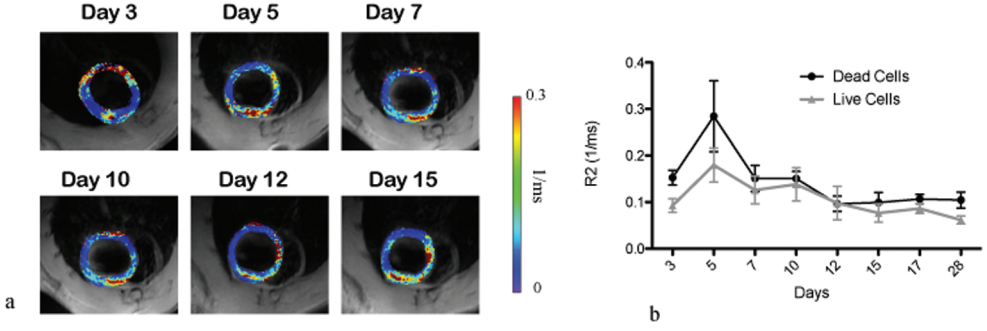


**Fig. 5** R2 MRI mapping in viable and non-viable cells. A. Representative images showing evolution of R2 values superimposed on a BBFSE image of a short axis slice of a rat heart at the level of injection with non-viable rMSC-Luc-SPIO cells intra-myocardially, over time according to the colorscale provided. B. Graph showing evolution of R2 values of rat hearts at the site of injection of living and dead rMSC-Luc-SPIO cells. SPIO labeled MSC-Fluc no longer viable (as an effect of repeated freeze/thawing cycles and brief sonication), containing the same amount of iron of viable cells but decompartmentalized were injected in the heart **(a)**. As an effect of decompartmentalization of SPIO, the implantation of non-viable cells is associated with higher R2 values compared to viable cells. However, this difference is statistically significant only at day 3 after implantation. In the following days despite a trend is clearly visible the difference is not statistically significant and it is probably related to the changes related to free SPIO in the extracellular matrix (uptake from endogenous cells).

associated with dead compared to the viable ones, however the difference was statistically significant only on day 3. The dead cells showed a similar trend to viable cells, consisting in an increase in R2 on day 5 followed by a decrease
Histological analysis of cryo-sections of hearts revealed that injections with non-viable SPIO-labelled cells were associated with a more puntiform appearance of the iron stain (due to the extracellular release of SPIO in the injection solution). Conversely the iron staining of viable SPIO-labelled cells depicted larger aggregates (Fig 6).

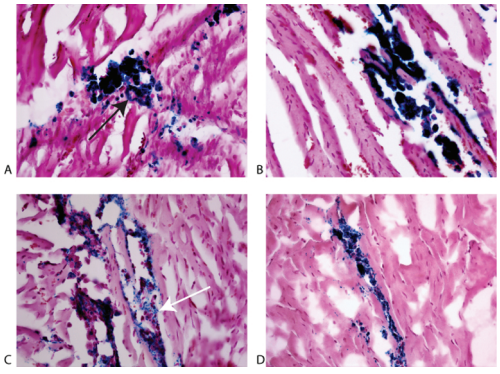


**Fig. 6** Representative histological sections of rat hearts injected with viable (upper panel) and non-viable (lower panel) SPIO-labeled cells harvested at 2 days (A, C) and 15 days (B, D) after injection. Iron staining (blue) depicts the presence of iron which is associated with larger aggregates in the viable cells (black arrow) compared to non-viable cells, which present a more puntiform appearance (white arrow) due to extracellular release of SPIO in the injection solution.

## Discussion

The ability to monitor the localisation, viability, proliferation and possibly the differentiation status of implanted stem cells provides massive benefit in regenerative medicine approaches. All of the pre-clinical and clinical imaging techniques have been leveraged towards this goal; each providing unique advantages and limitations (5). MRI is a widely established technique for the evaluation of cardiac anatomy and function. Taking advantage of its excellent spatial resolution (10–100 µm [preclinical]); 500–1500 µm [clinical]), stem cells labelled with superparamagnetic and paramagnetic agents can be visualised (22, 23). The choice of a proper labeling marker is however a crucial aspect in cell tracking by MRI. High sensitivity allows the long term evaluation of implanted stem cells, since probe dilution upon cell proliferation reduces the detection capabilities. Also, high specificity is demanded to investigate potential cell graft rejection at an early stage.
In this study, luciferase expressing MSC labelled with SPIO were implanted in the heart and longitudinally monitored by quantitative MRI (T2 mapping) and bioluminescence imaging. A vast amount of work has been performed on longitudinal imaging of implanted cells in the heart by MRI; SPIO-labelling and assessment of cell fate by means of (loss of) signal intensities on T2-weighted images being the most used approach. The detection of low signal intensity areas proves to be an insufficient method as it is associated with some limitations such as: a) inhomogeneity in the coil sensitivity (phased-array coils determine regional myocardial signal variations that may give an inaccurate interpretation); b) artefacts due to motion and flow; c) the inherent qualitative aspect of this approach, whose evaluation relies on regional differences in signal intensity, which strongly depend on the parameters of the sequences used (TR, TE, slice thickness, etc) (24).
To overcome these limitations, the alternative approach consists of the direct quantification of the T2 values of the myocardium. This allows the detection of subtle T2 differences in tissues, reducing the subjective interpretation of signal voids (and their dependence from parameters)

and minimizing flow or motion dependent artefacts (24). Many *in vivo* studies on T2 mapping of the heart have been performed in humans in the last two decades, mainly based on spin echo acquisitions. Novel approaches based on T2 prepared steady-state free precession (24), hybrid sequences (25), bright blood approaches (26) or additional adiabatic prepulses (27) have also been suggested recently. It is an area of active investigation for quantitative assessment of myocardial edema and iron overload. However, the use of quantitative mapping for quantification of SPIO-labelled cells implanted in the heart has been quite limited.

A few studies suggested R2 (1/T2) and R2* (1/T2*) parametric mapping as a reliable and reproducible quantification method of SPIO or SPIO labelled cells per voxel (14, 28, 29). Importantly, variation of R2 and R2* according to SPIO compartmentalization have been described. Phantom studies demonstrated that with identical iron concentration, cell bound SPIO show higher R2* values compared to free SPIO. Conversely, R2 measurements are higher for free iron than for intra-cellular iron (13, 14).

We sought to use R2 mapping as a means to detect, in vivo, changes associated with probe dilution and potential decompartmentalization of SPIO as a result of cell proliferation and cell death, respectively. We employed a double inversion recovery BBFSE sequence and tested its robustness in a reproducibility experiment. The signal was quite homogenous in the preferred regions for cell injection in these experiments such as the anterior and anterolateral segments with T2 values of 22.47±1.92 ms and 21.54±1.86 ms (prior to injection), respectively (Fig 2 and Fig 3). As expected, regions associated with higher cardiac motion such as the septal and the inferolateral segment) corresponded on R2 maps to unreliable curve fitting. However, this limitation did not interfere with the longitudinal assessment of the relaxivity of the injected cells. Overall, the difference in R2 and T2 values among the six different segments was not statistically significant.

In the longitudinal assessment of implanted cells, bioluminescence showed an initial increase of the optical signal (peak on day 7), most probably related to cell proliferation, followed by a decrease in signal strength. Limited persistence of bioluminescent signal has been observed previously (30) and the explanation of the signal decrease is not univocal. Cell manipulation impairs cell proliferative ability (Fig 1) and may induce further phenotypical changes that may lead to an immunogenic response by the host. Chen et al. reported from *in vivo* studies with bioluminescence, a half-life of Fluc labelled cells of 2.65 days, with an optical signal showing an increase within the first 3 days and further decrease with background levels on day 6. Our observations are in agreement with these and other findings, in which the majority (more than 70%) of cells implanted in the heart were reported to die within the first week of injection in immunocompetent animals (30-32). The decreasing signal might also result from epigenetic silencing of reporter gene expression which complicates the overall quantification (33). This phenomenon does not seem likely in our study, since identically generated rMSC-Luc-SPIO cells were also injected in other anatomical locations in rats within our group, without a corresponding quick loss of bioluminescent signal (34).

By using MRI to monitor cell proliferation, we and others previously reported that under *in vitro* conditions, cell proliferation/division is associated with a R2 decrease (T2 increase) (13, 16). On MRI, we observed a 2-fold significant R2 increase from day 3 to 5 after injection, which corresponded to the increasing optical bioluminescence signal (cell proliferation) (Fig 4).

Conversely, when cells die and spread their content to the extracellular matrix an increase of the R2 of SPIO labelled cells has been investigated reported only in *in vitro* studies and results have been consistent and reproducible. In fact, Simon *et al.* reported a statistically significant difference in R2 relaxation times between viable and non-viable lysed cells (15). Similarly, Nedopil *et al.* reported on ferumoxides-labelled human mesenchymal stem cells implanted in *ex vivo* joints and showed on T2-w images a markedly lower signal (thus shorter T2) of apoptotic compared to viable cells (35). To our knowledge, this is the first attempt to investigate

the quantitative approach of SPIO-labelled cell fate in an *in vivo* setting. We observed observed a 2-fold significant R2 increase from day 3 to 5 after injection, which corresponded to the increasing optical bioluminescence signal (cell proliferation) (Fig 4). From day 5 onwards, R2 values already decrease from day 5 onwards, while bioluminescence data still suggested ongoing proliferation.. Overall we found no significant correlation between bioluminescent signal profiles and MRI signal evolution (P=0.1). Moreover, we mimicked the release of SPIO content in the injection solution by inducing the death of SPIO-labelled MSC before implantion in the heart. As expected, higher R2 values were associated with the injection of non-viable versus viable cells. However, the difference was statistically significant only on day 3 (Fig 5 and Fig 6).

We argued that the processes happening *in vivo* (such as cell redistribution in the injection site or the re-absorption of the injection medium with further changes in the interactions of the SPIO particles) might obscure the detection of potential changes associated with probe dilution and cell death, making the overall quantitative assessment complicated.

In addition to the above mentioned physiological processes, endogenous cells (e.g. macrophages) might be involved in the potential re-uptake of the SPIO released in the extracellular matrix or phagocytosis of dead cells may intervene in the later days after injection hampering the detection of the difference in the later days. Chen et al. reported a change in the histological pattern of ferumoxides injected in the myocardium, from dispersed (day 2) to focal (day 9), suggesting the involvement of macrophages in scavenging and concentrating SPIO (30). This is a common issue in the use of SPIO as a labelling marker, Winter *et al.* reported (by means of signal intensity of the hypointensity) the absence of any discrimination between healthy successfully engrafted and dead SPIO labelled cells phagocytosed by macrophages within the heart. Particularly, no differences in signal voids up to more than 40 days were observed between dead and viable cells recipients with respect to size, number and localisation. Therefore, just signal loss in T2-w MR Images overestimates SPIO-labelled stem cells survival after transplantation in the heart (12). Similarly, by performing quantitative MRI mapping we were able to depict a slow decrease of the R2 values of the injected cells which remained higher than the relaxivity values of the normal myocardium for the length of our investigation. These findings confirmed for the first time by MRI mapping that SPIO is not a suitable probe for the longitudinal follow-up of the in vivo fate of implanted cells.

It is worth to observe that one limitation of this study was related to a quantitative MRI approach based only on R2 and not also R2* measurements. First, because R2* values are more sensitive to changes from the intracellular to the extracellular space (decrease) and second because a calculated R2' (R2*-R2) would probably have been more sensitive in depicting subtle changes. R2* measurements have been attempted, however we found this approach not possible to achieve at 7T, since the MR signal saturates at very short echo time, making impractical R2* curve fitting.

Cell proliferation, cell migration, cell death, extracellular SPIO dispersion or aggregation exhibit different relaxivities. Unless, there is only one well defined process happening in a restricted volume of interest *in vivo* quantification is very complex, as previously investigated in *vitro* by our previous study (13).

In conclusion, many of the techniques to image stem cells are promising but further work is required before a wide clinical translation becomes reality. From the review of the current literature it seems that there is "no single best method", rather an array of different techniques, each one with specific advantages in terms of spatial resolution, sensitivity and specificity. Reporter gene imaging, considered as the most reliable approach in the quantitative short and long term evaluation of engraftment and survival, is still associated with unsolved issues such as gene silencing, immunogenicity and debated safety. MRI offers great spatial resolution and quantitative capabilities; however currently available probes are sub-optimal. The development of hybrid techniques (MRI/PET) together with improved reporter genes would certainly play a role in the quantitative assessment of cell transplantation in longitudinal studies.

## Acknowledgements

The authors thank Mr RC Janssens (cell biology, ErasmusMC, Rotterdam, The Netherlands) for the technical assistance with the bioluminescence reporter gene. Prof. B Wolterbeek (Technical University Delft, Delft, The Netherlands) for assistance with the ICP-OES measurements. This work has been supported in part by ENCITE (funded by the European Community under the 7th Framework program).

# References


1. Orlic D, Kajstura J, Chimenti S, et al. Bone marrow cells regenerate infarcted myocardium. Nature 2001; 410:701-705.
2. Lipinski MJ, Biondi-Zoccai GG, Abbate A, et al. Impact of intracoronary cell therapy on left ventricular function in the setting of acute myocardial infarction: a collaborative systematic review and meta-analysis of controlled clinical trials. J Am Coll Cardiol 2007; 50:1761-1767.
3. Martin-Rendon E, Brunskill SJ, Hyde CJ, Stanworth SJ, Mathur A, Watt SM. Autologous bone marrow stem cells to treat acute myocardial infarction: a systematic review. Eur Heart J 2008; 29:1807-1818.
4. Korf-Klingebiel M, Kempf T, Sauer T, et al. Bone marrow cells are a rich source of growth factors and cytokines: implications for cell therapy trials after myocardial infarction. Eur Heart J 2008; 29:2851-2858.
5. Ruggiero A, Thorek DL, Guenoun J, Krestin GP, Bernsen MR. Cell tracking in cardiac repair: what to image and how to image. Eur Radiol.
6. Bernsen MR, Moelker AD, Wielopolski PA, van Tiel ST, Krestin GP. Labelling of mammalian cells for visualisation by MRI. Eur Radiol; 20:255-274.
7. Arbab AS, Pandit SD, Anderson SA, et al. Magnetic resonance imaging and confocal microscopy studies of magnetically labeled endothelial progenitor cells trafficking to sites of tumor angiogenesis. Stem Cells 2006; 24:671-678.
8. Delcroix GJ, Jacquart M, Lemaire L, et al. Mesenchymal and neural stem cells labeled with HEDP-coated SPIO nanoparticles: in vitro characterization and migration potential in rat brain. Brain Res 2009; 1255:18-31.
9. Farrell E, Wielopolski P, Pavljasevic P, et al. Cell labelling with superparamagnetic iron oxide has no effect on chondrocyte behaviour. Osteoarthritis Cartilage 2009; 17:961-967.
10. van Tiel ST, Wielopolski PA, Houston GC, Krestin GP, Bernsen MR. Variations in labeling protocol influence incorporation, distribution and retention of iron oxide nanoparticles into human umbilical vein endothelial cells. Contrast Media Mol Imaging; 5:247-257.
11. Amsalem Y, Mardor Y, Feinberg MS, et al. Iron-oxide labeling and outcome of transplanted mesenchymal stem cells in the infarcted myocardium. Circulation 2007; 116:I38-45.
12. Winter EM, Hogers B, van der Graaf LM, Gittenberger-de Groot AC, Poelmann RE, van der Weerd L. Cell tracking using iron oxide fails to distinguish dead from living transplanted cells in the infarcted heart. Magn Reson Med; 63:817-821.
13. Kotek G, van Tiel ST, Wielopolski PA, Houston GC, Krestin GP, Bernsen MR. Cell quantification: evolution of compartmentalization and distribution of iron-oxide particles and labeled cells. Contrast Media Mol Imaging; 7:195-203.
14. Kuhlpeter R, Dahnke H, Matuszewski L, et al. R2 and R2* mapping for sensing cell-bound superparamagnetic nanoparticles: in vitro and murine in vivo testing. Radiology 2007; 245:449-457.
15. Simon GH, Bauer J, Saborovski O, et al. T1 and T2 relaxivity of intracellular and extracellular USPIO at 1.5T and 3T clinical MR scanning. Eur Radiol 2006; 16:738-745.
16. Henning TD, Wendland MF, Golovko D, et al. Relaxation effects of ferucarbotran-labeled mesenchymal stem cells at 1.5T and 3T: discrimination of viable from lysed cells. Magn Reson Med 2009; 62:325-332.
17. Rad AM, Arbab AS, Iskander AS, Jiang Q, Soltanian-Zadeh H. Quantification of superparamagnetic iron oxide (SPIO)-labeled cells using MRI. J Magn Reson Imaging 2007; 26:366-374.
18. van Buul GM, Farrell E, Kops N, et al. Ferumoxides-protamine sulfate is more effective than ferucarbotran for cell labeling: implications for clinically applicable cell tracking using MRI. Contrast Media Mol Imaging 2009; 4:230-236.
19. van Buul GM, Kotek G, Wielopolski PA, et al. Clinically translatable cell tracking and quantification by MRI in cartilage repair using superparamagnetic iron oxides. PLoS One; 6:e17001.
20. Roth V. http://www.doubling-time.com/compute.php. In, 2006.
21. Cerqueira MD, Weissman NJ, Dilsizian V, et al. Standardized myocardial segmentation and nomenclature for tomographic imaging of the heart: a statement for healthcare professionals from the Cardiac Imaging Committee of the Council on Clinical Cardiology of the American Heart Association. Circulation 2002; 105:539-542.

22. Karamitsos TD, Francis JM, Myerson S, Selvanayagam JB, Neubauer S. The role of cardiovascular magnetic resonance imaging in heart failure. J Am Coll Cardiol 2009; 54:1407-1424.
23. Chen IY, Wu JC. Cardiovascular molecular imaging: focus on clinical translation. Circulation; 123:425-443.
24. Giri S, Chung YC, Merchant A, et al. T2 quantification for improved detection of myocardial edema. J Cardiovasc Magn Reson 2009; 11:56.
25. Aletras AH, Kellman P, Derbyshire JA, Arai AE. ACUT2E TSE-SSFP: a hybrid method for T2-weighted imaging of edema in the heart. Magn Reson Med 2008; 59:229-235.
26. Payne AR, Casey M, McClure J, et al. Bright-blood T2-weighted MRI has higher diagnostic accuracy than dark-blood short tau inversion recovery MRI for detection of acute myocardial infarction and for assessment of the ischemic area at risk and myocardial salvage. Circ Cardiovasc Imaging; 4:210-219.
27. Cocker MS, Shea SM, Strohm O, Green J, Abdel-Aty H, Friedrich MG. A new approach towards improved visualization of myocardial edema using T2-weighted imaging: a cardiovascular magnetic resonance (CMR) study. J Magn Reson Imaging; 34:286-292.
28. Boutry S, Forge D, Burtea C, et al. How to quantify iron in an aqueous or biological matrix: a technical note. Contrast Media Mol Imaging 2009; 4:299-304.
29. Peldschus K, Schultze A, Nollau P, et al. Quantitative MR imaging of targeted SPIO particles on the cell surface and comparison to flow cytometry. Magn Reson Imaging; 28:599-606.
30. Chen IY, Greve JM, Gheysens O, et al. Comparison of optical bioluminescence reporter gene and superparamagnetic iron oxide MR contrast agent as cell markers for noninvasive imaging of cardiac cell transplantation. Mol Imaging Biol 2009; 11:178-187.
31. Muller-Ehmsen J, Whittaker P, Kloner RA, et al. Survival and development of neonatal rat cardiomyocytes transplanted into adult myocardium. J Mol Cell Cardiol 2002; 34:107-116.
32. Nakamura Y, Yasuda T, Weisel RD, Li RK. Enhanced cell transplantation: preventing apoptosis increases cell survival and ventricular function. Am J Physiol Heart Circ Physiol 2006; 291:H939-947.
33. Krishnan M, Park JM, Cao F, et al. Effects of epigenetic modulation on reporter gene expression: implications for stem cell imaging. FASEB J 2006; 20:106-108.
34. Guenoun J, Ruggiero A, Doeswijk G, et al. In vivo quantitative assessment of cell viability of gadolinium or iron-labeled cells using MRI and bioluminescence imaging. Contrast Media Mol Imaging; 8:165-174.
35. Nedopil A, Klenk C, Kim C, et al. MR signal characteristics of viable and apoptotic human mesenchymal stem cells in matrix-associated stem cell implants for treatment of osteoarthritis. Invest Radiol; 45:634-640.

Chapter 7

# T1 Mapping in the rat myocardium at 7T using a modified CINE inversion recovery sequence

Henk Smit[1], Ruben Pellicer Guridi[2], Jamal Guenoun[2], Dirk H. J. Poot[1], Gabriela N. Doeswijk[2], Matteo Milanesi[3], Monique R. Bernsen[2,4], Gabriel P. Krestin[2], Stefan Klein[1], Gyula Kotek[2]

[1]Biomedical Imaging Group, Erasmus MC - University Medical Center Rotterdam, Rotterdam, the Netherlands
[2]Department of Radiology, Erasmus MC - University Medical Center Rotterdam, Rotterdam, the Netherlands
[3]Agilent Technologies Inc, Yarnton, Oxford, UK
[4]Department of Nuclear Medicine, Erasmus MC - University Medical Center Rotterdam, Rotterdam, the Netherlands

Published in *J Magn Reson Imaging*. 2014 Apr;39(4):901-10

## Abstract

**Purpose:** To evaluate the reproducibility and sensitivity of the modified CINE inversion recovery (mCINE-IR) acquisition on rats for measuring the myocardial T1 at 7T.
**Materials and Methods:** The recently published mCINE-IR acquisition on humans was applied on rats for the first time, enabling the possibility of translational studies with an identical sequence. Simulations were used to study signal evolution and heart rate dependency. Gadolinium phantoms, a heart specimen and a healthy rat were used to study reproducibility. Two cryo-infarcted rats were scanned to measure delayed enhancement (DE).
**Results:** In the phantom reproducibility studies the T1 measurements had a maximum coefficient of variation (COV) of 1.3%. For the in vivo reproducibility the COV was below 4.8% in the anterior cardiac segments. In simulations, phantoms and specimens a heart rate dependency of approximately 0.5 ms/bpm was present. The T1 maps of the cryo-infarcted rats showed a clear lowering of T1 in de DE region.
**Conclusion:** The results show that mCINE-IR is highly reproducible and that the sensitivity allows detecting T1 changes in the rat myocardium.

## Introduction

Estimating the T1 relaxation parameter of tissues is a promising MRI technique which can be used for detecting and characterizing different types of pathology in vivo. T1 estimation has drawn an increasing amount of attention in the past few years, as the quantitative measurements have the potential to be less vendor and scanner dependent than the conventional T1-weighted images (1), which are not normalized and are characterized by signal intensities and contrasts dependent on specific pulse sequences.

In clinical MRI, T1 mapping has been increasingly applied for the study of ischemic heart disease, adding valuable information to the more established technique of delayed contrast enhancement (DE) (2,3,4). With DE the relative signal difference between healthy and infarcted myocardium is used to assess tissue viability (5,6,7,8), but there is no calibrated quantification and it also does not identify diffuse interstitial myocardial fibrosis. Recent work has shown that T1 mapping can differentiate between viable and necrotic tissues after contrast administration (4,9,10,11) and that it can be used to identify diffuse myocardial fibrosis (3,12). In preclinical research, myocardial T1 mapping has already proved capable of detecting the presence of edema in the myocardium (10,13). Another interesting preclinical application of T1 mapping would be to enable the visualization and quantification of injected labeled stem cells (14,15).

Several methods and sequences have been introduced to measure the T1 in the cardiovascular system. The most common approaches include the Modified Look-Locker inversion recovery method (MOLLI), the variable flip angle method and the CINE Inversion recovery method.

The use of MOLLI sequences is frequently reported in human (9,16,17) and also applied in small animals (18). It is a single-slice technique that acquires data during a number of consecutive inversion recoveries and merges that into one image set. In humans the images are acquired in a single-shot balanced SSFP acquisition with an acquisition window of about 190 ms during the end diastolic phase when the myocardium is relatively stable. However, in small animals where the RR interval is only 100-200 ms this approach is not possible. A segmented acquisition can be performed but that leads to long scan times up to 43 minutes to create one T1 map (18). A recent work (19) used temporal undersampling and radial acquisition to reduce scan time. This led to reproducible cardiac T1 estimations but with an in-plane resolution of 0.60x0.60 mm. As the rat myocardium is approximately 1.5-2 cm it is desirable to achieve a higher resolution. The MOLLI method has been reported to show a heart rate dependency of the estimated T1 values in humans (20,21). In most other works the relation of the estimated T1 with heart rate is not investigated.

A three dimensional variable flip angle method has been implemented in small animals (22), and has shown reproducible results on mouse myocardium where it was able to detect regional differences in mice with induced infarction. The drawbacks of this method are the long scan duration up to 50 minutes to acquire 5 different flip angles and the sensitivity to B1 imperfections. The CINE inversion recovery method (CINE-IR) sequence was first developed for human studies. That implementation consists of an inversion pulse played out after a cardiac trigger, followed by data acquisition in a segmented multi-phase fashion (CINE) (23). A second heart cycle can be left unperturbed to allow the longitudinal magnetization to recover (24,25). This approach could potentially cause problems for small animal imaging, since the T1 values found in the heart can be in the range of 1000 ms, while the RR interval is around 150-180 ms. This implies that when the acquisitions are performed in one RR interval there is only a partial recovery of longitudinal magnetization and only a small part of the inversion recovery curve can be measured.

In the processing, one of the frequently reported options to estimate T1 by fitting the MRI data to the signal model is to make use of a Least Squares (LS) method (26,27,28). While this approach is accurate for a normal noise distribution, in MR magnitude images the noise distribution is Rician and the results of LS estimation are no longer accurate (29). Furthermore, in literature usually no uncertainty measure is reported for T1 estimations (4,16,22).

To deal with the fast heart rate of small animals, our study employs a modified version of the CINE inversion recovery (mCINE-IR) that has recently been applied for the estimation of myocardial T1 in humans (2). With respect to the original version of the CINE-IR sequence, in mCINE-IR the number of acquired cardiac phases is variable to allow sampling of a sufficient part of the relaxation curve. Since the sequence is applicable both on high and low heart beat rates and at various resolutions without modification, it facilitates translational studies from small animal to human models.

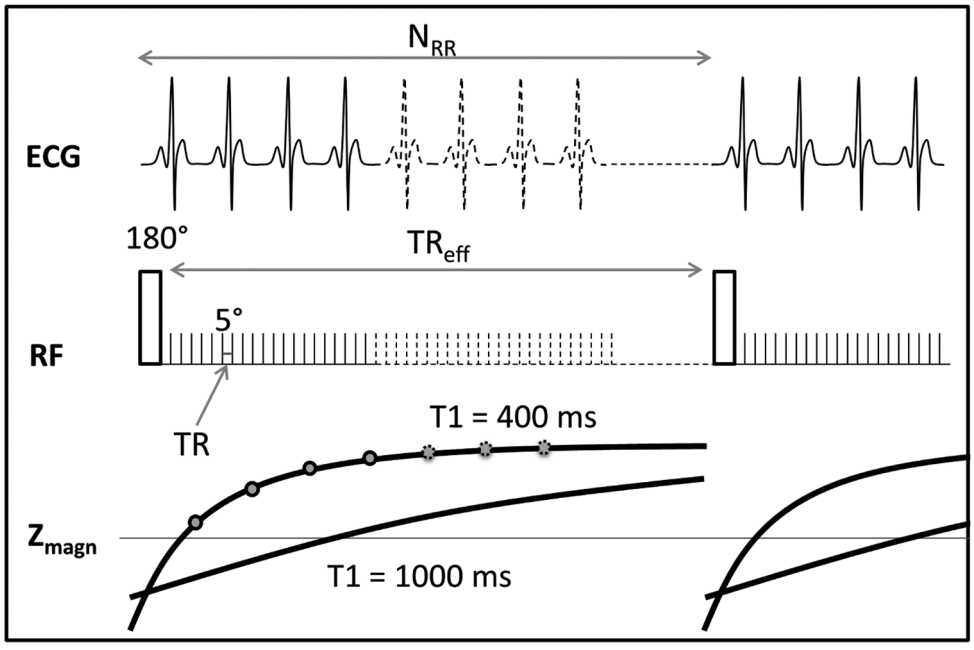


**Figure 1**: The mCINE-IR pulse sequence. A FSPGR, RF = 5°, CINE acquisition is performed between adiabatic inversion pulses. The number of cardiac cycles between two inversions, $N_{RR}$, can be chosen freely to achieve sufficient longitudinal regrowth of magnetization. In this example the magnetization of the tissue with T1 = 400 has reached equilibrium in the given time, but for the tissue with T1 = 1000 it could be beneficial to increase $N_{RR}$ to allow more regrowth of magnetization. The points on the T1 = 400 ms curve indicate the used points for the T1 estimation in the myocardium, taken during the diastolic phase.

The contribution of this work is that it evaluates this novel T1 mapping protocol for the first time on small animals in terms of reproducibility and sensitivity. Two sources of potential error are studied in more detail. The first is that the excitation could be heterogeneous due to the pulse profile and out of plane motion as mCINE-IR is a single-slice technique. This effect could lead to heterogeneous relaxation behavior. The second is the effect of different heart rates on the estimated T1 values, which change sequence timings and could therefore affect the acquisition. The effect of these two sources of error on the reproducibility and sensitivity of the T1 estimations are investigated. To do this a novel estimation method based on maximum likelihood estimation is deployed, which is more accurate than a LS method, includes estimation of the noise level and shows the uncertainty of the estimated T1. Simulations are used to investigate the propagation of the errors introduced by the heterogeneous relaxation behavior, heart rate changes and noise to the estimations and therefore the accuracy and precision of the estimated T1 values. Additionally, phantom and in vitro MRI studies with mCINE-IR are

performed to investigate the precision and reproducibility of the estimations from real MR images. Finally, mCINE-IR is used for acquisitions on rats to investigate the reproducibility in vivo and to evaluate whether the accuracy and reproducibility of mCINE-IR is sufficiently high to detect T1 changes in the rat myocardium due to the delayed enhancement of a cryo-infarcted region.

# Materials and Methods

## Pulse Sequence

The modified CINE acquisition (Figure 1) is based on the original CINE Inversion Recovery sequence (23,24,25). It uses a non-selective adiabatic inversion pulse, applied immediately after a cardiac trigger. It is followed by a continuously applied Fast Spoiled Gradient Echo (FSPGR) acquisition. As demonstrated earlier this continuous application of small angle RF pulses will affect the longitudinal relaxation of magnetization and decrease the apparent T1 (30). Unlike normal CINE sequences the acquisition is not limited to one or two RR intervals (24,25), but the number of heartbeats between two subsequent inversions can be chosen freely and optimized for the application. A viewsharing algorithm and linear retrospective interpolation are performed on the recorded data to reconstruct the subscribed number of images of cardiac phases per RR interval (31). Each individual image experiences a different time delay after the inversion pulse and therefore has a different T1 weighting.

## Data acquisition

For the acquisitions a 7.0 T preclinical scanner (Discovery MR901TM, Agilent Technologies – GE Healthcare) was used with a 72 mm volume transmit coil and a 4 channel phased-array surface receive coil. The acquisitions were performed using ECG triggering with a temporal resolution of 1 ms. The T1 values measured in the rat myocardium were expected to be in the range of 700-1000 ms, and with a typical RR interval ($T_{RR}$) of 165 ms, the number of heart cycles between two inversions ($N_{RR}$) was chosen to be 15 such that the effective repetition time ($TR_{eff}$ = $T_{RR}$ x $N_{RR}$) ranges up to approximately 2500 ms providing enough time for a sufficient signal recovery. The number of views per segment was 6. Since images were reconstructed from each of the $N_{RR}$ cardiac cycles in a CINE fashion, also $N_{RR}$ points of the inversion recovery curve in the same cardiac phase are available. We selected images from the diastolic phase, which made it possible to register images with different inversion times fairly easy, which results in a more accurate T1 estimation. The resulting TI values depend on heart rate, starting from the first diastolic phase and increasing with steps of $T_{RR}$. For a heart rate of 365 bpm this resulted in TI values from 91 ms up to 2380 ms. During $TR_{eff}$ the selected slice is continuously excited and sampled by the FSPGR RF pulses with a constant repetition time to maintain the steady state. For the FSPGR acquisition the flip angle = 5 degree, the TR = 3.8 ms and the TE = 1.3 ms. An open source electronics board (ARDUINO, http://arduino.cc) was used, for recording real heart rates from rats and for gating the scanner with simulated ECG pulses. This hardware allows real time interruptions at high temporal resolution. We scaled the temporal resolution to 64 µs. For all in vitro scans the temperature was controlled at a constant value with a hot air blowing system and a MR compatible thermometer (SA Instruments, Stony Brook, NY).

## T1 estimation

For the T1 estimation a three parameter exponential signal model was fitted through the data. The signal model used for the modified CINE acquisition was (30):

[1.]

With parameter vector θ = {A, B, T1}. To obtain θ a Maximum Likelihood (ML) estimator was used which maximizes the joint probability of the measurements and takes the Rician noise distribution of the magnitude MR images into account. The probability density function of the Rician distributed signal *y* is:

[2.]

Where $S_\theta$ is the predicted noise free magnitude, σ the standard deviation of the noise in the complex MR data, $I_0$ is the zeroth order Bessel function of the first kind and the Heaviside function. To obtain the parameters in θ the logarithm of the joint likelihood for the measured points was maximized in a numerical optimization with a gradient descent type procedure using a trust region method, solving:

[3.]

The noise level σ is also estimated during the optimization. To avoid that the estimator finds a local maximum the optimization was iteratively initialized with a range of different values for θ, after which the best fit was chosen. When using a ML estimator and when the derivative of the signal model to θ is known the square root of the Cramér-Rao lower bounds ($CRLB_\sigma$) (29) can be calculated, which gives a lower bound on the standard deviation of the estimated parameters and can therefore be used as an indication of the uncertainty of the estimated parameters.

Two types of estimations are used in our work. The first is a region-based estimation, in which all the voxels in a defined region are used for one single estimation. The second method is voxel-based, in which for each individual voxel within a region T1 estimation is performed. The whole estimation pipeline was implemented in an in-house written Matlab (The Mathworks, 2008) script.

## Simulation experiments

Bloch simulations of signal intensities were performed in Matlab. Signal evolution distorted with Rician noise was simulated with the parameters of the mCINE-IR sequence. The T1 was estimated by the same procedure as for the real MR data. Three experiments were performed. The first was a simulation of the magnetization components of three different homogenous tissues with T1 values of 450, 1150 and 2400 ms during an mCINE-IR acquisition at an heart rate of 365 bpm to see the signal evolution during the acquisition. Other simulation parameters were flip angle = 3.5 degree, TR = 3.8 ms, equilibrium magnetization = 1 and the σ of added Rician noise = 0.05. The second experiment consisted of 1000 T1 estimations with the same three tissues as in the first experiment. The T1 was estimated for 12 different heart rates between 265 and 485 bpm to investigate whether a heart rate dependency exists. The third experiment was designed to study the effect of heterogeneous relaxation behavior within a region of interest. As mCINE-IR is a single-slice technique the excitation can be heterogeneous due to the pulse profile and out of plane motion. This could lead to heterogeneous relaxation behavior within a volume, with apparent different T1 values. Also the T1 values in biological

tissue are not likely to be completely homogenous, even in a small region. To investigate this, the second experiment was repeated but now with a signal that was a mix of the tissues with T1 = 100 and 2100 ms in a ratio 1:3, thus simulating a region with a small compartment of short T1 tissue. To quantify the heart rate dependency a straight line was fitted through the means to obtain the slope with 95% confidence intervals.

## Phantom experiments

A phantom of different dilutions of the T1 modifying contrast agent Gadolinium (Magnevist, Bayer, Germany) was constructed to perform MRI experiments. Six different water solutions were created in which the Magnevist was diluted 750, 1500, 2250, 3000, 3750 and 4500 times respectively. The acquisition was always performed during $N_{RR}$ = 15 cardiac cycles, leading to $TR_{eff}$ values from respectively 1856 ms to 3396 ms depending on the simulated heart rate. The scan parameters for the phantom scans were matrix = 256x192, NEX = 6, FOV = 45x34 mm, in-plane voxel size = 0.17x0.17 mm, slice thickness = 2 mm and scan time approximately 6 minutes. To simulate a phantom with heterogeneous relaxation behavior, the signals of the 750 and 4500 times diluted Gd solutions were mixed by using all voxels in a single region-based fit. Since the protocol acquires 12 images per cardiac cycle, in total $12*N_{RR}$ images were acquired. Although all of these could be used in the T1 estimation since there is no motion in the phantoms, only one from each cardiac cycle was used to mimic the procedure taken in vivo where only the images from the diastolic phase are selected. A region-based estimation was performed by drawing regions of interest in the tubes covering the whole tubes except the outer 1 mm to avoid boundary effects. In a first experiment to study the reproducibility of the results of T1 estimation with the mCINE-IR the phantoms were scanned seven times with a heart rate of 365 bpm. The mean and standard deviation were calculated. The second experiment was to study the effect of different heart rates. The T1 of each individual phantom and of the mixed signal was estimated for 12 different heart rates between 265 bpm and 485 bpm with steps of 20 bpm. A line was fitted through the T1 values to obtain the slope with 95% confidence intervals.

## *Ex vivo* experiments

A rat heart was post mortem surgically removed from the body and fixated in agar gel. Scan parameters were acquisition matrix = 256x192, NEX = 6, FOV = 50x38 mm, in-plane voxel size = 0.20x0.20 mm, slice thickness = 2 mm, and scan time approximately 6 minutes. A region of interest of approximately 5x5 mm was drawn in the myocardium and a region-based T1 estimation was performed. To evaluate the reproducibility the specimen was scanned five times with a constant heart rate of 365 bpm. To study the heart rate dependency the specimen was scanned with the same heart rates as the phantoms, ranging from 265 to 485 bpm, and the slope with 95% confidence intervals was estimated.

## *In vivo* experiments

All experiments with animals were performed with prior approval of the institutional animal care committee and according to Dutch law.

To study the characteristics of the heart rate of rats in vivo, 1000 RR intervals of two healthy rats and four infarcted rats were recorded during scanning. The duration of each RR interval was measured, and the mean and standard deviation were calculated. For the imaging experiments the

heart rate of the scanned rat at the beginning of the examination was stored in the DICOM header. In a reproducibility experiment one healthy rat was scanned in four different scanning sessions to test the reproducibility of the T1 estimations with mCINE-IR in vivo. Scan parameters were acquisition matrix = 256x192, NEX = 6, FOV = 60x45 mm, in-plane voxel size = 0.23x0.23 mm, slice thickness = 2 mm, and scan time approximately 6 minutes. The triggering was provided by peripheral pulse oxygenation level monitoring on the hind leg of the rats (SA Instruments, Stony Brook, NY, USA). To define the region of interest, the inner and outer boundaries of the myocardium were manually drawn on the short axis image. Since the measurements were performed in separate scanning sessions, the positioning of the rat and the myocardium could be different for each case. Therefore a two-step image registration was applied to define corresponding regions of interest. In the first step five anatomical landmarks were selected, two points on the intersection of the ventricles and three points on a straight line through the apex and the centre of the right ventricle. These points were used for a rigid point based registration. The result of this registration was used as the initialization for the second step, which was intensity based rigid registration with a mutual information metric (32) using open source elastix software (33). The myocardium region was divided into six standardized regions (34) by using the selected landmarks. Then a voxel-based estimation was performed for all these segments. The voxels where the $CRLB_\sigma$ was less than 15% of the T1 value were defined as successful fits. The mean T1 and the standard deviation of the successful fits within one segment were then calculated per segment.
In two rats a cryo-infarct was created by exposing the heart through a thoracotomy and applying a cryoprobe for 14 seconds on the anterior LV wall. The rats were scanned at three time points with mCINE-IR: pre-contrast and at 5 and 16 minutes after administration of the gadobutrol (Gadovist, Gadovist, Bayer Schering Pharma AG, Berlin, Germany) with a concentration of 0.5 mmol/kg. Scan parameters were acquisition matrix = 256x192, NEX = 10, FOV = 50x38 mm, in-plane voxel size = 0.20x0.20 mm, slice thickness = 2 mm, and scan time approximately 10 minutes. A standard T1 weighted inversion recovery fast gradient echo sequence was used to show the presence of DE 3-5 minutes after injection. The scan parameters were matrix = 192x160, TE/TR = 1.2/3.4, NEX=40, flip angle = 14 degree, slice thickness = 2 mm, inversion time 100 ms, and scan time 2 minutes. In the processing the myocardium was defined by drawing the inner and outer boundary on the image with the longest inversion time and therefore highest SNR. Voxel-based T1 maps were created for the three time points.

# Results

## Simulation

Figure 2 shows the results of the simulated signal evolution. The three different grayscales represent the three tissues. As can be seen the magnetization goes to a different equilibrium value for each tissue. For longer T1 values this equilibrium is lower, which is an effect of the constant application of RF pulses. The estimated T1 values are 369, 735 and 1101 ms, lower than the true values of 450, 1150 and 2400 ms. Figure 3a is the outcome of the simulations of 1000 estimations per tissue and per heart rate for the three tissues. The scattered points are the outcomes of the estimations, 1000 for each heart rate and each tissue, and the gray box with the black line is the mean with 95% confidence intervals. The results show that for longer T1 values there is a larger variation in the estimations. This is in line with the results in Figure 2, which shows that for longer T1 values the signal to noise ratio (SNR) is lower. Also a smaller part of the total recovery curve is sampled with longer T1 values. Higher heart rates also result in a larger variation of the estimations. However, there is no significant effect on the mean of the estimated T1 values. All means are close to each other and with a large margin within each

other's 95% confidence intervals. There is no trend that the estimated T1 goes up or down with heart rate.

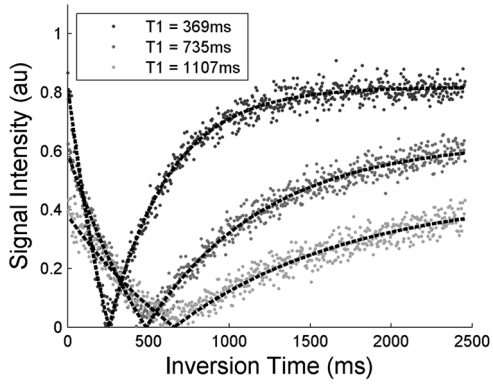


**Figure 2**: The simulated inversion recovery signal evolutions of the three different T1 values. The estimated T1 values are 369, 735 and 1101 for three tissues. TR = 3.8 ms, equilibrium magnetization = 1 and the σ of the added Rician noise is 0.05. The figure shows that SNR decreases for higher T1 values.

In Figure 3b the result of the simulation with the mixed tissue is shown, which was an approximation of a region with a long and a short T1 component. The T1 estimations show a significant slope, and a decrease of estimated T1 with an increasing heart rate occurs. With a linear fit through the means of the estimations it results that the slope of this line with 95% confidence interval is -0.51 (-0.54, -0.48) ms/bpm, meaning that the T1 for this mixed tissue decreases with 1 ms per extra two beats per minute.

## Phantom

The results of the reproducibility experiments are in Table 1 with the mean outcome per phantom, the standard deviation of the seven experiments, the mean $CRLB_{\sigma}$ for the estimations and

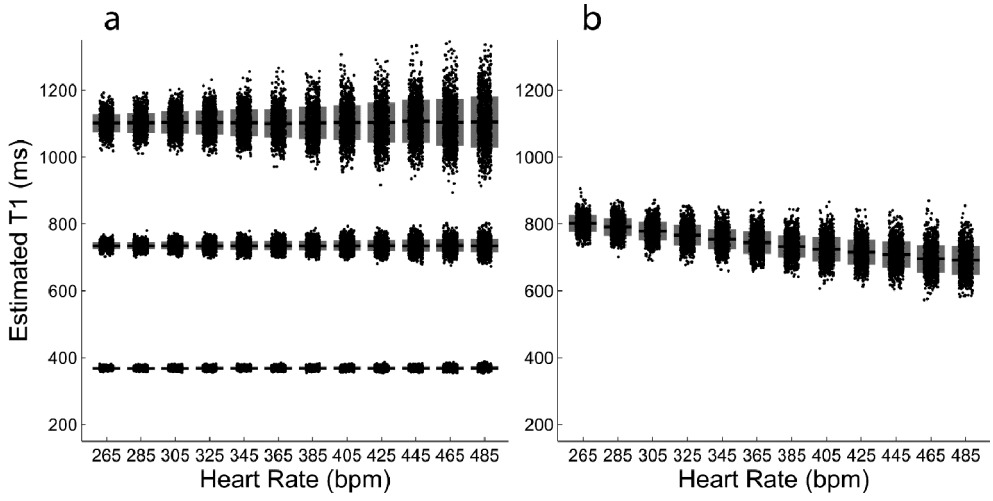


**Figure 3** Simulations of T1 estimations. Figure 3a are the estimations of the homogenous tissues; Figure 3b on the combined tissue of the highest and lowest T1. There are 1000 estimations per tissue for each heart rate. The gray boxes behind the points show the mean and the 95% confidence interval of the mean. For the homogeneous tissues the uncertainty increases for higher heart rate and higher T1, but the means do not change with heart rate. The T1 estimations of the mixed signal decrease with heart rate with a slope of 0.51 ms/bpm.

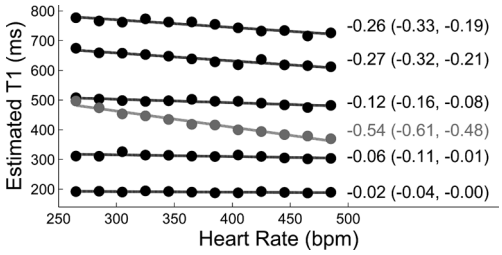


**Figure 4** The outcome of the T1 estimations on the phantoms for 12 different heart rates. The black scattered point are the estimated T1 values of the five phantoms. The gray points are the combination of the high and low dilution. The numbers printed on the right are the slopes of the dashed lines fitted through the measurements. The slope for the mixed signal is steeper than for each of the dilutions individually.

the COV. The 3750x diluted phantom has a high T1 and was the farthest from the receiver coil, which resulted in a poor SNR of a maximum value 1.5 at the equilibrium, which resulted in a COV of 5.4%. For the other five phantoms the COV was within 1.3%. The $CRLB_{\sigma}$ values are all in the same range, or a little lower than the standard deviations, as expected from lower bounds on the standard deviation. In Figure 4 the results of the experiment with the different heart rates are displayed. The 3750x diluted phantom was excluded from this figure for clarity as the error introduced by the low SNR exceeded the effect of the changing heart rate. The black lines are for the five phantoms. The gray points are for the fit on the mixed signal. Next to each curve the fitted slope is displayed with 95% confidence intervals. It shows that as the T1 increases the slope also slowly increases, going from -0.02 to -0.27 ms/bpm, which was not observed in the simulations. For the mixed signal the slope with 95% confidence intervals is -0.54 (-0.61, -0.48) ms/bpm, significantly steeper than for each of the phantoms separately, which is in agreement with the simulation results.

## *Ex vivo*

The reproducibility experiment resulted in a mean T1 of 643.2 ms of the region of interest in the myocardium with a standard deviation of 2.9 ms and a COV of 0.45%, showing a similar reproducibility as in the phantoms. The results of the heart rate dependency experiment are plotted with $CRLB_{\sigma}$ error bars in Figure 5. The slope of the line fitted through the points with 95% confidence intervals is -0.50 (-0.60, -0.40) ms/bpm, which is in the same range as the mixed phantom and significantly steeper than the homogenous phantoms.

**Figure 5**: The estimated T1 values for the myocardium specimen. The scattered points are T1 estimations at different heart rates. The error bars are calculated with the Cramér-Rao lower bounds. The dashed line is fitted through the measurements and has a slope with 95% confidence interval of 0.50 (0.40, 0.60) ms/bpm, displaying a heart rate dependency.

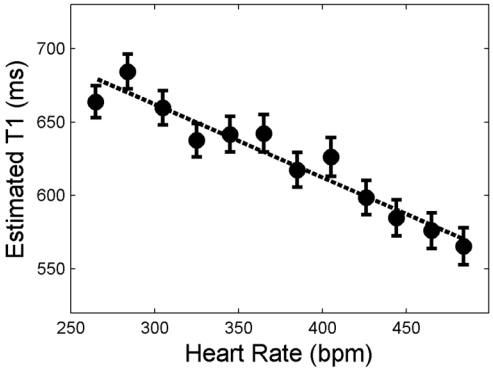

**Table 1**: Outcomes of the T1 estimations for the six different Gd dilutions. The measurement is repeated seven times and the mean, the standard deviation, the $CRLB_\sigma$ and the COV of these seven measurements are displayed.

| Dilution | Mean T1 (ms) | Std (ms) | $CRLB_\sigma$ (ms) | COV |
|---|---|---|---|---|
| 750 | 188.9 | 1.9 | 1.7 | 1.0% |
| 1500 | 314.0 | 3.9 | 3.4 | 1.2% |
| 2250 | 493.2 | 5.5 | 3.4 | 1.1% |
| 3000 | 633.7 | 5.5 | 5.6 | 0.8% |
| 3750 | 723.7 | 39.0 | 22.1 | 5.4% |
| 4500 | 749.6 | 9.8 | 6.8 | 1.3% |

## *In vivo*

The heart rate measurements of the four infarcted and two healthy rats resulted in a mean RR interval and standard deviation for each rat. For the infarcted rats the average mean RR interval and the average standard deviation were 365 and 13 bpm and for the healthy rats 370 and 13 bpm. Figure 6 shows the reproducibility results for the six segments of the myocardium. The percentage of successful fits, which have a $CRLB_\sigma$ of less than 15% of the estimated T1 value, is displayed for each segment, as well as the mean T1 with standard deviations. The reproducibility and the percentage of successful fits are higher for the three anterior segments than for the three inferior segments. The COV of the mean T1 is below 4.8% for the anterior segments, while it is above 12% for the inferior segments. The mean heart rate was 355 bpm with a standard deviation of 10 bpm.

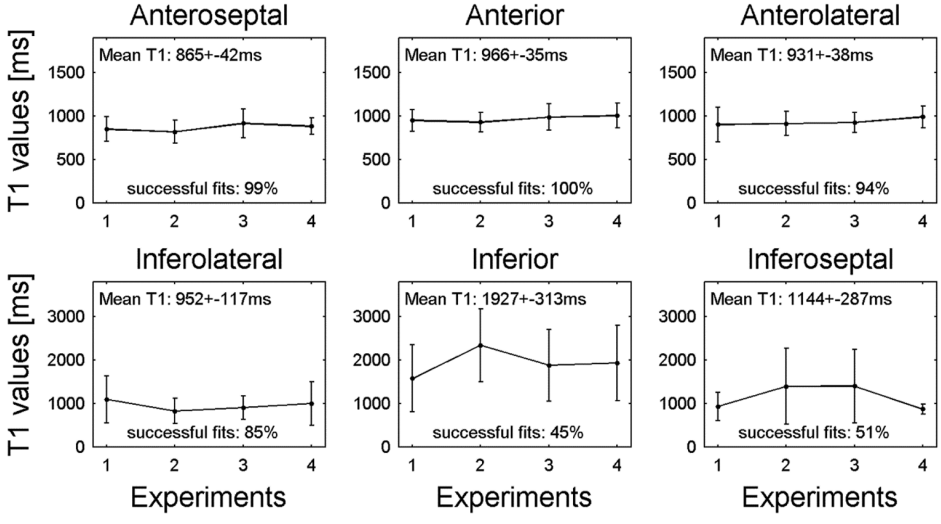


**Figure 6** The results of the reproducibility study on the six segments of the rat myocardium. Mean and standard deviation of are plotted for the four experiments. The mean T1 with standard deviation of the mean and the percentage of successful fits are displayed as text. The range of the T1 values axis is different for the upper and the bottom row. The anterior segments show both a high fit success rate and a reproducible outcome with all COV values below 5%. The inferior segments have lower success rates and less reproducible outcomes, all with a COV above 12%.

In Figure 7 the results for the DE experiments are displayed for both rats. On the left the pre-contrast T1 map estimated from mCINE-IR is displayed as an overlay over the myocardium. There are no distinct regions with a different T1. After contrast administration the standard T1W IR was acquired to demonstrate the presence of DE, shown in the figure with an arrow. For both the rats a distinct region of bright signal is visible in the myocardium. These regions are also present, at the same location, in the post-contrast T1 maps. As can be seen from the overlay the T1 in the infarcted regions is clearly lower than the T1 of the healthy myocardium. The infarcted T1 is also similar in both the time points, 5-15 minutes and 16-26 minutes after administration, while the T1 of the healthy myocardium is already increasing in the second time point with respect to the first.

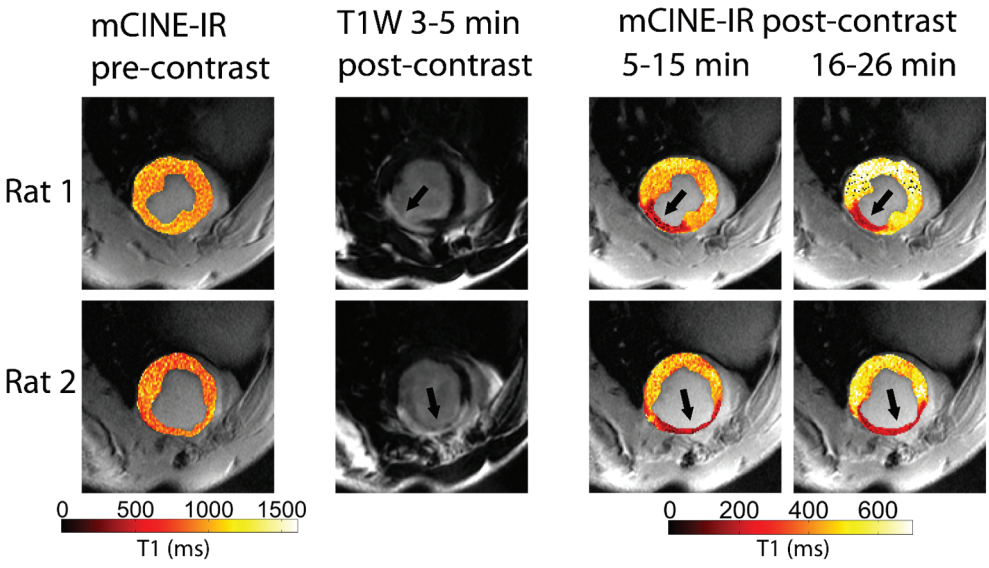


**Figure 7** The results of the DE experiments for both rats. The pre-contrast T1 map shows no distinct regions with a different T1. In the T1W images the DE of the infarct is clearly visible and indicated with an arrow. The post-contrast T1 maps show a substantial lowering of T1 in the infarcted region.

## Discussion

Our results have shown the reproducibility in vitro and in vivo of a T1 mapping technique based on the mCINE-IR sequence, applied on small animals. The dependency of the estimated T1 on heart rate for biological tissue is around 0.5 ms/bpm, as shown in Figure 4 and 5. The standard deviation of both the six recorded RR intervals and the heart rates of the reproducibility study was around 10 bpm, which would result in a T1 change of 5 ms. However, when the rats were under anesthesia it was sometimes observed that their heart rate slowly decreased during the scan, up to heart rate differences in the order of 50 bpm, corresponding with T1 changes of 25 ms. This is still only a small error in comparison with the T1 difference between the infarcted and healthy myocardium, as shown in Figure 7. However, in research where the goal is to detect smaller T1 differences the heart rates of the animals should be monitored to have the option to correct the T1 if large heart rate differences occur. But from the clear distinction in the T1 maps between infarcted and healthy myocardium, together with the repro-

ducibility results which show that the COV in vivo is below 5%, it is clear that mCINE-IR is a promising technique for measuring the T1 in the myocardium of small animals.
In our sequence, due to the continuous application of the small angle RF pulses the relaxation is characterized by an apparent time constant T1 (often referred as to T1*), which is shorter than the original T1. The relation between the observed T1* and T1 can be described with the following formula (35):

[4.]

with $\alpha$ flip angle in degrees and $T_R$ the repetition time of the small excitations. However, this correction is very sensitive to small changes in $\alpha$ and therefore $\alpha$ has to be known with a high precision. Although various B1 mapping methods exist (36,37), achieving such a precision a still a challenge. Another correction factor that is proposed and used in literature (30,35) is:

[5.]

where A and B are the two fitting constants from the signal model in equation 1. This correction factor can only be applied when the signal inversion recovery starts from the completely recovered equilibrium value. This is not the case since the magnetization has a smaller equilibrium value due to the constant RF pulse application.
The simulation results show that for a mixture of long and short T1 values a heart rate dependency is introduced that is not present in homogenous tissues. As the heart rate gets higher, $TR_{eff}$ gets shorter and a shorter part of the recovery can be sampled, which affects the estimation and causes the apparent T1 to be shorter. This is also shown by the results of the mixed phantom in Figure 4, which displayed a steeper heart rate dependency than each of the individual phantoms. However, the homogeneous solutions also show a mild heart rate dependency. Possible explanations are B1 inhomogeneities or a RF pulse profile that is not constant over the entire slice. When the flip angle changes over the volume, equation 4 shows that the apparent T1 will be influenced which could introduce a mixture of T1 values within a voxel or a region.
To address the heart rate dependency caused by a mixed signal an approach could be bi- or multi-exponential fitting. Several other works have tried this with mixed results. In (38) mono- and bi- exponential fitting was evaluated for both T1 and T2 mapping in the human brain. For the T1 estimations all the cases scored better with a mono-exponential fit. A problem of multi-exponential fittings is that the extra degrees of freedom increase the uncertainty of the T1 values. An iterative approach, starting with mono-exponential and increasing the number of fitted exponentials could be a solution. Likelihood ratio tests (39) could be applied to test whether the addition of extra variables really improves the estimation.
Another way to deal with the heart rate dependency could be to change $N_{RR}$ as demonstrated in (2). When the heart rate increases, $TR_{eff}$ decreases. By adding extra cycles the effective repetition time could then be increased again. However, this method has some limitations. It is not desirable to change the acquisition protocol during a scan in which heart rate changes occur. Also, only steps of at least one RR interval, around 160 ms, can be added to or subtracted from the $TR_{eff}$. However, this corresponds with heart rate changes of approximately 22 bpm and since that corresponds with a T1 change of only 11 ms, this step size could be small enough and could be an effective way to reduce heart rate dependency effects.
In the in vivo results, the fits were more successful on the anterior segments than on the inferior segments. The inferior segments are at the heart-lung interface which is known to give susceptibility problems (40). This could be a cause of the difference in results. In our case another source of error could come from the use of a surface coil, as the inferior segments are farther from the coil than the anterior segments, which lowers the SNR.

In conclusion, in this work the reproducibility of myocardial T1 mapping in small animals with mCINE-IR is evaluated and demonstrated to be good, and the capability to detect the T1 differences caused by DE is shown. It demonstrates that mCINE-IR is a promising new technique that could enable translational T1 mapping studies from small animal model to human with a single technique.

# References


1. Ashton, E. Quantitative MR in multi-center clinical trials. J Magn Reson Imaging 2010:31:279-288
2. Milanesi M, Barison A, Positano V, et al. Modified cine inversion recovery pulse sequence for the quantification of myocardial T1 and gadolinium partition coefficient 2012, J Magn Reson Imaging 2012:in press.
3. Iles L, Pfluger H, Phrommintikul A, et al. Evaluation of diffuse myocardial fibrosis in heart failure with cardiac magnetic resonance contrast-enhanced T1 mapping. J Am Coll Cardiol 2008:52:1574-1580.
4. Goldfarb JW, Arnorl S, Marguerite R. Gadolinium Pharmacokinetics of chronic myocardium infarcts: implications for late gadolinium-enhanced infarct imaging. J Magn Reson Imag 2009:30:763-770.
5. Edelman RR. Contrast-enhanced MR Imaging of the Heart: Overview of the Literature. Radiology 2004:232:653-668.
6. Kim, RJ, Fieno DS, Parrish TB, et al. Relationship of MRI delayed contrast enhancement to irreversible injury, infarct age, and contractile function. Circulation 1999: 100:1992-2002.
7. Klem RJ, Judd RM, Elliott M, et al. Improved detection of coronary artery disease by stress perfusion cardiovascular magnetic resonance with the use of delayed enhancement infarction imaging. 8, 2006, J Am Coll Cardiol 2006:47:1630-1638.
8. Ingkanisorn WP, Rhoads KL, Aletras AH, Kellman P, Arai AE. Gadolinium delayed enhancement cardiovascular magnetic resonance correlates with clinical measures of myocardial infarction. J Am Coll Cardiol 2004:43:2253-2259.
9. Sparrow PS, Messroghli DR, Reid S, Ridgway JP, Bainbridge G, Sivananthan MU. Myocardial TI mapping for detection of left ventricular myocardial fibrosis in chronic aortic regurgitation: pilot study. Am J Radiol 2006:187:W630:W635.
10. Messroghli DR, Walters K, Plein S, Sparrow P, Friedrich M, Ridgway J P, Sivananthan MU. Myocardial T1mapping: application to patients with acute and chronic myocardial infarction. Magn Reson Med 2007:58:34-40.
11. Piechnik SK, Ferreira VM, Dall'Armellina R. Shortened Modified Look-Locker Inversion recovery (ShMOLLI) for clinical myocardial T1-mapping at 1.5 and 3 T within 9 heartbeat breath-hold. J Card Magn Res 2010:12:69-80.
12. Broberg CS, Chugh SS, Conklin C, Sahn DJ, Jerosch-Herold M. Quantification of Diffuse Myocardial Fibrosis and Its Association With Myocardial Dysfunction in Congenital Heart Disease. Circulation 2010:3:727-734.
13. Protti A, Sirker A, Shah A, Botnar R. Late Gadolinium Enhancement of acute myocardial infarction in mice at 7T: Cine-flash versus inversion recovery. J Magn Reson Imaging 2010:32:878-886.
14. Liu W, Frank J. Detection and quantification of magnetically labeled cells by cellular MRI. Eur J Radiol 2009:70:258-264.
15. Daldrup-Link HE, Rudelius M, Metz S, et al. Cell tracking with gadophrin-2: a bifunctional contrast agent for MR imaging, optical imaging, and fluorescence microscopy. Eur J Nucl Med 2004:31:1312-1321.
16. Messroghli DR, Radjenovic A, Kozerke S. Modified Look-Locker inversion recovery (MOLLI) for high-resolution T1 mapping of the heart. et al. Magn Reson Med 2004:52:141-146.
17. Kawel N, Nacif M, Zavodni A, et al. T1 mapping of the myocardium: Intra-individual assessment of the effect of field strength, cardiac cycle and variation by myocardial region. J Card Magn Res 2012:1:27.
18. Waghorn B, Edwards T, Yang Y, et al. Monitoring dynamic alterations in calcium homeostasis by T1-weighted and T1-mapping cardiac manganese-enhanced MRI in a murine myocardial infarction model. NMR Biomed 2008:21:1102-1111.
19. Messroghli DR, Nordmeyer S, Buehrer M, et al. Small Animal Look-Locker Inversion Recovery (SALLI) for Simultaneous Generation of Cardiac T1 Maps and Cine and Inversion Recovery-prepared Images at High Heart Rates: Initial Experience. Radiology 2011:261:258-265.
20. Messroghli DR, Plein S, Higgins DM, et al. Human Myocardium: Single-Breath-hold MR T1 Mapping with High Spatial Resolution—Reproducibility Study. Radiology 2006:238:1004-1012.
21. Slavin GS, Song T, Stainsby JA. The effect of heart rate in Look-Locker Cardiac T1 mapping. Proceedings of the 18th Annual Meeting of ISMRM 2010 (abstract 2947).

22. Coolen BF, Geelen T, Paulis LEM, Nauerth A, Nicolay K, Strijkers GJ. Three-dimensional T1 mapping of the mouse heart using variable flip angle steady-state MR imaging. NMR in Biomedicine 2011:24:154-162.
23. Ho VB, Hood MN, Montequin M, Foo TK. Cine Inversion Recovery (IR): Rapid tool for optimized myocardial delayed enhancement imaging. Proceedings of the 13th Annual Meeting of the ISMRM 2005 (abstract 1675).
24. Goldfarb JW, Mathew ST, Reichek N. Quantitative breath-hold monitoring of myocardial gadolinium enhancement using inversion recovery TrueFISP. Magn reson Med 2005:53:367-371.
25. Gupta A, Lee VS, Chung Y-C, Babb JS, Simonetti OP. Myocardial infarction: optimization of inversion times at delayed contrast-enhanced MR imaging. Radiology 2004: 233:921-926.
26. Li XC, Ma B, Link T, et al. In vivo T1 and T2 mapping of articular cartilage in osteoarthritis of the knee using 3T MRI. Osteoarthritis Cartilage 2007:15:789-797.
27. Maier CF, Tan SG, Hariharan H, Potter HG. T2 quantitation of articular cartilage at 1.5T. J Magn Reson Med 2003:17:358-364.
28. Van Breuseghem I, Palmiere F, Peeters RR, Maes F, Bosmans HTC, Marchal GJ. Combined T1-T2 mapping of human femoro-tibial cartilage with turbo-mixed imaging at 1.5T. J Magn Reson Imaging 2005:22:368-372.
29. Sijbers J, Den Dekker AJ, Raman E, et al. Parameter estimation from magnitude MR images. Int J of Imag Sys and Tech 1999:10:109-114.
30. Deichmann R, Haase A. Quantification of T1 values by snapshot-FLASH NMR imaging. J Magn Reson 1992:96:608-612.
31. Feinstein JA, Epstein FH, Arai AE, et al. Using cardiac phase to order reconstruction (CAPTOR): a method to improve diastolic images. J Magn Reson Imaging 2005:7:794-798.
32. Thevenaz, P and Unser, M. Optimization of mutual information for multiresolution image registration. IEEE Transactions on Image Processing 2000:9:2083-2099.
33. Klein, S, Staring M, Murphy, M, et al. Elastix: a toolbox for intensity-based medical image registration. IEEE Transactions on Medical Imaging 2010:29:196-205.
34. Cerqueira MD, Weissman NJ, Dilsizian V. Standardized myocardial segmentation and nomenclature for tomographic imaging of the heart a statement for healthcare professionals from the cardiac imaging committee of the Council on Clinical Cardiology of the American Heart Association. Circulation 2002:105:539-542.
35. Deichmann R, Hahn D, Haase A. Fast T1 mapping on a whole-body scanner. Magn Reson Med 1999:42:206-209.
36. Yarnykh, VL. Actual flip-angle imaging in the pulsed steady state: A method for rapid three-dimensional mapping of the transmitted radiofrequency field. Magn Reson Med 2007:57:192-200.
37. Sacolick LI, Wiesinger F, Hancu I, Vogel MW. B1 mapping by Bloch-Siegert shift. Magn Reson Med 2010:63:1315-1322.
38. Larsson HBGW, Frederiksen J, Kjaer L, Henriksen O, Olesen. In vivo determination of T1 and T2 in the brain of patients with severe but stable multiple sclerosis. J. Magn Reson Med 2005:7:43-55.
39. Dickey DA, Fuller WA . Likelihood ratio statistics for autoregressive time series with a unit root. J Econ Society 1981:1057-1072.
40. Atalay MK, Poncelet BP, Kantor HL, Brady TJ, Weisskoff RM. Cardiac susceptibility artifacts arising from the heart-lung interface. Magn Reson Med 2001:45:341-345.

Chapter 8

# Discussion

In the past decades an upcoming use of stem cells to repair incurable, diseased tissue occurred. This relatively new field of *cell therapy* in itself holds great promise for a variety of diseases and disorders such as cancer, cardiovascular disease, neurodegenerative diseases, and musculoskeletal disorders by providing unique opportunities for tissue regeneration and targeted therapy or drug delivery (1–4). In both pre-clinical and clinical studies, therapeutic benefit of cell therapy for all these aspects has been demonstrated (5–10). However, the understanding of the processes by which stem cell therapy results in therapeutic benefit are poorly understood. The exact role and fate of stem cells in host tissue after transplantation is the subject of ongoing exploration. Therefore, the ability to track the fate of transplanted cells *in vivo*, has been the focus of increasing numbers of research efforts. Molecular and cellular imaging techniques enable a complete assessment of the implanted stem cells with regard to viability, proliferation, migration, differentiation and contribute to important insights into the mechanism of action of stem cell transplantation (11,12). The basic concept in cell imaging consists of the labeling of suitable cells with a powerful contrast agent to enable visualization by imaging modalities such as MRI. In this route from cell culture to MRI scanning, many hurdles need to be taken resulting in many research questions: the contrast agent has to be designed in such a way to facilitate an efficient uptake by the cells in culture. (i) The optimal labeling concentration needs to be titrated, with regard to both labeling efficiency and cellular toxicity. (ii) Not only direct cellular toxicity, but also occult permanent damage to the cells' genome needs to be established prior to cell transplantation. (iii) The contrast agent should not interfere with the cell's functionality, nor should it carry oncogenic potential. (iv) The contrast agent should be retained by the cell and not be transferrable to other cells *in vivo* (specificity). (v) The contrast agent should allow for a noninvasive assessment of cell engraftment and survival in the long term. (vi) The contrast agent should allow quantification using robust scanning sequences and sensitive coils. This thesis has addressed the above issues with regard to stem cell tracking using MRI, which will be discussed separately in the following sections.

## Feasibility of cell labeling with Gd-liposomes

We demonstrated the feasibility of labeling MSCs with liposome encapsulated Gd. Liposomes appeared an efficient vehicle to deliver Gd inside the cell. The attained intracellular Gd concentration was considerably higher -up to nearly 100 times- than most intracellular Gd loads reported in other studies (see Table I, chapter 2). The liposome as a vehicle thus perfectly met our expectations: to yield high intracellular buildup. Even higher Gd loads were achieved with increasing Gd addition, owing to the abundant uptake of cationic liposomal lipids (DOTAP) through binding to anionic charges in the cell membrane. The advantages of electrochemical interaction in cell labeling have been demonstrated before (13). Exploiting the attracting forces of opposing electrochemical charges therefore seems a promising strategy.

## Gd-liposomes and their impact on cell function and viability

With regard to toxicity, our results indicated a dose-dependent toxicity of Gd-liposomes. A slight toxic effect was observed, which was shown to be due to the lipid components rather than to Gd itself, in concordance with previous reports, indicating towards DOTAP as a cause of damage to cellular physiology (14).

Gd is toxic in its free, dechelated form, reported for the first time in 1992. Dechelated Gd is held responsible for the occurrence of the progressive, incurable and often crippling disease nephrogenic systemic fibrosis (NSF) in patients with renal failure. The awareness on this downside probably resulted in a collective reluctance to explore Gd-based formulations for

cellular labeling in the past decades, favoring T2 contrast agents like SPIO. This negative connotation of Gd was later on nuanced as being mainly a problem of the linear contrast agents. The macrocyclic Gadovist, as used in our thesis, is more resistant to dechelation and considered to be more stable (15) . Furthermore, NSF has only been identified to occur in patients with impaired renal function (16), allowing selection of suitable patient groups for cell transplantation. Although the long-term biological effect of intracellular Gd was not assessed, the absence of fluorescent Gd-liposomes in the cell nucleus renders their interference with the cell's DNA unlikely. Gd-liposome labeled MSCs maintained the multi-lineage differentiation capability, differentiating into both adipocytes and osteocytes. The absence of any Gd-related direct toxicity in our studies is therefore all the more important and offers opportunities to strengthen the future role for Gd as a cellular contrast agent.

## Quantification: the use of Gd-liposomes as a tool for functional read-out

In cell therapy, information on cell survival is of paramount importance since it is an absolute prerequisite of a favorable therapy outcome and because visualization of cell transplant viability will contribute to our understanding of transplanted cell fate *in vivo*. Without cell survival, the migration, engraftment, differentiation and integration into tissue obviously is impossible. The reported high cell death rates post-transplantation (17–19) play a role here as well. As histology provides only a snap-shot at a certain time point, an intra-individual longitudinal assessment of stem cell fate needs a different approach. The ability to noninvasively deduce basic functional information from cell transplants, would provide a powerful tool for evaluating therapy effect and initiate progress towards translational research.

Quantification is a trending item in radiology. Comparing the MRI contrast behavior of viable to nonviable Gd-liposomes MSCs, a striking visually perceivable difference existed: whereas viable cells appeared hypointense ('black'), nonviable Gd-liposome labeled cells appeared hyperintense ('white'). Although the concept of a quick visual perception is and has been of tremendous importance in radiology, a field which traditionally has leaned on the subjective assessment of morphological changes quantification, the value and importance of quantification is increasingly being recognized in radiology. To this end, we performed quantification of the T1 and T2 relaxation times of both SPIO- and Gd-labeled cells in a longitudinal follow-up study, with regard to cell viability, sensitivity and specificity. Little was known on the quantification of Gd-labeled cells. With regard to the quantification of MSCs labeled with SPIOs however, we expected some challenges. Reportedly, the intravoxel distribution of the agent (20–22), the macroscopic susceptibility artifacts (23) and the relatively large size of SPIOs (causing false-positives due to engulfment by macrophages) (24) were shown to cloud quantification attempts. Indeed, we confirmed SPIO-labeled cells to be difficult candidates for quantification. The persistent signal void from both viable and nonviable SPIO-labeled MSCs revealed no significant distinction in R2 relaxation rate, during longitudinal follow-up for two weeks. In contradistinction, a significantly lower R1 and higher R2 relaxation rate was measured for viable Gd-liposome labeled MSCs compared with nonviable cells. A cell status dependent contrast behavior was shown for Gd-liposome labeled cells, dynamically changing from quenching ('black signal') to dequenching ('white' signal) with ongoing proliferation.

## Quantification: specificity of signal

To ensure that perceived contrast or measured signal indeed is attributed to the originally labeled cells, the contrast label needs to be *labeled-cell specific*, even after death of the labeled cell. Ideally, the contrast label should be non-transferrable to other cell types. Irrelevant sig-

nal from non-viable Gd-MSCs resolved already at two hours post-transplantation, making Gd-liposomes a highly specific cell label. MRI signal from nonviable SPIO-MSCs however persisted for at least 15 days while at the original injection site. The superior performance of Gd-liposomes compared to SPIO was no surprise, realizing that SPIO reportedly produced false-positives up to 95 days post-transplantation (25), attributed to the persistence of SPIO-laden tissue macrophages after cell death (26). A high specificity is indispensable to detect cell graft rejection at an early stage. In contrast, the vast majority of extracellular complexed Gd is expected to diffuse out rapidly to end up intravascularly (27) as a result of its biological short half-life and low molecular weight. This allows an effective escape from reuptake by surrounding phagocytic cells. Indeed, only a tiny fraction of the initially injected Gd quantity, contained in nonviable MSCs, was retrieved at the site of injection at day 15.

## Quantification: sensitivity of signal

For translational purposes to the clinical setting, sensitivity is at least as essential as specificity, to facilitate investigation of the long-term fate of implanted stem cells. The MSCs, which had the luciferase construct incorporated, exhibited a tumoral growth rate, which was considered a serendipitous advantage as it offered insight in dynamic contrast transformation as a result of proliferation. Accelerated SPIO dilution in highly proliferating cells is thought to occur as a result of iron metabolism in the physiological cellular pathways (28). It was therefore no surprise that MRI signal from Gd-liposomes labeled MSCs remained longer visible than the signal void of diluting SPIO labeled MSCs. An additional problem of SPIOs, of which the availability SPIOs has become problematic since the cessation of their manufacturing for economic reasons (29), may have tipped the scales in cellular imaging in favor of Gd.

## Quenching effect

The 'black' (hypointense) signal generated by compartmentalized Gd is called "quenching" and is explained by the drop in r1 relaxivity caused by the decreased accessibility of $H_2O$ to compartmentalized (i.e. intracellular and/or intraliposomal) Gd (30,31). Our study was the first to show that the (de)quenching is related to cell viability and cell proliferation. Although the contrast range seems limited at first sight (black, white, or the grey in between), rules of thumb on the dynamic contrast behavior were defined, taking into account the pace at which contrast changes occur. To our belief, this is an important discovery, which can be added to the radiologist's tools equipment, evading the use of laborious off-line retrospective (and sometimes expensive) quantification techniques.

The quenching effect is dependent on several factors. Not only the compartmentalization state (viable vs non-viable state) is of influence, but also the availability of water in the proximity, the water exchange rate (dependent on the size of the liposomes), the Gd concentration per voxel and R2 effects play a role. These effects were all studied. For example, for equal voxel [Gd] less concentrated liposomes (0.3M Gd) yielded higher R1/R2 ratio because of the higher intraliposomal water fraction ($v_i$). Regarding compartmentalization, less membrane barriers means a higher R1/R2 ratio, effectuated by both R1 and R2 effects. Understanding the underlying principles allows one to tailor the optimal liposomal Gadolinium concentration according to the desired goal. Labeling cells with compartmentalized Gd is not simply a case of loading the vehicle to the maximum.

## Pre-clinical evaluation

To serve as a potential bridge towards a clinical translation we performed a preclinical evaluation in a cardiac environment. The aim was to assess the feasibility of quantification techniques in a four-dimensional dynamic environment (a beating heart), per se. After successfully testing a double inversion recovery BBFSE sequence for its robustness and reproducibility, the signal from luciferase expressing SPIO-labelled MSCs implanted in the heart was measured. No significant correlation was apparent between bioluminescent signal profiles and MRI signal evolution. We argued that several different confounders occurring in parallel may contribute to the ambiguous signal behavior in vivo, such as cell redistribution in the injection site, reabsorption of the injection medium, reuptake by bystander phagocytic cells or intracellular iron metabolism. Realizing that cell proliferation, cell migration, cell death, extracellular SPIO dispersion and aggregation all exhibit different relaxivities, we were able to demonstrate the difficulty to assess quantitatively in vivo, the properties of SPIO labeled cells by MRI.
With regard to T1 quantification, we also tested the reproducibility and sensitivity of the modified CINE inversion recovery (mCINE-IR) acquisition on rats for measuring the myocardial T1 at 7T. The published mCINE-IR acquisition on humans was applied on rats for the first time, enabling the possibility of translational studies with an identical sequence. These results showed that mCINE-IR is highly reproducible and that the sensitivity allows detecting T1 changes in the rat myocardium, offering new opportunities for Gd-labeled cell quantification. These results emphasize the translational challenges for SPIO as a cell label. Surely, other cell labels might as well encounter (a selection of) the mentioned issues, still making a swift clinical translation a major challenge. In general, small improvements in the field of sequence development, coil development the optimization of contrast labels, together with a tight collaboration between radiologists, basic MR researchers and MR physicists, might eventually result in a giant leap towards clinical practice.

## Future perspectives: Potential applications

Bearing in mind the ever ongoing shortage of donor organs, studies like these can be considered major breakthroughs and may ultimately turn out to be gamechangers in the field of cell therapy. We are convinced that, ever since the discovery of the 'reprogammability' of stem cells by Takahashi and Yamanaka in 2006 (32), more and more researchers will be attracted towards this field, demanding advanced methods to track their reprogrammed stem cells *in vivo.*
Realizing that liposomes allow for a tremendous build-up of contrast agent, it is thinkable that the application of Gd-loaded liposomes might be further elevated to a higher level by other researchers, aiming to *in vivo target* cells, expressing certain ligands, rather than to *label* them *in vitro*. This was already shown to be a realistic and viable approach in a recent report (33), showing that macrophages could be targeted *in vivo* specifically using phosphatidylserine-containing liposomes. The versatility of liposomes could finally be exploited to its fullest, combining a diagnostic contrast agent with a therapeutic agent ("theragnostics"). This fits very well in the currently emerging trend of personalized medicine, partially based on personal genomics (the personal genotyping of disease). Liposomes are to be seen as a potential important player in this new field of personalized medicine (34).
Instead of serving merely as a contrast label for studying the fate of transplanted stem cells, the application of Gd-liposomes could be extended into other fields as well. For example, the lack of intracellular Gd metabolism might prove beneficial in oncology. Recently, evidence accumulated in the field of oncology on the existence of a tumor subpopulation with distinct characteristics resembling stem cells, coined as cancer stem cell (CSCs) (35). Eradication of the stem-cell compartment of a tumor is hypothesized to be the key to cure cancer (36). As isolation of these CSCs is possible, labeling of these highly proliferating CSCs *in vitro* is theo-

retically possible. After implantation, this should allow to study the role of these CSCs by real time MR imaging *in vivo*, possibly offering new insights in cancer development *in vivo*.
Another possible application to think of, is to image *in vivo* the extent of tumor heterogeneity. As known, many tumors exhibit different regions with different biological behavior and expression of different markers. Targeting these specific markers by liposomes in the blood-pool might depict specific regions of interest in the tumor. This might visualize highly aggressive subregions to be able to better tune the therapy and to assess the response to therapy. It might also obviate the need for a histological biopsy, avoiding the problems which arise with sample errors, e.g. after taking a biopsy of a less aggressive region.

Stem cell therapy in its early days was embraced as the long-awaited solution to incurable diseases. Over the years, researchers in this field have had to acknowledge the complexity of stem cell therapy. Stem cell imaging has shown to be a strategic tool to elucidate some of the basic questions with regard to cell fate. This thesis contributed its parts by addressing several important questions with regard to cell labeling. Cell labeling with either SPIOs or Gd-liposomes {Kim, 2010 #399}was shown to be a feasible technique thus earning its place in the repertoire of cell therapy monitoring tools. Especially Gd-liposomes appear to be a user-friendly cell label candidate, allowing a functional read-out of cells *in vivo* both visually and a relatively easy and straightforward quantification. The absolute highlight in this thesis was the discovery that using Gd-liposomes stem cell fate (i.e. cell viability and cell proliferation) can be made apparent to the naked eye. In our opinion, this thesis adds a piece to the 'stem cell therapy' puzzle. Ongoing an upcoming collaborations across national and continental borders, bring new hope to further elucidate the 'black box' of stem cell fate *in vivo*.

# References


1. Cancedda R, Dozin B, Giannoni P, Quarto R. Tissue engineering and cell therapy of cartilage and bone. Matrix Biol J Int Soc Matrix Biol. 2003 Mar;22(1):81–91.
2. Corsten MF, Shah K. Therapeutic stem-cells for cancer treatment: hopes and hurdles in tactical warfare. Lancet Oncol. 2008 Apr;9(4):376–84.
3. Einstein O, Ben-Hur T. The changing face of neural stem cell therapy in neurologic diseases. Arch Neurol. 2008 Apr;65(4):452–6.
4. Smart N, Riley PR. The stem cell movement. Circ Res. 2008 May 23;102(10):1155–68.
5. Bang OY, Lee JS, Lee PH, Lee G. Autologous mesenchymal stem cell transplantation in stroke patients. Ann Neurol. 2005 Jun;57(6):874–82.
6. Brazelton TR, Rossi FM, Keshet GI, Blau HM. From marrow to brain: expression of neuronal phenotypes in adult mice. Science. 2000 Dec 1;290(5497):1775–9.
7. Dozin B, Malpeli M, Cancedda R, Bruzzi P, Calcagno S, Molfetta L, et al. Comparative evaluation of autologous chondrocyte implantation and mosaicplasty: a multicentered randomized clinical trial. Clin J Sport Med Off J Can Acad Sport Med. 2005 Jul;15(4):220–6.
8. Lipinski MJ, Biondi-Zoccai GGL, Abbate A, Khianey R, Sheiban I, Bartunek J, et al. Impact of Intracoronary Cell Therapy on Left Ventricular Function in the Setting of Acute Myocardial Infarction: A Collaborative Systematic Review and Meta-Analysis of Controlled Clinical Trials. J Am Coll Cardiol. 2007 Oct 30;50(18):1761–7.
9. Quarto R, Mastrogiacomo M, Cancedda R, Kutepov SM, Mukhachev V, Lavroukov A, et al. Repair of large bone defects with the use of autologous bone marrow stromal cells. N Engl J Med. 2001 Feb 1;344(5):385–6.
10. Winter EM, Grauss RW, Hogers B, van Tuyn J, van der Geest R, Lie-Venema H, et al. Preservation of left ventricular function and attenuation of remodeling after transplantation of human epicardium-derived cells into the infarcted mouse heart. Circulation. 2007 Aug 21;116(8):917–27.
11. Lee Z, Dennis JE, Gerson SL. Imaging stem cell implant for cellular-based therapies. Exp Biol Med Maywood. 2008 Aug;233(8):930–40.
12. Magnitsky S, Walton RM, Wolfe JH, Poptani H. Magnetic resonance imaging as a tool for monitoring stem cell migration. Neurodegener Dis. 2007;4(4):314–21.
13. Thorek DLJ, Tsourkas A. Size, charge and concentration dependent uptake of iron oxide particles by non-phagocytic cells. Biomaterials. 2008 Sep;29(26):3583–90.
14. Filion MC, Phillips NC. Toxicity and immunomodulatory activity of liposomal vectors formulated with cationic lipids toward immune effector cells. Biochim Biophys Acta. 1997 Oct 23;1329(2):345–56.
15. Karabulut N. Gadolinium deposition in the brain: another concern regarding gadolinium-based contrast agents. Diagn Interv Radiol. 2015;21(4):269–70.
16. Idée J-M, Port M, Dencausse A, Lancelot E, Corot C. Involvement of gadolinium chelates in the mechanism of nephrogenic systemic fibrosis: an update. Radiol Clin North Am. 2009 Sep;47(5):855–869, vii.
17. Müller-Ehmsen J, Whittaker P, Kloner RA, Dow JS, Sakoda T, Long TI, et al. Survival and development of neonatal rat cardiomyocytes transplanted into adult myocardium. J Mol Cell Cardiol. 2002 Feb;34(2):107–16.
18. van den Bos EJ, Davis BH, Taylor DA. Transplantation of skeletal myoblasts for cardiac repair. J Heart Lung Transplant Off Publ Int Soc Heart Transplant. 2004 Nov;23(11):1217–27.
19. van Laake LW, Passier R, Monshouwer-Kloots J, Verkleij AJ, Lips DJ, Freund C, et al. Human embryonic stem cell-derived cardiomyocytes survive and mature in the mouse heart and transiently improve function after myocardial infarction. Stem Cell Res. 2007 Oct;1(1):9–24.
20. Rad AM, Arbab AS, Iskander ASM, Jiang Q, Soltanian-Zadeh H. Quantification of superparamagnetic iron oxide (SPIO)-labeled cells using MRI. J Magn Reson Imaging JMRI. 2007 Aug;26(2):366–74.
21. Bowen CV, Zhang X, Saab G, Gareau PJ, Rutt BK. Application of the static dephasing regime theory to superparamagnetic iron-oxide loaded cells. Magn Reson Med. 2002 Jul;48(1):52–61.
22. Kotek G, van Tiel ST, Wielopolski PA, Houston GC, Krestin GP, Bernsen MR. Cell quantification: evolution of compartmentalization and distribution of iron-oxide particles and labeled cells. Contrast Media Mol Imaging. 2012 Apr;7(2):195–203.

23. Arbab AS, Janic B, Haller J, Pawelczyk E, Liu W, Frank JA. In Vivo Cellular Imaging for Translational Medical Research. Curr Med Imaging Rev. 2009 Feb 1;5(1):19–38.
24. Luciani N, Wilhelm C, Gazeau F. The role of cell-released microvesicles in the intercellular transfer of magnetic nanoparticles in the monocyte/macrophage system. Biomaterials. 2010 Sep;31(27):7061–9.
25. Baligand C, Vauchez K, Fiszman M, Vilquin J-T, Carlier PG. Discrepancies between the fate of myoblast xenograft in mouse leg muscle and NMR label persistency after loading with Gd-DTPA or SPIOs. Gene Ther. 2009 Jun;16(6):734–45.
26. Terrovitis J, Stuber M, Youssef A, Preece S, Leppo M, Kizana E, et al. Magnetic Resonance Imaging Overestimates Ferumoxide-Labeled Stem Cell Survival After Transplantation in the Heart. Circulation. 2008 Mar 25;117(12):1555–62.
27. Aime S, Caravan P. Biodistribution of gadolinium-based contrast agents, including gadolinium deposition. J Magn Reson Imaging JMRI. 2009 Dec;30(6):1259–67.
28. Weissleder R, Stark DD, Engelstad BL, Bacon BR, Compton CC, White DL, et al. Superparamagnetic iron oxide: pharmacokinetics and toxicity. AJR Am J Roentgenol. 1989 Jan;152(1):167–73.
29. Corot C, Warlin D. Superparamagnetic iron oxide nanoparticles for MRI: contrast media pharmaceutical company R&D perspective. Wiley Interdiscip Rev Nanomed Nanobiotechnol. 2013 Oct;5(5):411–22.
30. Strijkers GJ, Mulder WJM, van Heeswijk RB, Frederik PM, Bomans P, Magusin PCMM, et al. Relaxivity of liposomal paramagnetic MRI contrast agents. Magn Reson Mater Phys Biol Med. 2005 Sep;18(4):186–92.
31. Terreno E, Sanino A, Carrera C, Castelli DD, Giovenzana GB, Lombardi A, et al. Determination of water permeability of paramagnetic liposomes of interest in MRI field. J Inorg Biochem. 2008 Jun;102(5–6):1112–9.
32. Takahashi K, Yamanaka S. Induction of pluripotent stem cells from mouse embryonic and adult fibroblast cultures by defined factors. Cell. 2006 Aug 25;126(4):663–76.
33. Geelen T, Yeo SY, Paulis LEM, Starmans LWE, Nicolay K, Strijkers GJ. Internalization of paramagnetic phosphatidylserine-containing liposomes by macrophages. J Nanobiotechnology. 2012 Aug 28;10:37.
34. Petersen AL, Hansen AE, Gabizon A, Andresen TL. Liposome imaging agents in personalized medicine. Adv Drug Deliv Rev. 2012 Oct;64(13):1417–35.
35. Jordan CT, Guzman ML, Noble M. Cancer stem cells. N Engl J Med. 2006 Sep 21;355(12):1253–61.
36. Al-Hajj M, Becker MW, Wicha M, Weissman I, Clarke MF. Therapeutic implications of cancer stem cells. Curr Opin Genet Dev. 2004 Feb;14(1):43–7.

Chapter 9

# Summary/Samenvatting
# Curriculum vitae
# PhD portfolio
# Publications
# Acknowledgements

# Summary

This thesis has addressed important issues with regard to stem cell tracking using MRI, which will be summarized separately in the following sections.
In **chapter 2** cell labeling was performed with water soluble Gadolinium-DTPA containing liposomes, to allow for cell tracking by MRI. Liposomes were used to assure a highly concentrated intracellular buildup of Gd, aiming to overcome the relatively low MRI sensitivity of Gd (as compared to $T_2$ contrast agents). Liposomes were positively charged (cationic) to facilitate uptake by binding to anionic charges in the cell membrane of bone marrow-derived mesenchymal stem cells (MSCs). We determined the cellular Gd load by variations in labeling time (1h, 4h and 24h) and liposome concentration (125, 250, 500, 1000 µM lipid), closely monitoring effects on cell viability, proliferation rate and differentiation ability. Labeling was both time- and dose-dependent. Labeling for 4h was most efficient regarding the combination of processing time and final cellular Gd uptake. Labeling for 4h with low-dose concentration (125 µM lipid, corresponding to 52±3 µM Gd) yielded an intracellular load of 30±2.5 pg Gd cell-1, without any effects on cell viability, proliferation and cell differentiation. Gd-liposomes, co-labeled with fluorescent dyes, exhibited a prolonged cellular retention, with an endosomal distribution pattern. In vitro assay over 20 days demonstrated a drop in the average Gd load *per cell,* as a result of mitosis. However, there was no significant change in the sum of the Gd load in all daughter cells at endpoint (20 d.), indicating an excellent cellular retention of Gd. MSCs labeled with Gd-liposomes were imaged with MRI at both 1.5T and 3.0T, resulting in excellent visualization both *in vitro* and *in vivo.* Prolonged *in vivo* imaging of 500,000 Gd-labeled cells was possible for at least two weeks (3.0T).
In **chapter 3** the contribution of liposomal Gd concentration ([Gd]), size and compartmentalization state on relaxivity quenching were assessed. To this end, dependency of SI on intraliposomal [Gd] was assessed comparing three different intraliposomal [Gd] (0.3, 0.6 and 1.0M Gd) in both small (80nm) and large (120 nm) cationic liposomes. In addition, five compartmentalization states were compared: free Gd, intact Gd-liposomes, ruptured Gd-liposomes, Gd-liposomes in intact cells and Gd-liposomes in ruptured cells (simulating cell death). Gd also causes $R_2$ effects, which is often overlooked. Therefore both $R_1$ and $R_2$ relaxation rate of a dilution range were measured by $T_1$- and $T_2$-mapping on a 7T scanner. As the unidirectional water efflux rate (outbound across the liposome membrane, $\kappa_{lo}$) is proportional to the surface/volume ratio, smaller liposomes yielded a consistently higher $R_1$ than larger liposomes. For equal voxel [Gd] less concentrated liposomes (0.3M Gd) yielded higher $R_1$/ $R_2$ ratio because of the higher liposomal water fraction ($v_l$). Gd exhibits a dualistic behavior: from hypointensity to hyperintensity to hypointensity, with decreasing [Gd]. Regarding compartmentalization less membrane barriers means a higher $R_1$/ $R_2$ ratio. Gd-liposomes thus exhibit a versatile contrast behaviour, dependent on the compartmentalization state, liposomal size, intraliposomal [Gd] and liposome number. Both $R_1$ and $R_2$ effects contribute to this. The versatility allows one to tailor the optimal liposomal formulation to desired goals in cell labeling and tracking.
In **chapter 4** we investigated possible differences in $R_1$, $R_2$ or $R_2$* relaxation rate as a measure of overall cell viability for mesenchymal stem cells labeled with Gd-liposomes (Gd-MSCs) or iron oxide nanoparticles (SPIO-MSCs). Cells were also transduced with a luciferase vector, facilitating a correlation between MRI findings and cell viability using bioluminescence imaging (BLI). Viable Gd-MSCs were clearly distinguishable from nonviable Gd-MSCs under both *in vitro* and *in vivo* conditions, clearly differing quantitatively ($\Delta R_1$ and $\Delta R_2$) as well as by visual appearance (hypo- or hyperintense contrast). Immediately post-injection, viable Gd-MSCs caused a substantially larger $\Delta R_2$ and lower $\Delta R_1$ effect compared to nonviable MSCs. With time, the $\Delta R_1$ and $\Delta R_2$ relaxation rate showed a good negative correlation with increasing cell number following proliferation. Upon injection, no substantial quantitative or visual differences between viable and non-viable SPIO-MSCs were detected. Moreover, non-viable

SPIO-MSCs caused a persisting signal void *in vivo*, compromising the specificity of this contrast agent. *In vivo* persistence of SPIO particles was confirmed by histological staining. A large difference was found between SPIO- and Gd-labeled cells in the accuracy of MR relaxometry in assessing the cell viability status. Gd-liposomes provide a more accurate and specific assessment of cell viability than SPIO particles. Viable Gd-cells can be differentiated from nonviable Gd-cells even by visual interpretation. These findings clearly indicate Gd to be the favourable contrast agent in qualitative and quantitative evaluation of labeled cell fate in future cell therapy experiments.

**Chapter 5** presents an overview of the many facets of cell tracking in cardiac repair. Stem cell therapies hold the great promise and interest for cardiac regeneration among scientists, clinicians and patients. However, advancement and distillation of a standard treatment regimen are not yet finalised. Recent developments in the imaging biosciences offer promising opportunities. Thus far, these technical and protocol refinements have played a critical role not only in the evaluation of the recovery of cardiac function but also in providing important insights into the mechanism of action of stem cells. Molecular imaging, in its many forms, has rapidly become a necessary tool for the validation and optimisation of stem cell engrafting strategies in preclinical studies. These include a suite of radionuclide, magnetic resonance and optical imaging strategies to evaluate non-invasively the fate of transplanted cells. In this review, we highlight the state-of-the-art of the various imaging techniques for cardiac stem cell tracking presenting the strengths and limitations of each approach, with a particular focus on clinical applicability.

**Chapter 6** handles on the *in vivo* MRI mapping of iron oxide labeled stem cells transplanted in the heart. In various stem cell therapy approaches poor cell survival has been recognized as an important factor limiting therapeutic efficacy. Therefore noninvasive monitoring of cell fate is warranted for developing clinically effective stem cell therapy. In this chapter we investigated the feasibility of the use of voxel-based $R_2$ mapping as a tool to monitor the in vivo stem cell fate in myocardium when the cells are labeled with iron oxide particles (SPIO). To this end, single cardiac phase with cardiac triggered double inversion black blood 2D fast Spin echo (BBFSE) images were acquired on the short axis of hearts. Reproducibility studies were performed in normal rats imaged in different sessions. A double cell labeling approach was used in which mesenchymal stem cells were transduced with the luciferase gene and subsequently labeled with ferumoxide particles (SPIO). Living labeled cells were injected in the myocardium of healthy Wistar rats. For control purposes animals were also injected with dead, labeled cells or saline. Cell fate was monitored over a period of 8 weeks by bioluminescence imaging following injection of D-Luciferine and quantitative magnetic resonance imaging, using a black blood FSE sequence with multiple echo times. Bioluminescence imaging revealed a significant increase of cell number during the first week (peak day 7) with a steep decrease of cell numbers to undetectable levels during the second week. MR imaging showed a sharp increase of $R_2$ values shortly after injection at the injection site (peak day 5), followed by a very gradual decrease of $R_2$ over a period of 15 days. No difference in appearance on $T_2$-weighted images nor in $R_2$-values was observed between living and dead cells over the entire time period studied. No significant correlation between the bioluminescence optical data and $R_2$ values were observed. Quantitative MR imaging by means of $R_2$-mapping is not suitable for the *in vivo* assessment of stem cell fate in rat myocardium as validated by bioluminescence imaging. These results do not follow previous *in vitro* reports where it was proposed that based on the difference in $r_2$ relaxivity between intra-cellular and extra-cellular SPIO, living cells may be distinguished from death cells based on their $R_2$ profile. Cell proliferation, cell migration, cell death, extracellular SPIO dispersion or aggregation exhibit different relaxivities. In vivo these processes happen simultaneously, making quantification very complex, if not impossible.

In **chapter 7** we evaluated the reproducibility and sensitivity of the modified CINE inversion recovery (mCINE-IR) acquisition on rats for measuring the myocardial $T_1$ at 7T. The priorly published mCINE-IR acquisition on humans was applied on rats for the first time, enabling

the possibility of translational studies with an identical sequence. Simulations were used to study signal evolution and heart rate dependency. Gadolinium phantoms, a heart specimen and a healthy rat were used to study reproducibility. Two cryo-infarcted rats were scanned to measure delayed enhancement (DE). In the phantom reproducibility studies the $T_1$ measurements had a maximum coefficient of variation (COV) of 1.3%. For the *in vivo* reproducibility the COV was below 4.8% in the anterior cardiac segments. In simulations, phantoms and specimens a heart rate dependency of approximately 0.5 ms/bpm was present. The $T_1$ maps of the cryo-infarcted rats showed a clear lowering of $T_1$ in de DE region. The results show that mCINE-IR is highly reproducible and that the sensitivity allows detecting $T_1$ changes in the rat myocardium.

# Samenvatting

In dit proefschrift worden enkele belangrijke kwesties behandeld met betrekking tot de beeldvorming van stamcellen met MRI. Hieronder zullen de afzonderlijke hoofdstukken achtereenvolgens worden samengevat.

In **hoofdstuk 2** werden stamcellen geladen met gadolinium(Gd)-DTPA bevattende liposomen, om deze cellen vervolgens te kunnen visualiseren met MRI technieken. Om de relatief lage MRI sensitiviteit van Gd (vergeleken met T2 contrastmiddelen) trachten te overwinnen, werden liposomen als compacte en efficiënte contrastdragers gebruikt teneinde een zeer geconcentreerde intracellulaire Gd concentratie te bereiken. Dankzij de positieve lading van de liposomen was een effectieve opname door binding aan anionische ladingen in de celmembraan van uit beenmerg afkomstige mesenchymale stamcellen (MSCs) goed mogelijk. Wij hebben de uiteindelijke intracellulaire Gd concentratie bepaald voor verschillende incubatietijden (1, 4 en 24 uur) en verschillende intraliposomale Gd concentraties (125, 250, 500, 1000 µM lipiden), waarbij effecten op de levensvatbaarheid van de cellen, op de proliferatiesnelheid en het vermogen tot differentiatie nauwlettend werden bestudeerd. De uiteindelijke intracellulaire Gd concentratie was zowel tijd- en dosis-afhankelijk. Een incubatietijd van 4 uur was het meest efficiënt met betrekking tot de combinatie van de doorlooptijd en de uiteindelijke intracellulaire Gd opname. Een incubatietijd van 4 uur met de laagste liposoom concentratie (125 µM lipiden, overeenkomend met 52 ± 3 µM Gd) leverde een intracellulaire Gd concentratie op van 30 ± 2,5 pg Gd per cel, zonder enig effect op levensvatbaarheid van de cellen, proliferatie en cel differentiatie. Gd-liposomen, welke tevens waren uitgerust met fluorescente kleurstoffen, verdeelden zich in de cel over endosomen en vertoonden geen microscopisch waarneembare lekkage. *In vitro* studies gedurende 20 dagen lieten een daling zien in de gemiddelde Gd concentratie per cel als gevolg van mitose. Het feit dat de totale Gd hoeveelheid in alle cellen echter gelijk bleef, duidt op een goede intracellulaire retentie van het contrast. MSCs welke geladen waren met Gd-liposomen konden uitstekend afgebeeld worden met MRI bij een veldsterkte van 1.5T en 3.0T, zowel *in vitro* als *in vivo*. Een cluster van zeker 500.000 met Gd-liposomen geladen cellen konden met MRI zichtbaar gemaakt worden voor ten minste twee weken (bij 3.0T).

In **hoofdstuk 3** werd de invloed van de intraliposomale Gd concentratie ([Gd]), de liposomale grootte en de compartimentalisatie op relaxiviteit 'quenching' bepaald. Daartoe werd bekeken in hoeverre variaties in intraliposomale [Gd] (0,3, 0,6 en 1,0 M Gd) en variaties in liposomale grootte (80 nm en 120 nm) kationische liposomen de signaalintensiteit (SI) beinvloeden. Daarnaast werd ook het effect van verschillende vormen van compartimentalisatie bestudeerd: vrij Gd, intacte Gd-liposomen, afgebroken Gd-liposomen, Gd-liposomen in intacte cellen en Gd-liposomen in geruptureerde cellen (celdood simulatie). Naast de bekende R1 effecten veroorzaakt Gd ook - vaak genegeerde - R2 effecten. Daarom werd zowel het R1 als het R2 relaxatie tempo van een seriële verdunning gemeten door T1 en T2-mapping op een 7T scanner. Aangezien de unidirectionele water efflux snelheid (uitgaand over het liposoommembraan, $\kappa_{lc}$) evenredig is met de oppervlakte / volumeverhouding, leverden kleinere liposomen een consistent hogere R1 relaxatie tempo op dan grotere liposomen. Bij gelijkblijvende voxel [Gd] bleken de minst geconcentreerde liposomen (0,3 M Gd) de hoogste R1/R2 verhouding te hebben, als gevolg van een grotere extraliposomale waterfractie ($v_p$). Gd vertoont een dualistisch gedrag: van hypointensiteit tot hyperintensiteit en gradueel weer terug naar hypointensiteit, met afnemende [Gd]. Met betrekking tot compartimentalisatie kan gesteld worden dat minder membraanbarrières een hogere R1/R2 ratio betekent. Gd-liposomen worden dus gekenmerkt door een veelzijdig contrast gedrag, afhankelijk van de compartimentalisatie, de liposomale grootte, de intraliposomale [Gd] en het liposoom aantal. Zowel R1 en R2 effecten dragen hieraan bij. De veelzijdigheid maakt het mogelijk om de optimale liposomale formulering aan te passen aan de gewenste doelen in cel labeling en tracking.

In **hoofdstuk 4** onderzochten we mogelijke verschillen in R1, R2 of R2* relaxatie snelheid als maat voor cellulaire levensvatbaarheid voor mesenchymale stamcellen gelabeld met hetzij Gd-liposomen (Gd-MSC) hetzij ijzeroxide nanodeeltjes (SPIO-MSC's). De cellen werden ook genetisch gemodificeerd en uitgerust met een luciferase vector, om een correlatie tussen MRI bevindingen en de levensvatbaarheid van de cellen met behulp van bioluminescentie imaging (BLI) te faciliteren. Levende Gd-MSC's waren duidelijk te onderscheiden van dode Gd-MSCs onder zowel *in vitro* als *in vivo* omstandigheden, zowel kwantitatief (op basis van duidelijke verschillen in R1 en R2), alsook kwalitatief (hypo- of juist hyperintens contrast). Onmiddellijk na de injectie, veroorzaakten levende Gd-MSC's een aanzienlijk groter $\Delta R_2$ en lager $\Delta R_1$ effect in vergelijking met dode MSC's. Na verloop van tijd, lieten zowel de $\Delta R_1$ als de $\Delta R_2$ relaxatie snelheid een goede negatieve correlatie zien met toenemend aantal cellen na proliferatie. Na injectie werden geen substantiële kwantitatieve of visuele verschillen tussen levende en dode SPIO-MSC's gedetecteerd. Bovendien veroorzaakten dode SPIO-MSC's een aanhoudend signaalverlies *in vivo*, hetgeen ten koste gaat van de specificiteit. Persisterende aanwezigheid van SPIO deeltjes *in vivo* werd bevestigd door histologische kleuring. Met betrekking tot de beoordeling van de cel levensvatbaarheid blijkt er dus een groot verschil te bestaan tussen SPIO- en Gd-gelabelde cellen in de nauwkeurigheid van MR relaxometrie. Met Gd-liposomen is een meer accurate en specifieke beoordeling van de levensvatbaarheid van de cellen mogelijk dan met SPIO deeltjes. Levende Gd-gelabelde cellen kunnen worden onderscheiden van dode Gd-cellen, zelfs door visuele interpretatie. Deze resultaten wijzen in de richting van Gd(-liposomen) als hèt contrastmiddel bij voorkeur in de kwalitatieve en kwantitatieve evaluatie van gelabelde cellen in toekomstige celtherapie experimenten.

**Hoofdstuk 5** geeft een overzicht van de vele facetten van cel tracking in cardiale regeneratie. Stamceltherapie is een veelbelovende therapie welke de interesse heeft van vele wetenschappers, artsen en patiënten. Zowel de voortschrijding als de vormgeving in een standaard behandelingsprotocol zijn echter nog verre van voltooid. Recente ontwikkelingen in de beeldvormingsbiowetenschappen zijn onmisbaar geworden. De technische en protocollaire verfijningen op dat vlak hebben een cruciale rol gespeeld bij de evaluatie van het herstel van de hartfunctie maar ook inzicht verschaft in het mechanisme van de werking van stamcellen. Moleculaire beeldvorming, in zijn vele vormen, is in korte tijd een noodzakelijk instrument voor de validatie en optimalisatie van stamceltransplantatie in preklinische studies geworden. Deze omvatten een reeks van radionuclide, magnetische resonantie en optische beeldvorming strategieën om het lot van de getransplanteerde cellen op een niet-invasieve wijze te evalueren. In deze review is er aandacht voor de state-of-the-art van de verschillende beeldvormende technieken voor cardiale stamcel tracking, waarbij de sterke en zwakke punten van elke benadering de revue passeren, met een bijzondere aandacht voor de klinische toepasbaarheid.

**Hoofdstuk 6** is een *in vivo* studie naar de mogelijkheid tot MRI kwantificatie van met ijzeroxide geladen stamcellen, welke getransplanteerd werden in het hart. In diverse stamceltherapie studies wordt de matig tot slechte overleving van de getransplanteerde cel erkend als een belangrijke limiterende factor voor de therapeutische werkzaamheid. Daarom kan niet-invasieve monitoring van het lot van de getransplanteerde cel een belangrijke bijdrage leveren aan het ontwikkelen van klinisch effectieve stamceltherapie. In dit hoofdstuk onderzochten we de uitvoerbaarheid van het gebruik van voxel-gebaseerde R2 mapping als een instrument om *in vivo* het lot van stamcellen, geladen met ijzeroxidedeeltjes (SPIO), te kunnen monitoren in het myocardium. Daartoe werden met een speciale MRI sequentie (BBFSE) korte as beelden van het hart vervaardigd. De reproduceerbaarheid van de metingen met deze sequentie werden bepaald in gezonde ratten, welke gescand werden in verschillende sessies. De gebruikte cellen bevatten tevens het luciferasegen om de cellulaire levensvatbaarheid te kunnen valideren. Levende gelabelde cellen werden geïnjecteerd in het myocardium van gezonde Wistar ratten. Voor controledoeleinden werden de dieren ook geïnjecteerd met dode gelabelde cellen of zoutoplossing. De geïnjecteerde cellen werden gevolgd over een periode van 8 weken met biolu-

minescentie beeldvorming en kwantitatieve MRI. Bioluminescentie beeldvorming toonde een aanzienlijke toename van het aantal cellen tijdens de eerste week (piek dag 7) met een sterke afname van celaantallen tot onwaarneembare niveaus tijdens de tweede week. MRI kwantificatie toonde een sterk verhoogde R2 relaxatiesnelheid kort na injectie op de injectieplaats (piek op dag 5), gevolgd door een geleidelijke afname van de R2 relaxatiesnelheid gedurende 15 dagen. Op de T2-gewogen beelden waren noch visuele noch kwantitatieve (R2 waarden) verschillen merkbaar tussen levende en dode cellen gedurende de gehele periode. Er werd geen significante correlatie tussen de bioluminescentie waarden enerzijds en de R2 waarden anderzijds waargenomen. Dankzij de validatie middels bioluminescentie is dus gebleken dat SPIO niet geschikt is om *in vivo* het lot van stamcellen in het myocardium te bepalen middels kwantitatieve MR beeldvorminng (R2-mapping). Deze resultaten staan in schril contrast met eerdere *in vitro* studies waarin werd voorgesteld dat levende cellen van dode cellen onderscheiden konden worden op basis van het verschil in r2 relaxiviteit tussen intracellulair en extracellulair SPIO. Celproliferatie, celmigratie, celdood, extracellulaire SPIO dispersie of aggregatie vertonen verschillende r2 relaxiviteit. *In vivo* kunnen deze processen gelijktijdig gebeuren, waardoor kwantificatie zeer complex, zo niet onmogelijk is.

In **hoofdstuk 7** evalueerden we de reproduceerbaarheid en de gevoeligheid van een gemodificeerde CINE inversie sequentie (mCINE-IR) op ratten voor het meten van de myocardiale longitudinale relaxatietijd (T1) bij 7T. De reeds eerder gepubliceerde mCINE IR-acquisitie op mensen werd toegepast op ratten voor de eerste keer, met het oog op toekomstige translationele studies. Simulaties werden gebruikt om de signaal evolutie en hartslag afhankelijkheid te bestuderen. Gadolinium fantomen, een monster van het hart (specimens) en een gezonde rat werden gebruikt om de reproduceerbaarheid te bestuderen. Twee ratten, waarbij een cryo-infarct geïnduceerd was, werden gescand om de vertraagde aankleuring van het myocard (delayed enhancement, DE) te meten. In de fantoom reproduceerbaarheid studies hadden de T1 metingen een maximale variatiecoëfficiënt (COV) van 1,3%. Voor de *in vivo* reproduceerbaarheid was de COV minder dan 4,8% in de voorste cardiale segmenten. In simulaties, fantomen en specimens was een hartslag afhankelijkheid van ongeveer 0,5 ms / bpm aanwezig. De T1 metingen van de cryo-infarct ratten toonden een duidelijke verlaging van de T1 in de DE-regio. De resultaten tonen dat mCINE-IR een zeer reproduceerbare en gevoelige techniek is die het mogelijk maakt om T1 veranderingen in een rat myocardium te detecteren.

# Curriculum Vitae

**Personal Information**

| | |
|---|---|
| Name | Jamal Guenoun |
| Nationality | Dutch, Moroccan |
| Place, DOB | The Hague, 22 January 1982 |

**Education/Diplomas**

| | |
|---|---|
| 2016 | European Diploma in Radiology (EDiR) |
| 2007 | Medicine<br>Erasmus University Rotterdam, Rotterdam, the Netherlands |
| 2000 | Gymnasium (*cum Laude*)<br>Gymnasium Haganum, 's-Gravenhage |

**Professional Experience**

| | |
|---|---|
| 2016 – 2017 | Fellowship Musculoskeletal Radiology<br>Erasmus Medical Center, Rotterdam, the Netherlands |
| 2015 | Visiting internship musculoskeletal radiology (prof. dr. J. Gielen)<br>University Hospital Antwerpen (UZA), Belgium |
| 2012 – 2016 | Resident Radiology, sub-specialization musculoskeletal radiology<br>Erasmus Medical Center, Rotterdam, the Netherlands |
| 2008 – 2012 | PhD research<br>Molecular Imaging Group, Dept. of Radiology<br>Erasmus Medical Center, Rotterdam, the Netherlands |
| 2007 – 2008 | Resident Radiology<br>Erasmus Medical Center, Rotterdam, the Netherlands |

**Honours and Awards**

| | |
|---|---|
| 2015 | Invest in the Youth Award For abstract *'Distinguishing viable from dead transplanted stem cells by Gadolinium-nanoparticles'*<br>European Congress of Radiology (ECR), Vienna, Austria |
| 2015 | Award for best oral presentation *'Distinguishing viable from dead transplanted stem cells by Gadolinium-nanoparticles'*<br>European Congress of Radiology (ECR), Vienna, Austria |
| 2009 | Young Investigator Travel Stipend Award For abstract "*Quantification of r1 and r2 relaxivity of rat mesenchymal stem cells labelled with Gd-DTPA liposomes for cell tracking at 3,0T*"<br>World Molecular Imaging Congress, Montreal, Canada |

# Portfolio

## Oral communications at meetings

| Date | Title | Institution/Event | Location | ECTS |
|---|---|---|---|---|
| March 4-8 2015 | Making use of the intrinsic Gadolinium quenching effect for cellular imaging, a bimodal approach with BLI validation | European Congress of Radiology (ECR) | Vienna, Austria | 1 |
| March 7-11 2013 | Can MRI distinguish viable from dead stem cells? | European Congress of Radiology (ECR) | Vienna, Austria | 1 |
| Sept 30 2011 | Cellular imaging: In vivo assessment of Gd- or SPIO-labeled cell graft viability, combining MRI and bioluminescence imaging | Radiologendagen | 's-Hertogenbosch | 1 |
| May 7-8 2009 | Gd-liposomes for cell tracking | ENCITE meeting | Prague, Czech republic | 1 |
| Sept 30-Oct 4 2009 | Contrast behavior of Gd-liposome labeled MSCs reflects functional cell status in vivo | ESMRMB (European Society for Magnetic Resonance in Medicine and Biology) | Antalya, Turkey | 1 |
| Nov 30-Dec 4 2009 | Visualizing in vivo cellular viability on MRI using Gd-DTPA liposome labeled MSCs | Radiological Society of North America (RSNA) | Chicago, USA | 1 |
| Nov 26 2009 | Using Gd-DTPA liposome labeled mesenchymal stem cells in rat skeletal muscle as a tool for functional cell status in vivo | Imagination | Nijmegen, the Netherlands | 1 |

**Subtotal (ECTS): 7**

## Poster presentations at meetings

| Date | Title | Institution/Event | Location | ECTS |
|---|---|---|---|---|
| Nov 27-Dec 02 2011 | In vivo R2 mapping of SPIO-labeled MSC viability in the rat heart with bioluminescence validation | Radiological Society of North America (RSNA) | Chicago, USA | 1 |
| Nov 27-Dec 02 2011 | In vivo assessment of Gd- or SPIO-labeled cell graft viability: a bimodal approach combining MRI and bioluminescence imaging | Radiological Society of North America (RSNA) | Chicago, USA | 1 |
| Nov 27-Dec 02 2011 | Quantification of viable Gd-liposome labeled cells in vivo with MRI mapping with bioluminescence validation | Radiological Society of North America (RSNA) | Chicago, USA | 1 |
| June 19-21 2011 | Optimizing the cell labeling strategy with cationic Gd-liposomes: Longitudinal in vivo follow up of Gd-labeled MSCs | European Society for Molecular Imaging (ESMI) | Leiden, the Netherlands | 1 |
| June 19-21 2011 | In vivo R2 mapping of SPIO-labeled MSC viability in the rat heart with bioluminescence validation | European Society for Molecular Imaging (ESMI) | Leiden, the Netherlands | 1 |
| June 19-21 2011 | Quantification of Gd-liposome-labeled cell number in vivo using T1 and T2 MRI mapping techniques, validated by BLI | European Society for Molecular Imaging (ESMI) | Leiden, the Netherlands | 1 |
| May 27-31 2009 | Using Gd-DTPA liposome labeled mesenchymal stem cells in rat skeletal muscle as a tool for functional cell status in vivo | European Society for Molecular Imaging (ESMI) | Barcelona, Spain, | 1 |
| Sep 22-26 2009 | MRI tracking of ultrasound guided intramyocardially injected stem cells | World Molecular Imaging Congress (WMIC) | Montreal, Canada | 1 |

| | | | | |
|---|---|---|---|---|
| Sep 22-26 2009 | Quantification of the r1 and r2 relaxivities of mesenchymal stem cells with Gd-DTPA liposomes at 1.5 and 3.0T | World Molecular Imaging Congress (WMIC) | Montreal, Canada | 1 |
| Sep 30-Oct 4 2009 | Using Gd-DTPA liposome labeled mesenchymal stem cells in rat skeletal muscle as a tool for functional cell status in vivo | ESMRMB (European Society for Magnetic Resonance in Medicine and Biology) | Antalya, Turkey | 1 |
| Sept 30-Oct 4 2009 | Quantification of the r1 and r2 relaxivities of mesenchymal stem cells with Gd-DTPA liposomes at 1.5 and 3.0T | ESMRMB (European Society for Magnetic Resonance in Medicine and Biology) | Antalya, Turkey | 1 |
| Nov 30-Dec 4 2009 | Molecular imaging using lipid-based nanoparticles for MRI | Radiological Society of North America (RSNA) | Chicago, USA | 1 |

**Subtotal (ECTS): 12**

## Completed courses and skills

| Date | Title | Institution/Event | Location | ECTS |
|---|---|---|---|---|
| 2015 | Workshop Hospital Management | Erasmus Desideriusschool | Rotterdam | 0.4 |
| 2015 | Workshop Medical Ethics | Erasmus Desideriusschool | Rotterdam | 0.4 |
| 2014 | Workshop Communication | Erasmus Desideriusschool | Rotterdam | 0.4 |
| 2014 | Workshop Health law | Erasmus Desideriusschool | Rotterdam | 1.0 |
| 2013-2014 | Imaging techniques (CT, MRI, US, fluoroscopy, conventional radiography) | Regional Teachings Residents Radiology, UMCU | Eindhoven | 1.2 |

| | | | | |
|---|---|---|---|---|
| 2012 | 6th Animal Imaging Workshop | Applied Molecular Imaging Erasmus (AMIE) | Rotterdam | 1.5 |
| 2012 | Radiation Protection course for Radiologists, 3M | Boerhaave Instituut | Leiden | 8 |
| 2011 | Translational imaging workshop | Applied Molecular Imaging Erasmus (AMIE) | Rotterdam | 1.5 |
| 2010 | 4th Animal Imaging Workshop | Applied Molecular Imaging Erasmus (AMIE) | Rotterdam | 1.5 |
| 2010 | Biomedical English writing | Molecular Medicine (MOLMED), Erasmus MC | Rotterdam | 0.8 |
| 2010 | Statistics: Introduction to SPSS | Molecular Medicine (MOLMED), Erasmus MC | Rotterdam | 0.8 |
| 2009 | 3rd Animal Imaging Workshop | Applied Molecular Imaging Erasmus (AMIE) | Rotterdam | 1.5 |
| 2009 | Laboratory animal science (art. 9) | Erasmus MC | Rotterdam | 3 |
| 2009 | Student supervising and mentoring | Molecular Imaging Group, Erasmus MC | Rotterdam | 7 |
| 2008 | Small animal molecular imaging | ESMRMB (European Society for Magnetic Resonance in Medicine and Biology) | Marseille, France | 1 |

| | | | | |
|---|---|---|---|---|
| 2008 | Cardiovascular applications of Molecular imaging | DiMI/EMIL (Diagnostic in Molecular Imaging/ European Molecular Imaging Laboratories) | Munster, Germany | 1 |
| 2008 | Confocal laser scanning microscopy course | Erasmus MC | Rotterdam | |

**Subtotal (ECTS): 31.2**
**Total (ECTS): 50.2**

# List of publications

## Original articles

1 Karim AF, Verdijk RM, **Guenoun J**, van Hagen PM, van Laar JA.
An inflammatory condition with different faces: immunoglobulin G4-related disease, *Neth J Med. 2016 Mar;74(3):110-5.*

2 M.R. Bernsen, **J. Guenoun**, S.T. van Tiel, G.P. Krestin, Nanoparticles and clinically applicable cell tracking (review), *Br J Radiol. 2015 Oct;88(1054):20150375.*

3 A.F. Karim, L.E.H. Westenberg, R.M. Verdijk, **J. Guenoun**, A.D.A. Paridaens, P.M. van Hagen, J.A.M. van Laar, Infliximab for IgG4 related orbital disease, *Ophthal Plast Reconstr Surg. 2016 Jan 18. [Epub ahead of print]*

4 **J. Guenoun**, G.N. Doeswijk, G.P. Krestin, M.R. Bernsen, Compartmentalization of Gd-liposomes: The quenching effect explained, *Contrast Media Mol Imaging. 2016 Mar;11(2):106-14. doi: 10.1002/cmmi.1669*

5 H. Smit, R.P. Guridi, **J. Guenoun**, D.H.J. Poot, G.N. Doeswijk, M. Milanesi, M.R. Bernsen, G.P. Krestin, S.Klein, G. Kotek, T1 Mapping in the rat myocardium at 7T using a modified CINE inversion recovery sequence, *J Magn Reson Imaging. 2014 Apr;39(4):901-10*

6 **J. Guenoun**, A. Ruggiero, G.N. Doeswijk, R.C. Janssens, G.A. Koning, G. Kotek, G.P. Krestin, M.R. Bernsen, In vivo quantitative assessment of cell viability of Gadolinium or iron-labeled cells using MRI and bioluminescence imaging, *Contrast Media Mol Imaging 2013 Mar-Apr;8(2):165-74*

7 **J. Guenoun**, A. Ruggiero, H. Schmidt, G.N. Doeswijk, S. Klein, G.C. Houston, G.P. Krestin, G. Kotek, M.R. Bernsen, In vivo MRI mapping of iron oxide labeled stem cells transplanted in the heart, *Contrast Media Mol Imaging 2013 Nov-Dec;8(6):487-94*

8 **J. Guenoun**, G.A. Koning, G.N. Doeswijk, L. Bosman, P.A. Wielopolski, G.P. Krestin, M.R. Bernsen, Cationic Gd-DTPA liposomes for highly efficient labeling of mesenchymal stem cells and cell tracking with MRI, *Cell Transplant 2012;21(1):191-205*

## Review articles

9 Ruggiero, D.L.J. Thorek, **J. Guenoun**, G.P. Krestin, M.R. Bernsen, Cell tracking in cardiac repair: what to image and how to image (review), *Eur Radiol 2012 Jan;22(1):189-204*

# Acknowledgements, Dankwoord

Googling for 'how to write an acknowledgements section in a thesis' yields the paper by Hyland *Graduates' gratitude: the generic structure of dissertation acknowledgements*. Let's pretend I haven't read the paper.

It was during an appraisal interview somewhere in 2008, in my first year as a resident radiology, that *prof. dr. Gabriel Krestin* encouraged me to consider to broaden my horizon by performing research. During our conversation terms fell such as '*molecular imaging*', '*novel field in radiology*', '*if you choose for this research project you get to attend the 'World Molecular Imaging Congress' in Nice (WMIC)* and *'I'll sleep on it'.* (I think. I don't remember exactly, but that was about the moral of the story). Certainly, '*Nice*' sounded nice, but that was not a sufficient incentive to agree to the proposition.

The proposition occurred to me as a giant leap sideways, fearing the significant interference with my training in becoming a radiologist. Numerous scenarios crossed my mind. Including the worst case scenario in which I would defend my thesis 9 years after starting research, sharing though one common denominator: undoubtedly they would pose a tremendous personal challenge. As the common thread in my life is to seek challenges rather than avoiding them, I decided to throw myself diligently into this new chapter in life in May 2008. '*Nice*' turned out to be quite cool actually. I finished this thesis on the 12th of February 2016 and defende dit on the 19th of January 2017. Worst case came true.

*Prof. dr. Gabriel Krestin*, dear Gabriel, I thank you for the inexhaustive trust you had in our research projects and for your unconditional support as my promotor. In spite of the novelty of 'molecular imaging' you were always up to date and able to keep a helicopterview. I admire your strategic insight when you suggested me to patent the discovery of Gd-liposomes and their ability to visualize cell viability. Still at this very day, I am deeply grateful for allowing me in 2007 as a resident in perhaps the most challenging radiology department in the Netherlands. Thanks for your valuable and thorough reviews of our papers.

I thank *dr. Monique Bernsen*, *dr. Nico Mollet* and *prof. Aad van der Lugt* for giving me a clear and honest description of their research fields in 2008, while I was considering the choice between '*molecular imaging*', '*cardiac imaging*' and '*carotid imaging*', respectively. In 2008 the infrastructure of the *molecular imaging group* was at an embryonic stage of development (e.g. there was no laboratory of our own yet) and the specialized 'Animal Imaging Facility' (*AIF*) was yet to be finished. *Monique* was quite clear about this. '*Molecular imaging*' or '*cellular imaging*', at least at that time, was a relatively unexplored area. Although definitely offering challenges of their own kind, '*cardiac imaging*' and '*carotid imaging*' were relatively mature research fields at that time. I got a room next to *Monique*. On the 23rd floor. Overlooking '*de Maas*'. I was literally in higher spirits. The sky was the limit.

Early in 2009, gradually becoming aware of the complexity of the field, I was back on both feet again. I needed to learn skills on animal handling, thoracotomy, anesthesia, small animal intubation, stem cell isolation from bone marrow, cell culture, cell labeling, liposome generation and MRI scanning.

Fortunately research is performed in team-work. I am therefore much indebted to our lab technicians *Sandra T. van Tiel* and *Gabriela N. Doeswijk* for their clear instructions, their patience and their time while teaching me the basics of these skills. Without your kickstart, it probably would have taken me months of time to '*DIY*' it. *Gabriela*, you deserve special attention. Working together intensively on several projects, you went above and beyond to assist wherever needed, including (but not limited to): MR scanning, cell and animal care, ICP measurements, histology, confocal fluorescence, liposome creation. *Tal vez nunca lo dejé mostrar, pero su ayuda fue indispensable para mi investigación. Muchos gracias.*

Fortunately you, *dr. Monique Bernsen*, as my co-promotor, were able to motivate me through this maze. Your approachability and preparedness to exchange thoughts '*stante pede*' are unpar-

alleled. In spite of our different professional background - you rationalizing from a biological point of view and me from a medical point of view- owing to your creativity we were always able to forge a joint plan. Whenever you found me pondering on things too much, you used to encourage me to 'just go out there and start'. Indeed, etymologically, research derives from the French word '*recherche*', on its turn derived from Latin '*cercar*', meaning 'to go around', 'to wander'.
So I went out there and wandered, ending up at the 8th floor talking to *Roel Janssens*, an always cheerful technician in the laboratory of genetics. *Roel*, without hesitation you agreed to genetically modify our mesenchymal stem cells to contain the firefly luciferase gene. Needless to say that without your efforts, chapter 3 would have been useless with actual validation of stem cell viability. Thank you man!
*Alessandro*, I got to learn you as a tremendously dedicated, concentrated and mysteriously taciturn researcher. I remember trying to break the ice by playing Lady Gaga's track '*Alejandro*' loud in our room. Soon we started exchanging our experiences on molecular/cellular imaging and I discovered that we shared the same interest in nanoparticles. You were the best sparring partner I could imagine. We spent day and night at the AIF operating and scanning, where we laid the basis for chapter 3 and 6.
*Dr. Gerben Koning,* was king when it came to liposomes. You helped me out on several occasions with my liposomes and truly taught me the subtleties of using the lipid-film hydration technique. I have yet to encounter a man with your serenity. You provided such a fantastic learning environment, helping me to keep things on track. *May your gentle soul rest in peace.*
MRI stands for "*Magnificent Research Investigator".* At least when Piotr Wielopolski is around. Hearing you talk about MRI still makes me feel a complete novice. As I'm never sure whether to speak English, Polish, Spanish or Dutch I'll just tick to a mix of all four for simplicity's sake. Thanks for teaching me the advanced MRI skills, especially in cardiac scanning.
*Gyula "the Quantifier" Kotek.* 'Seeing is believing' is a lie. No quantification, no glory. I am much indebted for your assistance in the design, implementation and analysis of the MRI relaxation time mapping sequences. I haven't quantified the amount of hours we spent together, I hope you'll forgive me for that. *Köszönöm szépen*. Good luck with your company.
*Li Li, Bilyana, Lilia*: with you I shared frustrations, hints, tips and not to forget frustrations (and sometimes each other's HEPES without notifying). I won't forget the good laughs we had in the liposome lab. It really soothed the dull and repetitive process of creating liposomes. Many thanks to all the lab technicians in the liposome lab for their hospitality!
I am indebted to all the people in the lab of experimental cardiology, especially *Marcel de Jong-Popijus*, for all your valuable tips on cell culturing, *prof. dr. Dirk Jan Duncker*, for your hospitality, kindness and for making your lab available to us. Thank you *Ewout van den Bos*, for your time to show me the intricacies of performing cryo-infarctions on a 2 cm beating rat heart.
Thank you *Nicole Kops* for your assistance in the differentiation assays.
*Dr. Kristina Djanashvili*, thank you for your enlightening discussion moments on the quenching of carboxyfluorescin cationic liposomes.
*Dr. Ingrid Renes,* special thanks to you for your kindness in providing access to the lab of pediatrics and for the tools to perform immunohistochemistry (antibodies and fluorescence microscope).
To my roommates *Joost Haeck* and our graphical designer *Ton Everaers* I can say that it was great to having surfed with you guys. Not on the internet, but on a real surfboard! There should be a sequel soon. Thanks *Joost* for the laughs we had as roommates and thanks *Ton* for your support in designing the abstract posters for each congress and for the design of "Het Boekie". I think I was your easiest 'customer' of all times ("zwarte letters op wit papier is een briljant idee, nietje d'r doorheen, hoppa en weg ermee, geen hond die 't leest").
*Lizanne Bosman,* it was an honor to supervise a bright student like you. Your dedication and creativity contributed significantly to chapter 2.

Thanks to the rest of my world. Your words "*Is je boekje nou al af??*", really encouraged me to finish things (NOT).

Lieve *jeme* en *bebe (eth ja7em Sidi Rabbi)*, *3efek ie koulsjie*. Jullie hebben me een solide basis meegegeven, een warm nest, wat me mede gevormd heeft tot wie ik nu ben. Jullie hebben me altijd vrij gelaten in mijn beslissingen en me daarin onvoorwaardelijk gesteund. Ik ben jullie daar heel dankbaar voor.
Lieve *Kaoutar*, je hebt me steeds gestimuleerd om mijn promotie af te ronden en me daar ook altijd in gesteund. Je gaf me ruimte en tijd, ook al betekende dat nog minder tijd voor jou en de kinderen. Dank voor alles. De rest laat ik je weten in persoon.
Lieve broers en zus, bedankt dat jullie altijd voor me klaarstaan. Wat zou het leven toch saai zijn zonder de *fsjegth*.
*Nordin en Yosri*, onbeschrijflijk is het gevoel wanneer ik na een lange werkdag naar huis rijd om door jullie getrakteerd te worden op een omhelzing. Wat kunnen jullie al goed voetballen! Zodra het boekje af is gaan we *CR7* toejuichen in het *Estadio Santiago Bernabéu*. In jullie Real outfit. Beloofd is beloofd. En ja Yosri, je Bob de Bouwer koffer mag dan ook mee!